

**MOLECULE DESIGN AND SURFACE FUNCTIONALIZATION
STUDY OF METAL-OXIDE SEMICONDUCTORS**

by

YUAN CHEN

A Dissertation submitted to the

Graduate School-Newark

Rutgers, The State University of New Jersey

In partial fulfillment of the requirements

for the degree of

Doctor of Philosophy

Graduate Program in Chemistry

written under the direction of

Professor Elena Galoppini

and approved by

Newark, New Jersey

May 2019

©[2019]

YUAN CHEN

ALL RIGHTS RESERVED

ABSTRACT OF THE DISSERTATION

MOLECULE DESIGN AND SURFACE FUNCTIONALIZATION STUDY OF METAL-OXIDE SEMICONDUCTORS

By YUAN CHEN

Dissertation Director:

Professor Elena Galoppini

Metal-oxide semiconductor materials have found application in numerous fields such as photo-electronics, catalysis, and sensing. The interfaces between semiconductor materials and bio-, organic molecules used to functionalize the semiconductor materials have attracted considerable attention. It is necessary to better understand and improve the surface chemistry of semiconductor materials in order to develop a new generation of functional devices with excellent performance.

In the first project of this thesis, which is chapter B, we present an efficient functionalization and characterization method for $\text{Mg}_x\text{Zn}_{1-x}\text{O}$ ($4\% < x < 5\%$) nanorod (abbreviated MZO_{nano}) films. FTIR microscopic imaging, was employed, for the first time, to visualize the binding distribution of organic molecules on a large area (μm scale) of semiconductor films. The influence of various parameters including solvent, concentration, binding time, and morphology of MZO_{nano} film on the binding of 11-azidoundecanoic acid

on MZO_{nano} film were investigated. The stability of the functionalized MZO_{nano} film to etching and solvents was also evaluated.

In chapter C, a stepwise functionalization method was developed to bind hexadecyl alkynated folic acid (HAFA), which has a high affinity to the cancer cell biomarker-folate binding protein. The binding methodology involved two steps. Step A, binding with 11-azidoundecanoic acid, which was fully studied by FTIR microscopic imaging, and Step B, immobilization of HAFA via copper-catalyzed azide-alkyne click reaction (CuAAC). The surface click reaction between functionalized MZO_{nano} film and HAFA was monitored by FTIR microscopic imaging and fluorescence spectroscopy. The resulting MZO_{nano} film was bound with a bio-reactive HAFA layer that could be used in biosensing. This stepwise method was successfully applied in the functionalization of MZO_{nano}-modified quartz crystal microbalance (QCM) and MZO_{nano}-modified thin film transistor (TFT), leading to QCM- and TFT- based biosensors with high sensitivity. The sensing of a folate-binding protein is still in progress.

In the second project of this thesis, that is chapter D, we describe an innovative design of the organic molecules that will be used to functionalize semiconductor materials for renewable energy projects. For example, in a dye-sensitized solar cell (DSSC), the electron transfer between sensitizer molecule and semiconductor surface is the key step that might be affected by the energy level alignment between sensitizer molecule and semiconductor surface. This energy level alignment is directly related to the properties of the sensitizer molecule. In this thesis, we introduce a dipole containing bridge into the sensitizer to tune the energy alignment between sensitizer and semiconductor-TiO₂, using oligopeptides

made of α -aminoisobutyric acid (Aib). The synthesis and optical characterization of sensitizer molecules combining such dipole bridge with di-tert-butyl-perylene (DTBPe) and zinc tetraphenylporphyrin (ZnTPP) chromophores are reported in this thesis. The element composition and occupied and unoccupied electronic structure (particularly the HOMOs and LUMOs energy) of ZnTPP-(Aib)₆-COOH were probed by a combination of X-ray and Ultraviolet photoemission spectroscopies (XPS and UPS). The binding study of these sensitizers on TiO₂ film and the energy level alignment study are still in progress.

Acknowledgement

The first and foremost person that I would like to thank is my advisor, Dr Elena Galoppini, for her guidance and assistance during my five years at Rutgers. Her knowledge has always inspired me, and her kindness has always touched my heart. I would also thank everyone in my group, both past and present for their numerous helps. Thank you, Dr. Yan Cao, Dr. Andrew Kopecky, Dr. Hao Tang, Dr. Runkun Sun, Dr. Hao Fan, Xiuyuan Ma, Ian Weiss, Ryan Harmer, and Shiv Misra. I really enjoyed the time working with you.

I would like to thank all our collaborators, Dr. Pavel Ivanoff Reyes, Prof. Yicheng Lu, Keyang Yang, Rui Li, and Guangyuan Li from the department of electrical and computer engineering at Rutgers University-New Brunswick, without whom, the work in this dissertation can't be accomplished. I would especially thank Dr. Pavel Ivanoff Reyes and Prof. Yicheng Lu for your instant reply to my emails no matter how late it is. I want to thank our collaborators in our department, Dr. Qihong Zhang, Dr. Carol Flach, and Prof. Richard Mendelsohn for your generous help. Thank you Dr. Qihong Zhang for not only been a collaborator but also a lifetime friend of me. My thank also extends to our collaborators, Dr. Sylvie Rangan and Prof. Robert Bartynski from department of physics and astronomy at Rutgers University-New Brunswick and Prof. Lars Gundlach from department of physics and astronomy at University of Delaware, for helping me working in this multidisciplinary environment.

I am grateful to my committee members, Prof. Richard Mendelsohn and Prof. Huixin He from Rutgers University-Newark and Prof. Yicheng Lu from Rutgers University-New

Brunswick. Most of them are also my collaborators. Thank you so much for your time and effort in reading and correcting my thesis and giving valuable suggestions.

I want to thank NSF grant, NSF-CBET 1264488, for its support on my first project, MZO_{nano} films functionalization. I also want to thank DOE-BES grant, DE-FG02-01ER15256, for its support on my second project, the design of dipole peptide and chromophores.

I would also thank the faculty members of the department of Chemistry-Rutgers University. Thank you Dr. Roman Brukh for your help with ESI measurement and Dr. Lazaros Kakalis for your help with NMR measurement. Thank you, Judy Slocum, Lorraine McClendon, and Monika Dabrowski for your helpfulness.

Last but not least, I would like to thank my family members. Love you all with all my heart during all my life. Thank you, my mom and dad for giving me life and love. You are always my support whenever I am making any decisions. I would especially thank my husband, Dr. Xun Gao. You are the one who knows me and loves me the most in the world.

Dedication

To my grandfather

Xiaolin Pan

I will love myself as how you loved me

Table of Contents

Abstract of the Dissertation	ii
Acknowledgement	v
Dedication	vii
Table of Contents	viii
List of Figures.....	xi
List of Schemes	xxvi
List of Tables	xxvii
Objectives.....	xxviii
Chapter A: General Introduction.....	1
A.1 FTIR microscopic image	2
A.2 Stepwise functionalization	4
A.3 Click reaction	8
A.4 Molecular design of sensitizers for metal oxide surfaces.....	11
A.5 Aib-homopeptides	15
Chapter B: Surface modification of nanostructured ZnO/MZO films and characterization by FTIR microscopic imaging.....	19
B.1 Introduction	20
B.2 Study of modification of ZnO/MZO nanostructured film by FTIR microscopic imaging.....	24
B.2.1 Solvent effect	26
B.2.2 Time dependence	28
B.2.3 Morphology effect	30
B.2.4 Concentration effect.....	32

B.2.5 Stability test	34
B.3 Conclusions	36
B.4 Experimental Section	37
Chapter C: Stepwise functionalization of MZO nanostructured film for biosensors	42
C.1 Introduction	43
C.2 Synthesis of HAFA.....	47
C.3 Study of immobilization of HAFA on azido-functionalized MZO _{nano} films by FTIR microscopic imaging	49
C.3.1 Control experiment 1 (stability of azido-functionalized MZO _{nano} films in THF)	49
C.3.2 Control experiment 2 (physisorption of HAFA on MZO _{nano} films)	50
C.3.3 Immobilization of HAFA on azido-terminated MZO _{nano} films	52
C.4 Study of immobilization of HAFA on functionalized MZO _{nano} film by Fluorescence spectroscopy	54
C.5 Preparation of MZO _{nano} -QCM based biosensor.....	56
C. 6 Preparation of MZO _{nano} -TFT based biosensor.....	58
C.7 Conclusions	61
C.8 Experimental Section	62
Chapter D: Dipole-bridge design for chromophore-bridge-anchor at semiconductor surfaces.....	69
D.1 Introduction	70
D.2 Synthesis and conformational study of (Aib) _n peptide.....	72

D.3 Surface binding study of (Aib) _n peptide	80
D.4 Synthesis and spectroscopic investigation of Perylene-peptide sensitizers	83
D.5 Synthesis and spectroscopic investigation of Porphyrin-peptide sensitizers	86
D.6 Conclusions	91
D.7 Experimental Section	92
Chapter E: Summary	109
References	114
Appendix	126

List of Figures

Fig. A-1 Two methods for covalent binding of biomolecules to metal oxide semiconductor surface	5
Fig. A-2 ZnO nanotips stepwise surface modification via two routes, route A: thiol-disulfide exchange reaction and route B: NBS-ester hydrolysis. Adapted with permission from [31]......	5
Fig. A-3 Binding modes between carboxylic acid group and a metal oxide semiconductor surface	6
Fig. A-4 The binding of HQ-PA on In ₂ O ₃ nanowires, after electrochemical oxidation (step i), after immobilization of thiol-terminated DNA (step ii), and after attaching of complementary DNA strand (step iii). Adapted with permission from [33]	13
Fig. A-5 The immobilization scheme of covalent binding of antibodies to the ZnO surface using (3-glycidyloxypropyl)trimethoxysilane. Adapted with permission from [37]	7
Fig. A-6 The schematic representation of click reactions on surfaces. Adapted with permission from [38]......	8
Fig. A-7 The original Huisgen reaction and CuAAC	10
Fig. A-8 (a, left) Schematic overview of the light irradiation and electron injection process in a DSSC and (b, right) Simple energy level diagram of HOMO-LUMO of sensitizer and CB of semiconductor	11

Fig. A-9 Schematic energy level diagram of meta/polymer interfaces: (a) untreated interface. (b) insertion of a dipole layer pointing to metal surface and (c) insertion of a dipole layer pointing from metal surface. Adapted with permission from [57]	13
Fig. A-10 (a) Molecular structure of ZnTPP compounds used in this study. (b) Schematic diagram of how a dipole in a linker shifts the energy level of a ZnTPP compounds with respect to the CB edge of semiconductor. Adapted with permission from [60]	14
Fig. A- 11 The 3_{10} -helical structure of <i>para</i> -bromobenzoyl-(Aib) ₁₀ - <i>tert</i> -butoxy in the crystal state. Adapted with permission from [64]	15
Fig. A-12 Schematic diagram for the long-range electron transfer from the ferrocene moiety to gold surface through a helix peptide by a hopping mechanism. Adapted with permission from [65]	16
Fig. A-13 Fullerene-peptide-radical system with reversed dipole direction and the redox behavior. Adapted with permission from [77]	17
Fig.B-1 <i>Top</i> : FESEM images of MOCVD-grown ZnO _{nano} film (a) before, (b) after reacting with 10 mM 11-azidoundecanoic acid solution (solvent: 1:2 ethanol/1-butanol) for 17h at r.t, and (c). after reacting with 10 mM alkynated folic acid solution (solvent: dimethyl sulfoxide); <i>bottom</i> : FESEM images of MOCVD-grown MZO _{nano} film (a) before, (b) after reacting with 10 mM 11-azidoundecanoic acid solution (solvent: 1:2 ethanol/1-butanol) for 17h at r.t, and	

(c). after reacting with 10 mM alkynated folic acid solution (solvent: dimethyl sulfoxide).....	21
Fig. B-2 FESEM images of ~0.9 μm -thick MOCVD-grown MZO_{nano} film on sapphire (a) top view, (b) side view	22
Fig. B-3 FT-IR-ATR spectra of different detection areas on MZO_{nano} film after binding with 11-azidoundecanoic acid (solvent: 1:2 ethanol/1-butanol) for 17 hours at r.t	23
Fig. B-4 FTIR spectra of (a) neat 1 and (b) 1 / MZO_{nano} . Adapted with permission from [127]	25
Fig. B-5 Schematic representation of how images are reported: selected areas in a MZO_{nano} film and corresponding FTIR image grid	26
Fig. B-6 FTIR Images of the integrated band area of (i) the azido region $2212\text{-}2064\text{ cm}^{-1} (\pm \text{STD})$, (ii) the carboxylate region $1564\text{-}1480\text{ cm}^{-1} (\pm \text{STD})$ of MZO_{nano} films after binding with (a) 10 mM 1 solution (solvent: 1:2 ethanol/1-butanol) and (b) 10 mM 1 solution (solvent: 3-MPN). The data were collected after 17 h binding. Adapted with permission from [127].....	27
Fig. B-7 Top: Images of the integrated band area of $2212\text{-}2064\text{ cm}^{-1}$ region ($\pm \text{STD}$) of MZO_{nano} films before and after binding with a 10 mM 1 in 3-MPN solution over time. Bottom: FESEM image of the MZO_{nano} film used in the experiments (before binding) (left) and enlarged selected area (right). (Scale: 5 μm left, 1 μm right). Adapted with permission from [127]	29

Fig. B-8 Images of the integrated band area of the azido region $2212\text{-}2064\text{cm}^{-1}$ (\pm STD) of two areas after binding with 10 mM **1** in 3-MPN as function of time. Adapted with permission from [127]29

Fig. B-9 (a)-(c): SEM images at different scales of sharp nanotips morphology before binding, and (d) a visible micrograph (before binding, $200\times 200\text{ }\mu\text{m}^2$) taken of the same area from which FTIR images were acquired as a function of binding time (bottom). (e) FTIR images of the integrated band area, $2212\text{-}2064\text{ cm}^{-1}$ (\pm STD) of area 1 after binding with 10 mM **1** in 3-MPN as function of time. Adapted with permission from [127].....30

Fig. B-10 (a)-(c): SEM images at different scales of nanorods grown in different orientation type morphology (before binding, top) and (d) a visible micrograph (before binding, $200\times 200\text{ }\mu\text{m}^2$) taken of the same area from which FTIR images were acquired as a function of binding time (bottom). (e) FTIR images of the integrated band area of $2212\text{-}2064\text{ cm}^{-1}$ (\pm STD) of area 2 after binding with 10 mM **1** in 3-MPN as function of time. Adapted with permission from [127]31

Fig. B-11 Crystal structure of Wurtzite ZnO. Adapted with permission from [127]31

Fig. B-12 (a)-(b): SEM images at different scales of nanorods with different growth density type morphology (before binding, top) and (c) a visible micrograph (before binding, $200\times 200\text{ }\mu\text{m}^2$) taken of the same area from which FTIR

images were acquired as a function of binding time (bottom). (d) FTIR images of the integrated band area of 2212-2064 cm^{-1} (\pm STD) of area 3 after binding with 10 mM 1 in 3-MPN as function of time	32
Fig. B-13 FTIR images of the integrated band area of 2212-2064 cm^{-1} region (\pm STD) of MZO _{nano} films before and after binding with a 10 mM 1 in 3-MPN solution, 40 mM 1 in 3-MPN solution, and 100 mM 1 in 3-MPN solution over time.....	33
Fig. B-14 Proposed intermolecular hydrogen-bonding structures of 1 in 100 mM solutions of 1	33
Fig. B-15 Carbonyl region of the ^{13}C NMR spectra of 1 in CDCl_3 : (a) 10 mM, (b) 40 mM, and (c) 100 mM	34
Fig. B-16 Images of the integrated band area of 2212-2064 cm^{-1} (\pm STD) of a MZO _{nano} film (a) after 22h binding with 1 , (b) after immersion of such functionalized film in 3-MPN solution at r.t for 24 h, and (c) after immersion of such functionalized film in 3-MPN solution at 40 °C for 24 h.....	35
Fig. B-17 Images of the integrated band area of 2212-2064 cm^{-1} (\pm STD) of a MZO _{nano} film (a) after 22h binding with 1 and (b) after immersion of such functionalized film in ethanol solution at r.t for 24 h, (c) after immersion of such functionalized film in ethanol solution at 40 °C for 4 h, and (d) after immersion of such functionalized film in ethanol solution at 40 °C for 24 h	35

Fig. B-18 Images of the integrated band area of $2212\text{-}2064\text{cm}^{-1}$ (\pm STD) of a functionalized MZO_{nano} film (a) after immersed in ethanol solution at $40\text{ }^{\circ}\text{C}$ for 24 h, (b) after 22h binding with 10 mM 1 (solvent: 3-MPN).....	36
Fig. B-19 Transmission UV-vis spectra of ZnO_{nano} and MZO_{nano} film (aquired by Dr. Pavel Ivanoff Reyes from Dr. Lui's group)	39
Fig. B-22 Absorption spectra of ZnO and MZO film (aquired by Dr. Pavel Ivanoff Reyes from Dr. Lui's group).....	40
Fig. C-1 Structure of Folate receptor α react with folic acid. Adapted with permission from [134].....	45
Fig. C-2 Image (a) and schematic side image (b) of MZO_{nano} - QCM (taken by Dr. Pavel Ivanoff Reyes from Dr. Lu's group).....	46
Fig. C-3 Schematic and top image of MZO_{nano} - TFT (taken by Dr. Pavel Ivanoff Reyes from Dr. Lu's group).....	47
Fig. C-4 ATR-FTIR spectrum of HAFA	48
Fig. C-5 Images of the integrated band area of the azido region $2212\text{-}2064\text{cm}^{-1}$ (\pm STD) of (a) pristine MZO_{nano} film, (b) after binding with linker, (c) and after immersing in THF for 25 min under shaking	50
Fig. C-6 FTIR spectra of azido-functionalized MZO_{nano} film before (blue line) and after (red line) immersion in THF for 25 min under shaking	50

Fig. C-7 Physisorption experiment. Images of the integrated band area of the N-H stretching region $3460\text{-}2988\text{ cm}^{-1}$ (\pm STD) of (a) pristine MZO_{nano} film, (b) after immersed in HAFA ($\text{CuSO}_4/\text{TBTA}/\text{TCEP}$) THF solution under shaking for 15 min, (c) and after rinsing with THF for 10 min	51
Fig. C-8 FTIR spectra of pristine MZO_{nano} film after (a, red line) immersing in 20 mM HAFA ($\text{CuSO}_4/\text{TBTA}/\text{TCEP}$) THF solution under shaking for 15 min (red line), and after rinsing with THF for 10 min (b, blue line)	51
Fig. C-9 FTIR spectra of azido-terminated MZO_{nano} film before (a, black line) and after immobilization with HAFA for 5 min (b, blue line) and 15 min (c, red line)	53
Fig. C-10 Images of the integrated band area of the azide region $2212\text{-}2064\text{ cm}^{-1}$ (\pm STD) of (a) pristine MZO_{nano} film, (b) after binding with 1, (c) after immobilization of HAFA ($\text{CuSO}_4/\text{TBTA}/\text{TCEP}$) THF solution with shaking for 5 min, and (d) 15 min, respectively	53
Fig. C-11 Images of the integrated band area of the N-H stretching region $3460\text{-}2988\text{ cm}^{-1}$ (\pm STD) of (a) pristine MZO_{nano} film, (b) after binding with 1, (c) after immobilization of HAFA ($\text{CuSO}_4/\text{TBTA}/\text{TCEP}$) THF solution with shaking for 5 min, and (d) 15 min	54
Fig. C-12 Normalized absorption (left, black, solid line) and emission (right, red, dotted line) spectra of HAFA in methanol. $\lambda_{\text{ex}}=369\text{ nm}$	55

Fig. C-13 Fluorescence spectra of HAFA in methanol (a, green, dotted line), MZO _{nano} film before (b, black, solid line), after binding with 1 (c, blue, solid line), and after immobilization of HAFA (d, red, dash line). $\lambda_{ex}=369$ nm.....	56
Fig. C-14 Acoustic impedance spectra (Ohms) of MZO _{nano} -QCM before (black dots), after binding with 1 for 22 h (step A, red aquares), and after immobilization of HAFA for 5 min (step B, green triangles) and 15 min (step B, blue triangles) (taken by Dr. Pavel Ivanoff Reyes from Dr. Lu's group)	57
Fig. C-15 The I_{DS} - V_{GS} transfer characteristics of an MZO _{nano} -TFT before and after linker binding (taken by Guang yuan Li from Dr. Lu's group).....	59
Fig. C-16 Zoomed in linear region of transfer characteristics of an MZO _{nano} -TFT before and after linker binding (taken by Guang yuan Li from Dr. Lu's group)	60
Fig. C-17 Schematic of immersing method	65
Fig. C-18 FESEM image of MZO _{nano} -QCM.....	66
Fig.D-1 Design of dipole linker (Z-(Aib) ₆ -OtBu) and chromophores	70
Fig.D-2 Two forms of the deprotection of Z-(Aib) ₆ -OtBu releasing C- and N- reaction sites and the corresponding coupling with chromophores	71
Fig.D-3 Chemical structures of the target perylene-based and porphyrin-based sensitizers with reversed dipoles.....	72
Fig.D-4 Canonical helical conformations of α -helical structure (left) and 3_{10} -helical structure (right). Side views (top) and views along the axis of a helix (bottom).	

Dotted lines indicate hydrogen bonds between atoms in the backbone of peptide.	
Adapted with permission from [175]	75
Fig.D-5 Infrared spectra in the 1420-1780 cm ⁻¹ region for Z-(Aib) ₂ -OtBu, Z-(Aib) ₃ -OtBu and Z-(Aib) ₆ -OtBu in CHCl ₃ (5mM).....	76
Fig.D-6 The i→i+3 hydrogen bonding between the third N-H groups at N-terminus and the urethan carbonyl group of Z-(Aib) ₆ -OtBu.....	77
Fig.D-7 Infrared spectra in the region 3250-3550 cm ⁻¹ for the (Aib) _n peptides (Z-(Aib) ₂ - OtBu, Z-(Aib) ₃ -OtBu and Z-(Aib) ₆ -OtBu) in CHCl ₃ (5mM).....	78
Fig.D-8 ¹ HNMR of Z-(Aib) ₆ -OtBu in CDCl ₃ (a, bottom), and 4:5 (CD ₃) ₂ SO (DMSO- D ₆)/CDCl ₃ (b, top)	79
Fig.D-9 The 3 ¹⁰ -helical model for Z-(Aib) ₆ -OtBu.....	80
Fig.D-10 FTIR-ATR spectrum of neat Z-(Aib) ₆ -OH (top, blue line) and representative FTIR spectrum (one pixel) of pristine TiO ₂ (bottom, black line) and Z-(Aib) ₆ - OH/TiO ₂ (bottom, red line)	82
Fig.D-11 FTIR image of the integrated band area of the region 1700-1490 cm ⁻¹ (±STD) of pristine TiO ₂ (left) and Z-(Aib) ₆ -OH/TiO ₂ (right)	82
Fig.D-12 Synthesis of DTBPe-CONH-(Aib) ₆ -OH(+ ⁻) (7)	84
Fig.D-13 Synthesis of DTBPe-NHCO-(Aib) ₆ -succinate-OH(- ⁺) (11)	85

Fig.D-14 Normalized absorption (left) and emission (right) spectra of DTBPe-CONH-(Aib) ₆ -OH(+-) (7) and DTBPe-benzoic acid in methanol. $\lambda_{ex}=446$ nm	86
Fig.D-15 Synthesis of ZnTPP-CONH-(Aib) ₆ -OH(+-) (15)	87
Fig.D-16 Synthesis of ZnTPP-NHCO-(Aib) ₆ -succinate-OH(-+) (19)	88
Fig.D-17 Normalized absorption (left) and emission (right) spectra of ZnTPP-CONH-(Aib) ₆ -OtBu(+-) (14) and ZnTPP-benzoic acid (13) in methanol. $\lambda_{ex}=421$ nm..	89
Fig.D-18 Home-made flat bottom copper sample holder for XPS and UPS measurements (prepared by Dr. Sylvie Rangan from Dr. Bartynski's group)	89
Fig.D-19 XPS spectrum of ZnTPP-CONH-(Aib) ₆ -OH(+-) (15) (aquired by Dr. Sylvie Rangan from Dr. Bartynski's group)	90
Fig.D-20 UPS spectrums and calculated DOS of ZnTPP-CONH-(Aib) ₆ -OH(+-) (15) (aquired by Dr. Sylvie Rangan from Dr. Bartynski's group)	91
Fig.D-21 Steps of Nanostructured TiO ₂ thin film preparation	94
Fig. 0-1 Images of the integrated band area of 1564-1480 cm ⁻¹ region (\pm STD) of MZO _{nano} films before and after binding with 10 mM 11-azidoundecanoic acid in 3-MPN solution over time. Adapted with permission from [127]	130
Fig. 0-2 Images of the integrated band area of the azido region 1564-1480 cm ⁻¹ (\pm STD) of two areas after binding with 10 mM 1 in 3-MPN as function of time. Adapted with permission from [127]	130

Fig. 0-3 Visible micrograph (before binding, $200 \times 200 \mu\text{m}^2$) taken of nanorods grown in different orientation type morphology from which FTIR images were acquired as a function of binding time. FTIR images of the integrated band area, $1564\text{-}1480 \text{ cm}^{-1}$ (\pm STD) of area 1 after binding with 10 mM **1** in 3-MPN solution as function of time. Adapted with permission from [127].....130

Fig. 0-4 Visible micrograph (before binding, $200 \times 200 \mu\text{m}^2$) taken of nanorods grown in different orientation type morphology from which FTIR images were acquired as a function of binding time (bottom). FTIR images of the integrated band area, $1564\text{-}1480 \text{ cm}^{-1}$ (\pm STD) of area 1 after binding with 10 mM **1** in 3-MPN solution as function of time. Adapted with permission from [127]130

Fig. 0-5 Visible micrograph (before binding, $200 \times 200 \mu\text{m}^2$) taken of nanorods with different growth density type morphology from which FTIR images were acquired as a function of binding time (bottom). FTIR images of the integrated band area, $1564\text{-}1480 \text{ cm}^{-1}$ (\pm STD) of area 1 after binding with 10 mM **1** in 3-MPN solution as function of time. Adapted with permission from [127].....131

Fig. 0-6 Images of the integrated band area of $1564\text{-}1480 \text{ cm}^{-1}$ (\pm STD) of a MZO_{nano} film (a) after 22h binding with **1**, (b) after immersion of such functionalized film in 3-MPN solution at r.t for 24 h, and (c) after immersion of such functionalized film in 3-MPN solution at 40°C for 24 h131

Fig. 0-7 Images of the integrated band area of 1564-1480 cm^{-1} (\pm STD) of a MZO_{nano} film	
(a) after 22h binding with 1 and (b) after immersion of such functionalized film	
in ethanol solution at r.t for 24 h, (c) after immersion of such functionalized film	
in ethanol solution at 40 $^{\circ}\text{C}$ for 4 h, and (d) after immersion of such	
functionalized film in ethanol solution at 40 $^{\circ}\text{C}$ for 24 h.....	131
Fig. 0-8 Images of the integrated band area of 1564-1480 cm^{-1} (\pm STD) of a	
functionalized MZO_{nano} film (a) after immersed in ethanol solution at 40 $^{\circ}\text{C}$ for	
24 h, (b) after 22h binding with 10 mM 1 (solvent: 3-MPN).....	131
Fig. 0-9 FESEM image of MZO_{nano} film after immersing in EtOH at 40 $^{\circ}\text{C}$ for 24 h	132
Fig. 0-10 Droplet method.....	132
Fig. 0-11 ^1H NMR of 1 in CDCl_3	133
Fig. 0-12 ^{13}C NMR of 1 in CDCl_3	133
Fig. 0-13 ^1H NMR of II in DMSO-d_6	134
Fig. 0-14 ESI-MS spectra (top) and simulated (bottom) of II	134
Fig. 0-15 ^1H NMR of III in DMSO-d_6	135
Fig. 0-16 ESI-MS spectra (top) and simulated (bottom) of III	135
Fig. 0-17 ^1H NMR of 2 in CDCl_3	136
Fig. 0-18 ^{13}C NMR of 2 in CDCl_3	136

Fig. 0-19 ESI-MS spectra of 2	137
Fig. 0-20 ^1H NMR of 3 in CDCl_3	138
Fig. 0-21 ^{13}C NMR of 3 in CDCl_3	138
Fig. 0-22 ESI-MS spectra of 3	139
Fig. 0-23 ^1H NMR of 4 in CD_3OD	140
Fig. 0-24 ^{13}C NMR of 4 in CD_3OD	140
Fig. 0-25 ESI-MS spectra of 4	141
Fig. 0-26 ^1H NMR of 5 in CDCl_3	142
Fig. 0-27 ^{13}C NMR of 5 in CDCl_3	143
Fig. 0-28 ESI-MS spectra of 5	144
Fig. 0-29 ^1H NMR of 6 in CDCl_3	145
Fig. 0-30 ^{13}C NMR of 6 in CDCl_3	146
Fig. 0-31 ESI-MS spectra of 6	147
Fig. 0-32 ^1H NMR of 7 in CD_3OD	148
Fig. 0-33 ESI-MS spectra of 7	149
Fig. 0-34 ^1H NMR of 8 in DMSO-d_6	150
Fig. 0-35 ^{13}C NMR of 8 in DMSO-d_6	151

Fig. 0-36 ESI-MS spectra of 8	152
Fig. 0-37 ^1H NMR of 9 in CDCl_3	153
Fig. 0-38 ^{13}C NMR of 9 in CDCl_3	154
Fig. 0-39 ESI-MS spectra of 9	155
Fig. 0-40 ^1H NMR of 10 in CDCl_3	156
Fig. 0-41 ^{13}C NMR of 10 in CDCl_3	157
Fig. 0-42 ESI-MS spectra of 10	158
Fig. 0-43 ^1H NMR of 11 in CD_3OD	159
Fig. 0-44 ESI-MS spectra of 11	160
Fig. 0-45 ^1H NMR of 12 in CDCl_3	161
Fig. 0-46 ^1H NMR of 13 in CDCl_3	162
Fig. 0-47 ^{13}C NMR of 13 in CDCl_3	163
Fig. 0-48 ESI-MS spectra of 13	164
Fig. 0-49 ^1H NMR of 14 in CDCl_3	165
Fig. 0-50 ^{13}C NMR of 14 in CDCl_3	166
Fig. 0-51 ESI-MS spectra of 14	167
Fig. 0-52 ^1H NMR of 15 in CDCl_3	168

Fig. 0-53 ^{13}C NMR of 15 in CDCl_3	169
Fig. 0-54 ESI-MS spectra of 15	170
Fig. 0-55 ^1H NMR of 16 in $\text{DMSO}-d_6$	171
Fig. 0-56 ^{13}C NMR of 16 in $\text{DMSO}-d_6$	172
Fig. 0-57 ESI-MS spectra of 16	173
Fig. 0-58 ^1H NMR of 17 in CD_3OD	174
Fig. 0-59 ^{13}C NMR of 17 in CD_3OD	175
Fig. 0-60 ESI-MS spectra of 17	176
Fig. 0-61 ^1H NMR of 18 in CDCl_3	177
Fig. 0-62 ^1H NMR of 19 in CD_3OD	178
Fig. 0-63 ESI-MS spectra of 19	179

List of Schemes

Scheme B-1 Scheme of the functionalization of MZO_{nano} films	24
Scheme C-1 Stepwise functionalization of MZO_{nano} film	44
Scheme C-2 The copper catalyzed azide-alkyne Huisgen cycloaddition reaction	44
Scheme C-3 Synthesis of HAFA	48
Scheme D-1 Synthesis of $\text{Z}-(\text{Aib})_6\text{-OtBu}$	74
Scheme D-2 Deprotection at the C-terminus of $\text{Z}-(\text{Aib})_6\text{-OtBu}$	81
Scheme D-3 Proposed binding of TiO_2 thin films with $\text{Z}-(\text{Aib})_6\text{-OH}$	81

List of Tables

Table C-1 Frequency shifts of MZO _{nano} -QCM after each chemical step.....	58
Table C-2 Summarized the Drain currency shifts of MZO _{nano} -TFT after each chemical step	60
Table D-1 Measured and calculated element composition of ZnTPP-CONH-(Aib) ₆ -OH(+ -) (14)	90

Objectives

Metal oxide semiconductors, such as ZnO, $\text{Mg}_x\text{Zn}_{1-x}\text{O}$ ($4\% < x < 5\%$) (MZO), TiO_2 , that can be grown in a diversity of nanostructures on a variety of substrates and functionalized with molecular compounds of varying complexity, have attracted extensive attention, both theoretically and experimentally, in the photo-electronics, catalytical, and sensing fields. There are many approaches to improve the performance of devices made by these semiconductor materials: precise control of the chemical and physical properties of the semiconductors, innovative design of the bound molecules and effective modification methods. We are particularly interested in the study of the interface of semiconductor materials, specifically in the ability to control the surface functionalization at the molecular level.

To do that, it is necessary to control and characterize the binding. The development of surface modification methodology and the ability to design the next generation of functional devices largely depends on these abilities.

Metal oxide semiconductors ZnO/MZO are excellent platform for biosensors, because are multifunctional, form highly ordered nanostructures, are biocompatible, and can be made optically transparent and conductive, piezoelectric, or ferromagnetic through doping. ZnO/MZO-based biochemical sensors can be developed through functionalization of ZnO/MZO with bio-, organic molecules. The sensitivity and selectivity of biosensor largely depend on the precise control of the interfacial chemistry between molecule and ZnO/MZO films, which is possible by practical surface characterization technique.

Metal oxide semiconductors ZnO/TiO₂, which are low cost, non-toxic, photostable and wide band gap (3.2 eV), are also ideal materials for dye-sensitized solar cells (DSSCs). As the developing of renewable energy appears to be the most feasible solution to global warming and fossil fuel exhaustion, improving the efficiency of solar cells is one of the major goals of modern science and engineering. There are many aspects may affect the efficiency of solar cells, such as the light harvesting ability, charge transportation and recombination, and electron injection from sensitizer to semiconductor. The electron injection from sensitizer to semiconductor is highly dependent upon the energy level alignment of the sensitizer/ semiconductor interface. An interesting concept is that through precise design of the sensitizer molecule, the energy level alignment of the sensitizer/ semiconductor interface can be tuned.

This thesis encompasses two projects sharing the common interest in semiconductor functionalization methods. The first project focus on the developing of novel characterization technique to study the surface and interface chemistry of metal oxide semiconductors and the generating of efficient surface modification methodology. The second project emphasis on the preparation of novel functional molecules that can bring semiconductor innovative properties after modification.

In chapter A, a combined introduction of the both projects is presented with a description of FTIR microscopic imaging, stepwise functionalization, “click” reaction methods, and role of permanent dipoles at interface. Chapter B and Chapter C focus on the first project. The use of FTIR microscopic imaging in the functionalization study of MZO with bifunctional molecule was discussed in chapter B. Optimized functionalization parameters

were established. MZO-based biosensor utilizing quartz crystal microbalance (QCM) and thin film transistor (TFT) as substrates were prepared by stepwise functionalization method. The results and discussion of the functionalization and characterization work are presented in chapter C. Chapter D focuses on the second project, the synthesis and characterization of modular sensitizers. The binding of these modular sensitizers on TiO_2 surfaces and spectroscopic studies of the sensitizer molecules were described. Chapter E is a summary and outlines future work.

Chapter A: General introduction

A.1 FTIR microscopic imaging

Fourier transform infrared (FTIR) spectroscopy is one of the established analytical techniques that has been applied in research and applied sciences with a very long history. Since the first discovery of IR in the electromagnetic spectrum about two centuries ago, FTIR spectroscopy has been employed in medicine, chemistry, astronomy, material science, and many other disciplines¹⁻⁶. In particular, FTIR microscopic imaging has emerged as a very powerful method that has attracted significant attention⁷⁻¹¹. Like traditional FTIR spectroscopy, there are four types modes that can be used in FTIR microscopic imaging: transmission, reflection, transflection, and attenuated total reflection (ATR)¹².

A typical FTIR microscopic imaging involves the integration of an interferometer and a large number of mercury cadmium telluride (MCT). FTIR microscopic imager works similar to a standard interferometer with a single detector, but, instead of acquiring the signal of a single detector, it acquires the signal of a number of detectors. An FTIR microscopic image can be obtained with a single detector or with a linear array of individual detectors or with a highly sensitive focal plane array (FPA) detectors, which was invented by Lewis and Levin in 1995¹³. The detector element is also called “pixels”, each pixel contains an entire FTIR spectrum. The linear array detectors contain 16×1 to 256×1 detector element, it can capture an image of a small sized sample area rapidly. The spatial resolution of the FTIR microscopic image was directly determined by the size of pixels. The time frame was determined by the size of sample area of interest, the size of pixel, and the number of detectors in a linear array or FPA.

After mapping of sample of interest and data processing, a FTIR microscopic image is generated. In the image, the intensity (color) of pixels taken at a certain wavelength reflect the interaction of IR radiation with the chemical analyzed at the same sample area, generally speaking, the amount of chemicals. There is a correlation between image and visible information that helps to locate the mapping area.

FTIR microscopic imaging instruments are commercially available, however, the application is largely limited to biophysics studies¹⁴⁻¹⁶. The capability of FTIR microscopic imaging to provide detailed images make it particularly attractive in the imaging of biological samples such as skin surface. FTIR microscopic imaging was successfully applied in the study of the drug diffusion through heterogeneous sample, such as human skin¹⁷. The understanding of the penetration of drugs through the skin will be of great helpful in designing efficient reagent that can assist the drug delivery through skin^{18,19}.

FTIR microscopic imaging was also shown to be useful in the analysis and chemical monitoring of fingerprints^{20, 21}. Oils and skin can be visualized easily when using appropriate vibrational modes.

FTIR microscopic imaging, with high spatial resolution and different fields of view, has been applied in pharmaceutical industry²², to probe the distribution of different ingredients in a tablet/capsule manufactured in a pharmaceutical formulation process²³.

Although FTIR microscopic imaging has not been previously used in the study of metal oxide semiconductor surfaces, its intrinsic benefits that can generate chemical information of different areas of one sample at the microscopic level guarantee its feasibility of obtaining spatially resolved images from semiconductor films. The ability to image the

semiconductor films should prove to be a powerful and invaluable tool towards the in-depth understanding of the interaction between molecules and semiconductors and allow optimization of functionalization methods.

A.2 Stepwise functionalization

In this thesis, the purpose of developing practical analytical technique to study the modification process on semiconductor material with molecules is to design and develop innovative surface modification methods toward a new generation of biosensors with high selectivity and sensitivity. In the biosensing application, biomolecules need to be immobilized on the semiconductor surface to enable sensing a simple immobilization method to attach biomolecules onto semiconductor surface is non-covalent physical adsorption, via hydrogen bonds, Van der Waals force, ionic forces, and hydrophobic forces²⁴. For example, due to the high isoelectric point of ZnO, biomolecules with low isoelectric point can be physically immobilized onto this semiconductor material²⁵⁻²⁸. Although physical adsorption is simple, the interaction between adsorbents and semiconductor is weak and non-specific and does not lead to a highly ordered layer.

In covalent binding approaches, whether one step or the step-wise, the binding strength and uniformity is largely improved compared to physical adsorption (Fig. A-1).

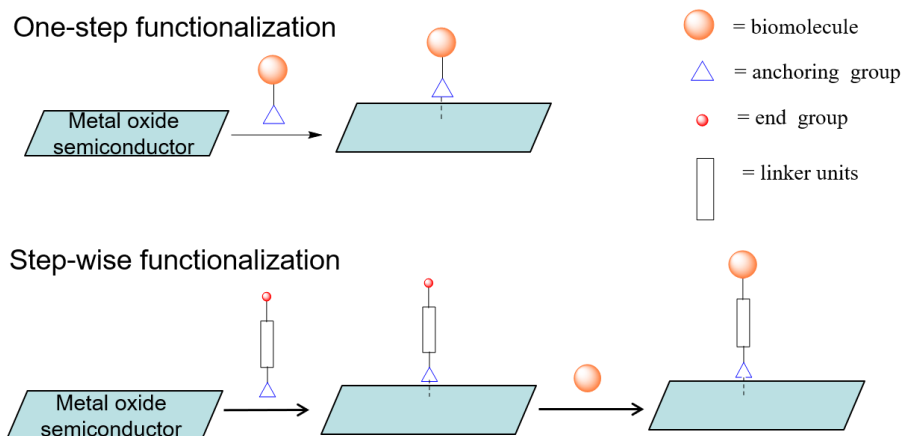


Fig. A-1 Two methods for covalent binding of biomolecules to metal oxide semiconductor surface

One-step functionalization with bulky biomolecules often results in low surface immobilization coverage, whereas stepwise functionalization significantly improves the surface coverage. This was demonstrated by Galoppini and coworkers, developed a stepwise functionalization method using a bifunctional linker²⁹⁻³¹. In this method (Fig. A-2), anchor-linker-end group linkers were attached onto the ZnO films, resulting a functional layer that can immobilize DNA with fluorescence tag in the second step.

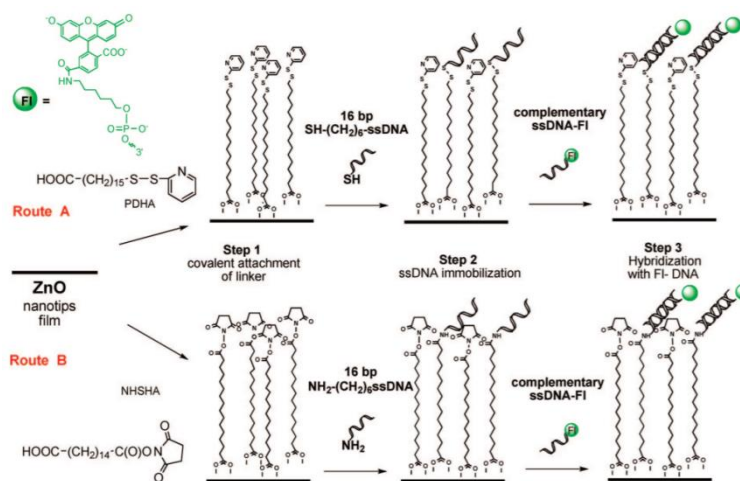


Fig. A-2 ZnO nanotips stepwise surface modification via two routes, route A: thiol-disulfide exchange reaction and route B: NBS-ester hydrolysis. Adapted with permission from [31]

There are a large number of functional groups that can be used as anchoring groups, including carboxylic acids and derivatives, phosphonic acid, alkylthiols, and silanes.

Alkylthiols, are frequently used in the functionalization of Au and CdS, and all others bind to metal oxide semiconductors.

Carboxylic acid group is the most effective and common anchoring group for metal oxide semiconductors, mainly through the bidentate chelating and bridging modes (Fig. A-3)³², As confirmed by FTIR measurements showing characteristic carboxylate bands at 1540 and 1480 cm^{-1} .

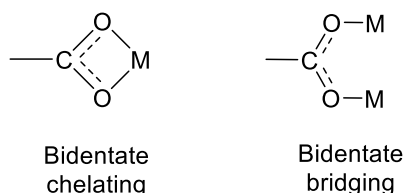


Fig. A-3 Binding modes between carboxylic acid group and a metal oxide semiconductor surface

Phosphonic acid group is an effective anchoring group for TiO_2 and other oxides. Zhou and coworkers demonstrated the stepwise functionalization of an array of In_2O_3 nanowires by 4-(1,4-dihydroxybenzene)butyl phosphonic acid (HQ-PA), to immobilize single-strand DNA (Fig. A-4)³³. However, Phosphonic acid is a very strong acid ($\text{pK}_{\text{a}1}=2.2$), and ZnO will be easily etched to form zincate salt³⁴⁻³⁶.

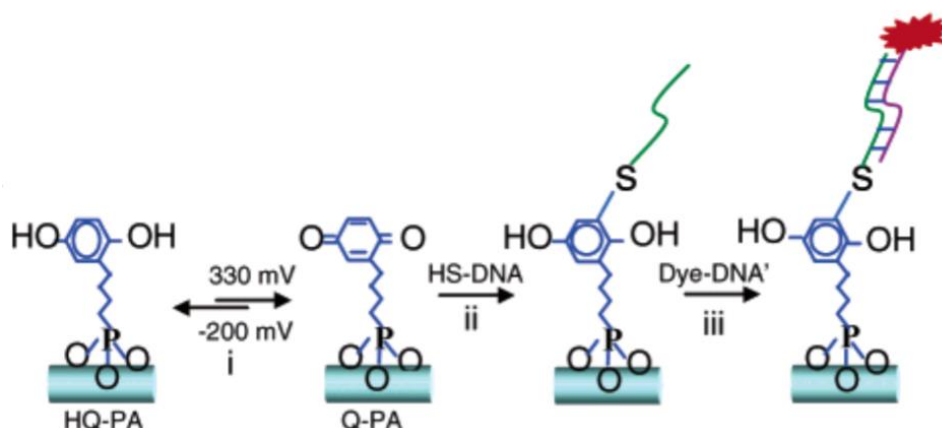


Fig. A-4 The binding of HQ-PA on In_2O_3 nanowires, after electrochemical oxidation (step i), after immobilization of thiol-terminated DNA (step ii), and after attaching of complementary DNA strand (step iii). Adapted with permission from [33]

There are also reports of binding of trichloro silanes onto metal oxide semiconductors. For instance, Corso and coworkers successfully functionalized planar ZnO surface with two different silane molecules and use this functionalized ZnO surface to immobilize an antibody (Fig.A-5)³⁷. However, trichlorosilane solution are very acidic (pH~0.5-1), and not suitable for ZnO.

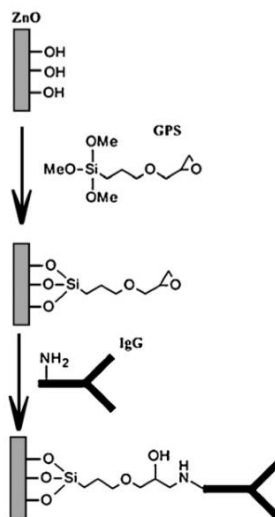


Fig. A-5 The immobilization scheme of covalent binding of antibodies to the ZnO surface using (3-glycidyloxypropyl)trimethoxysilane. Adapted with permission from [37]

The linker units in bifunctional linkers assist the formation of ordered layer through closely packing, and the distance between the semiconductor surface and end groups will affect other properties (such as fluorescence).

A reactive end group is needed in the stepwise functionalization process and its selection largely depends on the type of reaction needed in the second step, and on limitations imposed by surface chemistry on nanostructured materials. The functionalization method needs to be highly efficient, use mild conditions and surface compatible reagents. Click reaction (see next section) is, to date, the most successful reaction that was used in the stepwise functionalization of nanostructured metal oxide semiconductors. The classical

click reaction is the Cu^{I} -catalyzed Huisgen cyclization reaction between a terminus alkyne and an azide. Both the azide or the terminus alkyne can serve as end groups in the bifunctional linker.

A.3 Click chemistry

“click chemistry” refers to a series of reactions with high yield, high rate, high selectivity, and high (bio-)orthogonality. Click reactions can tolerate a wide range of temperature, solvent and pH values, and employ mild, and environmentally friendly reaction conditions. The surface modification with various type of click reaction is illustrated in Fig. A-6³⁸. The term “click reactions” was first introduced by Sharpless³⁹. There are several reasons why click reactions is suitable for surface stepwise functionalization of nanostructured metal oxide semiconductors.

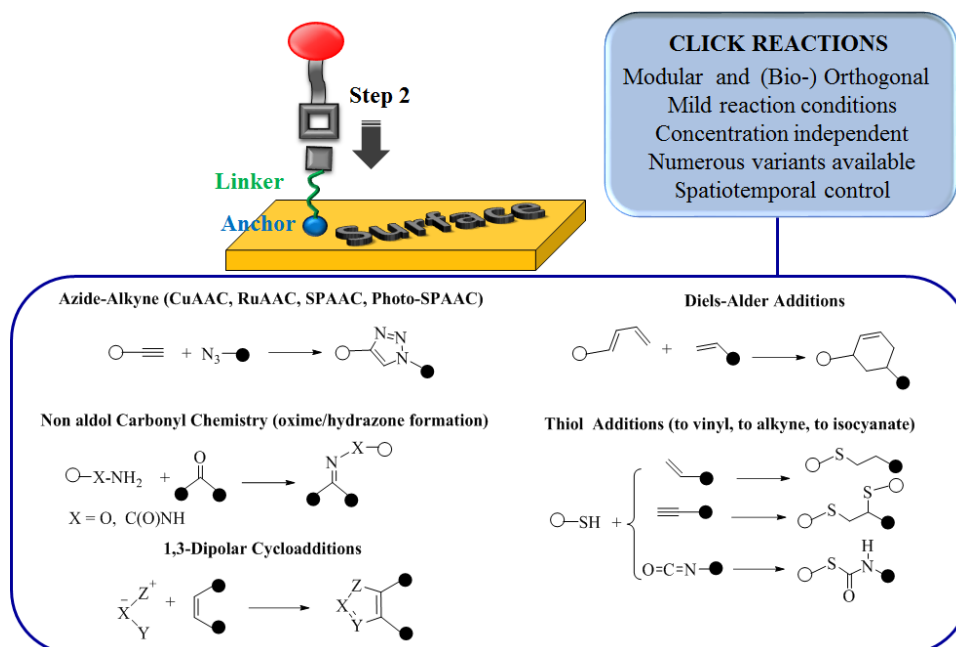


Fig. A-6 The schematic representation of click reactions on surfaces. Adapted with permission from [38]

- (1) Numerous types of reactions such as 1,3-dipolar cycloadditions, ring opening reactions, Diels Alder reactions, additions to carbon-carbon bonds or non-aldol carbonyl chemistry can be employed. Therefore, a variety of functional groups that can be employed as end groups. The scope of click reaction is quickly expanding. For example, the newly developed photoclick reaction by using light to activate reaction have proven to be very successful and useful in the patterning of surfaces⁴⁰⁻⁴².
- (2) Click reactions are regioselective, proceed in high yield, and with mild reaction conditions. Most click reactions can be carried out in water at moderate temperatures and neutral pH, in conditions that are compatible with biomolecules.
- (3) Click reactions are highly selective orthogonal reactions. Because tolerate a broad range of solvents, reagents, and other functional groups. The orthogonality of click reaction largely eliminates the possibility of producing by-product, and it is advantageous for surface chemistry in which purification steps are limited³⁹.
- (4) Recently, there is a great effort on developing click reactivity on surfaces, with a significant increase in papers reporting surface modification via click chemistry. The development of new surface click reactions could expand surface science applications dramatically.

Although the scope of “click reactions” is getting wider, Cu-catalyzed Azide-Alkyne Click reaction (CuAAC), first reported by Sharpless and Meldal⁴³⁻⁴⁵, remains the prototype click reaction and is considered the ‘ideal’ click reaction. CuAAC is the [3+2] cycloaddition, catalyzed by copper (I), between an azide and a terminus alkyne to form a disubstituted 1,2,3-triazole ring. Unlike the original version of azide-alkyne click reaction that was reported by Huisgen in 1963⁴⁶, which utilize heat to activate the reaction and result in a

mixture products of 1,5- and 1,4- substituted 1,2,3-triazole, the use of metal salts, originally copper (I), results in high regioselectivity, high yields and lower reaction temperatures (Fig. A-7).

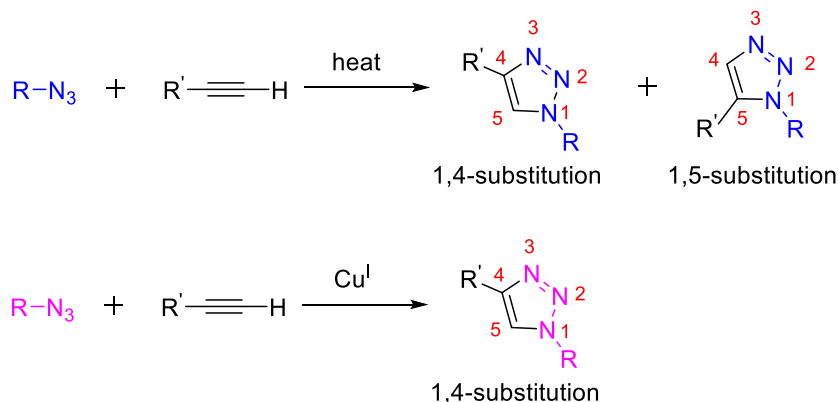


Fig. A-7 The original Huisgen reaction and CuAAC

Except for Cu catalysts, other metal salts including ruthenium (RuAAC), gold (AuAAC), nickel (NiAAC), lanthanide salt (LnAAC), zinc (ZnAAC), iridium (IrAAC), and silver (AgAAC) are employed as catalysts. Numerous papers about the click reaction using these catalysts have been reported^{47, 48}. Metal free click chemistry was also developed for surface chemistry. Ring strain from cyclic alkyne or substitution of alkynes with electro withdrawing groups can promote the click reaction in the absence of metal catalyst⁴⁹. Light irradiation was employed to photo initiate click reaction⁵⁰.

Surfaces can be functionalized by either azides or alkynes, followed by click with biomolecules substituted with the other click functional group. The best results are usually obtained when the surface is functionalized with the alkyne, because this prevents cross coupling of terminus alkynes in solution phase in the presence of copper (I). However, the immobilization of azides on surfaces offers tremendous advantages, such as the use of two unique spectroscopic handles, IR and X-ray photoelectron spectrum, to monitor the reaction progress, and the cross-coupling side reaction product of terminus alkynes can be

easily removed. In summary, both azides or alkynes can be immobilized on surfaces, depending on the reaction conditions.

A.4 Molecular design of sensitizers for metal oxide surfaces

The electron transfer processes taking place at the molecular light absorbers/wide-band-gap metal oxide semiconductor interface is a key step in solar energy conversion systems such as dye sensitized solar cells (DSSC)^{51, 52}. A schematic of the electron transfer from a photo-excited sensitizer to colloidal TiO_2 in a DSSC device is shown in Fig. A-8. Upon light irradiation, sensitizer is excited, followed by injection of an electron into the conducting band of TiO_2 , leaving the sensitizer in its oxidized state.

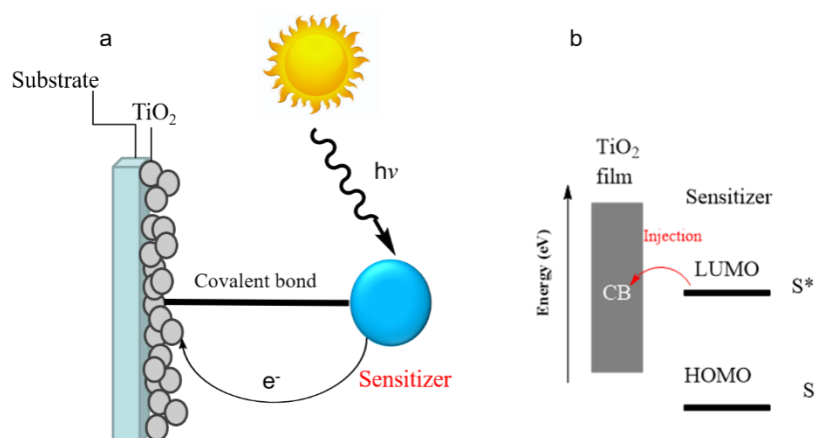


Fig. A-8 (a, left) Schematic overview of the light irradiation and electron injection process in a DSSC and (b, right) Simple energy level diagram of HOMO-LUMO of sensitizer and CB of semiconductor.

This type of electron transfer process is called Heterogeneous Electron Transfer (HET). Heterogeneous electron transfer continues to be the object of numerous experimental and theoretical studies.

HET directly depends on the energy levels at the sensitizer/metal oxide interface. The excited state (LUMO) level of the sensitizer should be higher in energy than the conduction

band edge of TiO_2 , so that an efficient electron transfer from the sensitizer to the conduction band (CB) of the TiO_2 can occur.

The control and understanding of the factors that affect energy level alignment at sensitizer/semiconductor has attracted considerable attention recently. Numerous papers have reported the importance of surface dipoles at organic/metal, organic/organic, organic/inorganic, hybrid interfaces⁵³⁻⁵⁵. The surface dipole layer can be formed right at the interface through charge transfer across the interface, or by other types of rearrangement of electronic charge^{56,57}. Band bending and level shifts due to dipoles at the interfaces were observed⁵⁸. For instance, Campbell and coworkers demonstrated the possibility of using dipole self-assembled monolayers (SAMs) to tune the electron transfer between metal/polymer interfaces^{59,60}. Thiol adsorbates on Ag and Cu electrodes were employed as SAMs and the dipole orientation was changed via substitution pattern of fluorine groups. Thiol adsorbates form well oriented, dense monolayers on these metal surface. After binding a layer of SAMs with opposite dipole orientation to the metal surface, a polymer film was deposited, and the electrostatic potentials were studied using a Kelvin probe. The electrical measurements indicate the changing of surface potentials and effective work function of the metal substrates after adding of built-in potentials due to dipoles. Schematic energy level diagrams of metal/polymer interfaces are shown in Fig. A-9. The energy difference between the metal Fermi energy and LUMO of polymer was changed accordingly when the opposite dipole was introduced.

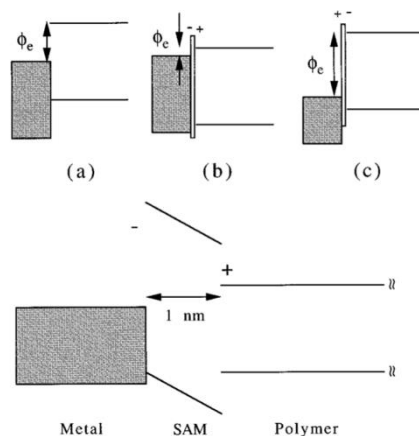


Fig. A-9 Schematic energy level diagram of meta/polymer interfaces: (a) untreated interface. (b) insertion of a dipole layer pointing to metal surface and (c) insertion of a dipole layer pointing from metal surface. Adapted with permission from [57]

Campbell's work pointed to a promising approach to control and improve the charge transfer in metal/polymer interfaces that could be extended to other interfaces, including metal oxide semiconductors.

This was pursued by Galoppini and coworkers, who synthesized Zinc tetraphenylporphyrins (ZnTPP) containing a dipole with different orientations⁶¹⁻⁶³. The ZnTPP compounds bearing a isophthalic acid group covalently binds onto metal-oxide semiconductors such ZnO. The intramolecular dipole was created by introducing electron accepting (NO_3) and electron donating (NMe_2) groups in the para position to each other in the bridge part, as shown in Fig. A-10 a. Thus, a pair of chromophores with reversed built-in dipole was synthesized. The incorporation of this built-in dipole introduced an electrostatic potential to the organic/inorganic interface, the HOMO and LUMO level of the ZnTPP compounds were shifted by 100 eV. The reversal of the dipole orientation resulted in a reversal of shift direction by the same amount as illustrated in Fig. A-10 b.

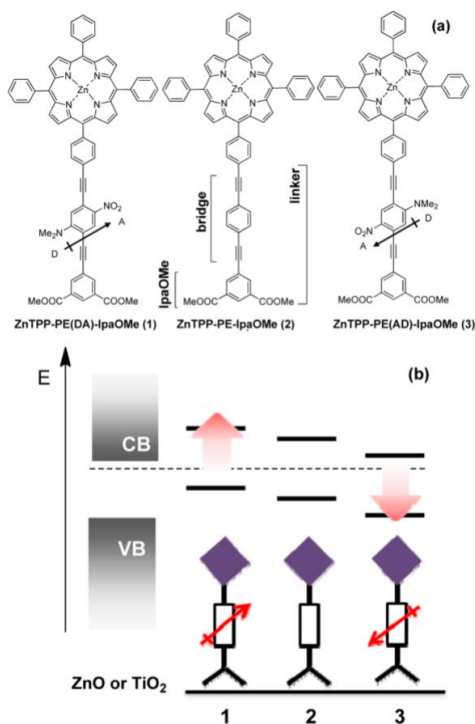


Fig. A-10 (a) Molecular structure of ZnTPP compounds used in this study. (b) Schematic diagram of how a dipole in a linker shifts the energy level of a ZnTPP compounds with respect to the CB edge of semiconductor. Adapted with permission from [60]

UV photoemission spectroscopy was employed in the study of the molecular energy levels of the chromophore bound to ZnO (110). The introduction of the built-in dipole didn't affect the HOMO-LUMO gap of the chromophore; however, the level alignment could be shifted as predicted by 200 eV.

The most important aspect of the molecular design is the dipole bridge. A dipole bridge should precisely allow to vary the dipole moment and should be well-aligned along the molecular axis. Finally, the dipole bridge should not be chromophoric or influence the HOMO-LUMO gap of the chromophores. Based on these requirements, we proposed Aib-containing peptides as the ideal model of dipole bridge.

A.5 Aib-homopeptides

α -Aminoisobutyric acid (Aib) is found in microbial proteins. The tetra-substitution at the C^α position largely restricted the possible rotations about the C- C^α and N- C^α bonds⁶⁴. And stabilizes the protein structure⁶⁵. Due to the severe restriction at backbone torsional angles, Aib-containing peptides have a high tendency to form 3_{10} -helical structures, even in short peptides (>4 residues). A variety of theoretical and experimental studies have focused on the study of Aib homopeptides. As Aib homopeptides favor the formation of single crystals, X-ray diffraction (XRD) analysis was proven to be an efficient tool to study the helix structure⁶⁶. Fig. A-11 shows the 3_{10} -helical structure of a protected (Aib)₁₀. A hydrogen bonding pattern characteristic of 3_{10} -helical structure with an intramolecular bonding between the carbonyl group in residue i and the hydrogen from the amide group of residue i+3.

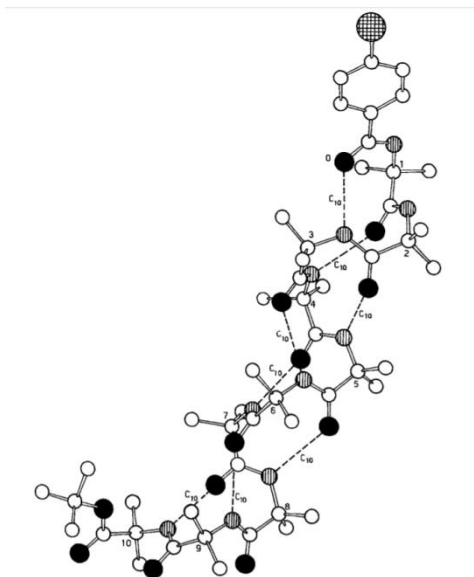


Fig. A- 11 The 3_{10} -helical structure of *para*-bromobenzoyl-(Aib)₁₀- *tert*-butoxy in the crystal state. Adapted with permission from [64]

One of the most important properties of helical peptides is their strong dipole pointing from N-terminus to C-terminus along the peptide axis (4.5 D per additional residue). The use of

dipole peptide as the molecular bridge between a donor (D) and an acceptor (A) and the study of the influence of this peptide dipole on electron transfer rate between D and A are widely documented⁶⁷.

Oligopeptides made by L-alanine (Ala) which form α -helix structure and (Aib)_n Which form 3₁₀-helix, were employed in electron transfer studies⁶⁸⁻⁷¹. The dipole pointing from N-terminus to C-terminus generate an electric field along the helix axis, and the orientation of this electric field significantly affects the electron transfer rate between D and A attached to either side of the peptide⁶⁷. Moreover, the peptide dipole moment was proven to be useful in exploring the mechanism of long-range electron transfer in proteins and on the surface of electrodes⁷². In the latter study, a ferrocene moiety was selected as the electron donor, and gold electrode was used as the electron acceptor⁷³. Studies revealed that the long-range electron transfers along the peptide molecule follows a hopping mechanism, where the amide group of the peptide serves as hopping site (Fig. A-12)^{68, 73}. The step of electron transfer through helix peptide chain determines the overall electron transfer rate, so that the length of the peptide chain can significantly alter the electron transfer rate.

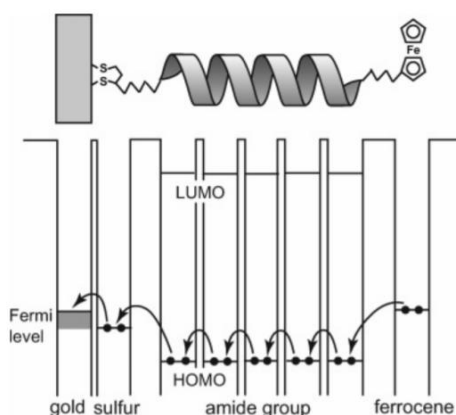


Fig. A-12 Schematic diagram for the long-range electron transfer from the ferrocene moiety to gold surface through a helix peptide by a hopping mechanism. Adapted with permission from [65]

Helical peptide also found application in tuning the electroactive moiety's redox potentials⁷⁴⁻⁷⁷. For instance, Garbuio and coworkers synthesized a pair of fullerene-peptide-nitroxide radical compounds with reversed dipole moment at the linker (Fig. A-13)⁷⁷. Electrochemical analysis indicated that the orientation of the peptide dipole moment can significantly affect optical, magnetic and redox properties⁷⁷.

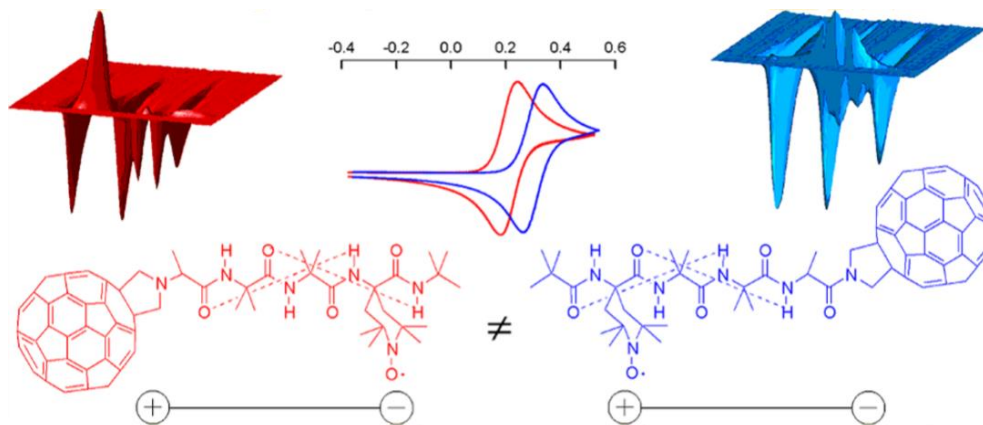


Fig. A-13 Fullerene-peptide-radical system with reversed dipole direction and the redox behavior.
Adapted with permission from [77]

Numerous structural studies and experiments about the application of 3_{10} -helical Aib-homopeptides elucidate the following advantages of $(\text{Aib})_n$ over other peptides including α -helical $(\text{Aib})_n$.

- (1) $(\text{Aib})_n$ homopeptides tend to be stiff due to severe conformational restrictions⁷⁸.
- (2) The 3_{10} -helical structure is robust and is retained on surfaces⁷⁹.
- (3) Aib is a non-chiral amino acid, further simplify the synthesis and purification process.
- (4) The dipole orientation of $(\text{Aib})_n$ homopeptide is aligned with the D-peptide-A axis.
- (5) A single helical turn in $(\text{Aib})_n$ homopeptides requires 3 amino acid residues.

Theoretical study indicates the addition of each Aib unit result in an increase of 4.5

D in dipole moment. The dipole moment and molecular length of $(\text{Aib})_n$ homopeptide can be tuned by changing the Aib unit containing in the peptide.

- (6) The dipole reversal can be attained by switching the position of D and A with respect to the peptide N- and C- terminus.

**Chapter B: Surface modification of
nanostructured ZnO/MZO films and
characterization by FTIR microscopic imaging**

B.1 Introduction

The interest in ZnO semiconductor materials goes back many decades⁸⁰⁻⁸³. Due to its direct wide band gap (3.3 eV)⁸⁴, redox properties⁸⁵, multifunctionality and biocompatibility^{86, 87}, following modification through interaction with organic or bio-molecules, ZnO semiconductor materials find application for optoelectronics⁸⁸⁻⁹⁰, catalysts^{91, 92}, and biosensing devices⁹³⁻⁹⁵. A prerequisite that is necessary for practical applications of ZnO semiconductor materials is the ability to control and characterize the modification of ZnO surfaces⁹⁶. Which is the focus of the work presented in this chapter.

One of the advantages of ZnO is that it can be grown in a rich variety of nanostructures⁹⁷⁻⁹⁹. Among them, the nanorod morphology is particularly attractive due to the ordered, vertical alignment and the high surface-to-volume ratio that can ensure a maximized binding of organic or bio-molecules on ZnO semiconductor materials^{100, 101}. ZnO nanorods can be grown on a variety kinds of substrates, including transparent or conductive, and growth techniques include sol-gel method¹⁰², pulsed-laser deposition (PLD)¹⁰³, molecular-beam epitaxy (MBE)¹⁰⁴, and metal-organic chemical-vapor deposition (MOCVD)¹⁰⁵. Metal-organic chemical-vapor deposition (MOCVD), the method used in this thesis, produces high-quality films with excellent morphology control and ability to dope or alloy with metals or semiconductors, with great control of the composition⁸⁰.

The applications of ZnO nanorod (ZnO_{nano}) films are largely limited by the need to control pH ($4 < \text{pH} < 9$) to avoid etching and formation of zincate salts³⁴⁻³⁶. To solve this problem, Lu's group has developed a ternary nanostructured material $\text{Mg}_x\text{Zn}_{1-x}\text{O}$ ($4\% < x < 5\%$) (termed MZO_{nano} in this thesis) as it possesses all the intrinsic properties of ZnO_{nano} but

shows increased resistance to acids and bases^{31, 106}. The improved resistance of MZO_{nano} to acids including carboxylic acids, which are commonly used to covalently bind compounds to ZnO , was evidenced by FESEM images of ZnO_{nano} and MZO_{nano} after reacting with 11-azidoundecanoic acid and alkynated folic, both discussed in this thesis (chapter B and C, respectively).

FESEM images (Fig. B-1, top (c)) shows that the nanorod morphology was destroyed after exposure to a 10 mM solution of alkynated folic acid ($\text{pK}_a = 3.7$). No noticeable etching, however was found for MZO_{nano} films.

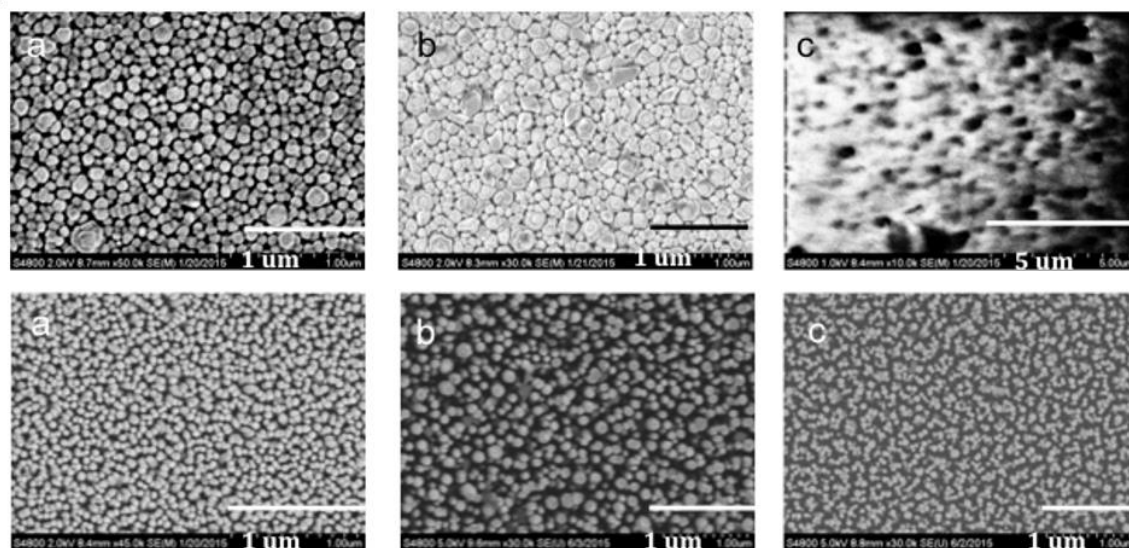


Fig.B-1 *Top*: FESEM images of MOCVD-grown ZnO_{nano} film (a) before, (b) after reacting with 10 mM 11-azidoundecanoic acid solution (solvent: 1:2 ethanol/1-butanol) for 17h at r.t, and (c). after reacting with 10 mM alkynated folic acid solution (solvent: dimethyl sulfoxide); *bottom*: FESEM images of MOCVD-grown MZO_{nano} film (a) before, (b) after reacting with 10 mM 11-azidoundecanoic acid solution (solvent: 1:2 ethanol/1-butanol) for 17h at r.t, and (c). after reacting with 10 mM alkynated folic acid solution (solvent: dimethyl sulfoxide)

Vertically aligned, highly crystalline MZO_{nano} used in our study was grown on sapphire by MOCVD by the Lu group as described in the Experimental Section B.3 and the FESEM of a typical film is shown in Fig. B-2. Nanorods are 20-40 nm wide and ~ 900 nm long.

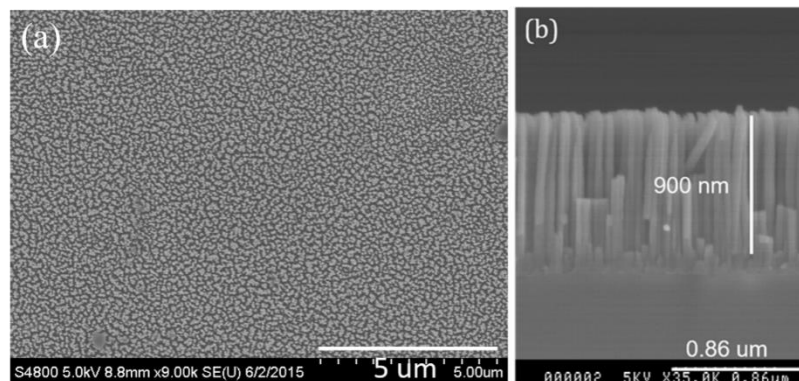


Fig.B-2 FESEM images of $\sim 0.9\ \mu\text{m}$ -thick MOCVD-grown MZO_{nano} film on sapphire (a) top view, (b) side view. Herein, we describe the modification of the MZO_{nano} films as shown in Fig. B-2 with a bifunctional linker molecule: 11-azidoundecanoic acid, $\text{N}_3\text{-(CH}_2\text{)}_{10}\text{-COOH}$ (**1**), by the droplet method described in the Appendix (Fig. 0-10).

The COOH group is one of the most common anchor group used to form covalent bonds between organic or inorganic molecules and metal oxide semiconductor materials³⁰. Through this modification method, a closely packed, homogeneous, and reactive organic molecular layer can be often obtained. In this case the presence of a second functional group, the azido group, at the end of the linker chain allows further reactivity through click chemistry.

The FTIR microscopic imaging technique, which is widely used in biophysics studies^{14,107, 108,109,110}, was for the first time employed in this MZO surface modification study. C-plane sapphire ($430\ \mu\text{m}$) was selected as the substrate because it is IR transparent¹¹¹. The FTIR spectral range was limited to the $1400\text{-}4000\ \text{cm}^{-1}$ region, because sapphire has an intense absorption below the $1400\ \text{cm}^{-1}$ region. Previously, FT-IR-ATR was used to characterize the reactive layer on semiconductor surfaces by our group²⁹ and others¹¹²⁻¹¹⁴. However, the intensity was often low as the films are only $0.5\ \mu\text{m}$ thick, and these substrates

were often destroyed while collecting data. Also binding on one film at different positions may greatly differ as shown in Fig. B-3, three FTIR spectra obtained at different location on MZO_{nano} film after the binding with 11-azidoundecanoic acid, show different binding. In summary, FT-IR-ATR does not provide information of the binding distribution on a large area of the film. FTIR spectroscopic imaging, which is a well-established method for the chemical identification and for visualizing the distribution of certain substances in complex environments, is a suitable tool for our research. The size of the pixel used in our study is 6.25×6.25 μm², images ranging from 39 μm² to cm² scale can be obtained.

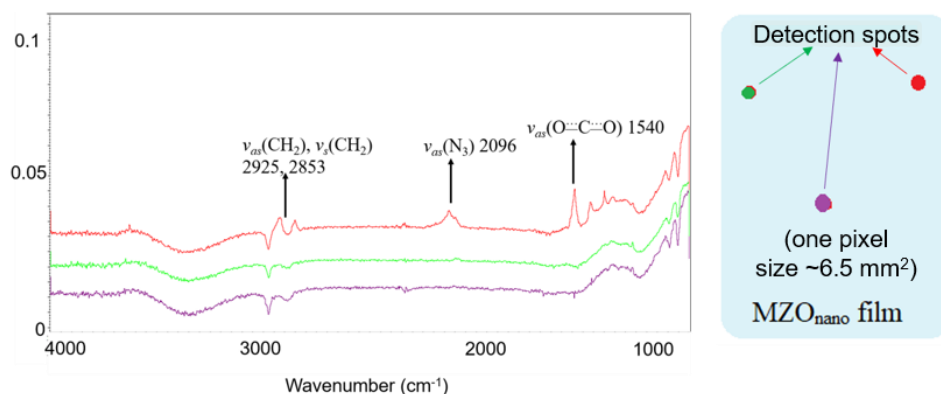
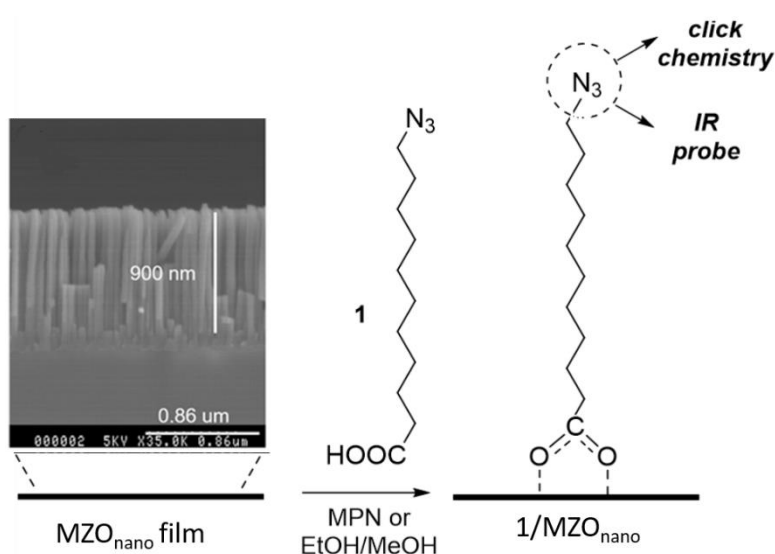


Fig. B-3 FT-IR-ATR spectra of different detection areas on MZO_{nano} film after binding with 11-azidoundecanoic acid (solvent: 1:2 ethanol/1-butanol) for 17 hours at r.t

Experimental conditions that may affect the binding of 11-azidoundecanoic acid (**1**) on MZO_{nano} film can be probed by FTIR microscopic imaging. The same film can be imaged before and after each step of the functionalization process, and binding on the same scan area can be monitored. These results allow us to improve the binding method and pave the road for a reproducible approach to prepare robust, homogenous organic layers on MZO_{nano} films that are ready for further reactivity.

B.2 Study of modification of ZnO/MZO nanostructured film by FTIR microscopic imaging

Scheme B-1 illustrates the functionalization of MZO_{nano} films with 11-azidoundecanoic acid (**1**). The bifunctional linker (**1**) binds onto MZO_{nano} films through the COOH group, leaving an azido functional group available for the click reaction with other molecules.



Scheme B-1 Scheme of the functionalization of MZO_{nano} films

Each step of the functionalization process illustrated in scheme B-1 was monitored by FTIR microscopic imaging. Fig. B-4 shows the IR spectra of neat **1** and of the MZO_{nano} film after binding of **1** (referred to **1**/MZO). Typically, upon binding, the COOH group forms carboxylate bonds as in Fig. A-3 in chapter A, leading to the following changes: the carbonyl stretching band ($\nu_{as}(\text{C}=\text{O})$) at 1706 cm^{-1} and the broad OH stretching band ($\nu_{as}(\text{O}-\text{H})$) over the $3300\text{--}2500\text{ cm}^{-1}$ region disappear, and new bands at 1540 and 1480 cm^{-1} emerge indicating that **1** is covalently bound onto MZO_{nano} film. The bands of the C-H stretching region ($\nu_{as}(\text{CH}_2)$ at $\sim 2925\text{ cm}^{-1}$ for neat **1** and 2930 cm^{-1} for **1**/MZO, $\nu_s(\text{CH}_2)$ at $\sim 2854\text{ cm}^{-1}$ for neat **1** and 2848 cm^{-1} for **1**/MZO) were observed on both neat **1** and **1**/MZO, as expected. The azido group of **1** has a characteristic asymmetric stretching band

($\nu_{as}(\text{N}=\text{N}=\text{N})$) at 2096 cm^{-1} , which is present in the spectrum of MZO_{nano} film after binding of **1** with a slight blue-shift to 2130 cm^{-1} . In conclusion, in our case both the carboxylate moiety band and azido band served as useful IR tags.

The spectral shifts upon binding and presence of shoulders in the main azido band that we have observed in this experiment, deserve a comment. We suspect that these changes and the presence of shoulders likely arise from differences in local environments, both in the neat sample of **1** and on $\text{1/MZO}_{\text{nano}}$. Regarding to the presence of shoulders, based on the NMR spectra (see Appendix Fig. 0-11 and 0-12) we do not attribute them to the presence of an impurity.

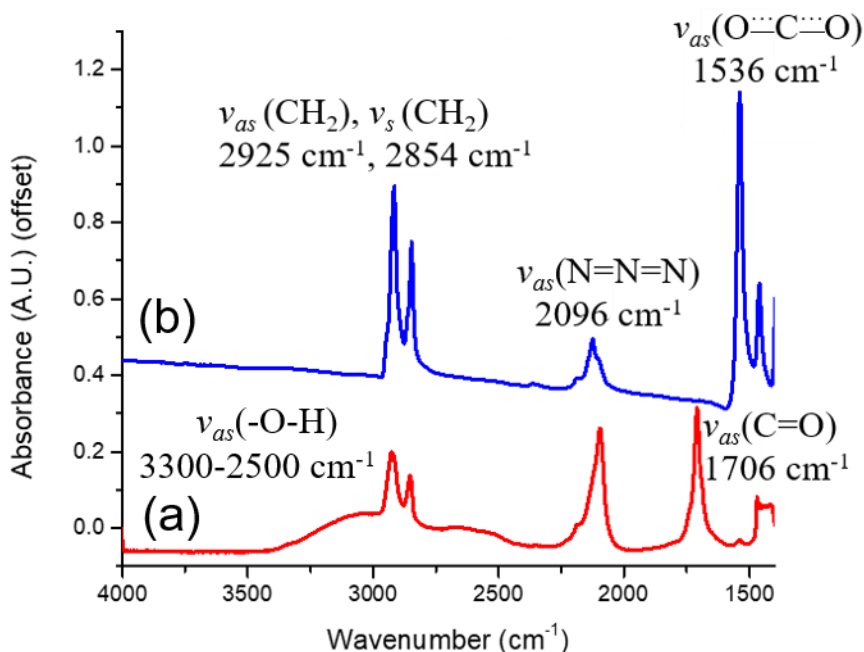


Fig. B-4 FTIR spectra of (a) neat **1** and (b) **1**/ MZO_{nano} . Adapted with permission from [127]

Generally, nine different areas ($200 \times 200\text{ }\mu\text{m}^2$) were selected from each MZO_{nano} film to be analyzed as schematically illustrated in Fig. B-5. FTIR images were obtained by integrating the area under two selected bands of interest, specifically, the carboxylate moiety ($\nu_{as}(\text{O}=\text{C}-\text{O})$ at $1564\text{--}1480\text{ cm}^{-1}$) and azido ($\nu_{as}(\text{N}=\text{N}=\text{N})$ at $2212\text{--}2064\text{ cm}^{-1}$) bands. In

both cases, baseline correction was applied. The detection limit was set based on a signal to noise ratio of 3 which is typical for this type of measurement. Regions below the detection limit were displayed in white. The limit of scale bar is \pm STD. By using this FTIR microscopic imaging, we were able to probe the following parameters: solvent and concentration of **1** solution, binding time, and morphology of MZO_{nano} films. The stability of functionalized MZO_{nano} film was also evaluated.

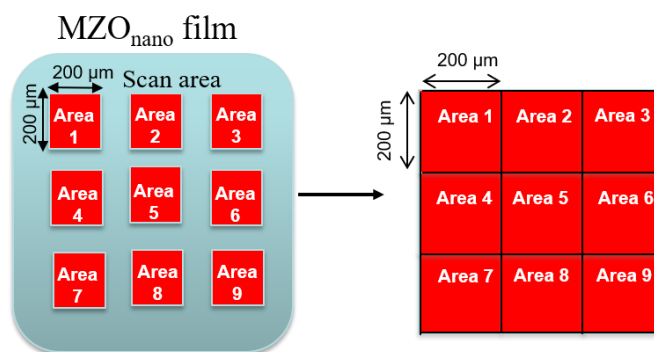


Fig. B-5 Schematic representation of how images are reported: selected areas in a MZO_{nano} film and corresponding FTIR image grid.

B.2.1 Solvent effect

Alcohols are frequently used in the binding of organic molecules and biomolecules on metal-oxide semiconductor films, since they are good organic solvents for molecules that contain polar groups, including the carboxylic acid group^{115, 116}. Previously, we reported that the binding of **1** in 1:2 ethanol/1-butanol solution on ZnO_{nano} film was successful, but we noticed that the binding was not always homogeneous²⁹. In this thesis work, the same qualitative observation was made for the MZO_{nano} films. One possible explanation for the non-homogeneous binding is that protic solvents (ethanol, 1-butanol) may displace the bound carboxylic acid group¹¹⁷. To prove our hypothesis and optimize binding, we used a polar, non-protic solvent: 3-methoxypropionitrile (CH₃O(CH₂)₂CN, 3-MPN) to prepare the binding solution of **1**.

FTIR images of **1**/MZO_{nano} films prepared by using 10 mM **1** solution in 1:2 ethanol/1-butanol and 10 mM **1** solution in 3-MPN are shown in Fig. B-6. The images were collected after 17 hours binding time. To minimize any differences that may introduced by morphology or other differences between the samples used for this solvent effect study, the experiments were carried out on the same MZO_{nano} film, which was cut in half. The spatial distribution of **1** on MZO_{nano} film was evaluated by mapping the azido band (2212-2064 cm⁻¹) or carboxylate band (1564-1480 cm⁻¹).

By comparing the FTIR images of **1**/MZO films formed using these two solvents (Fig. B-6 (a) vs Fig. B-6 (b)), we observed that the surface coverage of **1** on MZO_{nano} films bound from 3-MPN was significantly higher, suggesting that protic solvents such as alcohols can compete with **1** during the binding or replace the bound molecules of **1** on MZO_{nano} films.

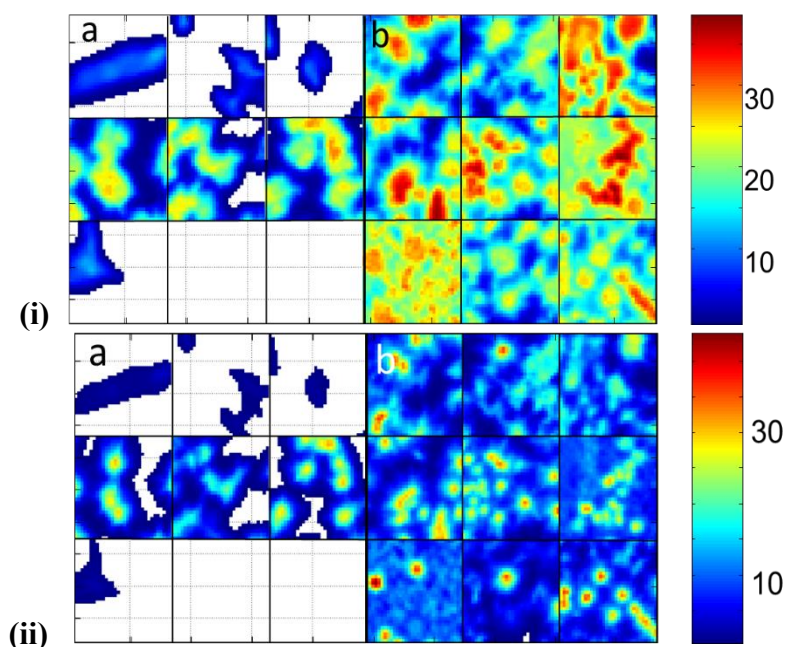


Fig. B-6 FTIR Images of the integrated band area of (i) the azido region 2212-2064 cm⁻¹(±STD), (ii) the carboxylate region 1564-1480 cm⁻¹ (± STD) of MZO_{nano} films after binding with (a) 10 mM **1** solution (solvent: 1:2 ethanol/1-butanol) and (b) 10 mM **1** solution (solvent: 3-MPN). The data were collected after 17 h binding. Adapted with permission from [127]

A comparison between FTIR images of the integrated area of the N₃ band and the carboxylate band (Fig. B-6 (i) vs Fig. B-6 (ii)) showed an identical spatial distribution of both functional groups, indicating that **1** is covalently bound not physisorbed onto the surface of MZO_{nano} films. These results were consistently observed for several samples and were reproducible. For simplicity, in our following discussion, only the FTIR images of integrated area of the azido band will be presented, and the data for the COOH band are reported in Appendix.

B.2.2 Time dependence

The FTIR images of the binding study of **1** at different binding times are shown in Fig. B-7. A relatively fast binding rate at the early stage (up to 5 hours) was observed, and no significant binding of **1** was observed after one day. The maximum coverage of **1** on MZO_{nano} film was obtained after binding for 22 hours.

FTIR images of the integrated area of azido band of two areas on MZO_{nano} film at early binding time (up to 3.5 hours) are shown in Fig. B-8. The binding is observed to occur in small, isolated areas (μm scale). These islands expanded over time, and finally merged together to attain a fully covered molecular layer. This suggests that molecules may promote binding, almost acting as “seeds”, possibly through hydrophobic interactions between the long, saturated alkyl chains of **1**.

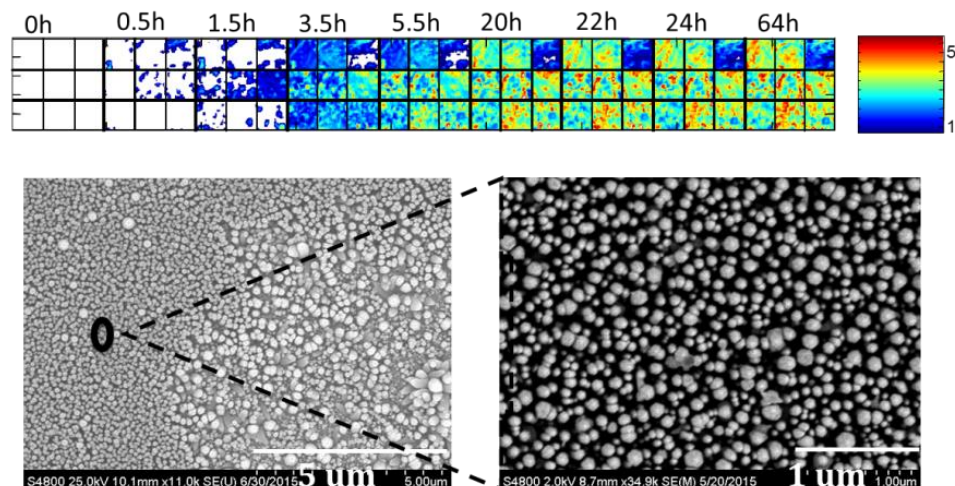


Fig. B-7 Top: Images of the integrated band area of 2212-2064cm⁻¹ region (\pm STD) of MZO_{nano} films before and after binding with a 10 mM **1** in 3-MPN solution over time. Bottom: FESEM image of the MZO_{nano} film used in the experiments (before binding) (left) and enlarged selected area (right). (Scale: 5 μ m left, 1 μ m right). Adapted with permission from [127]

FTIR images of fully covered MZO_{nano} film showed, however, an uneven distribution of **1** on MZO_{nano} (Fig. B-7). FESEM images of the pristine MZO_{nano} film indicate that contains areas with vertically oriented, closely packed, uniform nanorods, and also areas with non-uniform morphology. The heterogeneous growth of the film may result in an uneven binding of **1**. The relationship between binding homogeneity and film morphology is discussed below.

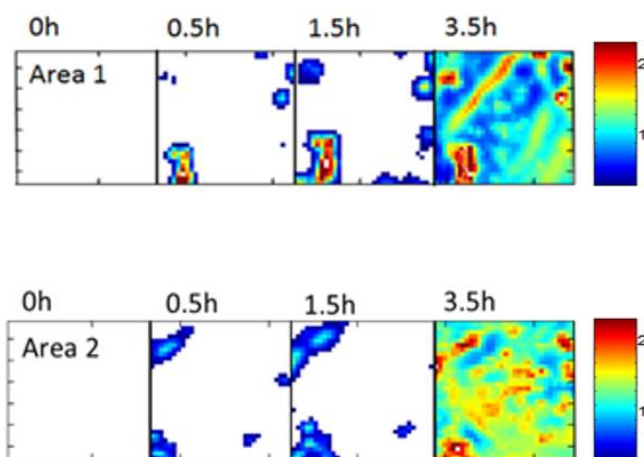


Fig. B-8 Images of the integrated band area of the azido region 2212-2064cm⁻¹ (\pm STD) of two areas after binding with 10 mM **1** in 3-MPN as function of time. Adapted with permission from [127]

B.2.3 Morphology effect

To probe the influence of areas with non-uniform morphology on the binding process, three different morphologies were identified by FESEM, and the binding of **1** on areas contain these morphologies were studied by FTIR microscopic imaging. The first morphology is the sharp nanotips. Fig. B-9 shows side-by-side the FESEM images and FTIR images of an area containing sharp nanotips (area inside the dark circle). Fig. B-8 shows that, at early binding stage (up to 2 hours), no detectable binding was observed. However, the images in Fig. B-9 suggest that **1** prefers to bind onto the areas consisting of uniform nanorod that is the area outside the dark circle. A possible explanation is that the hydrophilicity/wettability of nanorod and nanotip morphologies are different¹¹⁸, leading to the different performance of them on binding.

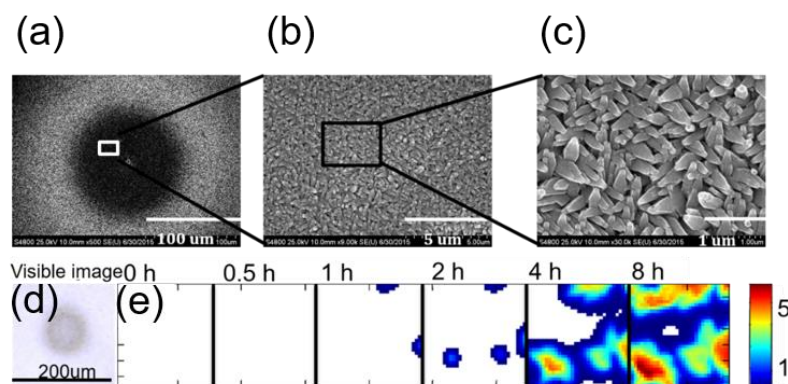


Fig. B-9 (a)-(c): SEM images at different scales of sharp nanotips morphology before binding, and (d) a visible micrograph (before binding, 200×200 μm²) taken of the same area from which FTIR images were acquired as a function of binding time (bottom). (e) FTIR images of the integrated band area, 2212-2064 cm⁻¹ (± STD) of area 1 after binding with 10 mM **1** in 3-MPN as function of time. Adapted with permission from [127]

The binding of **1** to nanorods that grow in different orientations was also probed by FTIR microscopic imaging (Fig. B-10). The FESEM and FTIR data suggest that binding is preferred in the areas where the nanorods are not vertically aligned but grow with different orientations (areas in the rectangle, along the vertical “ridge” feature in the FESEM). By

comparing the FTIR images in Fig. B-9 and B-10 at the same binding time (for instance at 1 h), we found that binding is much faster in the latter. A possible explanation is that different binding energies of different exposed facets of MZO nanorods impact the binding process¹¹⁹. At low doping level of Mg ($4\% < x < 5\%$), the crystal structure of $\text{Mg}_x\text{Zn}_{1-x}\text{O}$ is Wurtzite, the same as that of ZnO ¹²⁰. Fig. B-11 shows the crystal faces at the two side and one top facets of Wurtzite ZnO ¹²¹.

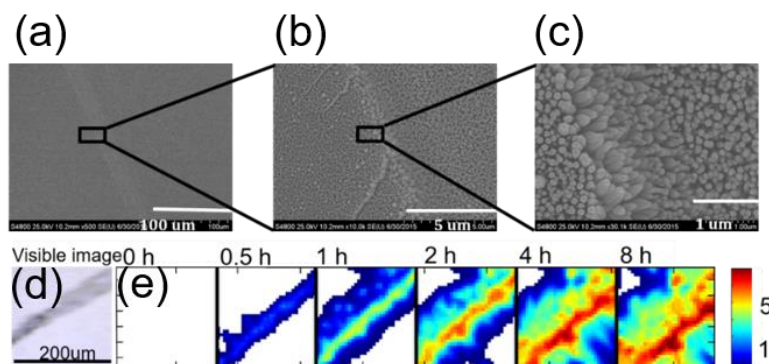


Fig. B-10 (a)-(c): SEM images at different scales of nanorods grown in different orientation type morphology (before binding, top) and (d) a visible micrograph (before binding, $200 \times 200 \mu\text{m}^2$) taken of the same area from which FTIR images were acquired as a function of binding time (bottom). (e) FTIR images of the integrated band area of $2212\text{--}2064 \text{ cm}^{-1}$ ($\pm \text{STD}$) of area 2 after binding with 10 mM **1** in 3-MPN as function of time. Adapted with permission from [127]

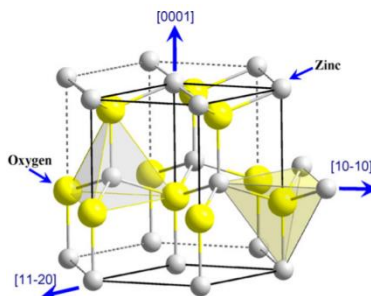


Fig. B-11 Crystal structure of Wurtzite ZnO . Adapted with permission from [127]

Finally, we probed the influence of different growth densities (Fig. B-12). No clear relationship between binding preference and such morphology was found, based on the FTIR images shown in Fig. B-12. The packing of nanorods does not appear to affect the binding of **1** on MZO_{nano} film.

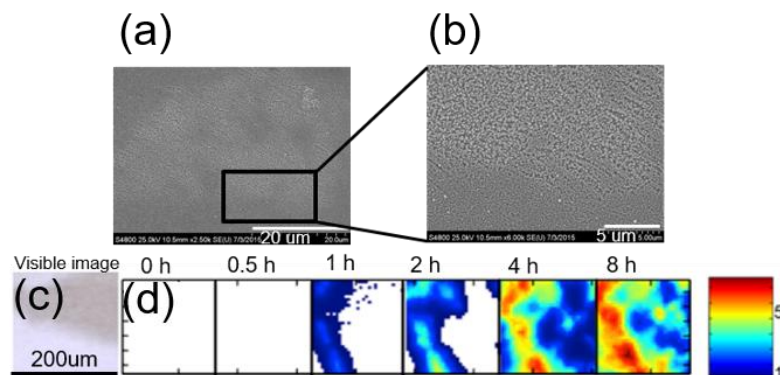


Fig. B-12 (a)-(b): SEM images at different scales of nanorods with different growth density type morphology (before binding, top) and (c) a visible micrograph (before binding, 200×200 μm²) taken of the same area from which FTIR images were acquired as a function of binding time (bottom). (d) FTIR images of the integrated band area of 2212-2064 cm⁻¹ (± STD) of area 3 after binding with 10 mM **1** in 3-MPN as function of time.

In conclusion, FTIR images collected in areas comprised of morphologies, that are different from vertically aligned densely packed nanorods, morphology can significantly influence the distribution and rate of binding, possibly due to differences in binding energy and hydrophilicity of these areas¹²².

B.2.4 Concentration effect

The binding of MZO_{nano} film with three different concentrations (10, 40 and 100 mM) of **1** in 3-MPN were studied by FTIR microscopic imaging. Fig. B-13 (top) shows the FTIR images of MZO_{nano} films after binding with a 10 mM 3-MPN solution. No significant binding was observed for about 11 hours. A full coverage of **1** on MZO_{nano} film was obtained after longer binding times (48 hours).

The binding rate was accelerated dramatically by using a more concentrated **1** solution (40 mM) (Fig. B-13, middle). Binding onto MZO_{nano} film started at 1.5 hours, and a fully covered MZO_{nano} film was obtained after 18 hours. However, a ten-fold increase in the concentration of **1** (100 mM) sharply decreased the binding rate (Fig. B-13, bottom). No

binding was observed for up to 15 hours. A fully covered and very homogeneous MZO_{nano} film was obtained at 18 hours.

We propose that inter-molecular hydrogen bonding between molecules of **1** in 100 mM 3-MPN solution could be responsible for this effect. High concentrations will promote strong $\text{C}=\text{O} \cdots \text{H}-\text{O}$ hydrogen bonding (Fig. B-14) or formation of carboxylate, thereby, inhibiting the binding at short binding times.

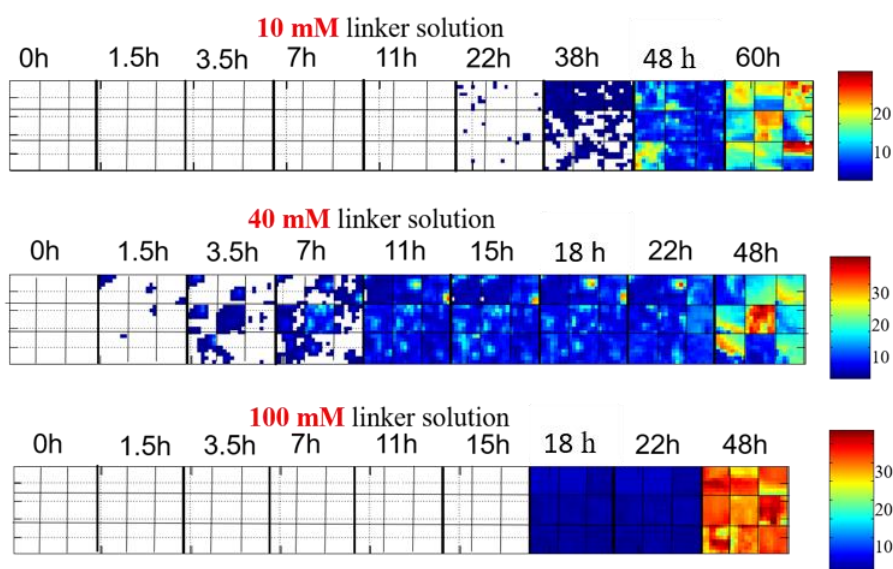


Fig. B-13 FTIR images of the integrated band area of $2212\text{-}2064\text{cm}^{-1}$ region (\pm STD) of MZO_{nano} films before and after binding with a 10 mM **1** in 3-MPN solution, 40 mM **1** in 3-MPN solution, and 100 mM **1** in 3-MPN solution over time.

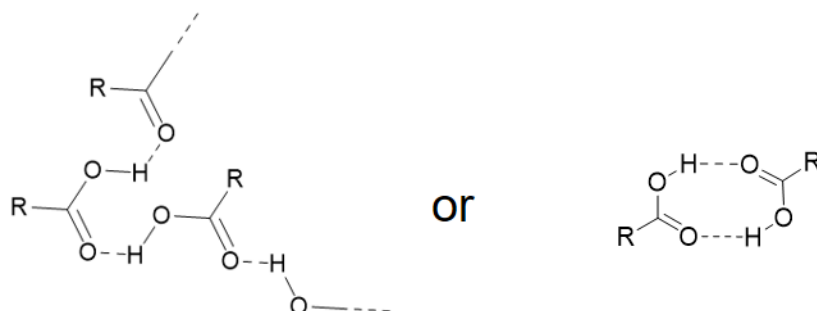


Fig. B-14 Proposed intermolecular hydrogen-bonding structures of **1** in 100 mM solutions of **1**

NMR spectroscopy has been widely used as a powerful tool to obtain detailed information of hydrogen bonding, both inter- and intra- molecular^{123, 124}. Here, ^{13}C NMR measurements

were used to probe the formation of *inter*-molecular hydrogen bonding in concentrated solutions of **1**. Solutions of **1** varying in concentration (10 mM, 40 mM, and 100mM) were prepared using CDCl₃ (polar and aprotic NMR solvent) and the carbonyl region is shown in Fig. B-15. A consistent shift to lower fields was observed as the concentration increased from 10 mM to 100 mM, suggesting the formation of hydrogen bonding. The formation of hydrogen bonding between the oxygen of carbonyl group and hydrogen from hydroxide group can lower the electron density around the carbon atom of the carbonyl group, hence lead to the shifting to lower fields.

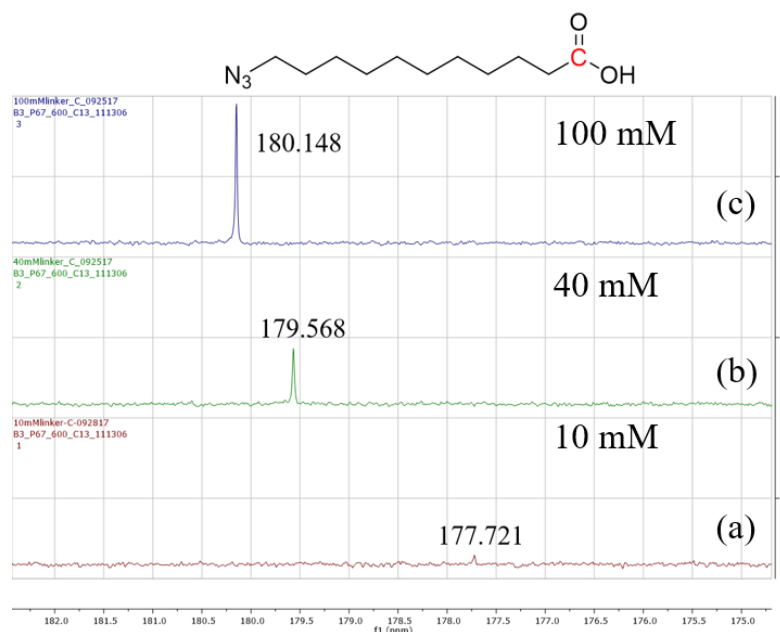


Fig. B-15 Carbonyl region of the ¹³CNMR spectra of **1** in CDCl₃: (a) 10 mM, (b) 40 mM, and (c) 100 mM

B.2.5 Stability test

The stability of functionalized MZO_{nano} films to solvents and temperature was also evaluated. The binding distribution and intensity of FTIR image of functionalized MZO_{nano} film after immersion in neat polar aprotic solvent 3-MPN at r.t and 40 °C for 24 hours resembles that of functionalized MZO_{nano} film before immersion, indicating little to no desorption (Fig. B-16). Our conclusion is that once the film is functionalized with a

lipophilic layer in 3-MPN solution, it becomes chemically stable in aprotic solvent environment.

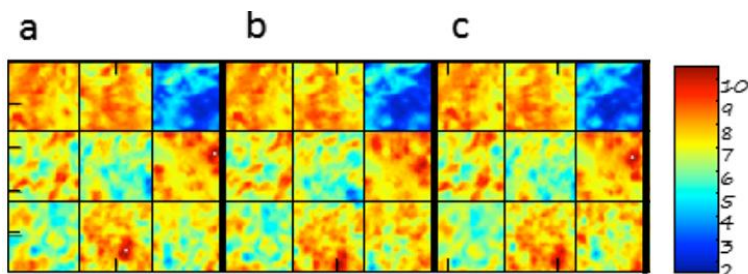


Fig. B-16 Images of the integrated band area of $2212\text{-}2064\text{cm}^{-1}$ (\pm STD) of a MZO_{nano} film (a) after 22h binding with **1**, (b) after immersion of such functionalized film in 3-MPN solution at r.t for 24 h, and (c) after immersion of such functionalized film in 3-MPN solution at 40 °C for 24 h

The stability of the same **1**/ MZO_{nano} film in EtOH was also tested. At room temperature, the **1**/ MZO_{nano} film was stable (Fig. B-17, b), however, at 40 °C, within 4 h, a significant desorption of **1** from MZO_{nano} film was observed (Fig. B-17, c). At 24 h, the film was fully stripped of **1**, indicating that desorption of **1**/ MZO_{nano} film occurs readily in a protic solvent and at high temperature (40 °C). This is consistent with the “competing effect” of protic solvent that we proposed earlier in this chapter. The binding of carboxylic acid on metal-oxide semiconductor is proposed to have high equilibrium binding constants (2×10^3 to $3 \times 10^5 \text{ M}^{-1}$)^{116, 125, 126}. Increasing temperature can promote both the binding and desorption processes, but since the solvent is present in large excess, it may bind onto MZO_{nano} film.

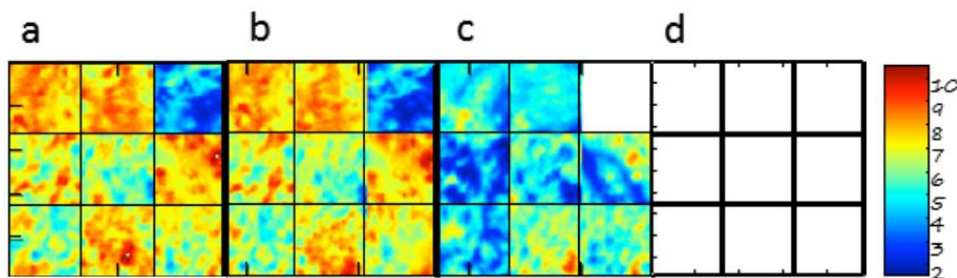


Fig. B-17 Images of the integrated band area of $2212\text{-}2064\text{cm}^{-1}$ (\pm STD) of a MZO_{nano} film (a) after 22h binding with **1** and (b) after immersion of such functionalized film in ethanol solution at r.t for 24 h, (c) after immersion of such functionalized film in ethanol solution at 40 °C for 4 h, and (d) after immersion of such functionalized film in ethanol solution at 40 °C for 24 h

The FESEM image of MZO_{nano} film after all treatments during stability test was shown in Appendix Fig. 0-8, indicating that the surface of the MZO_{nano} film is still intact.

After fully stripping **1** from MZO_{nano} film by immersing **1**/ MZO_{nano} film in EtOH at 40°C for 24 h, this film was bound with 10 mM solution of **1** in 3-MPN for 22h. FTIR images indicates the binding of **1** on MZO_{nano} film is comparable to that on **1**/ MZO_{nano} before the stability study (compare Fig.B-18, b with Fig. B-16, a), suggesting that it is possible to “re-use” MZO_{nano} films.

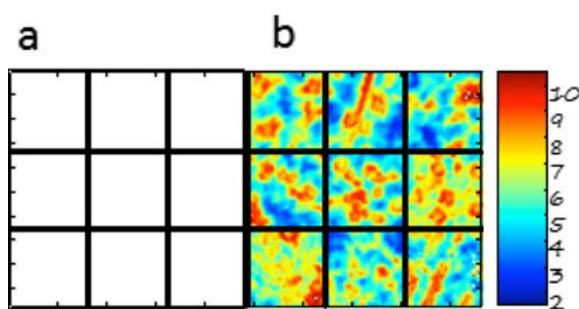


Fig. B-18 Images of the integrated band area of 2212-2064 cm^{-1} (\pm STD) of a functionalized MZO_{nano} film (a) after immersed in ethanol solution at 40 °C for 24 h, (b) after 22h binding with 10 mM **1** (solvent: 3-MPN)

B. 3 Conclusions

MZO_{nano} ($\text{Mg}_x\text{Zn}_{1-x}\text{O}$ ($4\% < x < 5\%$) nanorod) films were grown by MOCVD and functionalized with a bifunctional linker, 11-azidoundecanoic acid (**1**). The improved resistant to etching of MZO_{nano} compared to ZnO_{nano} was evidenced by FESEM images taken of MZO_{nano} film and ZnO_{nano} film after reacting with 11-azidoundecanoic acid and alkynated folic acid ($\text{pK}_a = 3.7$). The binding process was characterized by FTIR microscopic imaging. Both the bound carboxylate moiety and the azido end-group served as IR probes to monitor the distribution of 11-azidoundecanoic acid bound on the films. Changing in the C=O region indicate that 11-azidoundecanoic acid binds onto MZO_{nano} film via the carboxylic acid group. Factors that may affect binding were also probed: time,

morphology of nanorod film, solvent and concentration of the binding solution. We found that protic solvents, such as alcohols, can compete with 11-azidoundecanoic acid during binding and largely decrease the amount of bound linker. By using a polar, non-protic solvent such as 3-methoxypropionitrile, the coverage of bound linker on the film was dramatically improved. We also found that the binding of linker onto MZO_{nano} film occurs at first in small islands (μm -scale), then expand to form a fully covered layer after 22 h. Areas of the MZO_{nano} with uneven growth of the nanorod film influence the binding rate and molecular layer homogeneity dramatically. The concentration of binding solution also has a great influence on the binding rate and homogeneity. The stability of functionalized films to temperature and solvents was evaluated, indicating that functionalized films are very stable.

B. 4 Experimental section

General. All the following solvents and reagents were used as received from commercial sources: 3-methoxypropionitrile (MPN) (99%, Sigma Aldrich,), 1-butanol ($\geq 99.4\%$, Sigma Aldrich,), ethyl alcohol ($\geq 99.5\%$, Sigma Aldrich), *N,N*-dimethylformamide (anhydrous, 99.8%, Sigma Aldrich), dichloromethane ($\geq 99.5\%$, Sigma Aldrich), 11-bromoundecanoic acid (99%, Sigma Aldrich), and sodium azide (99%, Sigma Aldrich). The reactions were performed under N₂ gas and in oven-dried glassware.

Methods. ¹H and ¹³C nuclear magnetic resonance (NMR) spectra were collected on a Varian NMR spectrometer operating at 599.714 Hz for ¹H and 150.812 Hz for ¹³C. Chemical shifts (δ) are reported relative to the central line of the solvent for CDCl₃, δ 7.26 ppm for ¹H and δ 77.16 ppm for ¹³C, and spin-spin coupling constants (*J*) are reported in Hz. The Fourier transform infrared (FTIR) spectrum in Fig. B-4 (red line) was collected on

a Thermo Electron Corporation Nicolet 6700 FTIR utilizing the SMART MIRacle-single bounce ATR accessory (ZnSe crystal, with 128 scans and spectral resolution of 8 cm^{-1}). A liquid cell with CaF_2 windows and 0.164 mm path length was used. Field emission scanning electron microscopy (FESEM) images were collected on a Hitachi S4800.

Synthesis of 11-azidoundecanoic acid (1**)**^{29, 127}. Sodium azide (0.50 g, 7.7 mmol) was added to a solution of 11-bromoundecanoic acid (1.00 g, 3.8 mmol) in DMF (5 ml) while stirring. The reaction mixture was heated at $80\text{ }^\circ\text{C}$ for 3 h, then diluted with CH_2Cl_2 (25 ml), and washed by gently stirring with diluted (0.1 N) aqueous HCl solution. The organic layer was dried over Na_2SO_4 and the solvent was evaporated in vacuo to yield **1** as a pale-yellow oil (0.70 g, 3.1 mmol, 80%). ^1H NMR (CDCl_3) δ 10.08 (br, 1H), 3.26 (t, $J = 7.2$, 2 H), 2.35 (t, $J = 7.8$, 2 H), 1.66-1.57 (m, 4H), 1.39-1.29 (m, 12H). ^{13}C NMR (CDCl_3) δ 180.26, 51.38, 34.31, 29.68, 29.59, 29.48, 29.41, 29.32, 29.13, 26.99, 24.95. (see Appendix Fig. 0-10 and 0-11). **CAUTION: organic azides and sodium azide may decompose explosively. Azide waste should not come in contact with concentrated acids or metals.**

MZO_{nano} films growth¹²². MZO_{nano} films were grown on C-plane sapphire (c- Al_2O_3) (Saint-Gobain Crystals, $430\text{ }\mu\text{m}$, (0001)) substrates using Metal Organic Chemical Vapor Deposition (MOCVD) at $450\text{-}500\text{ }^\circ\text{C}$. Diethylzinc (DEZn) (Rohm and Haas, 99.999%), bis-(methyl-cyclopentadienyl) magnesium (MCp_2Mg) (Rohm and Haas, 99.999%) and ultra-high purity (99.999%) oxygen gas were used as the Zn and Mg metalorganic source and oxidizer, respectively. Ultra-high purity (99.999%) argon was used as the carrier gas. The thicknesses of MZO_{nano} films used in this work ranged from $0.50\text{--}1.0\text{ }\mu\text{m}$. Mg composition x in $\text{Mg}_x\text{Zn}_{1-x}\text{O}$ was kept in 4-5% for all films, and it was estimated using optical transmission spectroscopy. The transmission spectra of ZnO (0% Mg) and

Mg_{0.05}Zn_{0.95}O films were obtained at room temperature by the using of Beckman DU 530 UV-visible spectrometer, as shown in Fig. B-21. Based on the transmission data, the absorption coefficient α can be calculated using Beer's law. The bandgap values for MgxZn1-xO films were determined by plotting the absorption coefficients, α , as a function of the photo energy ($h\nu$) and by fitting these curves to the equation $\alpha = A^*(h\nu - E_g)^{1/2}$, where A^* is a frequency-independent constant; the results are shown in Fig. B-22. Based on the absorption coefficient spectra, we determined the bandgap for the ZnO_{nano} film to be 3.25 eV, and that for the MZO_{nano} film with 5% Mg to be 3.33 eV.

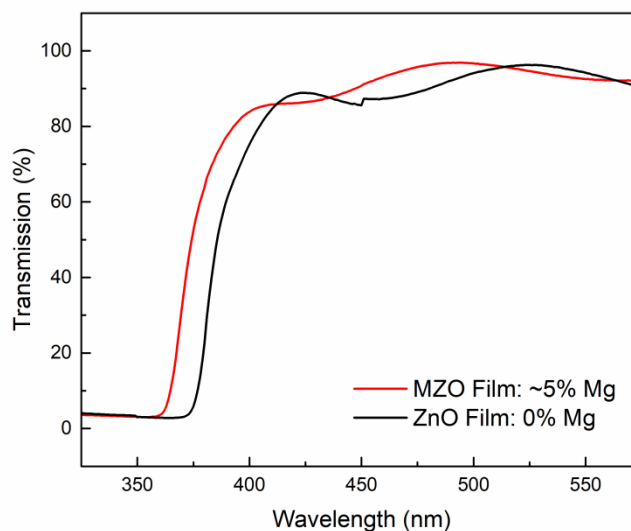


Fig. B-19 Transmission UV-vis spectra of ZnO_{nano} and MZO_{nano} film (aquired by Dr. Pavel Ivanoff Reyes from Dr. Lui's group)

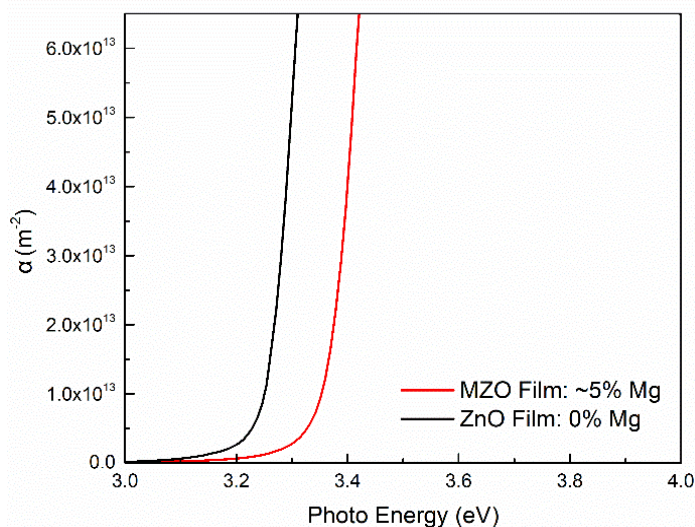


Fig. B-22 Absorption spectra of ZnO and MZO film (aquired by Dr. Pavel Ivanoff Reyes from Dr. Lui's group)

Binding of 11-azidoundecanoic acid onto MZO_{nano} film (droplet method, Appendix Fig. 0-12). A small volume (5 drops) of a 10 mM solution of **1** (either 2:1 1-butanol/ethanol or 3-methoxypropionitrile) was deposited onto a pristine MZO_{nano} film grown on a sapphire substrate placed flat in a glass Petri dish, which was then sealed to prevent evaporation. After reacting for the indicated period of time (between 0.5 hours to about 2 days, see section **B.2**), the film was thoroughly rinsed with neat solvent to remove weakly bound or physisorbed molecules, and then dried under gentle nitrogen flow.

FTIR Microscopic Imaging and Data Analysis^{14, 127}. FTIR microscopic images of MZO_{nano} films were collected with a Perkin-Elmer Spotlight 300 system (Perkin Elmer Life and Analytical Science, Inc., Waltham, MA) in the transmission mode with an essentially linear array (16×1) of mercury-cadmium-telluride (MCT) detector elements. Imaging size was 200×200 μm². Images were collected with a 6.25×6.25 μm² pixel size and 32 scans at a spectral resolution of 8 cm⁻¹, corresponding to 32×32 pixel images. Visible micrographs were obtained with the optical microscope integrated into the Spotlight 300 system. FTIR microscopic images were generated from FTIR spectral data

using ISys 3.1 software (Malvern Instruments, UK). Image planes of integrated band area were produced after linear baselines were applied in spectral regions of interest. The scale bar is color coded and selected to display the corresponding integrated area (\pm STD) above the detection limit to highlight differences upon treatments. The films used in our study were fixed onto a plate by clipper prior to data acquisition. Small shifts may occur during this process, resulting in small ($\sim \mu\text{m}$ scale) shifts of the images obtained.

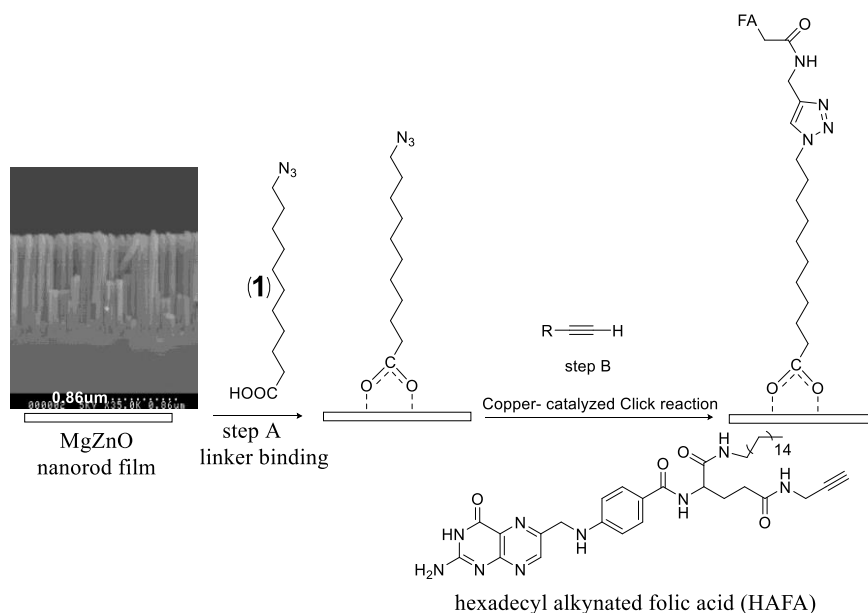
Chapter C: Stepwise functionalization of MZO nanostructured film for biosensors

C.1 Introduction

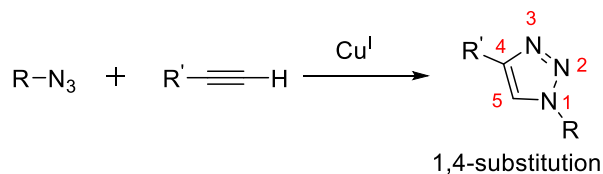
The using of FTIR microscopic imaging brings us in-depth understanding of the modification process and enabling the optimization of this process. This molecular level control of surface functionalization will helps developing stepwise functionalization method of MZO_{nano} film to enable a new generation of biosensors with high selectivity, sensitivity, and multi-modal operation.

Scheme. C-1 shows the stepwise functionalization of MZO_{nano} film. In Step A, a bifunctional linker molecule (1) was bound onto the MZO_{nano} film through carboxylic acid group, leaving a reactive azido functional group layer. This step was fully studied by FTIR microscopic imaging (see Chapter B). In Step B, hexadecyl alkynated folic acid (HAFA) was immobilized onto the MZO_{nano} film through click reaction with the reactive azido layer. This step was also studied by FTIR microscopic imaging and is described in this chapter.

The Cu (I) catalyzed azide-alkyne Huisgen cycloaddition reaction (CuAAC) is the prototype click reaction (Scheme C-2)^{44, 128-131}. Click reactions are regio- and stereospecific, biorthogonal, do not produce byproducts, and are intensely studied due to their utility in the modifications of surfaces with biomolecules³⁹. The functionalization of surface by click reaction has been reported in the fields of electronics, catalysis, solar energy, sensing, and medicine^{132, 133}.



Scheme C-1 Stepwise functionalization of MZO_{nano} film



Scheme C-2 The copper catalyzed azide-alkyne Huisgen cycloaddition reaction

Hexadecyl alkynated folic acid (HAFA) is a synthetic derivative of folic acid. Folic acid (vitamin B₉), is an important component of nucleic acids that is needed for the methylation of DNA, proteins and lipids¹³⁴⁻¹³⁷. Folic acid has a very high affinity ($K_d = 0.1-10$ nM) to folate receptors and for this reason is widely used as a biomarker in the detection and diagnosis of breast, ovarian and kidney cancer¹³⁸⁻¹⁴⁰. Folate receptors (especially Folate receptor α) are cysteine-rich cell-surface glycoproteins that are expressed in high levels in cancer cells. The interaction between folic acid and folate receptor follows endocytosis.

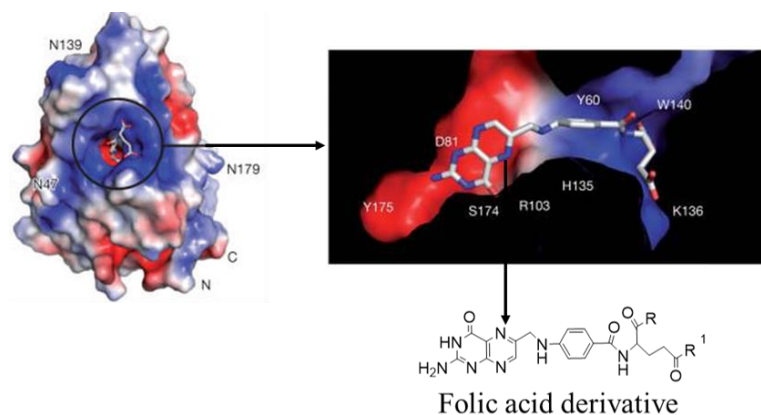


Fig. C-1 Structure of Folate receptor α react with folic acid. Adapted with permission from [134]

Although the functions of folic acid are widely documented and well understood¹⁴¹⁻¹⁴³, there is the need for the study of folic acid-based biosensors. In our study, a folic acid derivative was immobilized onto MZO_{nano} substrate via CuAAC, which is a much more specific and strong interaction compared to most other reported immobilization methods such as π - π interactions¹³⁸. The covalent attachment of folic acid allows precise control of the immobilization process and results in a stable bio-reactive layer suitable for biosensing applications.

In a proof-of-concept experiment, a MZO_{nano}- modified quartz crystal microbalance (QCM) biosensor functionalized with 11-azidoundecanoic acid (**1**) and HAFA via click reaction. The MZO_{nano}- QCM, fabricated by Dr. Yicheng Lu's group, consists of a conventional QCM with a ~400 nm MZO_{nano} layer directly grown on its sensing surface, as shown in Fig. C-2.

QCM¹⁴⁴⁻¹⁴⁶ is a high-resolution, low cost, simple mass sensing technique that is based on the piezoelectric effect. It has a wide detection capability that can be used to detect a single monolayer, and it is suitable to be used in a bio-environment. The integration of nanostructured MZO, which is also a piezoelectric material, and a conventional QCM

results in a surface-modified QCM with much enhanced sensitivity¹⁴⁷. The binding of **1** and immobilization of HAFA on MZO_{nano}- QCM was confirmed by the corresponding frequency change. The sensing of Folate receptor α by the as fabricated MZO_{nano}- QCM is still in progress.

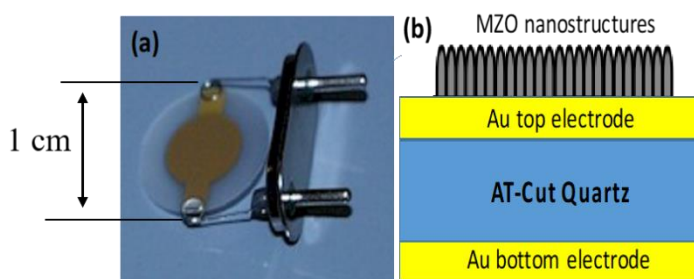


Fig. C-2 Image (a) and schematic side image (b) of MZO_{nano}- QCM (taken by Dr. Pavel Ivanoff Reyes from Dr. Lu's group)

The modification of thin film transistor (TFT) with the sensing layer (HAFA) by stepwise functionalization towards TFT-based biosensors is also described in this chapter. TFT is a kind of field-effect transistor made by depositing a thin layer of active semiconductor, a dielectric layer and metallic contacts over the glass substrate (Fig. C-3). Since its first production in 1962 by Weimer at the RCA laboratories¹⁴⁸⁻¹⁵⁰, TFTs have gained considerable attention as electronic devices¹⁵¹⁻¹⁵⁴, and due to their low power consumption, low cost, and biocompatibility, TFTs are used in biosensing¹⁵⁵⁻¹⁵⁷. TFT are particularly useful in the detection of analyte with limited amount, for example, in the in-vivo biomolecule detection¹⁵⁸.

There is a large range of semiconductor materials that can be employed in TFT fabrication, including GaN, amorphous silicon, polycrystalline silicon, SiC, and ZnO. Recently, Lu and coworkers developed a novel MZO based TFT built on a transparent glass substrate¹⁵⁹⁻¹⁶¹. The doping of Mg into ZnO to form the ternary oxide as the TFT channel increases its low

pH resistance, and increases its stability by reducing the oxygen vacancies density of the semiconductor material.

The modification of MZO_{nano} - TFT with linker **1** is discussed in this chapter, and subsequent binding of HAFA and the sensing of Folate receptor α are still in progress.

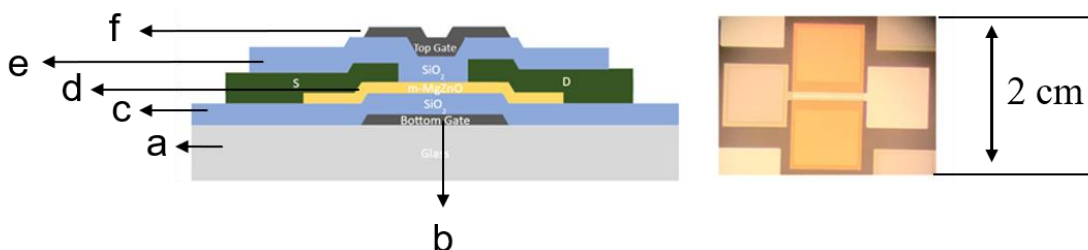
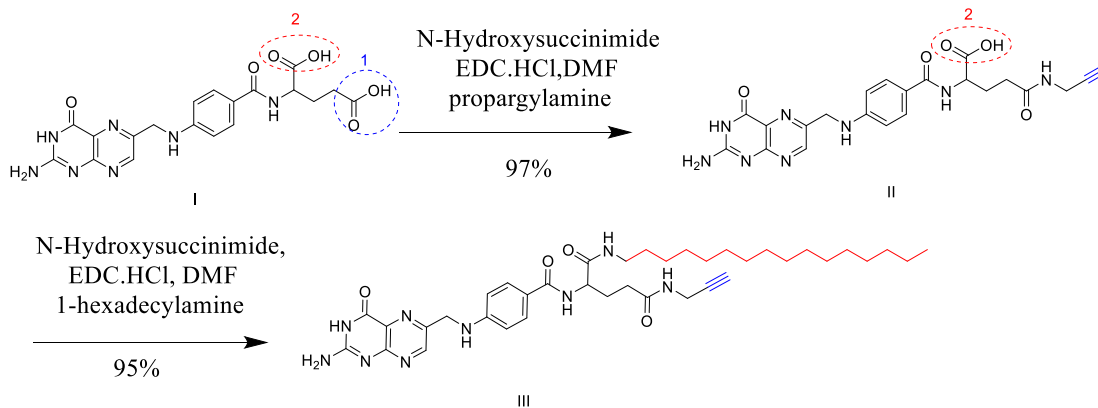


Fig. C-3 Schematic and top image of MZO_{nano} - TFT (taken by Dr. Pavel Ivanoff Reyes from Dr. Lu's group)

C.2 Synthesis of HAFA

The synthesis of HAFA is shown in scheme C-3. In the first step, folic acid was coupled with propargylamine to react carboxylic acid (1) to form amide in the presence of coupling reagents 1-(3-dimethyl-aminopropyl)-3-ethylcarbodiimide hydrochloride (EDC·HCl)/N-hydroxysuccinimide. In this way, it was introduced the alkyne group that can react with the azido-terminated MZO_{nano} film surface via CuAAC.

In the second step, carboxylic acid group (2) was reacted with 1-hexadecylamine. The blocking of this carboxylic acid group is important. Firstly, the introduction of this long alkyl chain improves the solubility of the folic acid derivative in organic solvents. Secondly, the protection of this carboxylic acid group will prevent it from replacing the linker molecules on functionalized MZO_{nano} films. Thirdly, amidification of this carboxylic acid group will reduce the acidity of this compound, helping to preserve the nanorod morphology.



Scheme C-3 Synthesis of HAFA

Fig. C-4 shows the ATR-FTIR spectrum of HAFA. The FTIR spectrum of HAFA did not overlap with that of azide-terminated MZO_{nano} film at the azide region and N-H stretching band region. There is overlapping between FTIR spectra of bands at amide I and II region of HAFA and bands at carboxylate moiety region of azide-terminated MZO_{nano} film (Fig. B-4). In our FTIR imaging study, the amide I and II region and carboxylate moiety region cannot be used as IR probes.

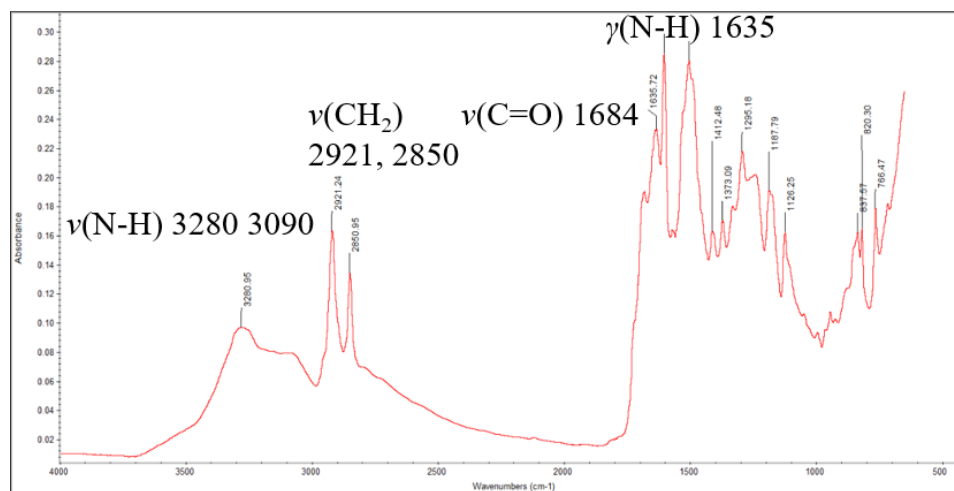


Fig. C-4 ATR-FTIR spectrum of HAFA

C.3 Study of the immobilization of HAFA on azido-functionalized MZO_{nano} films by FTIR microscopic imaging

HAFA was immobilized on azido-terminated MZO_{nano} film via surface CuAAC^{43, 45, 162}. The experimental set-up is shown in Fig C-17. In most conditions, CuAAC is catalyzed by Cu^I generated in-situ from Cu^{II} salts. A well-established protocol involves the use of copper sulfate as the copper source and, the reducing reagent, sodium ascorbate, which is a water soluble, mild, and biocompatible. Recently, the use of tris(2-carboxyethyl)phosphine (TCEP) as an efficient reducing reagent was reported¹⁶³⁻¹⁶⁵. To prevent the reducing agent from reducing Cu^{II} to copper metal, a copper-stabilizing agent, typically a coordinating ligand, is needed. Tris[(1-benzyl-1H-1,2,3-triazol-4-yl)methyl]amine (TBTA) was used as the stabilizing agent of Cu^I and prevents disproportionation and oxidation.

Copper byproducts that may be produced in CuAAC, include copper metal and Cu^I, which are cytotoxic. To avoid possible contamination of copper byproducts, MZO_{nano} film was placed faced down when immersing in HAFA solution during immobilization. After the immobilization step, the functionalized films were thoroughly rinsed by neat solvents to remove any copper byproduct left on the film surface.

C.3.1 Control experiment 1 (stability of azido-functionalized MZO_{nano} films in THF)

Prior to the surface CuAAC with HAFA, the stability of azido-terminated MZO_{nano} films in tetrahydrofuran (THF) solution, which is the solvent used in immobilization of HAFA, is studied by FTIR microscopic imaging. MZO_{nano} film was first bind with **1**, then immersed in THF solution while shaking on an incubator shaker at 150 rpm for 25min. FTIR images (Fig. C-5) of azido-functionalized MZO_{nano} film before and after immersion

in THF, clearly show that there is partial desorption of **1** from the MZO_{nano} film. The corresponding FTIR spectra shown in Fig. C-6 also indicate this trend. It is very important to control the immobilization time to avoid the desorption of **1**.

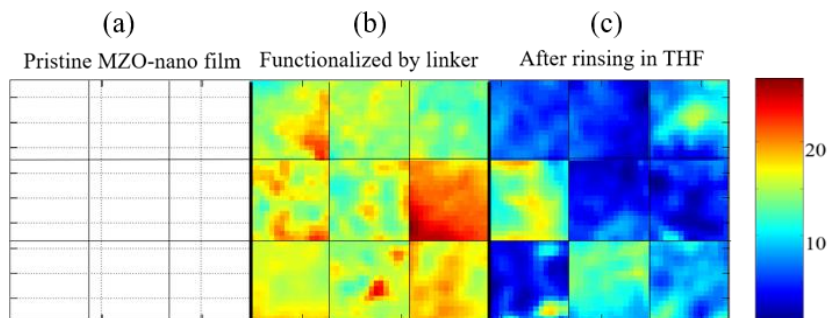


Fig. C-5 Images of the integrated band area of the azido region $2212\text{-}2064\text{cm}^{-1}$ (\pm STD) of (a) pristine MZO_{nano} film, (b) after binding with linker, (c) and after immersing in THF for 25 min under shaking

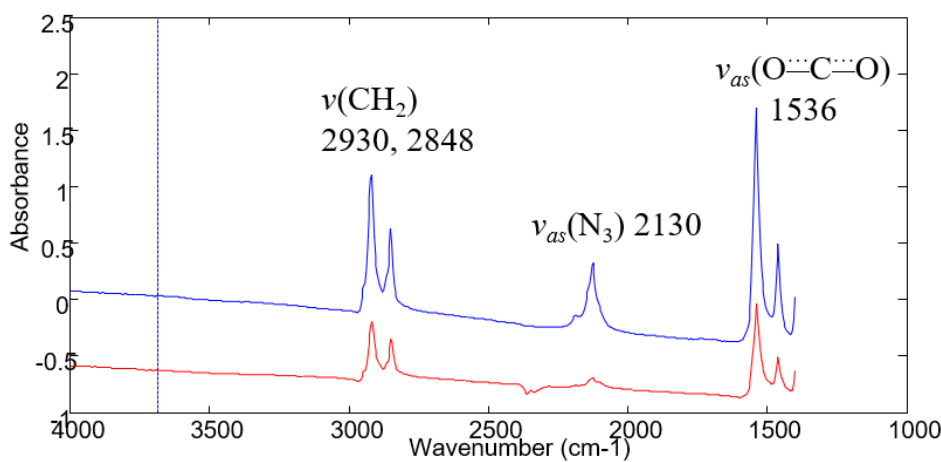


Fig. C-6 FTIR spectra of azido-functionalized MZO_{nano} film before (blue line) and after (red line) immersion in THF for 25 min under shaking

C.3.2 Control experiment 2 (physisorption of HAFA on MZO_{nano} films)

To study the possible physisorption of HAFA on MZO_{nano} film, pristine MZO_{nano} film was immersed in 20 mM HAFA (CuSO₄/TBTA/TCEP) THF solution while shaking on an incubator shaker at 150 rpm for 15 min. The FTIR image integrated at N-H stretching region shown in Fig.C-7 and the corresponding FTIR spectrum (Fig.C-8, red line) possess all the characteristic bands of HAFA (N-H stretching, C-H stretching, C=O stretching and

N-H bending), indicating the physisorption of HAFA on MZO_{nano} film. By immersing the film in pure THF solution under shaking for 10 min, all the physisorbed HAFA can be rinsed out (Fig. C-7, Fig. C-8 blue line). Therefore, in our following surface CuAAC studies, all films were rinsed by THF solution for 10 min each time after immobilization.

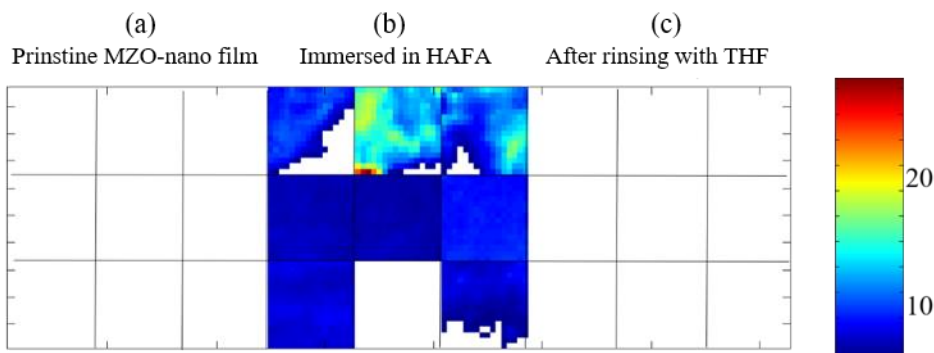


Fig. C-7 Physisorption experiment. Images of the integrated band area of the N-H stretching region 3460-2988 cm^{-1} (\pm STD) of (a) pristine MZO_{nano} film, (b) after immersed in HAFA ($\text{CuSO}_4/\text{TBTA}/\text{TCEP}$) THF solution under shaking for 15 min, (c) and after rinsing with THF for 10 min

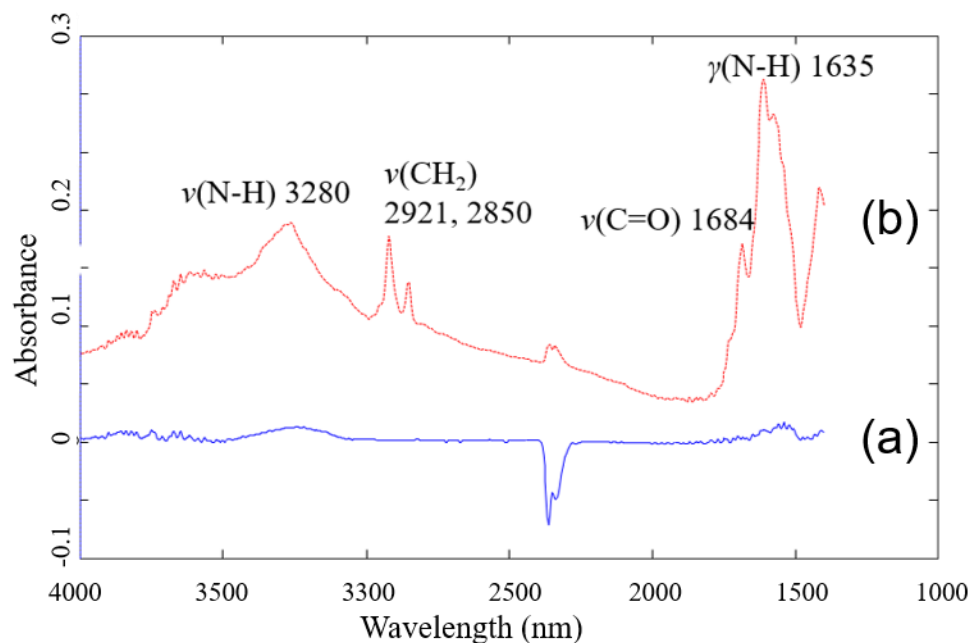


Fig. C-8 FTIR spectra of pristine MZO_{nano} film after (a, red line) immersing in 20 mM HAFA ($\text{CuSO}_4/\text{TBTA}/\text{TCEP}$) THF solution under shaking for 15 min (red line), and after rinsing with THF for 10 min (b, blue line)

C.3.3 Immobilization of HAFA on azido-terminated MZO_{nano} films

The immobilization of HAFA on azido-terminated MZO_{nano} film was studied by FTIR microscopic imaging. Fig. C-9 shows a typical FTIR spectrum of azido-terminated MZO_{nano} film before (black line) and after immobilization with HAFA after 5 min (blue line) and after 15 min (red line). Films were thoroughly rinsed by neat THF to remove any physisorbed HAFA. Upon immobilization, new band at 3300 cm⁻¹ which was assigned to N-H stretching band ($\nu(\text{N-H})$) of HAFA emerged, and its intensity increased with longer immobilization times. Also, the bands of C=O stretching mode ($\nu(\text{C=O})$) at 1684 cm⁻¹ and N-H bending mode ($\gamma(\text{N-H})$) at 1608 cm⁻¹ appear, indicating that HAFA was immobilized onto MZO_{nano} film. The bands of the C-H stretching region ($\nu_{as}(\text{CH}_2)$ at ~2930 cm⁻¹, $\nu_s(\text{CH}_2)$ at ~2848 cm⁻¹) remained unaltered. A consistent decreasing of azido band ($\nu_{as}(\text{N=N=N})$ at 2130 cm⁻¹) was observed, indicating reaction with alkyne group of HAFA to form the triazole ring. The disappearance of the azido band was observed after reaction with HAFA for 15 min. As the C=O stretching and N-H bending bands from the immobilized HAFA overlap with the carboxylic moiety ($\nu_{as}(\text{O}^{\cdots}\text{C}^{\cdots}\text{O})$) at 1536 cm⁻¹ and 1480 cm⁻¹ assigned to **1** on MZO_{nano} film, assignment of individual bands was not possible, whereas the azido and N-H stretching bands could be used as probes.

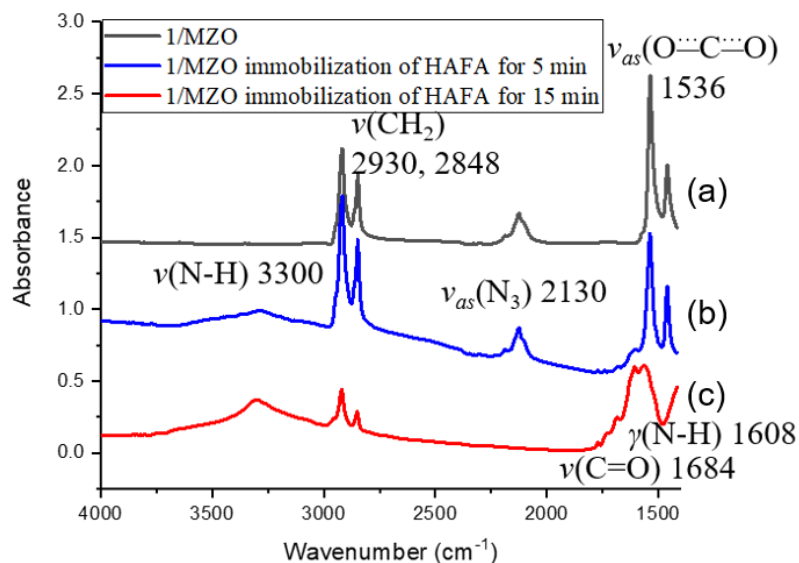


Fig. C-9 FTIR spectra of azido-terminated MZO_{nano} film before (a, black line) and after immobilization with HAFA for 5 min (b, blue line) and 15 min (c, red line)

Fig. C-10 is the image of integrated band area of azido region of azido-terminated MZO_{nano} film at different immobilization time. A fully reacted MZO_{nano} film with HAFA was obtained after immobilization for 15 min, before desorption of **1** may occur.

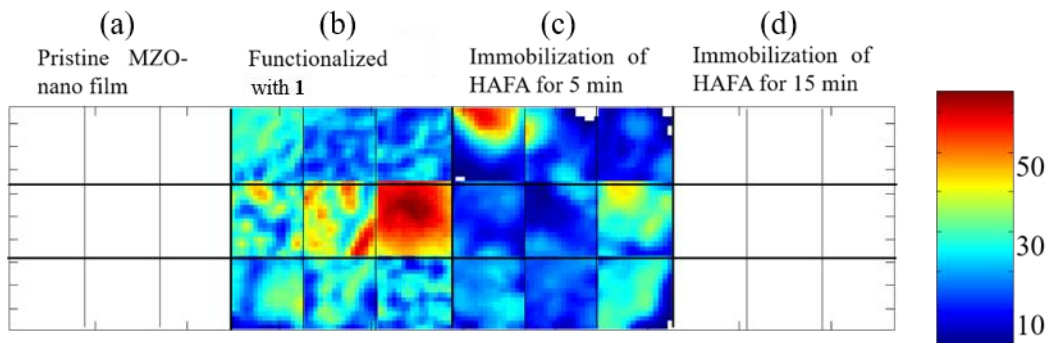


Fig. C-10 Images of the integrated band area of the azide region 2212-2064 cm^{-1} (\pm STD) of (a) pristine MZO_{nano} film, (b) after binding with **1**, (c) after immobilization of HAFA ($\text{CuSO}_4/\text{TBTA}/\text{TCEP}$) THF solution with shaking for 5 min, and (d) 15 min, respectively

The images of integrated band area of N-H stretching region shown in Fig. C-11 indicate that HAFA was fully immobilized onto azido-terminated MZO_{nano} film via surface CuAAC within 15 min.

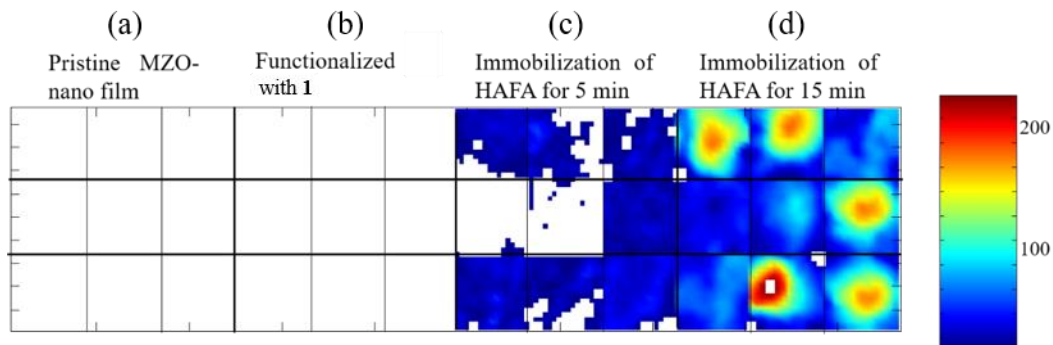


Fig. C-11 Images of the integrated band area of the N-H stretching region $3460\text{-}2988\text{ cm}^{-1}$ (\pm STD) of (a) pristine MZO_{nano} film, (b) after binding with **1**, (c) after immobilization of HAFA ($\text{CuSO}_4/\text{TBTA}/\text{TCEP}$) THF solution with shaking for 5 min, and (d) 15 min

In conclusion, the immobilization study by FTIR microscopic images, together with stability and physisorption studies, confirm that HAFA can be successfully covalently immobilized onto the MZO_{nano} film via surface CuAAC.

C.4 Study of immobilization of HAFA on functionalized MZO_{nano} film by Fluorescence spectroscopy

The stepwise functionalization of MZO_{nano} film was also studied by monitoring the fluorescence emission of HAFA. Folic acid derivatives are used as fluorescent probes in bioimaging and analysis¹⁶⁶⁻¹⁶⁸. The UV-vis absorption and fluorescence emission spectra of HAFA are shown in Fig. C-12.

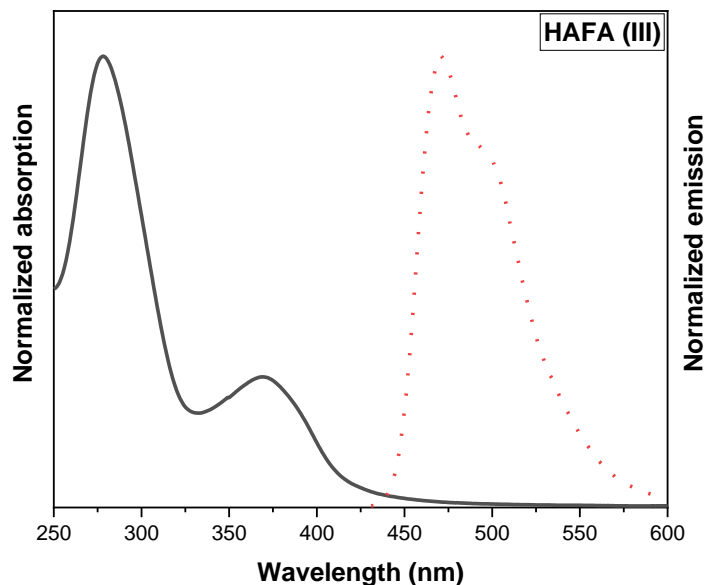


Fig. C-12 Normalized absorption (left, black, solid line) and emission (right, red, dotted line) spectra of HAFA in methanol. $\lambda_{\text{ex}}=369$ nm

As shown in Fig. C-12, HAFA exhibits two bands centered at 278 nm and 369 nm respectively in the absorption spectrum, and an intense band at 471 nm and a shoulder band at 492 nm in the emission spectrum ($\lambda_{\text{ex}}=369$ nm).

After surface CuAAC, upon excitation at 369 nm, the MZO_{nano} film was fluorescent as shown in Fig. C-13. The fluorescence emission spectrum of MZO_{nano} film after HAFA immobilization resembles that of free HAFA in solution, indicating that HAFA was successfully immobilized onto MZO_{nano} film.

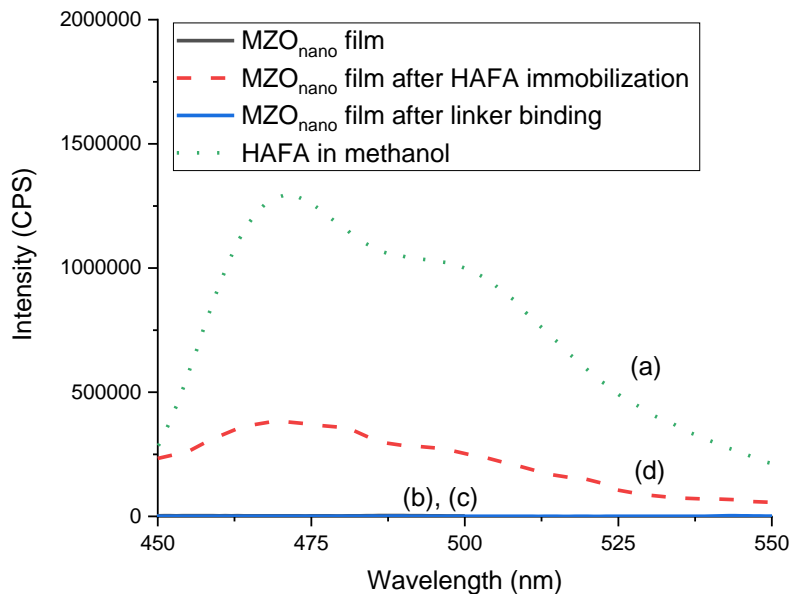


Fig. C-13 Fluorescence spectra of HAFA in methanol (a, green, dotted line), MZO_{nano} film before (b, black, solid line), after binding with **1** (c, blue, solid line), and after immobilization of HAFA (d, red, dash line). $\lambda_{ex}=369$ nm

C.5 Preparation of MZO_{nano}-QCM based biosensor

The work of this section was carried out in collaboration with Dr. Yicheng Lu's group at Rutgers University-New Brunswick. The stepwise functionalization method was applied to prepare a folic acid-modified MZO_{nano}-QCM biosensor. QCM measures the change in resonance frequency of the quartz crystal resonator that detects the binding of molecules at the surface of the acoustic resonator. The operating frequency of the MZO_{nano}-QCM is 9.9096 MHz. The characterization and testing of the devices were conducted using an HP 8573D Network Analyzer (Agilent Technologies, Palo Alto, CA). The acoustic impedance transmission ($Z_{21}(f)$) spectrum of the device was automatically measured and digitally stored for each step of the functionalization processes. These signals were analyzed by extracting the peak frequency shifts experienced by the device relative to their starting frequency due to the accumulation of mass on the sensing surface. According to

Sauerbrey¹⁶⁹, the frequency shift of the impedance spectrum is directly proportional to the mass accumulation on the sensing electrode of the QCM by the expression:

$$\frac{\Delta f}{f_0} = \frac{2f_0}{v_q \rho_q A} \Delta m \quad (\text{C-1})$$

Where Δf is the frequency shift, f_0 is the operating frequency of the device, v_q and ρ_q are the acoustic velocity and mass density of the AT-cut quartz layer respectively, A is the sensing area of the top electrode, and Δm is the accumulated mass on the sensing electrode.

MZO_{nano}-QCM was modified by stepwise functionalization with **1** (step A) and HAFA (step B) for 5 minutes and 15 minutes. The acoustic impedance spectra of the sensors were measured using a HP8753D Network Analyzer after each functionalization steps. The frequency of the acoustic impedance spectra of MZO_{nano}-QCM before and after these two steps were recorded and are reported in Fig. C-14.

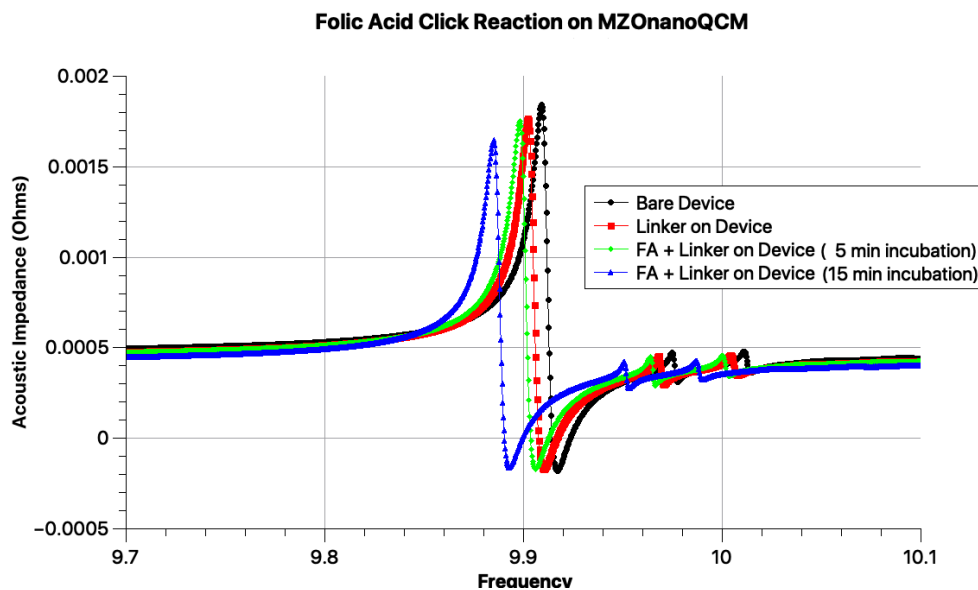


Fig. C-14 Acoustic impedance spectra (Ohms) of MZO_{nano}-QCM before (black dots), after binding with **1** for 22 h (step A, red squares), and after immobilization of HAFA for 5 min (step B, green triangles) and 15 min (step B, blue triangles) (taken by Dr. Pavel Ivanoff Reyes from Dr. Lu's group)

A consistent decrease of frequency was observed after step A and B, indicating the loading of **1** and HAFA respectively, on the MZO_{nano}-QCM. The change of frequency ΔF were calculated and are listed in Table C-1.

Table C-1 Frequency shifts of MZO_{nano}-QCM after each chemical step.

	ΔF (KHz)	ΔF (KHz)	ΔF (KHz)
	Step A	Step B (5 min)	Step C (15 min)
MZO _{nano} -QCM	7.6	3.0	65.5

As the mass loading on the QCM can be determined directly from the shift in its resonant frequency and its mass sensitivity, we can calculate the sensitivity of this fabricated MZO_{nano}-QCM sensor. The sensitivity (S) is given by the formula

$$S = \left(\frac{\Delta f}{f_0} \right) \left(\frac{A}{\Delta m} \right) \quad (C-2)$$

The device was then calibrated for detection by adding to the sensor 2 μ L of calibration liquid with known mass density of 20 μ g/mL, which yielded a frequency shift of 0.3 kHz due to mass loading. The device sensitivity of 154.817 cm^2/g was calculated using Equation C-2.

C.6 Preparation of MZO_{nano}-TFT based biosensor

The work of this section was carried out in collaboration with Dr. Yicheng Lu's group at Rutgers University-New Brunswick. MZO_{nano}-TFT was fabricated and modified by **1**. In a TFT device, the type of bio-organic molecules bound on the detection area and the interface

between the molecules and device surface greatly influence the electrical performance because they affect the carrier transport. The I_{DS} (Current between drain and source)- V_{GS} (Potential between gate and source) transfer characteristics of a MZO_{nano} -TFT were measured using an HP-4156C with an HP-41501b Pulse Generator. The transfer characteristics of an MZO_{nano} -TFT before and after step A were recorded and are reported in Fig. C-15.

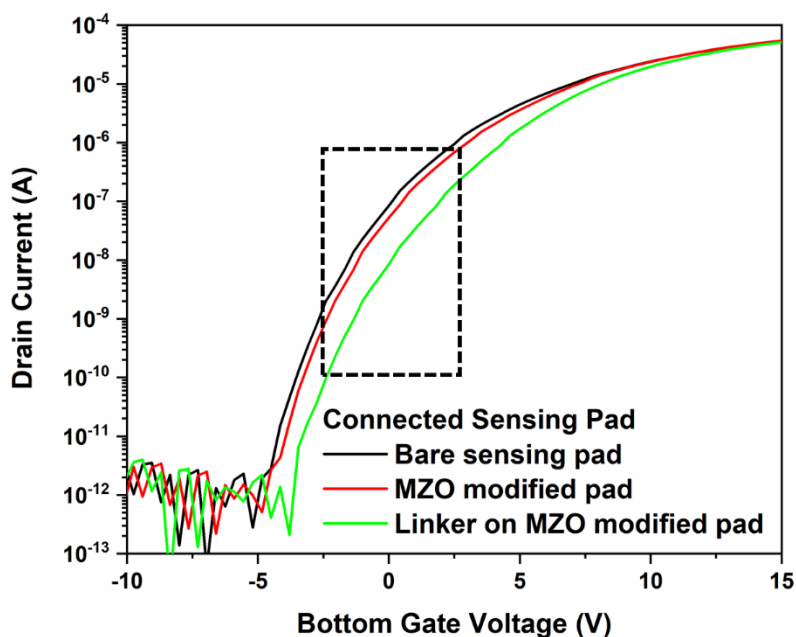


Fig. C-15 The I_{DS} - V_{GS} transfer characteristics of an MZO_{nano} -TFT before and after linker binding (taken by Guangyuan Li from Dr. Lu's group)

The linear region within the dashed box was zoomed in and is displayed in Fig. C-16.

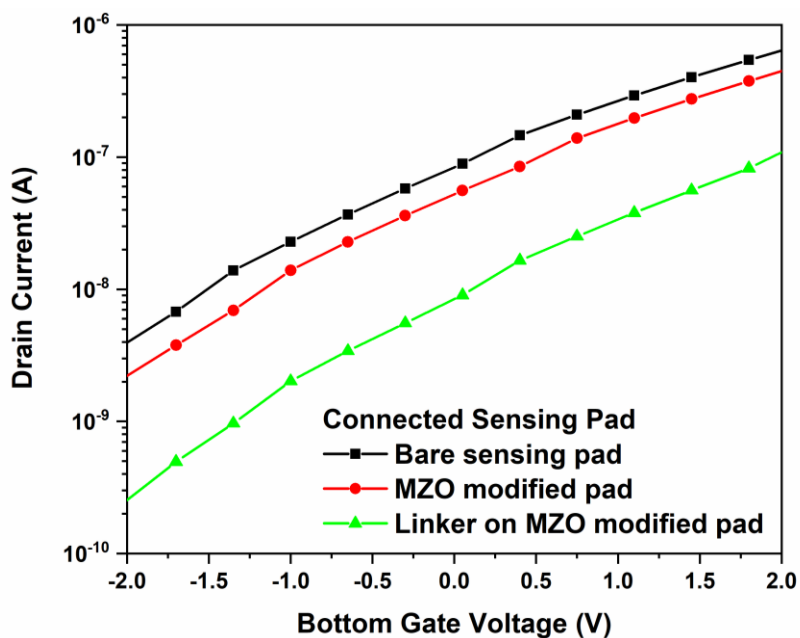


Fig. C-16 Zoomed in linear region of transfer characteristics of an MZO_{nano} -TFT before and after linker binding (taken by Guangyuan Li from Dr. Lu's group)

A sharp decrease of drain current was observed after step A. The change of current was calculated and it is listed in Table C-2.

Table C-2 Summarized the Drain current shifts of MZO_{nano} -TFT after each chemical step.

	Drain current (A) $\times 10^{-8}$
<i>Au pad</i>	8.92
<i>MZO_{nano}-TFT</i>	8.89
<i>MZO_{nano}-TFT after step A</i>	0.904

This decrease in drain current indicates the introduction of surface electrostatic potential on MZO_{nano} -TFT surface via the binding with 11-azidoundecanoic acid.

C.7 Conclusions

MZO_{nano} film was functionalized by 11-azidoundecanoic acid (discussed in last chapter) and, by click chemistry, with HAFA (hexadecyl alkynated folic acid). The substitution of folic acid with an alkyne group (carboxylic acid (1)) and a long aliphatic chain (carboxylic acid (2)) via amide formation, allowed to carry out click chemistry, enhanced solubility, reduced the acidity and blocked the carboxylic acid group from directly bind onto MZO_{nano} film. HAFA was immobilized onto the MZO_{nano} film bearing a reactive azido layer through CuAAC by an immersion method. This surface click reaction was monitored by FTIR microscopic imaging. Two control experiments were performed to study the stability of azido-functionalized MZO_{nano} film in THF and the physisorption of HAFA on MZO_{nano} film. Physisorption of HAFA on pristine MZO_{nano} film was observed, however this can be fully rinsed out by THF, and an appropriate reacting time (15 min) was determined. Fluorescence spectroscopy was also used to characterize the click immobilization process. Following this stepwise functionalization method, folic acid-modified MZO_{nano}-QCM biosensors were fabricated. The loading of 11-azidoundecanoic acid and HAFA on MZO_{nano}-QCM during each step resulted in a change in resonance frequency of the quartz crystal resonator. Due to the very high affinity ($K_d = 0.1\text{-}10\text{ nM}$) to of folic acid derivatives to folate receptors, this folic acid-modified MZO_{nano}-QCM biosensors can be used to detect folate receptors which accumulated in cancer cells, and this sensing work is still in progress. We are also attempting the fabrication of folic acid-modified MZO_{nano}-TFT. In replacing of QCM with TFT as the sensing matrix may increase the sensitivity of sensor devices and expand the using of such biosensor in in-vivo detection.

C.8 Experimental section

General. All the following solvents and reagents were used as received from commercial sources: 3-methoxypropionitrile (MPN) (99%, Sigma Aldrich), propargylamine (98%, Sigma Aldrich), dimethyl sulfoxide ($\geq 99.5\%$, Sigma Aldrich), *N,N*-dimethylformamide (anhydrous, 99.8%, Sigma Aldrich), dichloromethane ($\geq 99.5\%$, Sigma Aldrich), 11-bromoundecanoic acid (99%, Sigma Aldrich), folic acid ($\geq 97\%$, Sigma Aldrich), *N*-hydrosuccinimide (98%, Sigma Aldrich), 1-(3-Dimethylaminopropyl)-3-ethylcarbodiimide hydrochloride (EDC·HCl, BioXtra, Sigma-Aldrich), 1-Hexadecylamine (98%, Sigma Aldrich), Copper sulfate (anhydrous, $\geq 99.99\%$, Sigma Aldrich), Tris(2-carboxyethyl)phosphine hydrochloride (TCEP, powder, Sigma Aldrich), Tris[(1-benzyl-1H-1,2,3-triazol-4-yl)methyl]amine (TBTA, 97%, Sigma Aldrich), sodium azide ($\geq 99.5\%$, Sigma Aldrich), quartz crystal microbalance (QCM, GAMRY instruments), incubator shaker (New Brunswick Innova 4000). The reactions were performed under N_2 gas and in oven-dried glassware. 1H and ^{13}C nuclear magnetic resonance (NMR) spectra were collected on a Varian NMR spectrometer operating at 599.714 Hz for 1H and 150.812 Hz for ^{13}C . Chemical shifts (δ) are reported relative to the central line of the solvent: $CDCl_3$ (δ 7.27 ppm for 1H and δ 77.27 ppm for ^{13}C) and DMSO (δ 2.50 ppm for 1H and δ 39.52 ppm for ^{13}C), and spin-spin coupling constants (J) are reported in Hz. The Fourier transform infrared (FTIR) spectrum in Fig. C-4 was collected on a Thermo Electron Corporation Nicolet 6700 FTIR utilizing the SMART MIRacle-single bounce ATR accessory (ZnSe crystal, with 128 scans and spectral resolution of 8 cm^{-1}). Field emission scanning electron microscopy (FESEM) images were collected on a Hitachi S4800. ESI spectra were collected on an Apex-ultra 70 hybrid Fourier transform mass spectrometer

(Bruker Daltonics). Fluorescence emission spectra were collected on a Varian Cary-Eclipse. The films were placed diagonally at a 45° angle in a 1 cm cuvette in air while recording the spectra. UV-vis absorbance spectra were collected at room temperature on a Varian Cary 500 spectrophotometer.

Synthesis of 11-azidoundecanoic acid (1) and Binding of 11-azidoundecanoic acid (1) onto MZO_{nano} film (droplet method), see chapter B

Synthesis of alkynated folic acid (AFA. II): Folic acid (1.0 g, 2.2 mmol) was dissolved in DMF (15 ml) and cooled with an ice bath. N-hydroxysuccinimide (0.26 g, 2.5 mmol) and 1-(3-dimethylaminopropyl)-3-ethylcarbodiimide hydrochloride (EDC) (0.44 g, 2.5 mmol) were added in one portion, and the resulting mixture was stirred while cold (ice bath) for 30 min. Propargylamine (0.14 g, 2.3 mmol) was dissolved in DMF (5 ml) and the solution was added to the folic acid solution in one portion. The reaction mixture was warmed to room temperature and stirred for 24 h, then poured into water (100 ml) and stirred for 30 min to form orange precipitate. The mixture was vacuum filtered (filtration of the fine precipitated required several hours) to remove water soluble reagents such as EDC urea, the solid was collected, washed with acetone, and dried in high vacuum to yield AFA as a yellow orange solid (0.80 g, 1.8 mmol, 81%). ¹HNMR (DMSO-d₆) δ 11.43 (s, 1H, -CONHCNNH₂), 8.64 (s, 1H, PtC7H), 8.27 (br, 1H, -CONHCHCOOHCH₂), 8.14 (t, 1H, NHCH₂CCH), 8.01 (t, 1H, CH₂-NH-Ph), 7.64-7.66 (d, 2H, Ph-C2H and Ph-C6H), 6.92 (s, 2H, NH₂), 6.63-6.65 (d, 2H, Ph-C3H and Ph-C5H), 4.48-4.49 (d, 2H, PtC₆-CH₂NH-Ph), 4.25-4.33 (m, 1H, -CONHCHCOOH), 3.81-3.83 (d, 2H, -CONH-CH₂CCH), 3.06 (s, 1H, -CONH-CH₂CCH), 2.19-2.32 (m, 2H, -CHCH₂CH₂), 1.90-2.04 (m, 2H, -CHCH₂CH₂). HRMS (ESI): calculated for C₂₂H₂₃N₈O₅, 479.1786 [M+H]⁺; found: 479.1800 [M+H]⁺

Synthesis of hexadecyl alkynated folic acid (HAFA, III): Alkynated folic acid (3.5 g, 7.3 mmol) was dissolved in DMF (38 ml) and cooled in water/ice bath. N-hydroxysuccinimide (1.8 g, 14.6 mmol) and EDC (3 g, 14.6 mmol) were added, and the resulting mixture was stirred in the ice bath for 30 min. 1-Hexadecylamine (3.5 g, 14.6 mmol) was dissolved in DMF (19 ml) and the solution was added to the alkynated folic acid solution. The mixture was warmed to room temperature and stirred for 24 h, then poured into water (300 ml) and stirred for 30 min to form orange precipitate. The mixture was filtered overnight to remove water soluble reagents such as EDC urea, the filtrate was washed with acetone, acetonitrile, and dried under high vacuum to remove all the solvents to yield HAFA as an orange solid (3.9 g, 5.7 mmol, 78%). ¹HNMR (DMSO-d₆) δ 11.42 (s, 1H, -CONHCNNH₂), 8.64 (s, 1H, PtC7H), 8.25-8.27 (d, 2H, -CONHHCHCOOHCH₂ and -CONHHCH₂CH₂), 8.02 (t, 1H, NHCH₂CCH), 7.76 (t, 1H, CH₂-NHC-Ph), 7.65-7.66 (d, 2H, Ph-C2H and Ph-C6H), 6.92 (s, 2H, NH₂), 6.63-6.64 (d, 2H, Ph-C3H and Ph-C5H), 4.48 (s, 2H, PtC6-CH₂NH-Ph), 4.31-4.27 (m, 1H, -CONHCHCONH), 3.81-3.83 (d, 2H, -CONH-CH₂CCH), 3.05 (s, 1H, -CONH-CH₂CCH), 2.75 (s, 2H, -CONHCH₂CH₂), 2.08-2.29 (m, 2H, -CHCH₂CH₂), 1.84-1.96 (m, 2H, -CHCH₂CH₂), 1.36 (s, 2H, -CONHCH₂CH₂), 1.23 (s, 26H, -CONHCH₂CH₂(CH₂)₁₃), 0.85 (s, 3H, -CONHCH₂CH₂(CH₂)₁₃CH₃). HRMS (ESI): calculated for C₃₈H₅₅N₉O₄K, 740.4009 [M+K]⁺; found: 740.4330 [M+K]⁺

Immobilization of hexadecyl alkynated folic acid (HAFA) onto azido-terminated MZO_{nano} film ¹²¹. To a 10 ml 20 mM hexadecyl alkynated folic acid (HAFA) solution in freshly distilled THF in a glass dish were added CuSO₄-TBTA (1:1) ligand complex (0.5 ml of a 20 mM stock solution in H₂O/DMSO/t-BuOH 4:3:1) and tris(carboxyethyl)phosphine (TCEP, 0.5 ml of a 20 mM stock solution in DI water). The

azido-functionalized MZO film was immersed suspended face-down in this solution, which was continuously gently shaken on an incubator shaker at 150 rpm for indicated time (5 or 15 min respectively) at room temperature. The films were thoroughly rinsed with THF and ethanol to remove weakly bound or physisorbed molecules and dried under gentle nitrogen flow.

Immersion method

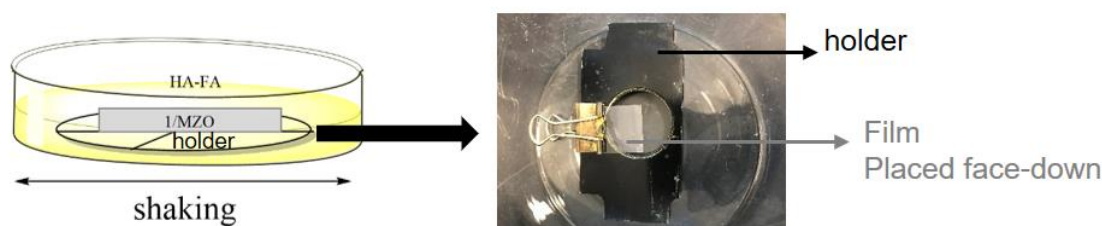


Fig. C-17 Schematic of immersing method

Preparation of MZO_{nano} film modified QCM device.

Procedure courtesy of Dr. Yicheng Lu's lab.

The MZO_{nano}-QCM comprises of a standard quartz crystal microbalance (QCM) coated with MZO nanorods on the sensing electrode. The standard QCM consists of a piezoelectric AT-cut quartz layer that has a thickness of 166.8 μm which is sandwiched between two 100 nm gold electrodes. The sensing area of the top electrode was 0.2047 cm^2 . The MZO nanorods were grown directly on the top electrode of the standard QCM (International Crystal Manufacturers, Inc.) using metal organic chemical vapor deposition (MOCVD) using Diethylzinc (DEZn), bio-(methyl-cyclopentadienyl) magnesium (MCp₂Mg) and ultra-high purity (99.999%) oxygen gas were used as the Zn metalorganic source, Mg metalorganic source and oxidizer, respectively. The film thickness was controlled as ~ 400 nm and the temperature was maintained at 450°C-500°C. The Mg

concentration is optimized to be at 4-5% through Mg/Zn ratio of the precursors. By using ultraviolet (UV) illumination the surface wettability of MZO nanorod film surface can be controlled to attain a hydrophilic surface. Making the nano-sensing area super-hydrophilic significantly decreases the liquid sample consumption. In this work, the MZO_{nano}-QCM was exposed under UV radiation (Modal 66002, Oriel Optics, Stratford CT) for 10 minutes to make the nano-sensing area super-hydrophilic. The resulting device is the MZO_{nano}-QCM with morphology and wettability controlled sensing surface. The FESEM image of the MZO nanorod film is shown in Fig. C-18

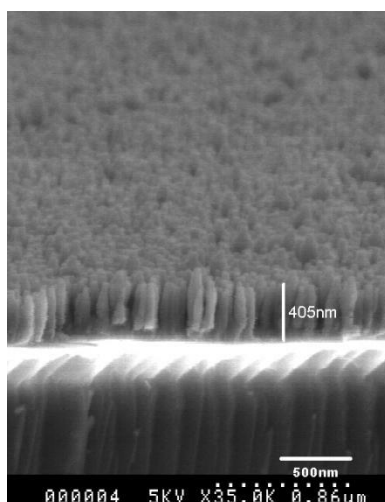


Fig. C-18 FESEM image of MZO_{nano}-QCM

Stepwise functionalization of MZO_{nano} film modified QCM. The Stepwise functionalization of MZO_{nano}-QCM follows the general procedure described in the section of functionalization of MZO_{nano} film: binding of 11-azidoundecanoic acid onto MZO_{nano} film in chapter B, and immobilization of hexadecyl alkynated folic acid (HAFA) onto azido-terminated MZO_{nano} film in chapter C, respectively.

Preparation of MZO_{nano} film modified TFT device (DGTFT)

Procedure courtesy of Dr. Yicheng Lu's lab.

To prepare the thin film transistor (TFT) bearing a layer of MZO nanorods, firstly, a 50 nm thick Cr layer was deposited and patterned to form the bottom gate electrode (b in Fig. C-3) on a glass substrate (a in Fig. C-3), Followed by the deposition of a layer of 100 nm thick SiO₂ (c in Fig. C-3) on the top of Cr bottom gate as the gate insulator layer using plasma enhanced chemical vapor deposition (PECVD). A 40 nm Mg_{0.03}Zn_{0.97}O channel layer with a 5 nm MgO interface modification layer (d in Fig. C-3), were grown using metal organic chemical vapor deposition (MOCVD) at 40 °C, resulting in the formation of a SiO₂/MgO/MZO structure. The MgO modification layer was used as a barrier to prevent the Zn ions diffuse to the dielectric layer^{159, 170}. Diethylzinc (DEZn), bio-(methylcyclopentadienyl) magnesium (MCp₂Mg) and ultra-high purity (99.999%) oxygen gas were used as the Zn metalorganic source, Mg metalorganic source and oxidizer, respectively. The active measurement area was wet etched and fixed at a width/length (W/L) = 160 μm/15 μm. The source and drain contacts are formed with Ti (85 nm)/Au (35 nm)/Ti (5 nm) by a normal lift-off process. Then a 70 nm thick top SiO₂ dielectric layer was deposited by PECVD again (e in Fig. C-3). Then, a 150 nm thick Al layer was deposited by electron beam evaporation as the top gate electrode (f in Fig. C-3) and then patterned. Finally, VIA openings were made using diluted buffered oxide etch.

Stepwise functionalization of MZO_{nano} film modified TFT. The Stepwise functionalization of MZO_{nano}-TFT follows the general procedure described in the section of functionalization of MZO_{nano} film: binding of 11-azidoundecanoic acid onto MZO_{nano} film in chapter B, and immobilization of hexadecyl alkynated folic acid (HAFA) onto azido-terminated MZO_{nano} film in chapter C, respectively.

FTIR Microscopic Imaging and Data Analysis¹⁷¹. FTIR microscopic images of MZO_{nano} films were collected with a Perkin-Elmer Spotlight 300 system (Perkin Elmer Life and Analytical Science, Inc., Waltham, MA) in the transmission mode with an essentially linear array (16×1) of mercury-cadmium-telluride (MCT) detector elements. Imaging size was 200×200 μm^2 . Images were collected with a 6.25×6.25 μm^2 pixel size and 32 scans at a spectral resolution of 8 cm^{-1} , corresponding to 32×32 pixel images. Visible micrographs were obtained with the optical microscope integrated into the Spotlight 300 system. FTIR microscopic images were generated from FTIR spectral data using ISys 3.1 software (Malvern Instruments, UK). Image planes of integrated band area were produced after linear baselines were applied in spectral regions of interest. The scale bar is color coded and selected to display the corresponding integrated area ($\pm\text{STD}$) above the detection limit to highlight differences upon treatments. The films used in our study were fixed onto a plate prior to data acquisition. Small shifts may occur during this process, resulting in small ($\sim \mu\text{m}$ scale) shifts of the images obtained.

Chapter D: Dipole-bridge design for chromophore-bridge-anchor at semiconductor surfaces

D.1 Introduction

As briefly described in chapter A, the study of the interfacial dipole effect on the energy level alignment between photo-excited sensitizer molecules and semiconductor such as colloidal TiO_2 is interest for photovoltaics and photocatalytis⁶¹⁻⁶³ (Fig. D-1). In this chapter, we describe a new approach to dipole bridge design for sensitizers, there characterization and binding studies.

Due to the presence of N to C permanent, Aib-peptides have been used to introduce dipole moments in solution¹⁷² and on gold electrodes¹⁷³. In this chapter, we present the synthesis of the Aib-peptide (Z-(Aib)₆-OtBu, Z (Cbz): carboxybenzyl, Fig.D-1) as the dipole linker.

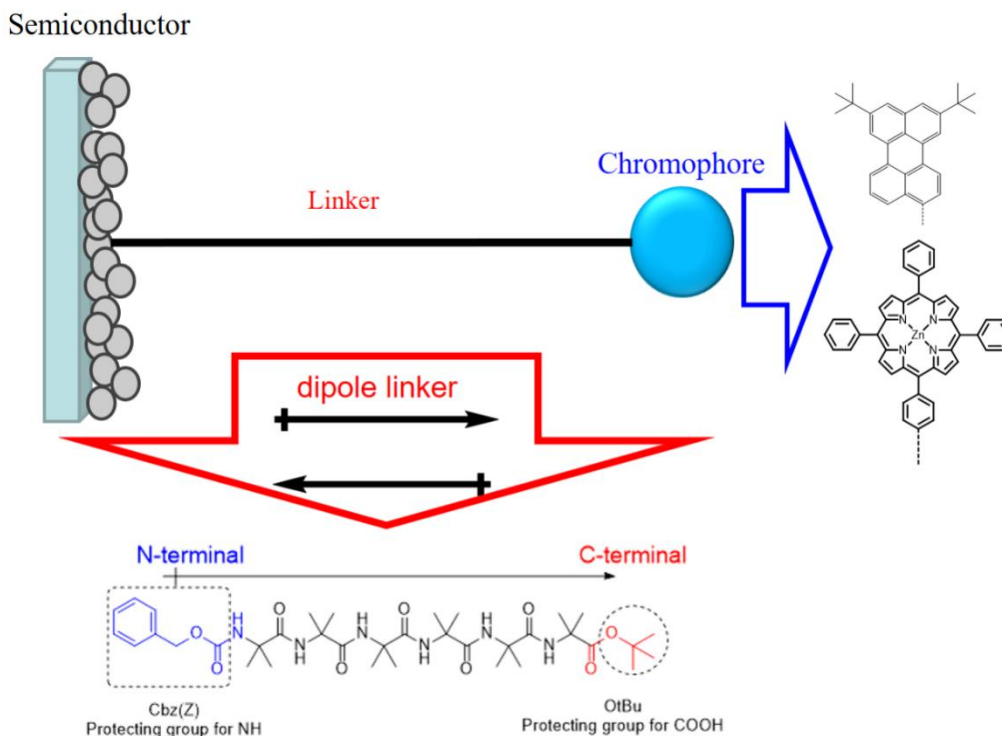


Fig.D-1 Design of dipole peptide (Z-(Aib)₆-OtBu) and chromophores

The Aib-peptide linker was protected at both N-terminus and C-terminus prior to reaction with the chromophores, as illustrated in Fig.D-2, The (Aib)_n-peptide has a dipole pointing

from N-terminus to C-terminus which arises from the helical conformation⁷⁷. The conformation was confirmed by the study of its characteristic H-bonding^{66, 174-176}. The dipole moment of the Aib-peptide depends on the number of Aib units employed. In our study, six Aib units were used to ensure a strong enough dipole (~ 18 D).

For coupling to chromophores, Z-(Aib)₆-OtBu was firstly deprotected at either the N-terminus or the C-terminus (Fig. D-2). Chromophores were coupled to the Aib-peptide at the deprotected terminus through amide bond formation. The other terminus was converted to carboxylic acid group, which is a typical anchoring group to metal-oxide semiconductors.

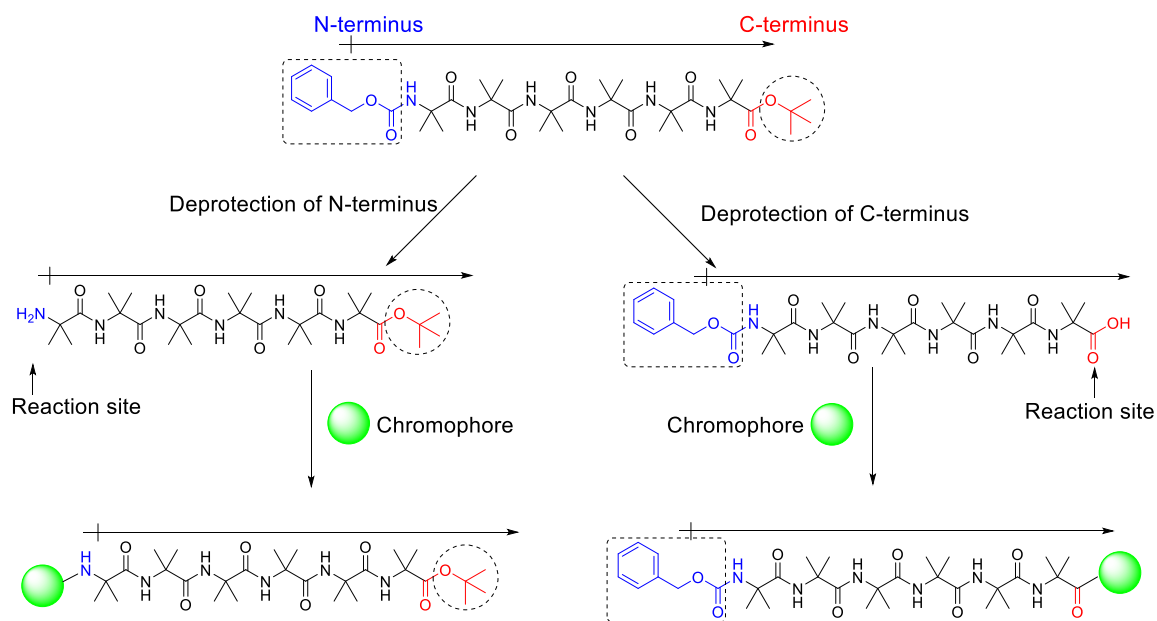


Fig.D-2 Two forms of the deprotection of Z-(Aib)₆-OtBu releasing C- and N- reaction sites

For the purpose of sensitizer design, di-*tert*-butyl-perylene (DTBPe) and zinc tetraphenylporphyrin (ZnTPP) were selected as the chromophore head group. Fig.D-3 shows the target sensitizers that were synthesized.

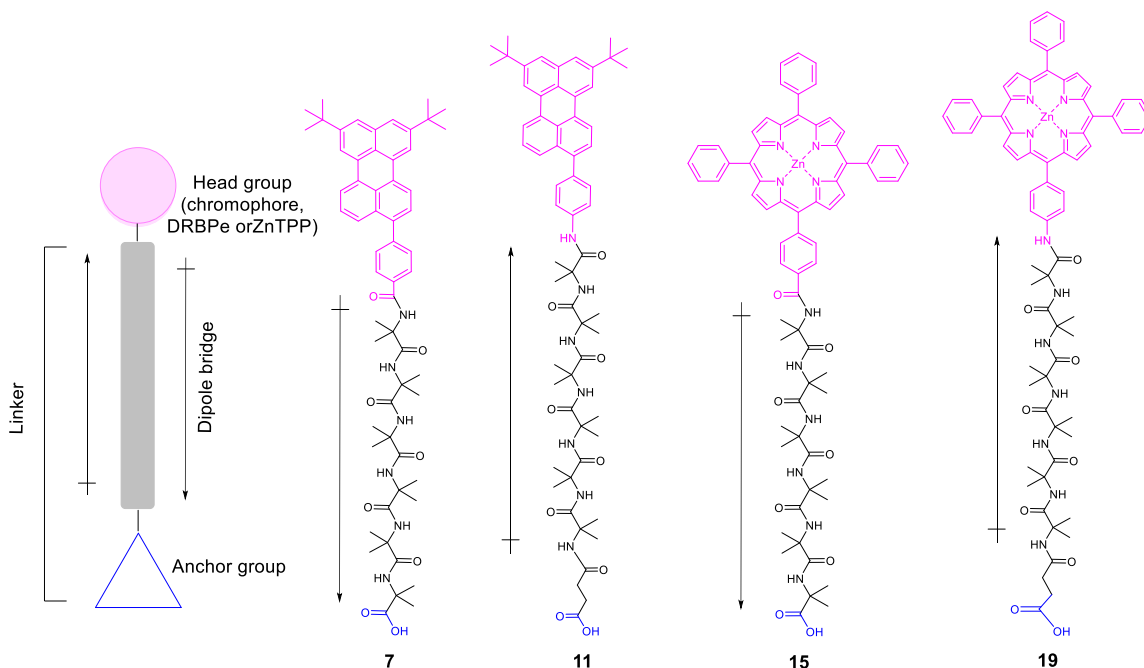


Fig.D-3 Chemical structures of the target perylene-based and porphyrin-based sensitizers with reversed dipoles

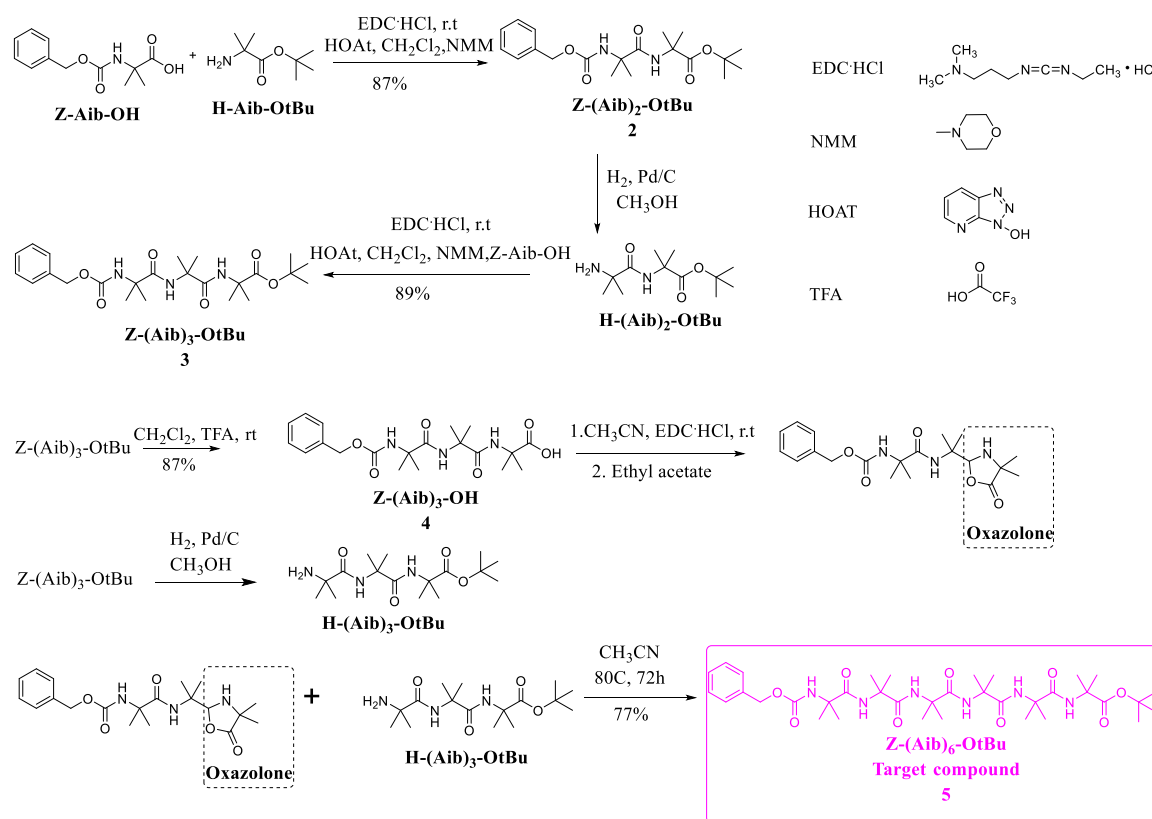
The coupling of chromophore DTBPe or ZnTPP to Aib peptide at different terminus (N-or C-) leads to the formation of a pair of sensitizers with opposite built-in dipole moments in the linker unit.

The synthesis and characterization of these four sensitizers in solution and on surfaces are described in this chapter.

D.2 Synthesis and conformational study of (Aib)_n peptides

Aib (α -Aminoisobutyric acid) is a non-natural amino acid. Unlike peptides made by L-alanine (Ala) which form α -helix structure, (Aib)_n peptides form 3_{10} -helix that requires less residues per turn. Aib is a non-chiral amino acid, will not produce racemic mixtures, further simplify the synthesis and purification process. The presence of two methyl groups at the C $^{\alpha}$ position imposes a steric hindrance that makes the coupling of Aib-peptides inherently complicated¹⁷⁷. Due to the difficulty of coupling two Aib, the solid-phase peptide synthesis

of Aib containing peptide always result in unsatisfactory yields. To improve the coupling efficiency, an Aib dipeptide (Fmoc-Aib-Aib-OH) was pre-synthesized and employed¹⁷⁸. Other reports point to the use of Fmoc amino acid fluorides as coupling reagent¹⁷⁹. Finally, microwave irradiation was also employed in the solid-phase peptide synthesis with improved reaction yield, purity and reduced reaction time¹⁸⁰⁻¹⁸². However, such methods, either require extra steps, or non-practical reaction conditions. In our study, we selected liquid-phase peptide synthesis to prepare the target (Aib)₆ peptide. Scheme D-1 illustrates the reaction scheme towards the target (Aib)_n compound. The synthesis follows classical peptide synthesis methodologies¹⁸³⁻¹⁸⁵.



Scheme D-1 Synthesis of Z-(Aib)₆-OtBu

The synthesis of Z-(Aib)₆-OtBu starts with the coupling of two Aib amino acids that are protected at either N-terminus or C-terminus. The N-protecting group (carboxybenzyl,

Cbz, Z) is a commonly used amine protecting group that can be easily deprotected by catalytic hydrogenation with Pd/H₂ in methanol. The C-protecting group (*tert*-butyl ester, OtBu) is readily deprotected by treatment with trifluoroacetic acid (TFA). Following deprotection, the carboxylic acid group was activated with the 1-(3-dimethyl-aminopropyl)-3-ethylcarbodiimide hydrochloride (EDC·HCl)/1-hydroxy-7-azabenzotriazole (HOAT) method¹⁸⁶. 4-Methylmorpholine (NMM) was used as the organic base. The Z-(Aib)₂-OtBu synthesized in the first step was deprotected at the N-terminus and further coupled with N-protected Aib amino acid to form Z-(Aib)₃-OtBu. The synthesis (from Z-(Aib)₃-OtBu to Z-(Aib)₆-OtBu) involves a “segment condensation”. During the segment condensation process, an Aib₃ oxazolone was obtained by treatment of Z-(Aib)₃-OtBu with 1-(3-dimethyl-aminopropyl)-3-ethylcarbodiimide hydrochloride in CH₃CN resulting in an Aib₃ protected at the N-terminus. The Aib₃ oxazolone protected at N-terminus was then coupled with Aib₃ deprotected at the N-terminus to form the final product Z-(Aib)₆-OtBu, protected at both ends. The yield of the first (1 to 2 in Scheme D-1) and second (2 to 3 in Scheme D-1) Aib coupling steps are 87% and 89% respectively, and the yield of “segment condensation” (3 to 4 in Scheme D-1) is 77%.

The backbone angle of an (Aib)_n is hindered, resulting in an extremely strong tendency of (Aib)_n to form helical structures⁶⁴. A variety of studies were conducted on the helical structures of (Aib)_n indicates that they tend to form a regular 3₁₀-helical structure, while the α -helical structure is more favored with (Ala)_n or with few Aib residues in a longer peptide⁶⁵. The difference between an α -helical structure and 3₁₀-helical structure is illustrated in Fig.D-4. The 3₁₀-helix exhibits intramolecular hydrogen bonding between the carbonyl group in residue *i* and the nitrogen of an amide group in residue *i*+3^{79, 175}, and 3

residues are required to form a turn in a 3_{10} -helix, with an angle of 120° between consecutive residues and a 1.93-2.0 Å pitch (Fig. D-4 (a)). The α -helical structure exhibits intramolecular hydrogen bonding between the carbonyl group in residue i and the nitrogen of an amide group in residue $i+4$, which means 3.6 residues are required per turn⁷, resulting in an angle of 100° between consecutive residues and a pitch of 1.5 Å (Fig. D-4 (b)). In summary, the 3_{10} -helix is narrower, more rigid and more elongated.

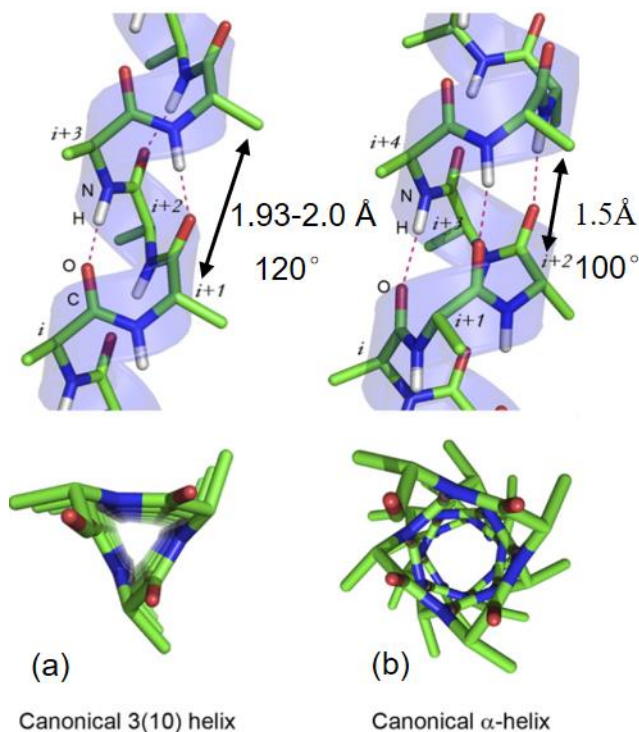


Fig.D-4 Canonical helical conformations of α -helical structure (left) and 3_{10} -helical structure (right). Side views (top) and views along the axis of a helix (bottom). Dotted lines indicate hydrogen bonds between atoms in the backbone of peptide. Adapted with permission from [175]

Infrared spectroscopy can also be employed for structure determination of peptides¹⁸⁷. The strengths of the bond vibrations in a molecule directly determined by the structure of the molecule, and the formation of hydrogen-bonding can clearly change the strengths of the bond vibration. In our study, we explore the IR experiments of amide-I (mainly the stretching vibration of C=O), amide-II (mainly the bending vibration of N-H) and N-H stretching modes, which are characteristic of 3_{10} -helical structure, to determine the $(Aib)_n$

secondary structure. The concentration of (Aib)_n solutions prepared were 5mM to exclude the presence of intermolecular hydrogen-bonding.

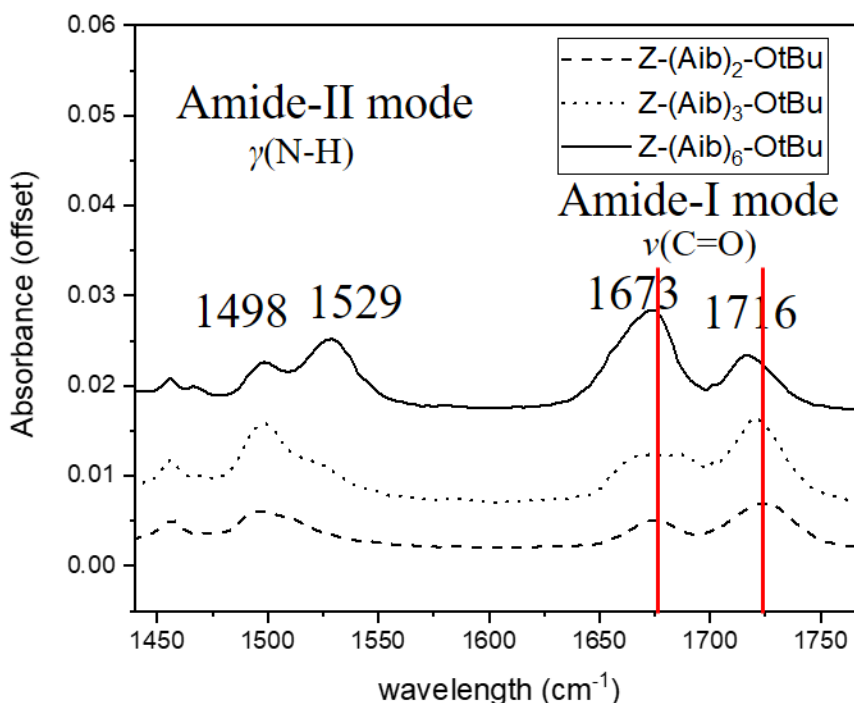


Fig.D-5 Infrared spectra in the 1420-1780 cm⁻¹ region for Z-(Aib)₂-OtBu, Z-(Aib)₃-OtBu and Z-(Aib)₆-OtBu in CHCl₃ (5mM)

Three (Aib)_n (n=2, 3, and 6) were studied by FTIR. Fig.D-5 shows the FTIR spectra in the region covering the C=O amide-I mode and the N-H bending/C-N stretching amide II modes. The amide-I mode, which arises mainly from the C=O stretching vibration, only depends on the secondary structure of backbone and therefore is most commonly used for secondary structure analysis. The downshift of amide-I frequency from Z-(Aib)₂-OtBu to Z-(Aib)₆-OtBu (2-10 cm⁻¹) indicates the formation of intramolecular hydrogen-bonding. The relative intensity of the lower frequency band increases as more H-bonds form¹⁸⁷.

The amide-II mode, mainly arise from the C-N stretching and N-H bending, vibrational modes which are connected through a 3₁₀-helical C=O...H-N hydrogen bond and involve the significant motion of these atoms¹⁸⁸. For Z-(Aib)₆-OtBu, two amide-II bands were

observed, at 1498 and 1528 cm^{-1} respectively. The higher frequency band was assigned to the hydrogen-bonded amide-II modes. The relative intensity of these two bands is determined by the number of Aib residues in the peptide chain. The spectrum of Z-(Aib)₂-OtBu indicates that the first two N-H groups at N-terminus were not involved in the intramolecular hydrogen bonding. The appearance of a shoulder band at $\sim 1525 \text{ cm}^{-1}$ shows that the intramolecular hydrogen bonding is starting from the third N-H groups at N-terminus with the urethan carbonyl group as a hydrogen bond acceptor. The blue shift of amide-II modes together with the intensity change indicate that Z-(Aib)₆-OtBu adopt the 3_{10} -helical conformation¹⁸⁸.

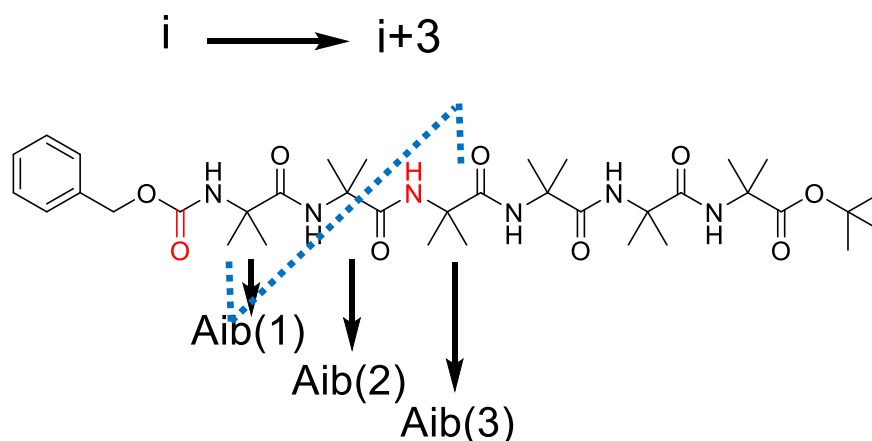


Fig.D-6 The $i \rightarrow i+3$ hydrogen bonding between the third N-H groups at N-terminus and the urethan carbonyl group of Z-(Aib)₆-OtBu

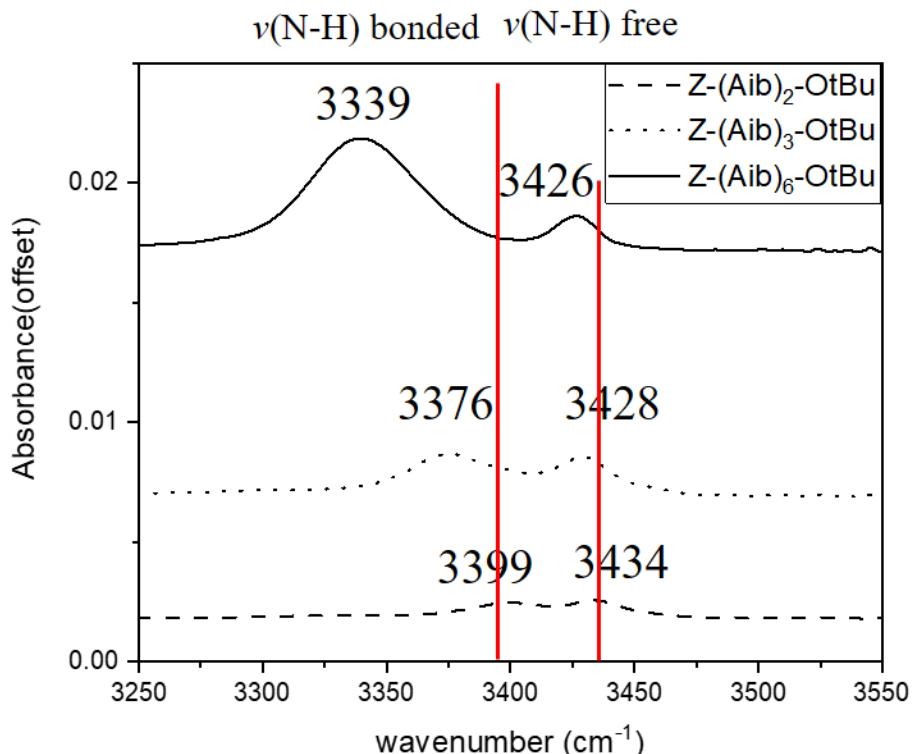


Fig.D-7 Infrared spectra in the region 3250-3550 cm^{-1} for the (Aib)_n peptides Z-(Aib)₂-OtBu, Z-(Aib)₃-OtBu and Z-(Aib)₆-OtBu in CHCl_3 (5mM)

The IR region at 3250-3550 cm^{-1} which is assigned to the N-H stretching modes was also investigated. The band at 3330-3400 cm^{-1} region was assigned to the NH group incorporated into H-bonded network¹⁸⁹. The band at 3420-3440 cm^{-1} region correspond to the free NH stretching¹⁸⁹. Fig.D-7 shows an almost constant intensity of the free NH stretching band, and a sharp increase in intensity of the NH stretching band related to hydrogen-bond as the peptide chain increase from Aib₂ to Aib₆. A red shift as n increases was also observed. This suggest the strong hydrogen-bonding formed in Z-(Aib)₆-OtBu.

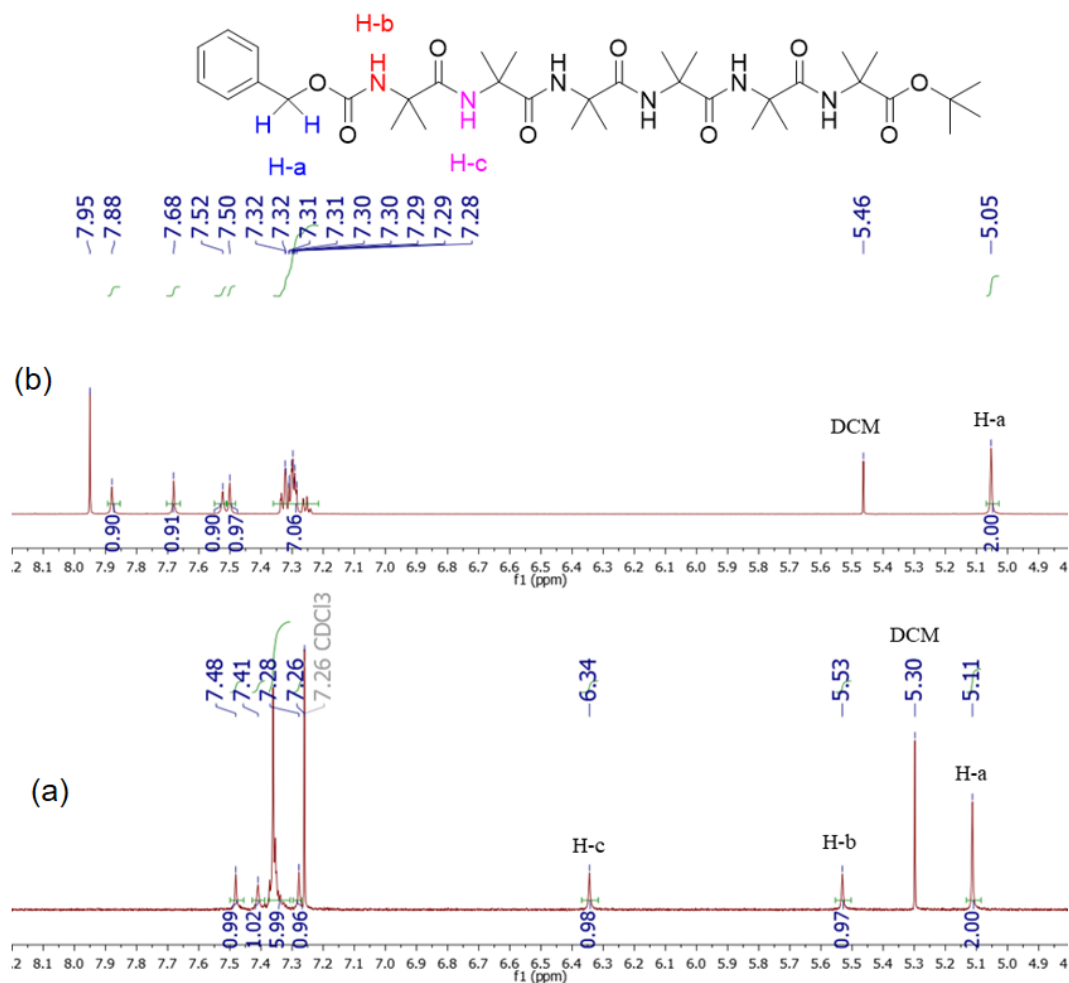


Fig.D-8 ¹HNMR of Z-(Aib)₆-OtBu in CDCl₃ (a, bottom), and 4:5 (CD₃)₂SO (DMSO-D₆)/CDCl₃ (b, top)

¹HNMR (1D and 2D) is widely used to study the secondary structure of peptides¹⁹⁰⁻¹⁹². The introduction Aib residues into the peptide sequence largely restricts the number of conformations that the peptide can adopt. Fig. D-6 shows the effect of changing solvent on the chemical shifts of the NH and benzyl protons in the Z-(Aib)₆-OtBu. In the bottom spectrum (in CDCl₃), the resonances at δ 5.53 (H-a) and 6.34 (H-b) were assigned to the hydrogens of the first and second amide from the N-terminus. When adding H-bond accepting solvent like DMSO-D₆ to a poor H-bond accepting solvent like CDCl₃ (Fig.D-8, top), large downfield shifts of these two NH were observed, while the other four NH resonances were left much less affected. The change in chemical shift values of the NH

indicate that the first two amide protons (H-a and H-b) from the N-terminus were solvent-exposed hydrogens that were not involved in hydrogen bonding, while other four amide protons were solvent-shielded hydrogens involved in hydrogen bonding network¹⁹³. This is consistent with the 3_{10} -helical model which involve $i \rightarrow i+3$ hydrogen bonding (Fig. D-9).

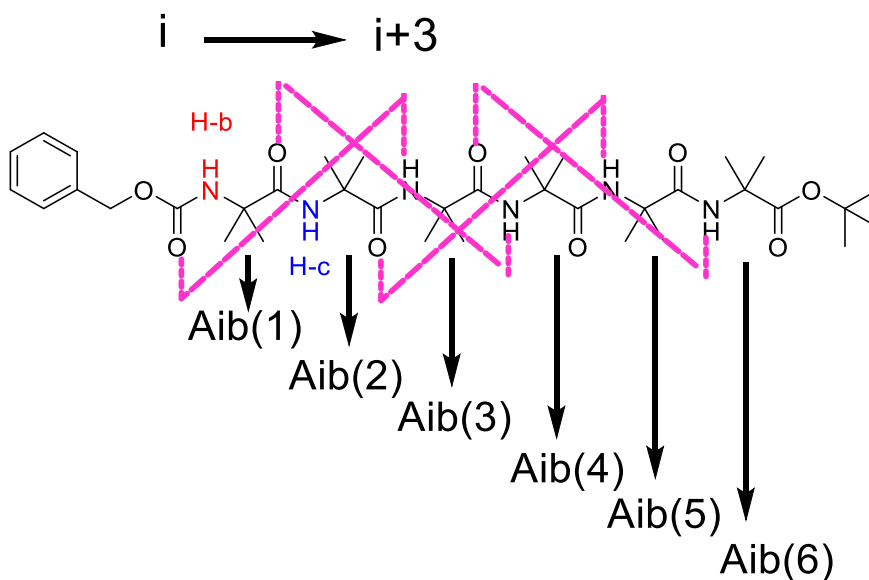


Fig.D-9 The 3_{10} -helical model for Z-(Aib)₆-OtBu

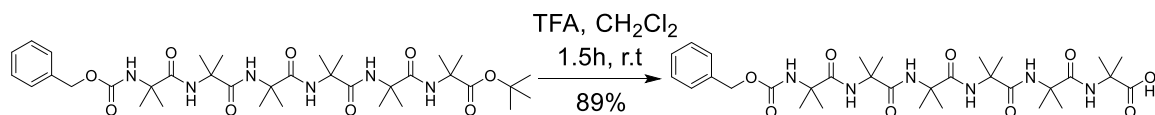
Other characterization methods including 2D NMR (NOESY, ROESY) and circular dichroism (CD) are also employed in the studying of the helix structure of (Aib)_n, this part of work is still in progress.

D.3 Surface binding study of (Aib)_n peptide

Nanostructured TiO₂ thin films¹⁹⁴⁻¹⁹⁷ (see experimental section) were prepared and used for the binding study of (Aib)_n. Because of its potentially higher conduction band edge energy and lower recombination rate of electron-hole pairs, TiO₂, with a band gap of 3.2 eV, is widely used in photovoltaic devices, such as dye-sensitized solar cells, inorganic solid-state solar cells, quantum dot-sensitized solar cells, polymer-inorganic hybrid solar cells, and perovskite solar cells^{196, 198, 199}. The physical and chemical properties of TiO₂

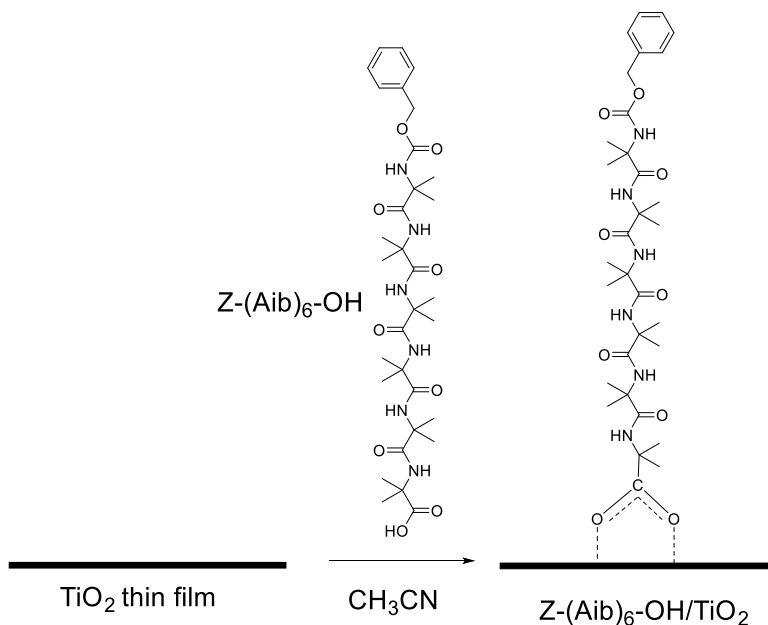
nanocrystals are affected by numerous factors such as the size, morphology, shape, and surface properties. To enhance the reaction at the interface between TiO_2 and reactant, it is important to maximize the surface of TiO_2 . Nanoscale particles have a very high surface-to-volume ratio, making them an excellent candidate for binding study²⁰⁰.

Carboxylic acid was proven to be an efficient functional group that covalently bind onto semiconductor films. Prior to binding, the $(\text{Aib})_n$ ($\text{Z-(Aib)}_6\text{-OtBu}$) was deprotected from the C-terminus, leaving a free carboxylic acid group as the anchoring group to TiO_2 (Scheme D-2).



Scheme D-2 Deprotection at the C-terminus of $\text{Z-(Aib)}_6\text{-OtBu}$

The proposed binding of TiO_2 thin films with $\text{Z-(Aib)}_6\text{-OH}$ is illustrated in Scheme D-3. In the schematic, $\text{Z-(Aib)}_6\text{-OH}$ is shown binding to TiO_2 thin film through the COOH group.



Scheme D-3 Proposed binding of TiO_2 thin films with $\text{Z-(Aib)}_6\text{-OH}$

The binding process was monitored by IR microscopic imaging. IR spectra of pristine TiO_2 , neat $\text{Z-(Aib)}_6\text{-OH}$ and $\text{Z-(Aib)}_6\text{-OH/TiO}_2$ are shown in Fig. D-9 to illustrate the spectral changes that take place upon binding.

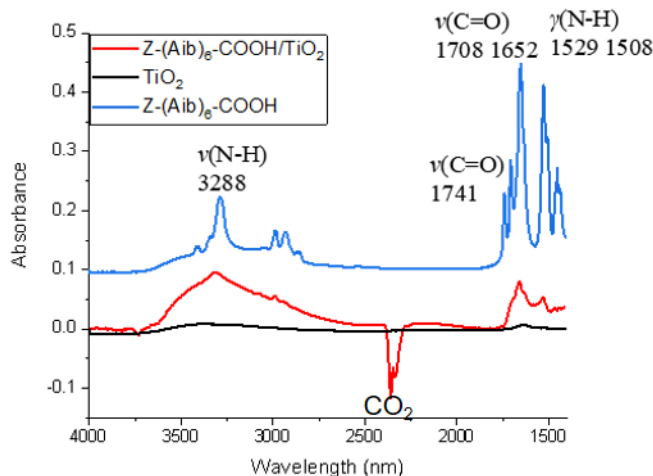


Fig.D-10 FTIR-ATR spectrum of neat $\text{Z-(Aib)}_6\text{-OH}$ (top, blue line) and representative FTIR spectrum (one pixel) of pristine TiO_2 (bottom, black line) and $\text{Z-(Aib)}_6\text{-OH/TiO}_2$ (bottom, red line)

The characteristic bands of NH stretching ($\nu(\text{N-H})$) at 3288 cm^{-1} , carbonyl stretching ($\nu(\text{C=O})$) at $1708, 1652\text{ cm}^{-1}$, and NH bending modes ($\gamma(\text{N-H})$) at $1529, 1508\text{ cm}^{-1}$ of free $\text{Z-(Aib)}_6\text{-OH}$ are preserve after binding onto TiO_2 film. A broadening effect of these band were observed, and dramatic decrease of intensity due to poor binding of $\text{Z-(Aib)}_6\text{-OH}$ on TiO_2 film. The area under $1700\text{-}1490\text{ cm}^{-1}$ was integrated, corresponding IR image was displayed in Fig. D-11. The IR image together with the FTIR spectra indicate that $\text{Z-(Aib)}_6\text{-OH}$ was bound on TiO_2 films.

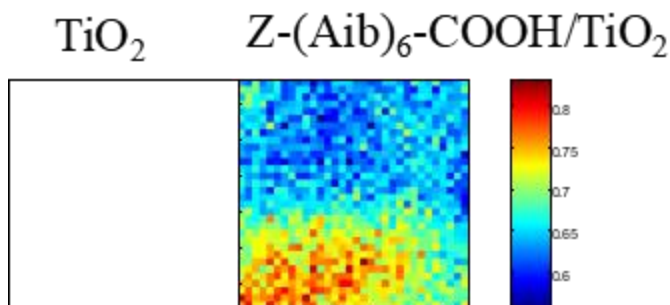


Fig.D-11 FTIR image of the integrated band area of the region $1700\text{-}1490\text{ cm}^{-1}$ ($\pm\text{STD}$) of pristine TiO_2 (left) and $\text{Z-(Aib)}_6\text{-OH/TiO}_2$ (right)

D.4 Synthesis and spectroscopic investigation of Perylene-peptide sensitizers

The synthesis of Perylene-peptide sensitizers (Fig. D-12 and D-13) involves firstly either the deprotection of the N-terminus of Z-(Aib)₆-OtBu to release the free amine that can react with di-*tert* butyl perylene benzoic acid (DTBPe-benzoic acid), or the deprotection of C-terminus of Z-(Aib)₆-OtBu to release carboxylic acid groups that can react with di-*tert* butyl perylene aniline (DTBPe-aniline). DTBPe-benzoic acid and DTBPe-aniline were synthesized by Dr. Hao Fan and Ryan Harmer in our group.

The coupling between NH-(Aib)₆-OtBu and DTBPe-benzoic acid to DTBPe-CONH-(Aib)₆-OtBu(+/-) (**6**) follows general peptide coupling method (Fig. D-12). 1-[Bis(dimethylamino) methylene]-1H-1,2,3-triazolo[4,5-b]pyridinium 3-oxid hexafluorophosphate (HATU) was used as a very efficient coupling reagent²⁰¹. Removal of the -OtBu protecting group leads to the formation of final product DTBPe-CONH-(Aib)₆-OH(+/-) (**7**) with a carboxylic acid anchor group.

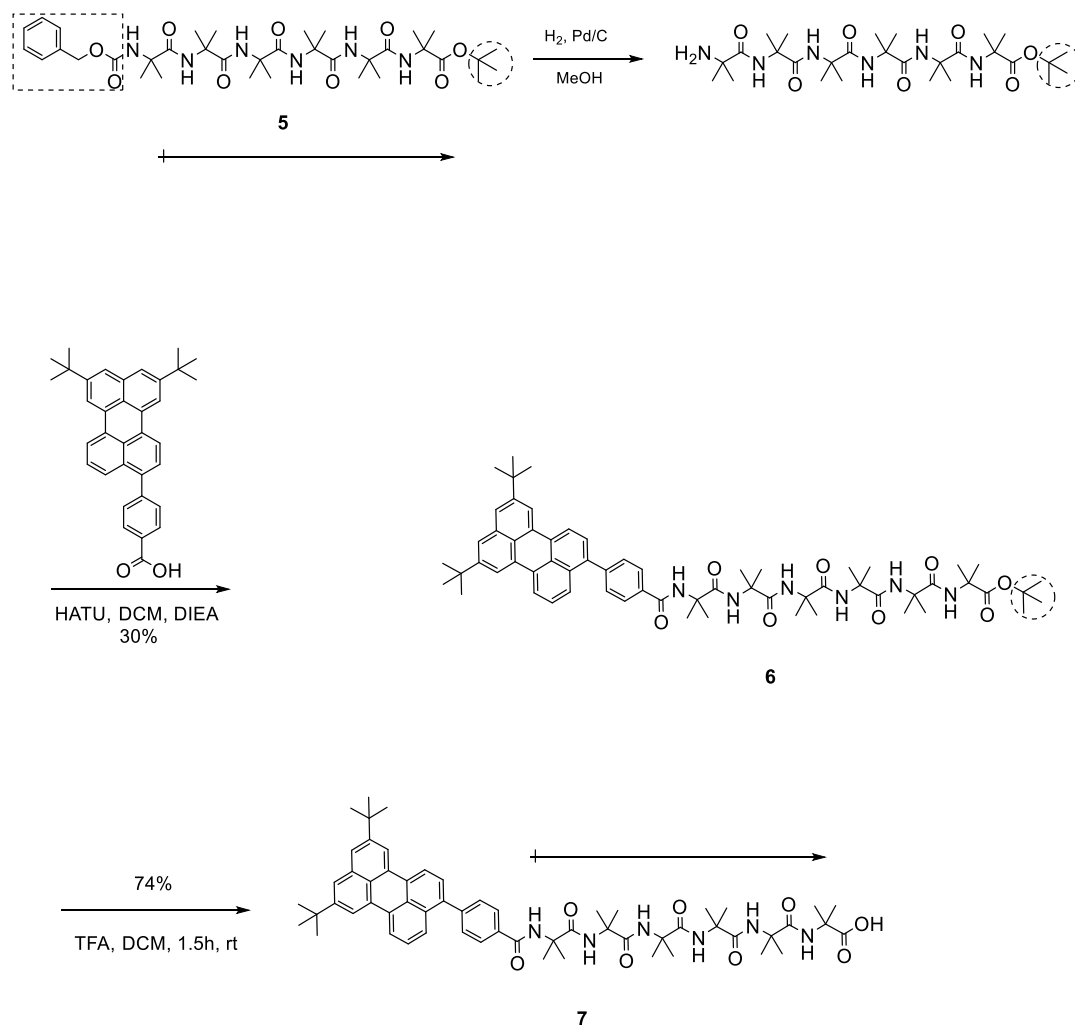


Fig.D-12 Synthesis of DTBPe-CONH-(Aib)₆-OH(+/-) (**7**)

Due to the poor reactivity of amine which was directly attached to a phenyl ring, Tetramethylfluoroformamidinium hexafluorophosphate (TFFH) was employed to prompt the coupling between Z-(Aib)₆-OH and DTBPe-aniline. TFFH is an in situ coupling reagent that can readily convert the carboxylic acid group of Z-(Aib)₆-OH to the corresponding acyl fluoride in the presence of base (4-methylmorpholine (NMM))^{202, 203}. Acyl fluorides have proven to be highly effective at coupling amino acids with poor reactivity or hindered amino acids such as Aib. The coupling product was deprotected at the N-terminus, then the linker *tert*-butyl hydrogen succinate was attached. After the hydrolysis of the *tert*-butyl

ester, the final product DTBPe-NHCO-(Aib)₆-succinate-OH(-+) (**11**) was obtained (Fig. D-13).

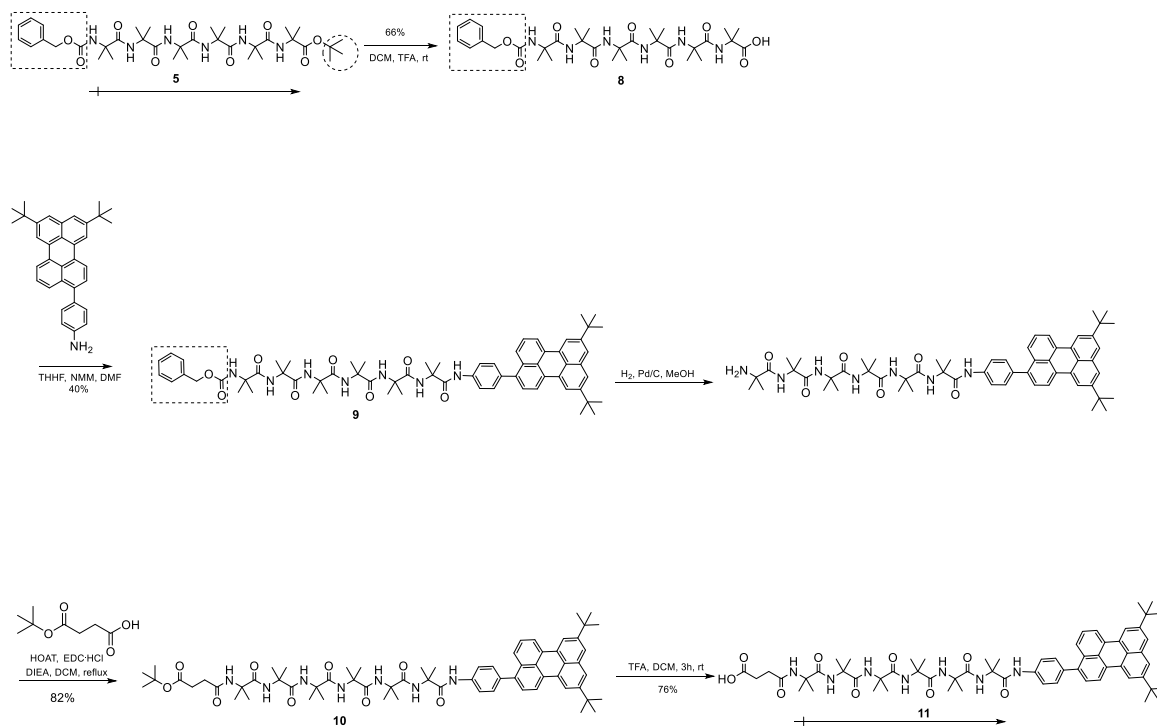


Fig.D-13 Synthesis of DTBPe-NHCO-(Aib)₆-succinate-OH(-+) (**11**)

The normalized absorption and emission spectra of DTBPe-CONH-(Aib)₆-OH(+/-) (**7**) and DTBPe-benzoic acid were collected and are shown in Fig. D-14. Both the absorption and emission spectra of **7** and DTBPe-benzoic acid are nearly identical except for a slight blue shift of about 2 nm after the introducing of dipole peptide bridge. Introducing of a dipole bridge to perylene compound has no significant influence on its electronic properties.

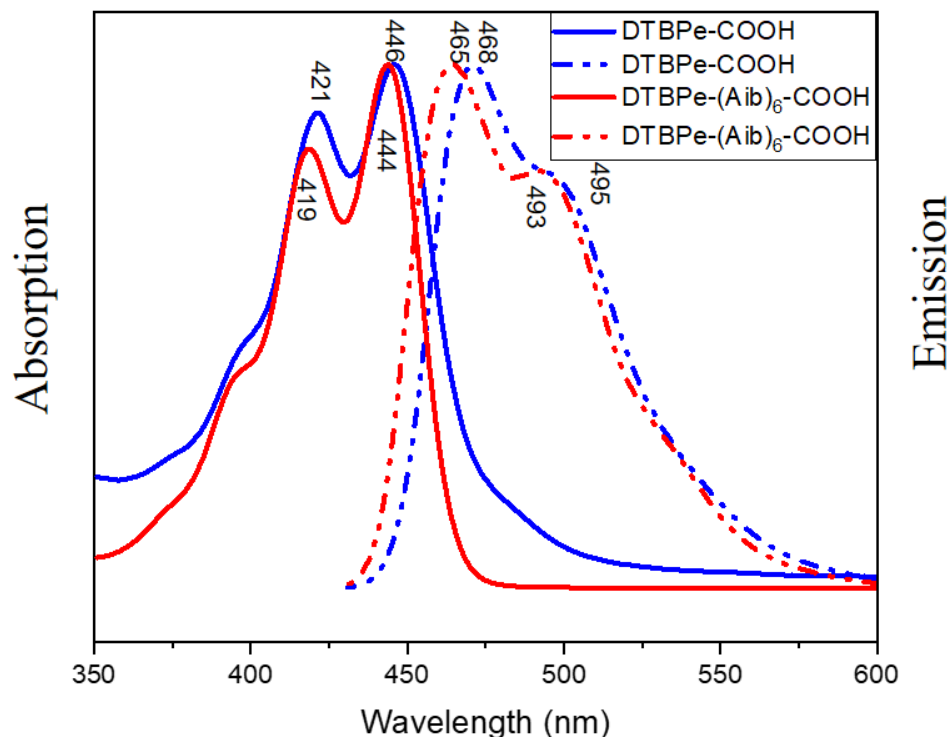


Fig.D-14 Normalized absorption (left) and emission (right) spectra of DTBPe-CONH-(Aib)₆-OH(+/-) (**7**) and DTBPe-benzoic acid in methanol. λ_{ex} =446 nm

D.5 Synthesis and spectroscopic investigation of Porphyrin-peptide sensitizers

The synthesis of Porphyrin-peptide sensitizers (Fig. D-15 and D-16, ZnTPP-CONH-(Aib)₆-OH(+/-) (**15**) and ZnTPP-NHCO-(Aib)₆-succinate-OH(+/-) (**19**)) followed the same procedures used for that of Perylene-peptide sensitizers as shown in Fig. D-15 and D-16. ZnTPP-aniline and ZnTPP-carboxylic acid were synthesized from starting material: ZnTPP-aniline and ZnTPP-iodophenyl.

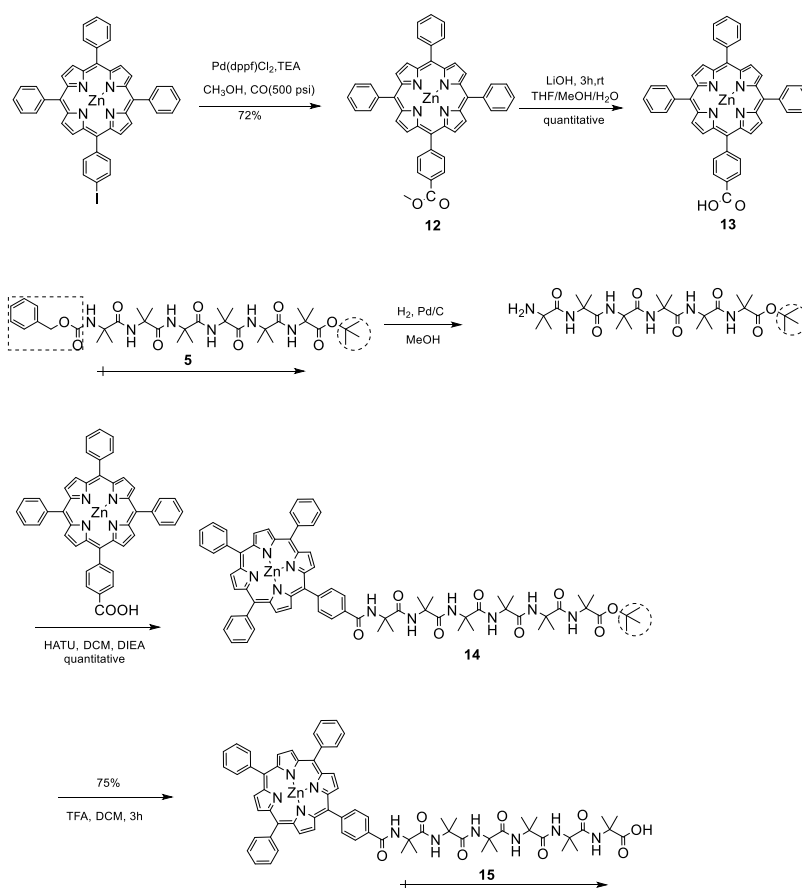


Fig.D-15 Synthesis of ZnTPP-CONH-(Aib)₆-OH(+/-) (15)

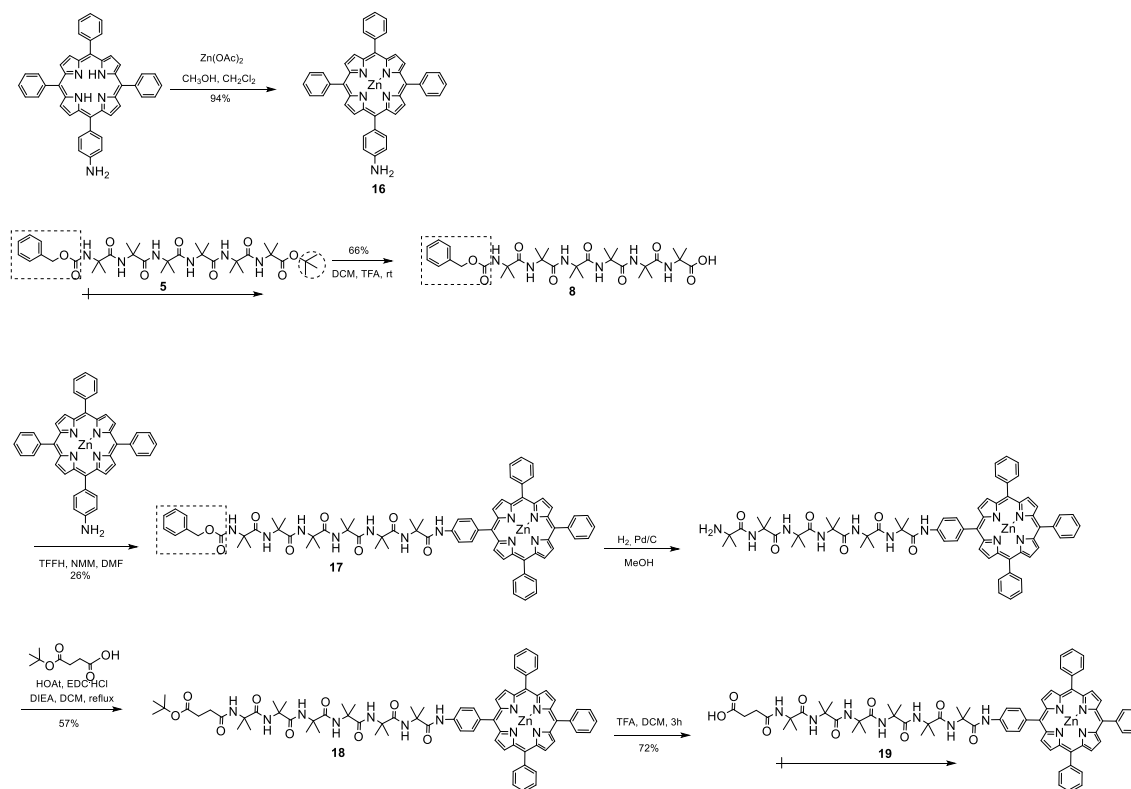


Fig.D-16 Synthesis of ZnTPP-NHCO-(Aib)₆-succinate-OH(-) (**19**)

The absorption and emission spectra of ZnTPP-CONH-(Aib)₆-OtBu(+/-) (**14**) and ZnTPP-benzoic acid (**13**) were collected and was shown in Fig. D-17. The absorption spectra of these two compounds are nearly identical, while the emission spectra of ZnTPP-CONH-(Aib)₆-OtBu(+/-) (**14**) has a 4 nm blue-shift at the Q(0,0) band and 2 nm at Q(1,0) band respectively, indicating no significant influence on electronic properties of ZnTPP after attaching the dipole bridge.

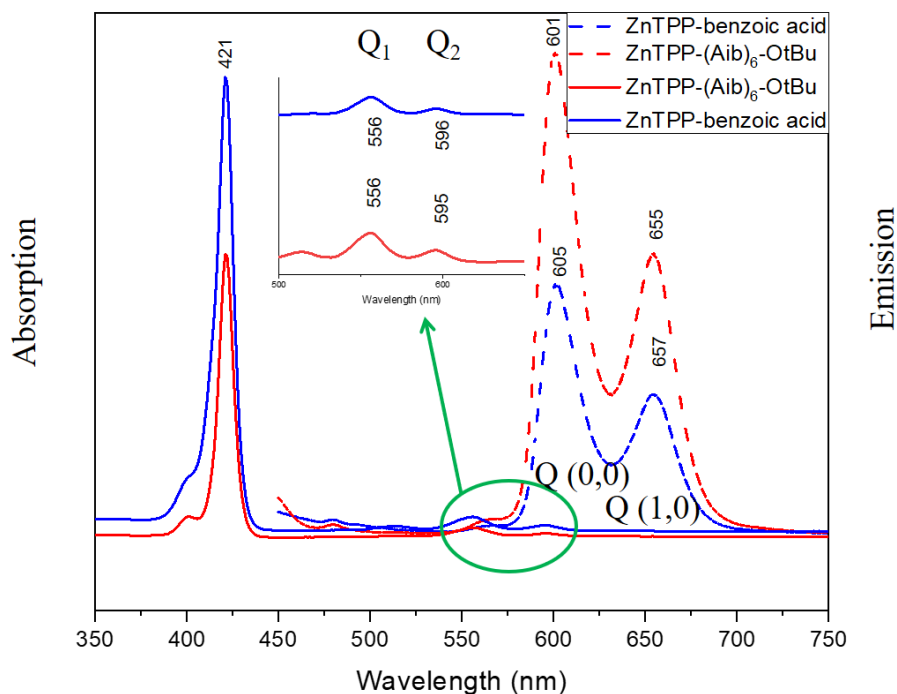


Fig.D-17 Normalized absorption (left) and emission (right) spectra of ZnTPP-CONH-(Aib)₆-OtBu(+/-) (**14**) and ZnTPP-benzoic acid (**13**) in methanol. λ_{ex} =421 nm

The element composition and the HOMOs and LUMOs energy of ZnTPP-CONH-(Aib)₆-OH(+/-) (**15**) were probed by a combination of X-ray and Ultraviolet photoemission spectroscopies (XPS and UPS) by our collaborator Dr. Sylvie Rangan from Dr. Bartynski's group. A solid sample of ZnTPP-CONH-(Aib)₆-OH(+/-) was prepared by solvent evaporation of a few drops of a ZnTPP-CONH-(Aib)₆-OH(+/-) (**15**) solution in acetonitrile from a custom-made copper sample holder (Fig. D-18).



Fig.D-18 Home-made flat bottom copper sample holder for XPS and UPS measurements (prepared by Dr. Sylvie Rangan from Dr. Bartynski's group)

Fig. D-19 displays the XPS spectrum taken the deposited ZnTPP-CONH-(Aib)₆-OH(+/-) (**15**). The corresponding element composition measured through XPS (Table D-1) matches the calculated data.

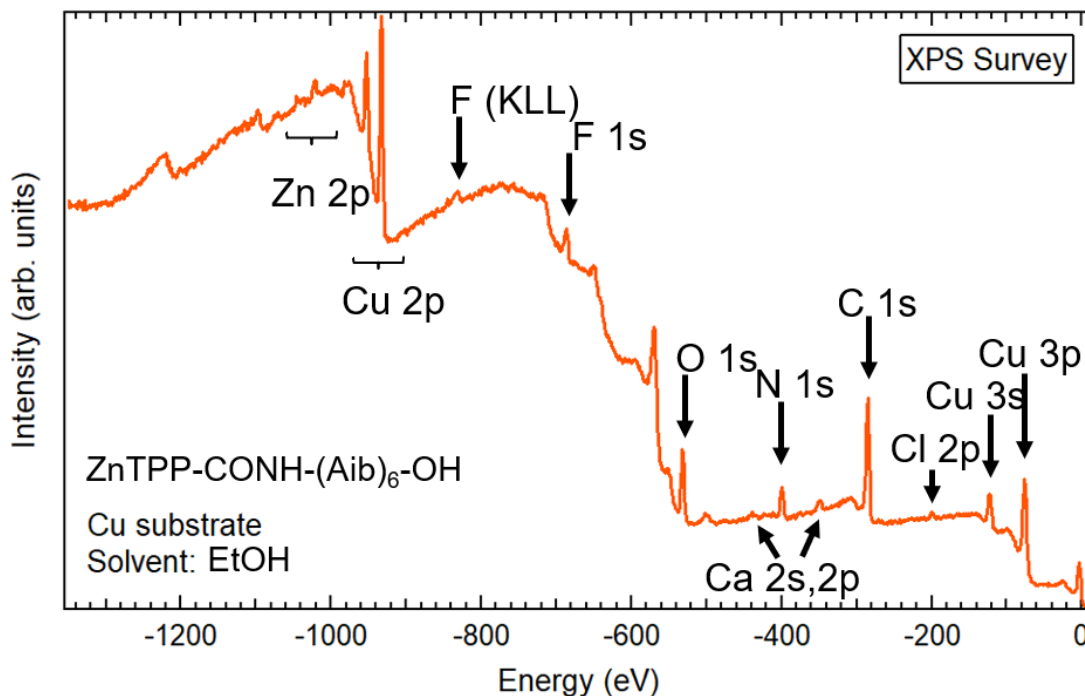


Fig.D-19 XPS spectrum of ZnTPP-CONH-(Aib)₆-OH(+/-) (**15**) (aquired by Dr. Sylvie Rangan from Dr. Bartynski's group)

Table D-1. Measured XPS and calculated element composition of ZnTPP-CONH-(Aib)₆-OH(+/-) (**14**)

<i>Element</i>	<i>C</i>	<i>O</i>	<i>N</i>	<i>Zn</i>
<i>Measured</i>	73.6%	10.4%	15.0%	1.0%
<i>Calculated</i>	78.4%	11.4%	9.1%	1.1%

UPS was used to probe the occupied state (HOMO) of the compound. In UPS, ultraviolet photons are used to excite electrons at the highest occupied molecular orbital in the compound. The source of monochromatic UV light was a He discharge lamp. The UPS measurements and the density of state (DOS) of ZnTPP-CONH-(Aib)₆-OH(+/-) (**15**) are shown in Fig. D-20. The UPS of ZnTPP-CONH-(Aib)₆-OH(+/-) (**15**) possessed a strong

and well-defined occupied electronic structure (HOMO), which was in reasonable agreement with the calculated density of state (DOS).

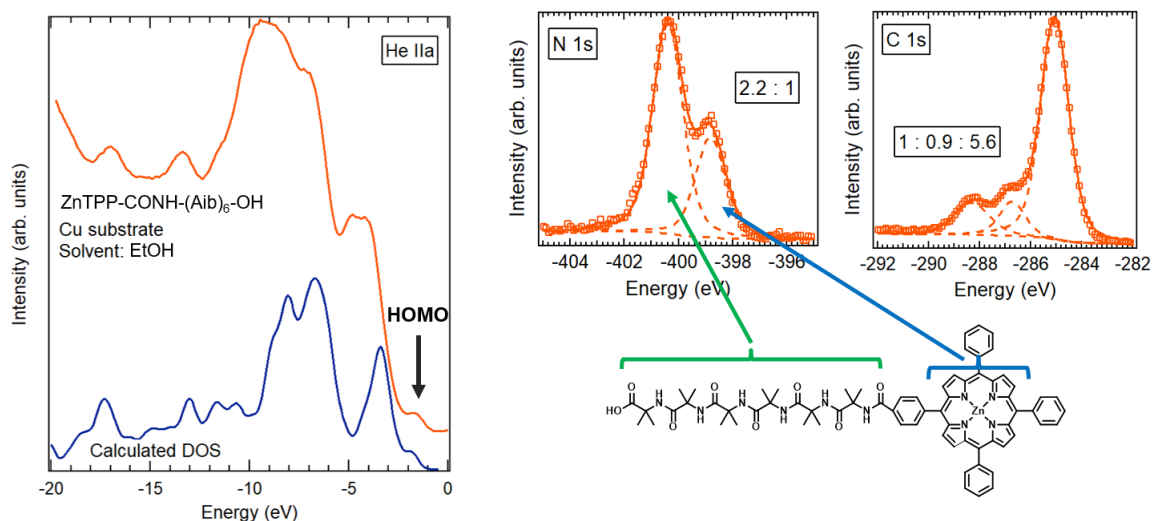


Fig.D-20 UPS spectra and calculated DOS of ZnTPP-CONH-(Aib)₆-OH(+-) (**15**) (acquired by Dr. Sylvie Rangan from Dr. Bartynski's group)

D.6 Conclusions

Z-(Aib)₆-OtBu was synthesized and fully characterized. Its secondary helix structure resulting from intramolecular H-bonding that leading to the formation of dipole pointing from N-terminus to C-terminus was confirmed by NMR and FTIR. Additional characterizations including circular dichroism (CD), 2D ¹HNMR (COSY, ROESY, NOESY) are in progress. The binding of Z-(Aib)₆-OH to TiO₂ thin films through the COOH group was carried out.

A pair of perylene-peptides sensitizers (DTBPe-CONH-(Aib)₆-OH(+-) (**6**) and DTBPe-NHCO-(Aib)₆-succinate-OH(-+) (**10**)) with opposite dipole directions were synthesized. The synthetic routes involve the deprotection of either the N-terminus or C-terminus of Z-(Aib)₆-OtBu, respectively, to release the free amine or carboxylic acid reacting sites followed by the coupling with di-*tert* butyl perylene benzoic acid (DTBPe-benzoic acid)

or di-*tert* butyl perylene aniline (DTBPe-aniline), respectively, via classic amidation processes. Following the same methodologies, a pair of porphyrin-peptides sensitizers (ZnTPP-CONH-(Aib)₆-OH(+/-) (**14**) and ZnTPP-NHCO-(Aib)₆-succinate-OH(-/+) (**18**)) were synthesized. The absorption and emission spectra of **6**, **10**, **14**, and **18** indicate that the linker has no significant influence on the electronic properties of the chromophoric unit. The electronic and photophysical properties of these compounds are still being investigated. The UPS study of ZnTPP-CONH-(Aib)₆-OH(+/-) (**14**) indicate that ZnTPP-CONH-(Aib)₆-OH(+/-) (**14**) possesses a strong and well-defined occupied electronic structure (HOMO), a promising result for the proposed surface studies.

D.7 Experimental section

General.

Materials: All the following solvents and reagents were used as received from commercial sources: N-benzyloxycarbonyl-2-aminoisobutyric acid (Z-Aib-OH, 97%, Combi Block), 1-[Bis(dimethylamino) methylene]-1H-1,2,3-triazolo[4,5-b]pyridinium 3-oxid hexafluorophosphate (HATU, 97%, Sigma-Aldrich), N,N-Diisopropylethylamine (DIEA, 99.5%, Sigma-Aldrich), Tetramethylfluoroformamidinium hexafluorophosphate (TFFH, Sigma-Aldrich), 1-(3-dimethyl-aminopropyl)-3-ethylcarbodiimide hydrochloride (EDC·HCl, BioXtra, Sigma-Aldrich), 1-hydroxy-7-azabenzotriazole (HOAT, 98%, Sigma-Aldrich), 4-methylmorpholine (NMM, ≥99.5%, Sigma-Aldrich), 2-Aminoisobutyric acid t-butyl ester (H-Aib-OtBu, 98%, Combi Block), Trifluoroacetic acid (TFA, 99%, Sigma-Aldrich), 10% Palladium on activated charcoal (10% Pd/C, Sigma-Aldrich), *tert*-butyl hydrogen succinate (97%, Sigma-Aldrich), Zinc acetate (Zn(OAc)₂, 99.99%, Sigma-Aldrich), Sodium sulfate anhydrous (Na₂SO₄, Sigma-Aldrich), Lithium hydroxide

monohydrate (LiOH·H₂O, 99.995%, Sigma-Aldrich), Sodium bicarbonate (NaHCO₃, ≥99.7%, Sigma-Aldrich), Ammonium chloride (NH₄Cl, 99.998%, Sigma-Aldrich), Potassium bisulfate (KHSO₄, Sigma-Aldrich), Acetonitrile (anhydrous, 99.8%, Sigma-Aldrich), N,N-dimethylformamide (anhydrous, 99.8%, Sigma-Aldrich), Dichloromethane (anhydrous, ≥99.8%, Sigma-Aldrich), Methanol (anhydrous, Sigma-Aldrich), Ethyl acetate (anhydrous, 99.8%, Sigma-Aldrich), Diethyl ether (anhydrous, ≥99.0%, Sigma-Aldrich), Ti-Nanoxide (T/SP, ~18 wt%, Solaronix), Silica gel (porosity: 60Å, particle size: 40-63µm, surface area: 500-600 m²/g, Sorbtech), Sephadex (LH-20, GE Healthcare), TLC silica gel 60 F₂₅₄ plates (Aluminum TLC plate, silica gel coated, EMD Millipore), Hexane was freshly glass distilled from hexane (Pharmco Aaper, ACS grade), Tetrahydrofuran (THF) was freshly distilled over sodium and benzophenone from THF (Pharmco Aaper, glassed distilled), The reactions were performed under N₂ gas and in oven-dried glassware.

Methods: ¹H and ¹³C nuclear magnetic resonance (NMR) spectra were collected on a Varian NMR spectrometer operating at 599.714 Hz for ¹H and 150.812 Hz for ¹³C. Chemical shifts (δ) are reported relative to the central line of the solvent: CDCl₃ (δ 7.27 ppm for ¹H and δ 77.27 ppm for ¹³C), CD₃OD (δ 3.31, 4.78 ppm for ¹H and δ 49.15 ppm for ¹³C), DMSO-d₆ (δ 2.5 ppm for ¹H and δ 39.51 ppm for ¹³C), and spin-spin coupling constants (*J*) are reported in Hz. ESI spectra were collected on an Apex-ultra 70 hybrid Fourier transform mass spectrometer (Bruker Daltonics). The Fourier transform infrared (FTIR) spectrum in Fig. D-5 and D-7 were collected on a Thermo Electron Corporation Nicolet 6700 FTIR with 128 scans and spectral resolution of 8 cm⁻¹, cells with CaF₂ windows were used (pathway length 0.0164 mm). UV-vis absorbance spectra were collected at room temperature on a Varian Cary 500 spectrophotometer. Fluorescence

emission spectra were collected on a VARIAN CARY-Eclipse. X-ray and ultraviolet photoemission spectroscopy measurements were performed in a single ultrahigh vacuum system in the Bartynski group. He I α line, at 40.8 eV, corresponds to the transition between the 2*p* to 1*s* state in the singly ionized He atoms. All the yields are calculated based on theoretical yield, not based on recovered starting materials.

TiO₂ films growth. Nanocrystalline titanium dioxide film was prepared by doctor blade techniques. The TiO₂ nanoparticle paste was purchased from Solaronix. This highly dispersed and concentrated (~18 wt%) Titania nanoparticle paste with a 15~20 nm anatase Titania particle size is good for the deposition of transparent active mesoporous films. Fig. D-21 shows the preparation of Nanostructured TiO₂ thin film.

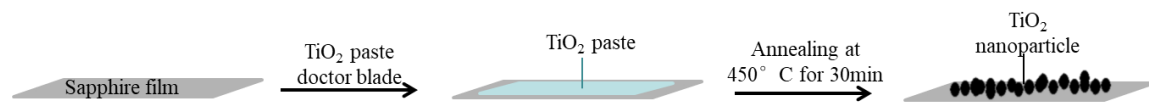


Fig.D-21 Steps of Nanostructured TiO₂ thin film preparation

Briefly, the TiO₂ nanoparticle paste was coated on double-polished C-plane sapphire (c-Al₂O₃) (Saint-Gobain Crystals, 430 μ m, (0001)) substrate by slot-coating (doctor blade) method. The use of double-polished C-sapphire as the substrate makes the study of these films by FTIR microscopic imaging possible. The using of different preparation methods and annealing temperature has a great influence on the performance of nanostructured TiO₂ thin film and also the photovoltaic devices prepared from that²⁰⁴. In our study, the coated film was then annealed at 450°C for 30 min to remove all the solvents and organic binder such as terpineol by evaporation or burning, leaving a sintered film with a high surface area.

Synthesis.

Z-(Aib)₂-OtBu (2)⁷⁹: To a stirring solution of Z-Aib-OH (4.5 g, 19 mmol) in anhydrous DCM (38 ml) at room temperature was added EDC·HCl (1-(3-dimethyl-aminopropyl)-3-ethylcarbodiimide hydrochloride, 3.65 g, 19 mmol), HOAT (1-hydroxy-7-azabenzotriazole, 2.6 g, 19 mmol), NMM (4-methylmorpholine, 2.9 ml, 19 mmol), the solution was stirred for 20 min to activate the acid. Then, H-Aib-OtBu (3.0 g, 19 mmol) was added, stirred for 16h at room temperature under N₂. The solution remains colorless and clear. The reaction was diluted with ethyl acetate (100 ml), then washed with sat. NH₄Cl (aq, 2×80 ml), sat. NaHCO₃ (aq, 2×80 ml), DI water (80 ml), brine (80 ml). The organic layer was dried over Na₂SO₄ and the solvent was removed in vacuum, the crude was purified by column chromatography (20%-50% EtOAc/Hexanes) to give Z-(Aib)₂-OtBu as white solid in 87% yield (6.4 g). ¹H NMR (CDCl₃) δ 7.35-7.31 (m, 5H), 6.91 (brs, 1H), 5.40 (brs, 1H), 5.09 (s, 2H), 1.53 (s, 6H), 1.50 (s, 6H), 1.45 (s, 9H). ¹³C NMR (CDCl₃) δ 174.00, 173.25, 155.09, 136.54, 128.65, 128.25, 128.18, 81.69, 66.70, 57.04, 56.96, 27.96, 25.51, 24.28. HRMS (ESI): calculated for C₂₀H₃₀N₂O₅Na, 401.2047 [M+Na]⁺; found: 401.2060 [M+Na]⁺

Z-(Aib)₃-OtBu (3): Z-(Aib)₂-OtBu (5.5 g, 14 mmol) was dissolved in anhydrous methanol (90 ml) and 10% Pd/C (20 mg) was added slowly to the solution, turned the solution to black color. After purged with N₂ and evacuated under vacuum, a H₂ balloon was carefully fitted to the reaction vessel and the reaction stirred vigorously for 16 h at room temperature. The H₂ balloon was removed and the solution was filtered through a Celite bed. The solvent was removed in vacuum to afford the free amine (NH₂-(Aib)₂-OtBu) as a gummy solid, which was directly used for the next reaction without purification. Z-Aib-OH (2.8 g, 12

mmol), EDC·HCl (2.73 g, 14 mmol), HOAT (1.93 g, 14 mmol) and NMM (2.2 ml, 14 mmol) were dissolved in anhydrous DCM (50 ml) and stirred for 20 min at room temperature under N₂. NH₂-(Aib)₂-OtBu was dissolved in anhydrous DCM (20 ml), then added dropwise. The reaction was stirred for 16 h under N₂ at room temperature. The solution remains colorless and clear. The solvent was evaporated in vacuum and the crude residue was redissolved in ethyl acetate (100 ml), washed with sat. NH₄Cl (aq, 2×80 ml), sat. NaHCO₃ (aq, 2×80 ml), DI water (80 ml), brine (80 ml). The organic layer was dried over Na₂SO₄. The solvent was removed in vacuum. Purified by column chromatography (50%-70% EtOAc/Hexanes) to give Z-(Aib)₃-OtBu as white solid in 89% yield (5.8 g). ¹H NMR (CDCl₃) δ 7.40-7.37 (m, 5H), 7.10 (brs, 1H), 6.52 (brs, 1H), 5.20 (brs, 1H), 5.13 (s, 2H), 1.51 (s, 6H), 1.50 (s, 6H), 1.48 (s, 6H), 1.47 (s, 9H). ¹³C NMR (CDCl₃) δ 173.89, 173.05, 172.81, 155.45, 136.22, 128.81, 128.57, 128.30, 80.87, 67.15, 57.38, 56.92, 56.61, 28.02, 25.54, 25.34, 24.63. HRMS (ESI): calculated for C₂₄H₃₇N₃O₆Na, 486.2575 [M+Na]⁺; found: 486.2593 [M+Na]⁺

Z-(Aib)₃-OH (4): To a stirring solution of Z-(Aib)₃-OtBu (3.1 g, 6.7 mmol) in anhydrous DCM (70 ml), 70 ml TFA (Trifluoroacetic acid) was added. The solution was stirred for 1.5h at room temperature. The solution remains colorless and clear. The solvent was evaporated and the remaining traces of TFA were removed by adding anhydrous diethyl ether (3×30 ml) and evaporation in vacuum. The crude product was recrystallized from anhydrous diethyl ether to give Z-(Aib)₃-OH as a white solid in 87% yield (2.4g). ¹H NMR (CD₃OD) δ 7.73 (brs, 1H), 7.63 (brs, 1H), 7.38-7.29 (m, 5H), 5.12 (s, 2H), 1.45 (s, 6H), 1.39 (s, 6H), 1.36 (s, 6H). ¹³C NMR (CD₃OD) δ 178.44, 176.42, 176.26, 157.82, 138.41,

129.60, 129.09, 128.84, 67.53, 57.74, 57.63, 57.09, 25.35, 25.34, 25.22. HRMS (ESI): calculated for $C_{20}H_{29}N_3O_6Na$, 430.1949 $[M+Na]^+$; found: 430.1969 $[M+Na]^+$

Z-(Aib)₆-OtBu (5): Z-(Aib)₃-OtBu (2.4 g, 5.2 mmol) was dissolved in anhydrous methanol (70 ml) and 10% Pd/C (50mg) was added slowly to the solution, turned the solution to black color. After purged with N₂ and evacuated under vacuum, a H₂ balloon was carefully fitted to the reaction vessel and stirred for 16 h at room temperature. The H₂ balloon was removed and the solution was filtered through a Celite bed. The solvent was removed in vacuum to afford free amine (NH₂-(Aib)₃-OtBu) as a gummy solid, which was directly used for the next reaction without purification. To a solution of Z-(Aib)₃-OH (2.4 mg, 5.2 mmol) in anhydrous acetonitrile (3 ml), cooled to 0°C, EDC·HCl (1 g, 5.2 mmol) was added, and stirred at room temperature for 30 min. The solvent was evaporated in vacuum and the oily residue was dissolved in ethyl acetate (200 ml), then washed with 10% KHSO₄ (200 ml). The organic layer was dried over Na₂SO₄ and the solvent was removed in vacuum. The oily residue was dissolved in 60 ml anhydrous acetonitrile. To this solution, NH₂-(Aib)₃-OtBu in 70 ml anhydrous acetonitrile was added. The solution remains colorless and clear. After stirring for 3 days at 80°C under reflux under N₂, the solvent was evaporated in vacuum under reduced pressure. The crude residue was purified by column chromatography (50%-75% EtOAc/Hexanes) to give Z-(Aib)₆-OtBu as white solid in 77% yield (2.9g). ¹H NMR (CDCl₃) δ 7.46 (brs, 1H), 7.43-7.34 (m, 7H), 7.25 (brs, 1H), 6.31 (brs, 1H), 5.31 (brs, 1H), 5.12 (s, 2H), 1.51 (s, 6H), 1.48 (s, 6H), 1.47 (s, 12H), 1.44 (s, 6H), 1.44 (s, 9H). ¹³C NMR (CDCl₃) δ 174.99, 174.19, 174.12, 174.04, 173.80, 156.01, 136.19, 128.68, 128.56, 128.16, 79.71, 67.33, 57.24, 56.83, 56.73, 56.61, 56.46, 56.02,

27.91, 25.50, 25.42, 25.22, 25.07, 24.96, 24.87. HRMS (ESI): calculated for $C_{36}H_{58}N_6O_9Na$, 741.4157 $[M+Na]^+$; found: 741.4111 $[M+Na]^+$

DTBPe-CONH-(Aib)₆-OtBu(+·) (6): Z-(Aib)₆-OtBu (54 mg, 0.075 mmol) was dissolved in anhydrous methanol (1 ml) and 10% Pd/C (2 mg) was added slowly to the solution, turned the solution to black color. After purged with N₂ and evacuated under vacuum, a H₂ balloon was carefully fitted to the reaction vessel and the solution was stirred for 16 h at room temperature. The H₂ balloon was removed and the solution was filtered through a Celite bed. The solvent was removed in vacuum to afford free amine (NH₂-(Aib)₆-OtBu) as a gummy solid, which was directly used in the next reaction without purification. To an ice-cold solution of DTBPe-benzoic acid (36 mg, 0.075 mmol) in anhydrous DCM (2 ml), HATU (29 mg, 0.075 mmol) and DIEA (0.02 ml, 0.075 mmol) were added, and stirred 10 min at room temperature under N₂. NH₂-(Aib)₆-OtBu in anhydrous DCM (2 ml) was added. The resulting solution was heated to reflux for 4 days with stirring under N₂. The solvent was evaporated in vacuum and the crude residue was redissolved in ethyl acetate (40 ml), washed with 10% KHSO₄ (25 ml), DI water (25 ml), 5% NaHCO₃ (25 ml), DI water (25 ml). The organic layer was dried over Na₂SO₄ and the solvent was removed in vacuum. The crude residue was purified by column chromatography (50%-80% EtOAc/Hexanes) to give DTBPe-CONH-(Aib)₆-OtBu(+·) as a dark-green solid in 30% yield (22 mg). ¹H NMR (CDCl₃) δ 8.28-8.25 (m, 4H), 7.97 (d, *J*= 12 Hz, 2H), 7.77 (brs, 1H), 7.68-7.64 (m, 5H), 7.62 (brs, 1H), 7.45-7.40 (m, 3H), 7.36 (brs, 1H), 6.88 (brs, 1H), 6.49 (brs, 1H), 1.65 (s, 6H), 1.61 (s, 6H), 1.56 (s, 6H), 1.53 (s, 18H), 1.49 (s, 24H), 1.46 (s, 6H), 1.44 (s, 9H). ¹³C NMR (CDCl₃) δ 174.34, 173.95, 167.97, 149.48, 149.43, 135.95, 138.09, 134.92, 132.93, 132.31, 132.21, 131.84, 130.82, 130.53, 130.30, 129.70, 127.90, 127.55, 127.01, 125.43,

125.24, 124.14, 124.01, 120.41, 119.68, 118.96, 118.79, 57.78, 57.19, 57.09, 57.02, 56.91, 56.33, 35.24, 31.58, 31.20, 28.47, 25.13. HRMS (ESI): calculated for $C_{63}H_{83}N_6O_8$, 1051.6272 $[M+H]^+$; found: 1052.0343 $[M+H]^+$

DTBPe-CONH-(Aib)₆-OH(+/-) (7): To a stirred solution of DTBPe-CONH-(Aib)₆-OtBu(+/-) (20 mg, 0.02 mmol) in anhydrous DCM (0.2 ml), 0.2 ml TFA was added. The solution was stirred for 3h at room temperature. The solution was dark green and clear. The solvent was evaporated and the remaining traces of TFA were removed by adding anhydrous diethyl ether (3×30 ml) and evaporation in vacuum. The crude product was recrystallized from anhydrous diethyl ether to give DTBPe-CONH-(Aib)₆-OH(+/-) as a white solid in 74% yield (14 mg). ¹H NMR (CD₃OD) δ 8.56 (brs, 1H), 8.38-8.34 (m, 3H), 8.12 (d, J = 6 Hz, 2H), 8.04 (brs, 1H), 7.98 (brs, 1H), 7.90 (brs, 1H), 7.72-7.70 (m, 3H), 7.67-7.64 (m, 3H), 7.48-7.45 (m, 2H), 7.40-7.39 (m, 2H), 5.13 (brs, 1H), 1.61 (s, 6H), 1.57 (s, 6H), 1.51-1.49 (m, 30H), 1.47 (s, 6H), 1.44 (s, 6H). HRMS (ESI): calculated for $C_{59}H_{75}N_6O_8$, 10017.5468 $[M+H]^+$; found: 1017.5470 $[M+H]^+$

Z-(Aib)₆-OH (8): To a stirred solution of Z-(Aib)₆-OtBu (1.4 g, 2.0 mmol) in anhydrous DCM (20 ml), 20 ml TFA was added. The solution was stirred for 1.5h at room temperature. The solution remains colorless and clear. The solvent was evaporated and the remaining traces of TFA were removed by adding anhydrous diethyl ether (3×30 ml) and evaporation in vacuum. The crude product was recrystallized from anhydrous diethyl ether to give Z-(Aib)₆-OH as a white solid in 89% yield (1.2g). ¹H NMR (DMSO) δ 8.25 (brs, 1H), 7.83 (brs, 1H), 7.67 (brs, 1H), 7.55 (brs, 1H), 7.39-7.29 (m, 6H), 7.24 (brs, 1H), 5.09 (s, 2H), 1.33-1.32 (m, 24H), 1.27 (s, 6H), 1.26 (s, 6H). ¹³C NMR (DMSO) δ 175.57, 175.14, 175.07, 174.90, 173.44, 155.81, 137.15, 128.35, 127.74, 127.27, 65.56, 55.99, 55.93,

55.87, 55.76, 55.69, 54.58, 25.03, 24.89, 24.69, 24.68, 24.38. HRMS (ESI): calculated for $C_{32}H_{50}N_6O_9Na$, 685.3531 $[M+Na]^+$; found: 685.3511 $[M+Na]^+$

Z-(Aib)₆-CONH-DTBPe(+/-) (9)²⁰⁵: To a stirring solution of Z-(Aib)₆-OH (60 mg, 0.09 mmol) in anhydrous DMF (2 ml) at 0°C, DTBPe-aniline (42 mg, 0.09 mmol), NMM (0.04 ml, 0.09 mmol) and TFFH (24 mg, 0.09 mmol) were added. The solution is dark green and clear. The reaction mixture was stirred for 3 days at room temperature under N₂ and solvent was evaporated in vacuum. The crude residue was subjected to preparative TLC (SiO₂, 60% EtOAc/Hexanes) and Saphadex (DCM) to give Z-(Aib)₆-CONH-DTBPe(+/-) as a dark-green solid in 40% yield (40 mg). ¹H NMR (CDCl₃) δ 9.30 (brs, 1H), 8.25-8.22 (m, 3H), 8.09 (d, *J*= 6 Hz, 2H), 7.83 (d, 1H), 7.68 (brs, 1H), 7.64 (brs, 1H), 7.62 (m, 2H), 7.59 (brs, 1H), 7.49 (brs, 1H), 7.49-7.41 (m, 4H), 7.37-7.35 (m, 5H), 6.41 (brs, 1H), 5.36 (brs, 1H), 5.12 (s, 2H), 1.68 (s, 6H), 1.55 (s, 6H), 1.54 (s, 6H), 1.48 (s, 18H), 1.47 (s, 6H), 1.46 (s, 6H), 1.35 (s, 6H). ¹³C NMR (CDCl₃) δ 207.02, 175.84, 175.02, 174.46, 174.39, 174.03, 173.93, 155.85, 149.04, 148.99, 135.94, 135.39, 134.68, 133.25, 131.53, 130.80, 130.44, 130.11, 129.39, 128.77, 128.73, 128.19, 127.53, 119.97, 119.93, 119.65, 118.25, 118.01, 67.59, 57.64, 57.27, 56.99, 56.79, 56.75, 56.53, 53.44, 34.95, 31.35, 30.95. HRMS (ESI): calculated for $C_{66}H_{81}N_7O_8Na$, 1122.6039 $[M+Na]^+$; found: 1122.6022 $[M+Na]^+$

DTBPe-NHCO-(Aib)₆-succinate-OtBu(-/+) (10)⁷⁹: Z-(Aib)₆-CONH-DTBPe(+/-) (30 mg, 0.027 mmol) was dissolved in anhydrous methanol (1 ml) and 10% Pd/C (5 mg) was added slowly to the solution, turned the solution to black color. After purged with N₂ and evacuated under vacuum, a H₂ balloon was carefully fitted to the reaction vessel and the solution was stirred for 16 h at room temperature. The H₂ balloon was removed and the solution was filtered through a Celite bed. The solvent was removed in vacuum to afford

free amine (NH₂-(Aib)₆-CONH-DTBP_e(+-)) as a gummy solid, which was directly used for the next reaction without purification. To an ice-cold solution of *tert*-butyl hydrogen succinate (7 mg, 0.027 mmol) in anhydrous DCM (2 ml), HOAt (6 mg, 0.027 mmol) and EDC·HCl (6 mg, 0.027 mmol) were added, followed by the adding of NH₂-(Aib)₆-CONH-DTBP_e(+-) and DIEA (0.015 mg, 0.027 mmol). The solution is dark green and clear. The reaction mixture was stirred for 5 days at room temperature under N₂ and the solvent was evaporated in vacuum. The crude residue was purified by column chromatography (75%-100% EtOAc/Hexanes) and Sephadex (DCM) to give DTBP_e-NHCO-(Aib)₆-succinate-OtBu(-+) as a dark-green solid in 82% yield (25 mg). ¹H NMR (CDCl₃) δ 9.32 (brs, 1H), 8.25-8.22 (m, 3H), 8.09 (d, *J*= 12 Hz, 2H), 7.84 (d, *J*= 6 Hz, 1H), 7.72 (brs, 1H), 7.68 (brs, 1H), 7.63-7.62 (m, 2H), 7.46-7.41 (m, 4H), 7.35 (brs, 1H), 6.99 (brs, 1H), 6.50 (brs, 1H), 2.62 (t, 2H), 2.37 (t, 2H), 1.67 (s, 6H), 1.56 (s, 6H), 1.55 (s, 6H), 1.48 (s, 18H), 1.47 (s, 6H), 1.46 (s, 6H), 1.44 (s, 15H). ¹³C NMR (CDCl₃) δ 176.07, 175.40, 175.01, 174.61, 174.46, 174.21, 172.94, 72.69, 149.05, 149.00, 140.05, 135.41, 134.69, 131.54, 130.78, 130.12, 128.74, 128.14, 127.54, 126.19, 125.32, 119.95, 119.93, 119.64, 118.26, 118.02, 81.35, 57.62, 56.96, 56.94, 56.78, 56.74, 56.67, 34.95, 31.34, 29.71, 28.72, 28.22, 25.05. HRMS (ESI): calculated for C₆₆H₈₇N₇O₉Na, 1144.6457 [M+ Na]⁺; found: 1144.6497 [M+ Na]⁺

DTBP_e-NHCO-(Aib)₆-succinate-OH(++) (11): To a stirring solution of DTBP_e-NHCO-(Aib)₆-succinate-OtBu(-+) (25 mg, 0.022 mmol) in anhydrous DCM (0.4 ml), 0.4 ml TFA was added. The solution was stirred for 3h at room temperature. The solution is dark green-black and clear. The solvent was evaporated and the remaining traces of TFA were removed by adding anhydrous diethyl ether (3×30 ml) and evaporation in vacuum. The

crude product was recrystallized from anhydrous diethyl ether to give DTBPe-NHCO-(Aib)₆-succinate-OH(-+) as a dark-green solid in 76% yield (18 mg). ¹H NMR (CD₃OD) δ 9.42 (brs, 1H), 8.35-8.30 (m, 3H), 8.02 (brs, 1H), 7.98-7.96 (m, 2H), 7.95 (brs, 1H), 7.78 (brs, 1H), 7.71 (brs, 1H), 7.69-7.67 (m, 2H), 7.47-7.43 (m, 5H), 7.35-7.33 (m, 3H), 6.91 (brs, 1H), 2.64 (t, 2H), 2.50 (t, 2H), 1.55 (s, 6H), 1.52 (s, 6H), 1.51 (s, 6H), 1.49 (d, 18H), 1.48 (s, 6H), 1.48 (s, 6H). HRMS (ESI): calculated for C₆₂H₇₉N₇O₉Na, 1088.5831 [M+ Na]⁺; found: 1088.5826 [M+ Na]⁺

Zinc tetraphenylporphyrin methyl benzoate (ZnTPP-COOMe) (12): A mixture of the (SM, triethyl amine (2eq), PddppfCl₂(0.05eq)), in CH₃OH (1g sm vs 10mL ch3oh) was heated at 120°C with stirring in an autoclave under carbon monoxide (500psi) for 20 h. After cooling to room temperature, the reaction mixture was filtered, and the solvent was evaporated in vacuum, then the crude was isolated by column chromatography. The desired product was obtained in 63% yield. ¹H NMR (CDCl₃) δ 8.97-8.96 (m, 6H), 8.89 (d, 2H), 8.39 (d, *J*= 6 Hz, 2H), 8.31 (d, *J*= 6 Hz, 2H), 8.23-8.22 (m, 6H), 7.78-7.74 (m, 9H), 4.06 (s, 3H).

Zinc tetraphenylporphyrin benzoic acid (ZnTPP-COOH) (13): To a stirring solution of ZnTPP-COOMe (220 mg, 0.29 mmol) in 1:1:3 H₂O/CH₃OH/THF (11 ml), LiOH.H₂O (36 mg, 0.87 mmol) was added. The solution was stirred at room temperature for 2h. The solvents were evaporated in vacuum and the crude residue was redissolved in DI H₂O (10 ml), then washed with methyl *tert*-butyl ether (10 ml×2). Acidified to PH=1~2 by 1N HCl aqueous solution then extracted by ethyl acetate (20 ml×3). The organic phase was washed with DI H₂O (20 ml) and brine (20 ml), dried over Na₂SO₄ and the solvent was removed in vacuum. The crude residue was purified by column chromatography (DCM) to give

ZnTPP-COOH as a dark-purple solid in 100% yield (220 mg). ^1H NMR (CDCl_3) δ 8.99-8.96 (m, 6H), 8.92 (d, 2H), 8.53 (d, J = 6 Hz, 2H), 8.38 (d, J = 6 Hz, 2H), 8.24-8.22 (m, 6H), 7.79-7.75 (m, 9H). ^{13}C NMR (CDCl_3) δ 150.57, 150.48, 150.39, 149.68, 142.84, 134.75, 134.58, 132.55, 132.35, 132.28, 131.63, 128.56, 127.74, 126.75, 121.76, 121.56, 119.51. HRMS (ESI): calculated for $\text{C}_{45}\text{H}_{28}\text{N}_4\text{O}_2\text{Zn}$, 720.1498 [M]; found: 720.1479 [M]

ZnTPP-CONH--(Aib)₆-OtBu(+/-) (14): Z-(Aib)₆-OtBu (210 mg, 0.29 mmol) was dissolved in anhydrous methanol (4 ml) and 10% Pd/C (10 mg) was added slowly to the solution, turned the solution to black color. After purged with N_2 and evacuated under vacuum, a H_2 balloon was carefully fitted to the reaction vessel and the solution was stirred for 16 h at room temperature. The H_2 balloon was removed and the solution was filtered through a Celite bed. The solvent was removed in vacuum to afford free amine (NH_2 -(Aib)₆-OtBu) as a gummy solid, which was directly used for the next reaction without purification. To an ice-cold solution of ZnTPP-COOH (220 mg, 0.29 mmol) in anhydrous DCM (6 ml), HATU (110 mg, 0.29 mmol) and DIEA (0.08 ml, 0.29 mmol) were added, and stirred for 10 min under N_2 . NH_2 -(Aib)₆-OtBu in anhydrous DCM (2 ml) was added. The resulting solution was heated to reflux for 5 days under N_2 with stirring. The solution was dark purple and clear. The solvent was evaporated to dryness under reduced pressure and the crude residue was redissolved in ethyl acetate (40 ml), then washed with 10% KHSO_4 (25 ml), DI water (25 ml), 5% NaHCO_3 (25 ml), DI water (25 ml). The organic layer was dried over Na_2SO_4 and the solvent was removed in vacuum. The crude residue was purified by column chromatography (0-30% EtOAc/DCM) to give ZnTPP-CONH-(Aib)₆-OtBu(+/-) as a dark-purple solid in 99% yield (380 mg). ^1H NMR (CDCl_3) δ 8.96-8.95 (m, 6H), 8.92-8.91 (m, 2H), 8.36 (d, J = 12 Hz, 2H), 8.29 (d, 2H), 8.23-8.20 (m, 6H),

8.02 (brs, 1H), 7.87 (brs, 1H), 7.85 (brs, 1H), 7.77- 7.71 (m, 9H), 7.57 (brs, 2H), 1.73 (s, 6H), 1.61 (s, 6H), 1.55 (s, 6H), 1.53 (s, 6H), 1.52 (s, 6H), 1.49 (s, 6H), 1.45 (s, 9H). ^{13}C NMR (CDCl_3) δ 175.82, 175.06, 174.93, 174.77, 174.60, 171.27, 168.48, 150.49, 150.42, 150.31, 149.75, 147.38, 142.87, 134.85, 134.53, 132.39, 132.34, 132.27, 132.20, 131.66, 127.66, 126.68, 125.87, 121.63, 121.42, 119.49, 57.78, 56.99, 56.93, 56.89, 56.80, 56.37, 28.04, 25.11. HRMS (ESI): calculated for $\text{C}_{73}\text{H}_{79}\text{N}_{10}\text{O}_8\text{Zn}$, 1287.5368 $[\text{M} + \text{H}]^+$; found: 1287.5347 $[\text{M} + \text{H}]^+$

ZnTPP-CONH-(Aib)₆-OH(+/-) (15): To a stirring solution of ZnTPP-CONH-(Aib)₆-OtBu(+/-) (150 mg, 0.12 mmol) in anhydrous DCM (1.5 ml), 1.5 ml TFA was added. The solution was stirred for 3h at room temperature. The solution was dark purple and clear. The solvent was evaporated and the remaining traces of TFA were removed by adding anhydrous diethyl ether (3×30 ml) and evaporation in vacuum. The crude product was recrystallized from anhydrous diethyl ether to give ZnTPP-CONH-(Aib)₆-OH(+/-) as a dark-purple solid in 75% yield (108 mg). ^1H NMR (CDCl_3) δ 8.93-8.91 (m, 6H), 8.87 (d, J = 6 Hz, 2H), 8.62 (brs, 1H), 8.54 (brs, 1H), 8.28 (d, 2H), 8.23-8.19 (m, 6H), 8.10 (brs, 1H), 8.02 (brs, 2H), 7.96 (brs, 2H), 7.83 (brs, 1H), 7.76- 7.72 (m, 9H), 7.49 (brs, 1H), 1.68 (s, 6H), 1.58 (s, 6H), 1.55 (s, 6H), 1.53 (s, 6H), 1.51 (s, 6H), 1.50 (s, 6H). ^{13}C NMR (CDCl_3) δ 177.26, 177.00, 176.15, 175.68, 175.19, 168.69, 150.45, 150.38, 150.26, 149.74, 143.05, 134.69, 134.55, 132.24, 132.18, 132.12, 131.59, 127.59, 126.64, 126.61, 125.98, 121.48, 121.26, 119.51, 65.90, 58.10, 57.66, 57.28, 56.96, 56.87, 56.85, 25.46, 25.14. HRMS (ESI): calculated for $\text{C}_{69}\text{H}_{71}\text{N}_{10}\text{O}_8\text{Zn}$, 1231.4742 $[\text{M} + \text{H}]^+$; found: 1231.4725 $[\text{M} + \text{H}]^+$

Zinc tetraphenylporphyrin aniline (ZnTPP-NH₂) (16)¹⁷¹: 4-(10,15,20-triphenylporphyrin-5-yl)aniline (200 mg, 0.24 mmol) was dissolved in DCM (53 ml) and

the solution was purged with N₂ for 10 min. Zn(OAc)₂ (67 mg, 0.36 mmol) was firstly dissolved in methanol (13 ml) and then added to above solution and stirred for 16 h under N₂ at room temperature. The solution was dark purple and clear. The solvent was evaporated to dryness under reduced pressure and the crude residue was redissolved in DCM (60 ml), then washed with 5% NaHCO₃ (40 ml×3) and DI water (40 ml). The organic layer was dried over MgSO₄ and the solvent was removed in vacuum. Purified by column chromatography (DCM) to give ZnTPP-NH₂ as a dark-purple solid in 94% yield (200 mg). ¹H NMR (DMSO-d₆) δ 8.89 (d, *J*= 6 Hz, 2H), 8.73-8.71 (m, 6H), 8.16-8.14 (m, 6H), 7.81-7.76 (m, 11H), 6.95 (d, *J*= 12 Hz, 2H), 5.45 (brs, 2H). ¹³C NMR (DMSO-d₆) δ 159.56, 158.74, 158.67, 158.50, 152.36, 144.74, 143.65, 141.50, 140.96, 140.84, 140.64, 136.90, 136.07, 131.56, 129.55, 129.18, 121.74, 40.18. HRMS (ESI): calculated for C₄₄H₂₉N₅Zn, 691.1714 [M]; found: 691.1691 [M]

Z-(Aib)₆-CONH-ZnTPP(+/-) (17): To a stirring solution of Z-(Aib)₆-OH (190 mg, 0.29 mmol) in anhydrous DMF (7.5 ml) at 0°C, ZnTPP-aniline (200 mg, 0.29 mmol), NMM (0.15 ml, 0.29 mmol) and TFFH (80 mg, 0.29 mmol) were added. The solution was dark purple and clear. The reaction mixture was stirred for 5 days under N₂ at room temperature and the solvent was evaporated in vacuum. The crude residue was subjected to preparative TLC (SiO₂, 50% EtOAc/Hexanes) and Saphadex (DCM) to give Z-(Aib)₆-CONH-ZnTPP(+/-) as a dark-purple solid in 26% yield (100 mg). ¹H NMR (CD₃OD) δ 9.64 (brs, 1H), 8.91 (d, *J*= 6 Hz, 2H,), 8.83-8.81 (m, 6H), 8.22-8.19 (m, 9H), 8.15 (d, 2H), 8.06 (d, 2H), 8.00 (brs, 1H), 7.77- 7.75 (m, 11H), 7.38- 7.35 (m, 5H), 5.12 (s, 2H), 1.74 (s, 6H), 1.59 (s, 6H), 1.58 (s, 6H), 1.43 (s, 6H), 1.42 (s, 6H), 1.36 (s, 6H). ¹³C NMR (CD₃OD) δ 178.18, 177.68, 177.23, 177.11, 176.57, 157.94, 151.63, 151.42, 151.38, 151.36, 144.96,

140.42, 139.86, 138.70, 135.74, 135.62, 132.58, 132.48, 132.40, 129.58, 129.04, 128.59, 128.36, 127.44, 121.77, 121.70, 121.63, 119.55, 67.65, 66.89, 59.03, 58.25, 57.68, 30.66, 25.58, 25.22, 15.43. HRMS (ESI): calculated for $C_{76}H_{77}N_{11}O_8ZnNa$, 1358.5140 $[M+Na]^+$; found: 1358.5192 $[M+Na]^+$

ZnTPP-NHCO-(Aib)₆-succinate-OtBu(-+) (**18**): Z-(Aib)₆-CONH-ZnTPP(+/-) (30 mg, 0.022 mmol) was dissolved in anhydrous methanol (1 ml) and 10% Pd/C (5 mg) was added slowly to the solution, turned the solution to black color. After purged with N₂ and evacuated under vacuum, a H₂ balloon was carefully fitted to the reaction vessel and the solution was stirred for 3 days at room temperature. The H₂ balloon was removed and the solution was filtered through a Celite bed. The solvent was removed in vacuum to afford free amine (NH₂-(Aib)₆-CONH-ZnTPP(+/-)) as a gummy solid, which was directly used for the next reaction without purification. To an ice-cold solution of *tert*-butyl hydrogen succinate 6 mg, 0.022 mmol) in anhydrous DCM (2 ml), HOAt (4 mg, 0.022 mmol) and EDC·HCl (6 mg, 0.022 mmol) were added, followed by the adding of NH₂-(Aib)₆-CONH-ZnTPP(+/-) and DIEA (0.15 mg, 0.027 mmol). The solution was dark purple and clear. The reaction mixture was stirred for 6 days under N₂ at room temperature and the solvent was evaporated in vacuum. The crude residue was purified by column chromatography (75%-100% EtOAc/Hexanes) and Sphadex (DCM) to give ZnTPP-NHCO-(Aib)₆-succinate-OtBu(-+) as a dark-purple solid in 57% yield (18 mg). ¹H NMR (CDCl₃) δ 9.55 (brs, 1H), 9.01 (d, *J*= 6 Hz, 2H), 8.90 (m, 6H), 8.64 (d, *J*= 6 Hz, 2H), 8.32 (brs, 1H), 8.19-8.18 (m, 6H), 8.10 (d, *J*= 12 Hz, 2H), 7.93 (brs, 1H), 7.81 (brs, 1H), 7.79 (brs, 1H), 7.72- 7.70 (m, 11H), 2.38 (t, 2H), 2.17 (t, 2H), 1.73 (s, 6H), 1.61 (s, 6H), 1.60 (s, 6H), 1.50 (s, 6H), 1.47 (s, 6H), 1.44 (s, 15H).

ZnTPP-NHCO-(Aib)₆-succinate-OH(-+) (**19**): To a stirring solution of ZnTPP-NHCO-(Aib)₆-succinate-OtBu(-+) (18 mg, 0.013 mmol) in anhydrous DCM (0.4 ml), 0.4 ml TFA was added. The solution was stirred for 3h at room temperature. The solution was dark purple and clear. The solvent was evaporated and the remaining traces of TFA were removed by adding anhydrous diethyl ether (3×30 ml) and evaporation in vacuum. The crude product was recrystallized from anhydrous diethyl ether to give ZnTPP-NHCO-(Aib)₆-succinate-OH(-+) as a dark-purple solid in 72% yield (13 mg). ¹H NMR (CD₃OD) δ 9.66 (brs, 1H), 8.91 (d, *J*= 6 Hz, 2H), 8.83-8.82 (m, 6H), 8.43 (brs, 1H), 8.22-8.24 (m, 8H), 8.20-8.19 (d, *J*= 6 Hz, 2H), 8.15 (m, 1H), 8.09-7.98 (m, 1H), 7.87 (brs, 1H), 7.78-7.75 (m, 11H), 2.28 (t, 2H), 2.20 (t, 2H), 1.75 (s, 6H), 1.61 (s, 6H), 1.60 (s, 6H), 1.52 (s, 6H), 1.46 (s, 6H), 1.44 (s, 6H). HRMS (ESI): calculated for C₇₂H₇₆N₁₁O₉Zn, 1302.5113 [M+H]⁺; found: 1302.5121 [M+H]⁺

D.7.3 Binding of Z-(Aib)₆-OH onto TiO₂ film (droplet method). A small volume (5 drops) of a 2 mM solution of Z-(Aib)₆-OH (solvent: CH₃CN) was deposited onto a pristine TiO₂ film grown on a sapphire substrate placed flat in a glass Petri dish, which was then sealed to prevent evaporation. After reacting for 1 day, the film was thoroughly rinsed with neat solvent to remove weakly bound or physisorbed molecules, and then dried under gentle nitrogen flow.

D.7.4 FTIR Microscopic Imaging and Data Analysis¹²⁷. FTIR microscopic images of TiO₂ films were collected with a Perkin-Elmer Spotlight 300 system (Perkin Elmer Life and Analytical Science, Inc., Waltham, MA) in the transmission mode with an essentially linear array (16×1) of mercury-cadmium-telluride (MCT) detector elements. Imaging size was 100×100 μm^2 . Images were collected with a 6.25×6.25 μm^2 pixel size and 32 scans at

a spectral resolution of 8cm^{-1} , corresponding to 16×16 pixel images. Visible micrographs were obtained with the optical microscope integrated into the Spotlight 300 system. FTIR microscopic images were generated from FTIR spectral data using ISys 3.1 software (Malvern Instruments, UK). Image planes of integrated band area were produced after linear baselines were applied in spectral regions of interest. The scale bar is color coded and selected to display the corresponding integrated area ($\pm\text{STD}$) above the detection limit to highlight differences upon treatments.

Chapter E: Summary

The need to improve the final performance of devices made by metal-oxide semiconductor materials functionalized with molecules requires the precise control of the molecule/semiconductor interface. Efficient modification methods and characterization techniques are necessary to achieve this goal. The innovative design of molecules that functionalize the metal-oxide semiconductor materials can also affect the performance of the devices prepared. This thesis addressed both topics, as summarized below.

The functionalization of $\text{Mg}_x\text{Zn}_{1-x}\text{O}$ ($4\% < x < 5\%$) (MZO_{nano}) film with bifunctional linker molecule- 11-azidoundecanoic acid (**1**) and the binding studies of the films by FTIR microscopic imaging are discussed in Chapter B. The improved acid resistance by using MZO_{nano} instead of ZnO_{nano} was confirmed by FESEM images of films before and after binding with bifunctional linker 11-azidoundecanoic acid (**1**) and hexadecyl alkynated folic acid (HAFa). **1** was bound on MZO_{nano} films via droplet method. By using FTIR microscopic imaging, the influence of reaction conditions on the binding performance was investigated. It is found that the protic solvent such as ethanol or butanol can also bind onto MZO_{nano} film, whereas by using polar, aprotic solvents 3- methoxypropionitrile (3-MPN), this competing effect can be eliminated, resulting in a functionalized film with much higher coverage. The binding of 10 mM solution of **1** in 3-MPN solvent starts at small areas that expand with the binding time, suggesting that bound **1** can induce further binding due to hydrophobic interactions. A fully covered molecular layer can be obtained after 22 hours binding. The influence of film morphology on binding was studied on three different morphologies. It was found that nanotip morphology disfavors binding, areas with nanorod grown in different directions favor binding, and that the packing density of nanorods does not affect the binding. The morphology, and concentration of the binding solution can also

influence the binding rate. When the concentration was increased to 40 mM, the binding rate increased significantly, resulting in a fully covered film within 18 hours. However, further increasing the concentration to 100 mM will dramatically decrease the binding rate but result in a highly homogenous layer due to intermolecular hydrogen bonding between **1** molecule in solution as proven by the ^{13}C NMR spectra. The stability of functionalized films to solvents and temperature was probed: films were stable to aprotic solvents at room temperature and at elevated temperature up to 40 °C and to protic solvents at room temperature. Desorption of bound **1** was observed in protic solvents at 40 °C.

In chapter C, the **1**/MZO_{nano} films were further functionalized, in a stepwise approach, with hexadecyl alkynated folic acid (HAFA), a biomolecule with a high affinity to folate binding protein, and a biomarker of cancer cells. HAFA was synthesized via two steps amidation reactions. The introduction of the alkyne functional group allows CuAAC click chemistry, whereas the hexadecyl long chain increases solubility, improves acid and basic resistance, and prevents direct binding of HAFA to MZO_{nano} film. The stepwise binding involved two steps: step A, **1** binding; step B, HAFA immobilization via CuAAC. In the binding method developed in this work, the functionalized MZO_{nano} film was placed face-down when immersing in the HAFA solution to avoid the possible contamination of copper byproducts. FTIR spectra of functionalized MZO_{nano} film before and after immobilization of HAFA were thoroughly analyzed. The FTIR microscopic imaging study of step B revealed that after 15 min, the azide functional layer on the MZO_{nano} surface fully reacted with HAFA. Fluorescence spectroscopy was also used to probe the immobilization process, indicating that HAFA was successful immobilized onto MZO_{nano} film. Two control experiments were conducted to exclude the possibility of physisorption of HAFA on MZO_{nano} film to test

conditions leading to desorption of **1**. This stepwise method was successfully applied in the modification of the sensitive devices: a MZO_{nano}- modified quartz crystal microbalance (QCM) and a MZO_{nano}- modified thin film transistor (TFT). The acoustic impedance spectra of the MZO_{nano}- modified QCM before and after step A and B were measured. The frequency change due to the mass loading at each step was as expected. The folic acid-modified MZO_{nano}- based QCM biosensor can be used in further sensing study of folate binding protein. The preparation of folic acid-modified MZO_{nano}- based TFT biosensor follows similar procedures. The conductivity of MZO_{nano}- modified TFT before and after each step was measured and changed as expected.

In the last chapter of this thesis, the need of an ideal model of the dipole bridge for energy level alignment studies was described. Z-(Aib)₆-OtBu was selected as the dipole bridge, and its synthesis and characterization are reported. The synthesis of Z-(Aib)₆-OtBu followed classical peptide synthesis methodologies. ¹H NMR, ¹³C NMR, and ESI were used to characterize the products. The helical structure is a key property of Aib-peptides as it directly relates to the formation of the intrinsic dipole pointing from the N-terminus to C-terminus in the peptide chain. Aib-peptides are known to form 3¹⁰-helical structure via intramolecular H-bonding between the carbonyl group in residue i and the hydrogen of an amide group in residue i+3. FTIR of Z-(Aib)_n-OtBu (n=2, 3, 6) was used to study the hydrogen bonding network. By monitoring changes in the amide-I, amide-II and N-H stretching bands. ¹H NMR was employed to study hydrogen bonding. By monitoring changes in chemical shifts of two solvent-exposed hydrogens in CDCl₃ (a poor hydrogen bonding accepting solvent). FTIR spectra and images indicate a weak binding of Z-(Aib)₆-OH on nanostructured TiO₂ films. Zinc tetraphenyl porphyrin (ZnTPP) and di-tert butyl

perylene (DTBPe) derivatives were employed as ideal modal of chromophores then attached to the N or C end of (Aib)_n peptides. Four compounds were synthesized and fully characterized by ¹H NMR, ¹³C NMR, UV-Vis, fluorescence and ESI (DTBPe-CONH-(Aib)₆-OH(+), DTBPe-NHCO-(Aib)₆-succinate-OH(-), ZnTPP-CONH-(Aib)₆-OH(+), ZnTPP-NHCO-(Aib)₆-succinate-OH(-)). Each pair was comprised of two compounds with same chromophoric head but opposite dipole orientation. The influence of the built-in dipole on the electrical property of moieties and how it affects the level alignment after binding onto ZnO/ TiO₂ film are under investigation.

References

1. Chittur, K. K., FTIR/ATR for protein adsorption to biomaterial surfaces. *Biomaterials* **1998**, *19* (4-5), 357-369.
2. Byler, D. M.; Susi, H., Examination of the secondary structure of proteins by deconvolved FTIR spectra. *Biopolymers: Original Research on Biomolecules* **1986**, *25* (3), 469-487.
3. Madejova, J., FTIR techniques in clay mineral studies. *Vibrational spectroscopy* **2003**, *31* (1), 1-10.
4. Salimi, A.; Yousefi, A., Analysis method: FTIR studies of β -phase crystal formation in stretched PVDF films. *Polymer Testing* **2003**, *22* (6), 699-704.
5. Schmitt, J.; Flemming, H.-C., FTIR-spectroscopy in microbial and material analysis. *International Biodeterioration Biodegradation* **1998**, *41* (1), 1-11.
6. Movasaghi, Z.; Rehman, S.; ur Rehman, D. I., Fourier transform infrared (FTIR) spectroscopy of biological tissues. *Applied Spectroscopy Reviews* **2008**, *43* (2), 134-179.
7. Bhargava, R., Infrared spectroscopic imaging: the next generation. *Applied spectroscopy* **2012**, *66* (10), 1091-1120.
8. Steiner, G.; Koch, E., Trends in Fourier transform infrared spectroscopic imaging. *Analytical and Bioanalytical Chemistry* **2009**, *394* (3), 671-678.
9. Schultz, C. P., „Precision Infrared Spectroscopic Imaging “. *Spectroscopy* **2001**, *16* (10), 24-28.
10. Gautam, R.; Samuel, A.; Sil, S.; Chaturvedi, D.; Dutta, A.; Ariese, F.; Umapathy, S., Raman and mid-infrared spectroscopic imaging: applications and advancements. *Current science* **2015**, *108* (3), 341-356.
11. Bhargava, R.; Levin, I. W., Fourier transform mid-infrared spectroscopic imaging. *Spectrochemical Analysis Using Infrared Multichannel Detectors* **2005**, 1-24.
12. Kazarian, S. G.; Chan, K. A., Micro-and macro-attenuated total reflection Fourier transform infrared spectroscopic imaging. *Applied spectroscopy* **2010**, *64* (5), 135A-152A.
13. Lewis, E. N.; Treado, P. J.; Reeder, R. C.; Story, G. M.; Dowrey, A. E.; Marcott, C.; Levin, I. W., Fourier transform spectroscopic imaging using an infrared focal-plane array detector. *Analytical chemistry* **1995**, *67* (19), 3377-3381.
14. Zhang, Q.; Saad, P.; Mao, G.; Walters, R. M.; Correa, M. C. M.; Mendelsohn, R.; Flach, C. R., Infrared spectroscopic imaging tracks lateral distribution in human stratum corneum. *Pharmaceutical Research* **2014**, *31* (10), 2762-2773.
15. Kohno, S.; Miyai, I.; Seiyama, A.; Oda, I.; Ishikawa, A.; Tsuneishi, S.; Amita, T.; Shimizu, K., Removal of the skin blood flow artifact in functional near-infrared spectroscopic imaging data through independent component analysis. *Journal of biomedical optics* **2007**, *12* (6), 062111.
16. Pilling, M.; Gardner, P., Fundamental developments in infrared spectroscopic imaging for biomedical applications. *Chemical Society reviews* **2016**, *45* (7), 1935-1957.
17. Andanson, J.-M.; Hadgraft, J.; Kazarian, S. G., In situ permeation study of drug through the stratum corneum using attenuated total reflectance Fourier transform infrared spectroscopic imaging. *Journal of Biomedical optics* **2009**, *14* (3), 034011.
18. Attas, M.; Posthumus, T.; Schattka, B.; Sowa, M.; Mantsch, H.; Zhang, S., Long-wavelength near-infrared spectroscopic imaging for in-vivo skin hydration measurements. *Vibrational spectroscopy* **2002**, *28* (1), 37-43.

19. Kuimova, M. K.; Chan, K. A.; Kazarian, S. G., Chemical imaging of live cancer cells in the natural aqueous environment. *Applied spectroscopy* **2009**, *63* (2), 164-171.
20. Chen, T.; Schultz, Z. D.; Levin, I. W., Infrared spectroscopic imaging of latent fingerprints and associated forensic evidence. *Analyst* **2009**, *134* (9), 1902-1904.
21. Crane, N. J.; Bartick, E. G.; Perlman, R. S.; Huffman, S., Infrared spectroscopic imaging for noninvasive detection of latent fingerprints. *Journal of forensic sciences* **2007**, *52* (1), 48-53.
22. Chan, K. A.; Hammond, S. V.; Kazarian, S. G., Applications of attenuated total reflection infrared spectroscopic imaging to pharmaceutical formulations. *Analytical chemistry* **2003**, *75* (9), 2140-2146.
23. Punčochová, K.; Ewing, A. V.; Gajdošová, M.; Sarvašová, N.; Kazarian, S. G.; Beránek, J.; Štěpánek, F., Identifying the mechanisms of drug release from amorphous solid dispersions using MRI and ATR-FTIR spectroscopic imaging. *International Journal of Pharmaceutics* **2015**, *483* (1-2), 256-267.
24. Arya, S. K.; Saha, S.; Ramirez-Vick, J. E.; Gupta, V.; Bhansali, S.; Singh, S. P., Recent advances in ZnO nanostructures and thin films for biosensor applications. *Analytica chimica acta* **2012**, *737*, 1-21.
25. Zhang, F.; Wang, X.; Ai, S.; Sun, Z.; Wan, Q.; Zhu, Z.; Xian, Y.; Jin, L.; Yamamoto, K., Immobilization of uricase on ZnO nanorods for a reagentless uric acid biosensor. *Analytica Chimica Acta* **2004**, *519* (2), 155-160.
26. Kong, T.; Chen, Y.; Ye, Y.; Zhang, K.; Wang, Z.; Wang, X. J. S.; Chemical, A. B., An amperometric glucose biosensor based on the immobilization of glucose oxidase on the ZnO nanotubes. *Sensors and Actuators B: Chemical* **2009**, *138* (1), 344-350.
27. Lei, Y.; Yan, X.; Luo, N.; Song, Y.; Zhang, Y., ZnO nanotetrapod network as the adsorption layer for the improvement of glucose detection via multiterminal electron-exchange. *Colloids Surfaces A: Physicochemical Engineering Aspects* **2010**, *361* (1-3), 169-173.
28. Ahmad, M.; Pan, C.; Gan, L.; Nawaz, Z.; Zhu, J., Highly sensitive amperometric cholesterol biosensor based on Pt-incorporated fullerene-like ZnO nanospheres. *The Journal of Physical Chemistry C* **2009**, *114* (1), 243-250.
29. Cao, Y.; Galoppini, E.; Reyes, P. I.; Lu, Y., Functionalization of nanostructured ZnO films by copper-free click reaction. *Langmuir* **2013**, *29* (25), 7768-7775.
30. Taratula, O.; Galoppini, E.; Wang, D.; Chu, D.; Zhang, Z.; Chen, H.; Saraf, G.; Lu, Y., Binding studies of molecular linkers to ZnO and MgZnO nanotip films. *The Journal of Physical Chemistry B* **2006**, *110* (13), 6506-6515.
31. Taratula, O.; Galoppini, E.; Mendelsohn, R.; Reyes, P. I.; Zhang, Z.; Duan, Z.; Zhong, J.; Lu, Y., Stepwise functionalization of ZnO nanotips with DNA. *Langmuir* **2009**, *25* (4), 2107-2113.
32. Persson, P.; Ojamäe, L., Periodic Hartree-Fock study of the adsorption of formic acid on ZnO (1010). *Chemical Physics Letters* **2000**, *321* (3-4), 302-308.
33. Curreli, M.; Li, C.; Sun, Y.; Lei, B.; Gundersen, M. A.; Thompson, M. E.; Zhou, C., Selective functionalization of In₂O₃ nanowire mat devices for biosensing applications. *Journal of the American Chemical Society* **2005**, *127* (19), 6922-6923.
34. Yang, J.; Lin, Y.; Meng, Y., Effects of dye etching on the morphology and performance of ZnO nanorod dye-sensitized solar cells. *Korean Journal of Chemical Engineering* **2013**, *30* (11), 2026-2029.
35. Torbrügge, S.; Ostendorf, F.; Reichling, M., Stabilization of zinc-terminated ZnO (0001) by a modified surface stoichiometry. *The Journal of Physical Chemistry C* **2009**, *113* (12), 4909-4914.
36. Luo, B.; Rossini, J. E.; Gladfelter, W. L., Zinc oxide nanocrystals stabilized by alkylammonium alkylcarbamates. *Langmuir* **2009**, *25* (22), 13133-13141.

37. Corso, C. D.; Dickherber, A.; Hunt, W. D., An investigation of antibody immobilization methods employing organosilanes on planar ZnO surfaces for biosensor applications. *Biosensors Bioelectronics* **2008**, *24* (4), 805-811.
38. Chen, Y.; Fan, H.; Galoppini, E., Click Chemistry and Nitrogen-Containing Heterocycles Formed in Surface Functionalization Reactions. *PATAI'S Chemistry of Functional Groups*, 1-46.
39. Kolb, H. C.; Finn, M.; Sharpless, K. B., Click chemistry: diverse chemical function from a few good reactions. *Angewandte Chemie International Edition* **2001**, *40* (11), 2004-2021.
40. Wang, Y.; Song, W.; Hu, W. J.; Lin, Q., Fast alkene functionalization in vivo by photoclick chemistry: HOMO lifting of nitrile imine dipoles. *Angewandte Chemie International Edition* **2009**, *48* (29), 5330-5333.
41. Song, W.; Wang, Y.; Qu, J.; Madden, M. M.; Lin, Q., A photoinducible 1, 3-dipolar cycloaddition reaction for rapid, selective modification of tetrazole-containing proteins. *Angewandte Chemie International Edition* **2008**, *47* (15), 2832-2835.
42. Chan, J. W.; Yu, B.; Hoyle, C. E.; Lowe, A. B., Convergent synthesis of 3-arm star polymers from RAFT-prepared poly (N, N-diethylacrylamide) via a thiol-ene click reaction. *Chemical Communications* **2008**, (40), 4959-4961.
43. Meldal, M.; Tornøe, C. W., Cu-catalyzed azide-alkyne cycloaddition. *Chemical reviews* **2008**, *108* (8), 2952-3015.
44. Rostovtsev, V. V.; Green, L. G.; Fokin, V. V.; Sharpless, K. B., A stepwise Huisgen cycloaddition process: copper (I)-catalyzed regioselective "ligation" of azides and terminal alkynes. *Angewandte Chemie* **2002**, *114* (14), 2708-2711.
45. Tornøe, C. W.; Meldal, M., Peptidotriazoles: Copper (I)-catalyzed 1, 3-dipolar cycloadditions on solid-phase. In *Peptides: The Wave of the Future*, Springer: 2001; pp 263-264.
46. Huisgen, R., 1, 3-dipolar cycloadditions. Past and future. *Angewandte Chemie International Edition in English* **1963**, *2* (10), 565-598.
47. Wang, C.; Ikhlef, D.; Kahlal, S.; Saillard, J.-Y.; Astruc, D., Metal-catalyzed azide-alkyne "click" reactions: Mechanistic overview and recent trends. *Coordination Chemistry Reviews* **2016**, *316*, 1-20.
48. Zhang, L.; Chen, X.; Xue, P.; Sun, H. H.; Williams, I. D.; Sharpless, K. B.; Fokin, V. V.; Jia, G., Ruthenium-catalyzed cycloaddition of alkynes and organic azides. *Journal of the American Chemical Society* **2005**, *127* (46), 15998-15999.
49. Jewett, J. C.; Bertozzi, C., Cu-free click cycloaddition reactions in chemical biology. *Chemical Society Reviews* **2010**, *39* (4), 1272-1279.
50. Kumar, P.; Joshi, C.; Srivastava, A. K.; Gupta, P.; Boukherroub, R.; Jain, S. L.; Engineering, Visible light assisted photocatalytic [3+ 2] azide-alkyne "click" reaction for the synthesis of 1, 4-substituted 1, 2, 3-triazoles using a novel bimetallic Ru-Mn complex. *ACS Sustainable Chemistry* **2015**, *4* (1), 69-75.
51. Listorti, A.; O'Regan, B.; Durrant, J. R., Electron transfer dynamics in dye-sensitized solar cells. *Chemistry of Materials* **2011**, *23* (15), 3381-3399.
52. Gong, J.; Liang, J.; Sumathy, K., Review on dye-sensitized solar cells (DSSCs): fundamental concepts and novel materials. *Renewable Sustainable Energy Reviews* **2012**, *16* (8), 5848-5860.
53. Hill, I.; Rajagopal, A.; Kahn, A.; Hu, Y., Molecular level alignment at organic semiconductor-metal interfaces. *Applied Physics Letters* **1998**, *73* (5), 662-664.
54. Braun, S.; Osikowicz, W.; Wang, Y.; Salaneck, W., Energy level alignment regimes at hybrid organic-organic and inorganic-organic interfaces. *Organic electronics* **2007**, *8* (1), 14-20.

55. Koller, G.; Blyth, R.; Sardar, S.; Netzer, F.; Ramsey, M., Band alignment at the organic-inorganic interface. *Applied Physics Letters* **2000**, *76* (7), 927-929.
56. Ishii, H.; Sugiyama, K.; Ito, E.; Seki, K., Energy level alignment and interfacial electronic structures at organic/metal and organic/organic interfaces. *Advanced materials* **1999**, *11* (8), 605-625.
57. Witte, G.; Lukas, S.; Bagus, P. S.; Wöll, C., Vacuum level alignment at organic/metal junctions: "Cushion" effect and the interface dipole. *Applied Physics Letters* **2005**, *87* (26), 263502.
58. Endres, J.; Pelczer, I.; Rand, B. P.; Kahn, A., Determination of energy level alignment within an energy cascade organic solar cell. *Chemistry of Materials* **2016**, *28* (3), 794-801.
59. Campbell, I.; Rubin, S.; Zawodzinski, T.; Kress, J.; Martin, R.; Smith, D.; Barashkov, N.; Ferraris, J., Controlling Schottky energy barriers in organic electronic devices using self-assembled monolayers. *Physical Review B* **1996**, *54* (20), R14321.
60. Campbell, I.; Kress, J.; Martin, R.; Smith, D.; Barashkov, N.; Ferraris, J., Controlling charge injection in organic electronic devices using self-assembled monolayers. *Applied Physics Letters* **1997**, *71* (24), 3528-3530.
61. Nieto-Pescador, J.; Abraham, B.; Li, J.; Batarseh, A.; Bartynski, R. A.; Galoppini, E.; Gundlach, L., Heterogeneous electron-transfer dynamics through dipole-bridge groups. *The Journal of Physical Chemistry C* **2015**, *120* (1), 48-55.
62. Chitre, K.; Batarseh, A.; Kopecky, A.; Fan, H.; Tang, H.; Lalancette, R.; Bartynski, R. A.; Galoppini, E., Synthesis of zinc tetraphenylporphyrin rigid rods with a built-in dipole. *The Journal of Physical Chemistry B* **2015**, *119* (24), 7522-7530.
63. Rangan, S.; Batarseh, A.; Chitre, K. P.; Kopecky, A.; Galoppini, E.; Bartynski, R. A., Tuning energy level alignment at organic/semiconductor interfaces using a built-in dipole in chromophore-bridge-anchor compounds. *The Journal of Physical Chemistry C* **2014**, *118* (24), 12923-12928.
64. Karle, I. L.; Balaram, P., Structural characteristics of. α -helical peptide molecules containing Aib residues. *Biochemistry* **1990**, *29* (29), 6747-6756.
65. De Filippis, V.; De Antoni, F.; Frigo, M.; Polverino de Laureto, P.; Fontana, A., Enhanced protein thermostability by Ala \rightarrow Aib replacement. *Biochemistry* **1998**, *37* (6), 1686-1696.
66. Toniolo, C.; Crisma, M.; Formaggio, F.; Peggion, C., Control of peptide conformation by the Thorpe-Ingold effect ($C\alpha$ -tetrasubstitution). *Peptide Science: Original Research on Biomolecules* **2001**, *60* (6), 396-419.
67. Cordes, M.; Giese, B., Electron transfer in peptides and proteins. *Chemical Society Reviews* **2009**, *38* (4), 892-901.
68. Watanabe, J.; Morita, T.; Kimura, S., Effects of dipole moment, linkers, and chromophores at side chains on long-range electron transfer through helical peptides. *The Journal of Physical Chemistry B* **2005**, *109* (30), 14416-14425.
69. Lauz, M.; Eckhardt, S.; Fromm, K. M.; Giese, B., The influence of dipole moments on the mechanism of electron transfer through helical peptides. *Physical Chemistry Chemical Physics* **2012**, *14* (40), 13785-13788.
70. Galoppini, E.; Fox, M. A., Effect of the electric field generated by the helix dipole on photoinduced intramolecular electron transfer in dichromophoric α -helical peptides. *Journal of the American Chemical Society* **1996**, *118* (9), 2299-2300.
71. Fox, M. A.; Galoppini, E., Electric field effects on electron transfer rates in dichromophoric peptides: the effect of helix unfolding. *Journal of the American Chemical Society* **1997**, *119* (23), 5277-5285.

72. DeFelippis, M. R.; Faraggi, M.; Klapper, M. H., Evidence for through-bond long-range electron transfer in peptides. *Journal of the American Chemical Society* **1990**, *112* (14), 5640-5642.
73. Morita, T.; Kimura, S., Long-range electron transfer over 4 nm governed by an inelastic hopping mechanism in self-assembled monolayers of helical peptides. *Journal of the American Chemical Society* **2003**, *125* (29), 8732-8733.
74. Nakayama, H.; Morita, T.; Kimura, S., Electric field effect of helical peptide dipole in self-assembled monolayers on electronic structure of oligo (Phenyleneethynylene). *The Journal of Physical Chemistry C* **2010**, *114* (10), 4669-4674.
75. Holm, A. H.; Ceccato, M.; Donkers, R. L.; Fabris, L.; Pace, G.; Maran, F., Effect of peptide ligand dipole moments on the redox potentials of Au₃₈ and Au₁₄₀ nanoparticles. *Langmuir* **2006**, *22* (25), 10584-10589.
76. Morita, T.; Kimura, S.; Kobayashi, S.; Imanishi, Y., Photocurrent generation under a large dipole moment formed by self-assembled monolayers of helical peptides having an N-ethylcarbazolyl group. *Journal of the American Chemical Society* **2000**, *122* (12), 2850-2859.
77. Garbuio, L.; Antonello, S.; Guryanov, I.; Li, Y.; Ruzzi, M.; Turro, N. J.; Maran, F., Effect of orientation of the peptide-bridge dipole moment on the properties of fullerene-peptide-radical systems. *Journal of the American Chemical Society* **2012**, *134* (25), 10628-10637.
78. Zanuy, D.; Nussinov, R.; Alemán, C., From peptide-based material science to protein fibrils: discipline convergence in nanobiology. *Physical Biology* **2006**, *3* (1), S80-S90.
79. Kaplan, J. M.; Shang, J.; Gobbo, P.; Antonello, S.; Armelao, L.; Chatare, V.; Ratner, D. M.; Andrade, R. B.; Maran, F., Conformationally constrained functional peptide monolayers for the controlled display of bioactive carbohydrate ligands. *Langmuir* **2013**, *29* (26), 8187-8192.
80. Özgür, Ü.; Alivov, Y. I.; Liu, C.; Teke, A.; Reshchikov, M.; Doğan, S.; Avrutin, V.; Cho, S.-J.; Morkoç, H., A comprehensive review of ZnO materials and devices. *Journal of Applied Physics* **2005**, *98* (4), 041301.
81. Ozgur, U.; Hofstetter, D.; Morkoc, H., ZnO devices and applications: a review of current status and future prospects. *Proceedings of the IEEE* **2010**, *98* (7), 1255-1268.
82. Shi, L.-E.; Li, Z.-H.; Zheng, W.; Zhao, Y.-F.; Jin, Y.-F.; Tang, Z.-X., Synthesis, antibacterial activity, antibacterial mechanism and food applications of ZnO nanoparticles: a review. *Food Additives Contaminants: Part A* **2014**, *31* (2), 173-186.
83. Wang, Z. L., From nanogenerators to piezotronics—A decade-long study of ZnO nanostructures. *MRS bulletin* **2012**, *37* (9), 814-827.
84. Djurišić, A.; Ng, A.; Chen, X., ZnO nanostructures for optoelectronics: material properties and device applications. *Progress in quantum electronics* **2010**, *34* (4), 191-259.
85. Kumar, B. V.; Naik, H. S. B.; Girija, D.; Kumar, B. V., ZnO nanoparticle as catalyst for efficient green one-pot synthesis of coumarins through Knoevenagel condensation. *Journal of Chemical Sciences* **2011**, *123* (5), 615-621.
86. Liu, J.; Guo, C.; Li, C. M.; Li, Y.; Chi, Q.; Huang, X.; Liao, L.; Yu, T., Carbon-decorated ZnO nanowire array: a novel platform for direct electrochemistry of enzymes and biosensing applications. *Electrochemistry Communications* **2009**, *11* (1), 202-205.
87. Gu, B.; Xu, C.; Zhu, G.; Liu, S.; Chen, L.; Wang, M.; Zhu, J., Layer by layer immobilized horseradish peroxidase on zinc oxide nanorods for biosensing. *The Journal of Physical Chemistry B* **2009**, *113* (18), 6553-6557.
88. Gonzalez-Valls, I.; Lira-Cantu, M., Vertically-aligned nanostructures of ZnO for excitonic solar cells: a review. *Energy Environmental Science* **2009**, *2* (1), 19-34.

89. Hakola, H.; Sariola-Leikas, E.; Efimov, A.; Tkachenko, N. V., Effect of hole transporting material on charge transfer processes in zinc phthalocyanine sensitized ZnO nanorods. *The Journal of Physical Chemistry C* **2016**, *120* (13), 7044-7051.
90. Song, J.; Kulinich, S. A.; Yan, J.; Li, Z.; He, J.; Kan, C.; Zeng, H., Epitaxial ZnO Nanowire-on-Nanoplate Structures as Efficient and Transferable Field Emitters. *Advanced Materials* **2013**, *25* (40), 5750-5755.
91. Tian, C.; Zhang, Q.; Wu, A.; Jiang, M.; Liang, Z.; Jiang, B.; Fu, H., Cost-effective large-scale synthesis of ZnO photocatalyst with excellent performance for dye photodegradation. *Chemical Communications* **2012**, *48* (23), 2858-2860.
92. Mishra, Y. K.; Modi, G.; Cretu, V.; Postica, V.; Lupan, O.; Reimer, T.; Paulowicz, I.; Hrkac, V.; Benecke, W.; Kienle, L.; interfaces, Direct growth of freestanding ZnO tetrapod networks for multifunctional applications in photocatalysis, UV photodetection, and gas sensing. *ACS applied materials* **2015**, *7* (26), 14303-14316.
93. Kumar, N.; Dorfman, A.; Hahm, J.-i., Ultrasensitive DNA sequence detection using nanoscale ZnO sensor arrays. *Nanotechnology* **2006**, *17* (12), 2875-2881.
94. Zhou, J.; Gu, Y.; Hu, Y.; Mai, W.; Yeh, P.-H.; Bao, G.; Sood, A. K.; Polla, D. L.; Wang, Z. L., Gigantic enhancement in response and reset time of ZnO UV nanosensor by utilizing Schottky contact and surface functionalization. *Applied Physics Letters* **2009**, *94* (19), 191103/1-3.
95. Menzel, A.; Subannajui, K.; Güder, F.; Moser, D.; Paul, O.; Zacharias, M., Multifunctional ZnO-Nanowire-Based Sensor. *Advanced Functional Materials* **2011**, *21* (22), 4342-4348.
96. Ruther, R. E.; Franking, R.; Huhn, A. M.; Gomez-Zayas, J.; Hamers, R., Formation of smooth, conformal molecular layers on ZnO surfaces via photochemical grafting. *Langmuir* **2011**, *27* (17), 10604-10614.
97. Wang, Z. L., Nanostructures of zinc oxide. *Materials Today* **2004**, *7* (6), 26-33.
98. Schmidt-Mende, L.; MacManus-Driscoll, J. L., ZnO-nanostructures, defects, and devices. *Materials Today* **2007**, *10* (5), 40-48.
99. Xu, S.; Wang, Z. L., One-dimensional ZnO nanostructures: solution growth and functional properties. *Nano Research* **2011**, *4* (11), 1013-1098.
100. Lupan, O.; Chai, G.; Chow, L., Fabrication of ZnO nanorod-based hydrogen gas nanosensor. *Microelectronics journal* **2007**, *38* (12), 1211-1216.
101. Park, S.-H.; Kim, S.-H.; Han, S.-W., Growth of homoepitaxial ZnO film on ZnO nanorods and light emitting diode applications. *Nanotechnology* **2007**, *18* (5), 055608/1-6.
102. Prabakar, K.; Kim, H., Growth control of ZnO nanorod density by sol-gel method. *Thin Solid Films* **2010**, *518* (24), e136-e138.
103. Nishimura, R.; Sakano, T.; Okato, T.; Obara, M. In *Fabrication and characterization of ZnO nanorods by pulsed laser deposition method through catalyst-free process*, Photon Processing in Microelectronics and Photonics VI, International Society for Optics and Photonics: 2007; p 645817.
104. Heo, Y.; Varadarajan, V.; Kaufman, M.; Kim, K.; Norton, D.; Ren, F.; Fleming, P., Site-specific growth of ZnO nanorods using catalysis-driven molecular-beam epitaxy. *Applied physics letters* **2002**, *81* (16), 3046-3048.
105. Park, W. I.; Kim, D. H.; Jung, S.-W.; Yi, G.-C., Metalorganic vapor-phase epitaxial growth of vertically well-aligned ZnO nanorods. *Applied Physics Letters* **2002**, *80* (22), 4232-4234.
106. Brenner, T. M.; Flores, T. A.; Ndione, P. F.; Meinig, E. P.; Chen, G.; Olson, D. C.; Furtak, T. E.; Collins, R. T., Etch-Resistant Zn_{1-x}Mg_xO Alloys: An Alternative to ZnO for

Carboxylic Acid Surface Modification. *The Journal of Physical Chemistry C* **2014**, *118* (24), 12599-12607.

107. Attas, M.; Hewko, M.; Payette, J.; Posthumus, T.; Sowa, M.; Mantsch, H., Visualization of cutaneous hemoglobin oxygenation and skin hydration using near-infrared spectroscopic imaging. *Skin Research Technology* **2001**, *7* (4), 238-245.

108. Mendelsohn, R.; Flach, C. R.; Moore, D. J., Determination of molecular conformation and permeation in skin via IR spectroscopy, microscopy, and imaging. *Biochimica et Biophysica Acta -Biomembranes* **2006**, *1758* (7), 923-933.

109. Bhargava, R.; Fernandez, D. C.; Hewitt, S. M.; Levin, I. W., High throughput assessment of cells and tissues: Bayesian classification of spectral metrics from infrared vibrational spectroscopic imaging data. *Biochimica et Biophysica Acta -Biomembranes Analyst* **2006**, *1758* (7), 830-845.

110. Sun, X.; Liu, Z.; Welsher, K.; Robinson, J. T.; Goodwin, A.; Zaric, S.; Dai, H., Nano-graphene oxide for cellular imaging and drug delivery. *Nano Research* **2008**, *1* (3), 203-212.

111. Merberg, G. N.; Harrington, J. A., Optical and mechanical properties of single-crystal sapphire optical fibers. *Applied optics* **1993**, *32* (18), 3201-3209.

112. Palanisamy, S.; Chen, S.-M.; Sarawathi, R., A novel nonenzymatic hydrogen peroxide sensor based on reduced graphene oxide/ZnO composite modified electrode. *Sensors and Actuators B: Chemical* **2012**, *166*, 372-377.

113. Zhang, B.; Kong, T.; Xu, W.; Su, R.; Gao, Y.; Cheng, G., Surface functionalization of zinc oxide by carboxyalkylphosphonic acid self-assembled monolayers. *Langmuir* **2010**, *26* (6), 4514-4522.

114. Gupta, A.; Kim, B. C.; Edwards, E.; Brantley, C.; Ruffin, P., Covalent functionalization of zinc oxide nanowires for high sensitivity p-nitrophenol detection in biological systems. *Materials Science Engineering: B* **2012**, *177* (18), 1583-1588.

115. Qu, Q.; Geng, H.; Peng, R.; Cui, Q.; Gu, X.; Li, F.; Wang, M., Chemically binding carboxylic acids onto TiO₂ nanoparticles with adjustable coverage by solvothermal strategy. *Langmuir* **2010**, *26* (12), 9539-9546.

116. Rossini, J. E.; Huss, A. S.; Bohnsack, J. N.; Blank, D. A.; Mann, K. R.; Gladfelter, W. L., Binding and static quenching behavior of a terthiophene carboxylate on monodispersed zinc oxide nanocrystals. *The Journal of Physical Chemistry C* **2010**, *115* (1), 11-17.

117. Chen, J.; Ruther, R. E.; Tan, Y.; Bishop, L. M.; Hamers, R., Molecular adsorption on ZnO (1010⁻) single-crystal surfaces: morphology and charge transfer. *Langmuir* **2012**, *28* (28), 10437-10445.

118. Ye, D.-X.; Lu, T.-M.; Karabacak, T., Influence of nanotips on the hydrophilicity of metallic nanorod surfaces. *Physical Review Letters* **2008**, *100* (25), 256102.

119. Liu, X.; Ye, L.; Liu, S.; Li, Y.; Ji, X., Photocatalytic reduction of CO₂ by ZnO micro/nanomaterials with different morphologies and ratios of {0001} facets. *Scientific reports* **2016**, *6*, 38474.

120. Rouchdi, M.; Salmani, E.; Fares, B.; Hassanain, N.; Mzerd, A., Synthesis and characteristics of Mg doped ZnO thin films: Experimental and ab-initio study. *Results in physics* **2017**, *7*, 620-627.

121. Fu, Y. Q.; Luo, J.; Du, X.; Flewitt, A.; Li, Y.; Markx, G.; Walton, A.; Milne, W., Recent developments on ZnO films for acoustic wave based bio-sensing and microfluidic applications: a review. *Sensors Actuators B: Chemical* **2010**, *143* (2), 606-619.

122. Duan, Z. MOCVD growth of MGxZN1-xO films and nanostructures for photovoltaics. Rutgers University-Graduate School-New Brunswick, 2012.

123. Asakawa, N.; Kuroki, S.; Kurosu, H.; Ando, I.; Shoji, A.; Ozaki, T., Hydrogen-bonding effect on carbon-13 NMR chemical shifts of L-alanine residue carbonyl carbons of peptides in the solid state. *Journal of the American Chemical Society* **1992**, *114* (9), 3261-3265.
124. Brzezinski, B.; Brycki, B.; Maciejewska-Urjasz, H.; Zundel, G., ¹H and ¹³C NMR studies of proton transfer in intramolecular hydrogen bonds in substituted 2-diethylaminomethylphenol N-oxides. *Magnetic resonance in chemistry* **1993**, *31* (7), 642-644.
125. Shi, J.; Hong, H.; Ding, Y.; Yang, Y.; Wang, F.; Cai, W.; Wang, X., Evolution of zinc oxide nanostructures through kinetics control. *Journal of Materials Chemistry* **2011**, *21* (25), 9000-9008.
126. Saunders, J. E., Synthesis and characterization of ensembles containing zinc oxide nanocrystals and organic or transition metal dyes to probe the early events in a dye-sensitized solar cell. *University of Minnesota digital conservancy* **2011**.
127. Chen, Y.; Zhang, Q.; Flach, C.; Mendelsohn, R.; Galoppini, E.; Reyes, P. I.; Yang, K.; Li, R.; Li, G.; Lu, Y., Functionalization of MgZnO nanorod films and characterization by FTIR microscopic imaging. *Analytical & bioanalytical chemistry* **2017**, *409* (27), 6379-6386.
128. Fokin, V. V.; Matyjaszewski, K., CuAAC: the quintessential click reaction. *Organic Chemistry—Breakthroughs Perspectives* **2012**, 247-277.
129. Fokin, V. V.; Matyjaszewski, K. In *Organic Chemistry-Breakthroughs and Perspectives*, Wiley-VCH Verlag, 2012.
130. Hein, J. E.; Fokin, V. V., Copper-catalyzed azide-alkyne cycloaddition (CuAAC) and beyond: new reactivity of copper (I) acetylides. *Chemical Society Reviews* **2010**, *39* (4), 1302-1315.
131. Haldon, E.; Nicasio, M. C.; Perez, P. J., Copper-catalysed azide-alkyne cycloadditions (CuAAC): An update. *Organic biomolecular chemistry* **2015**, *13* (37), 9528-9550.
132. Escorihuela, J.; Marcelis, A. T.; Zuilhof, H., Metal-Free Click Chemistry Reactions on Surfaces. *Advanced Materials Interfaces* **2015**, *2* (13), 1500135.
133. He, H.; Gao, C., Click chemistry on nano-surfaces. *Current Organic Chemistry* **2011**, *15* (21), 3667-3691.
134. Chen, C.; Ke, J.; Zhou, X. E.; Yi, W.; Brunzelle, J. S.; Li, J.; Yong, E.-L.; Xu, H. E.; Melcher, K., Structural basis for molecular recognition of folic acid by folate receptors. *Nature* **2013**, *500* (7463), 486.
135. Blakley, R. L., Biochemistry of folic acid and related pteridines. *Annals of internal medicine* **1969**, *1*.
136. Pufulete, M.; Al-Ghnaniem, R.; Khushal, A.; Appleby, P.; Harris, N.; Gout, S.; Emery, P.; Sanders, T., Effect of folic acid supplementation on genomic DNA methylation in patients with colorectal adenoma. *Gut* **2005**, *54* (5), 648-653.
137. Lillycrop, K. A.; Phillips, E. S.; Jackson, A. A.; Hanson, M. A.; Burdge, G. C., Dietary protein restriction of pregnant rats induces and folic acid supplementation prevents epigenetic modification of hepatic gene expression in the offspring. *The Journal of nutritional biochemistry* **2005**, *135* (6), 1382-1386.
138. Castillo, J. J.; Svendsen, W. E.; Rozlosnik, N.; Escobar, P.; Martínez, F.; Castillo-León, J., Detection of cancer cells using a peptide nanotube-folic acid modified graphene electrode. *Analyst* **2013**, *138* (4), 1026-1031.
139. Toffoli, G.; Cernigoi, C.; Russo, A.; Gallo, A.; Bagnoli, M.; Boiocchi, M., Overexpression of folate binding protein in ovarian cancers. *International Journal of Cancer* **1997**, *74* (2), 193-198.

140. Kim, D.-K.; Lee, T.; Castilleja, A.; Anderson, B.; Peoples, G.; Kudelka, A.; Murray, J.; Sittisomwong, T.; Wharton, J.; Kim, J., Folate binding protein peptide 191-199 presented on dendritic cells can stimulate CTL from ovarian and breast cancer patients. *Anticancer research* **1999**, *19* (4B), 2907-2916.
141. Lucock, M., Folic acid: nutritional biochemistry, molecular biology, and role in disease processes. *Molecular genetics and metabolism* **2000**, *71* (1), 121-138.
142. Kim, Y.-I., Folate and carcinogenesis: evidence, mechanisms, and implications. *The Journal of nutritional biochemistry* **1999**, *10* (2), 66-88.
143. Duthie, S. J., Folic acid deficiency and cancer: mechanisms of DNA instability. *British medical bulletin* **1999**, *55* (3), 578-592.
144. Marx, K. A., Quartz crystal microbalance: a useful tool for studying thin polymer films and complex biomolecular systems at the solution– surface interface. *Biomacromolecules* **2003**, *4* (5), 1099-1120.
145. O'sullivan, C.; Guilbault, G., Commercial quartz crystal microbalances–theory and applications. *Biosensors and Bioelectronics* **1999**, *14* (8-9), 663-670.
146. Huang, H.; Zhou, J.; Chen, S.; Zeng, L.; Huang, Y., A highly sensitive QCM sensor coated with Ag+-ZSM-5 film for medical diagnosis. *Sensors Actuators B: Chemical* **2004**, *101* (3), 316-321.
147. Reyes, P. I.; Duan, Z.; Lu, Y.; Khavulya, D.; Boustany, N., ZnO nanostructure-modified QCM for dynamic monitoring of cell adhesion and proliferation. *Biosensors and Bioelectronics* **2013**, *41*, 84-89.
148. Weimer, P. K., The TFT a new thin-film transistor. *Proceedings of the IRE* **1962**, *50* (6), 1462-1469.
149. Weimer, P., IRE-AICE Device Research Conference. ed: *Stanford, CA* **1961**.
150. Fortunato, E.; Barquinha, P.; Martins, R., Oxide semiconductor thin-film transistors: a review of recent advances. *Advanced materials* **2012**, *24* (22), 2945-2986.
151. Hoffman, R.; Norris, B. J.; Wager, J., ZnO-based transparent thin-film transistors. *Applied Physics Letters* **2003**, *82* (5), 733-735.
152. Kamiya, T.; Nomura, K.; Hosono, H., Present status of amorphous In–Ga–Zn–O thin-film transistors. *Science and Technology of Advanced Materials* **2010**, *11* (4), 044305.
153. Kamiya, T.; Nomura, K.; Hosono, H., Origins of high mobility and low operation voltage of amorphous oxide TFTs: Electronic structure, electron transport, defects and doping. *Journal of display Technology* **2009**, *5* (12), 468-483.
154. Kagan, C. R.; Andry, P., *Thin-film transistors*. CRC Press: 2003.
155. Huang, W.; Besar, K.; LeCover, R.; Dulloor, P.; Sinha, J.; Hardigree, J. F. M.; Pick, C.; Swavola, J.; Everett, A. D.; Frechette, J., Label-free brain injury biomarker detection based on highly sensitive large area organic thin film transistor with hybrid coupling layer. *Chemical Science* **2014**, *5* (1), 416-426.
156. Huang, J.; Ng, A. L.; Piao, Y.; Chen, C.-F.; Green, A. A.; Sun, C.-F.; Hersam, M. C.; Lee, C. S.; Wang, Y., Covalently functionalized double-walled carbon nanotubes combine high sensitivity and selectivity in the electrical detection of small molecules. *Journal of the American Chemical Society* **2013**, *135* (6), 2306-2312.
157. Kim, J.-M.; Jha, S. K.; Chand, R.; Lee, D.-H.; Kim, Y.-S., DNA hybridization sensor based on pentacene thin film transistor. *Biosensors and Bioelectronics* **2011**, *26* (5), 2264-2269.
158. Cavallari, M. R.; Izquierdo, J. E.; Braga, G. S.; Dirani, E. A.; Pereira-da-Silva, M. A.; Rodríguez, E. F.; Fonseca, F., Enhanced sensitivity of gas sensor based on poly (3-hexylthiophene) thin-film transistors for disease diagnosis and environment monitoring. *Sensors* **2015**, *15* (4), 9592-9609.

159. Hong, W.-C.; Ku, C.-J.; Li, R.; Abbaslou, S.; Reyes, P.; Wang, S.-Y.; Li, G.; Lu, M.; Sheng, K.; Lu, Y., MgZnO High Voltage Thin Film Transistors on Glass for Inverters in Building Integrated Photovoltaics. *Scientific Reports* **2016**, *6*, 34169.
160. Ku, C.-J.; Duan, Z.; Reyes, P. I.; Lu, Y.; Xu, Y.; Hsueh, C.-L.; Garfunkel, E., Effects of Mg on the electrical characteristics and thermal stability of Mg x Zn 1– x O thin film transistors. *Applied Physics Letters* **2011**, *98* (12), 123511.
161. Ku, C.-J.; Reyes, P.; Duan, Z.; Hong, W.-C.; Li, R.; Lu, Y., MgxZn1– xO Thin-Film Transistor-Based UV Photodetector with Enhanced Photoresponse. *Journal of Electronic Materials* **2015**, *44* (10), 3471-3476.
162. Tornøe, C. W.; Christensen, C.; Meldal, M., Peptidotriazoles on solid phase:[1, 2, 3]-triazoles by regiospecific copper (I)-catalyzed 1, 3-dipolar cycloadditions of terminal alkynes to azides. *The Journal of organic chemistry* **2002**, *67* (9), 3057-3064.
163. Zhan, W.-h.; Barnhill, H. N.; Sivakumar, K.; Tian, H.; Wang, Q., Synthesis of hemicyanine dyes for 'click' bioconjugation. *Tetrahedron Letters* **2005**, *46* (10), 1691-1695.
164. Viswanathan, R.; Labadie, G. R.; Poulter, C. D., Regioselective covalent immobilization of catalytically active glutathione S-transferase on glass slides. *Bioconjugate Chemistry* **2013**, *24* (4), 571-577.
165. Pujari, S. S.; Seela, F., Cross-linked DNA: propargylated ribonucleosides as "click" ligation sites for bifunctional azides. *The Journal of organic chemistry* **2012**, *77* (9), 4460-4465.
166. Wang, X.; Morales, A. R.; Urakami, T.; Zhang, L.; Bondar, M. V.; Komatsu, M.; Belfield, K. D., Folate receptor-targeted aggregation-enhanced near-IR emitting silica nanoprobe for one-photon in vivo and two-photon ex vivo fluorescence bioimaging. *Bioconjugate Chemistry* **2011**, *22* (7), 1438-1450.
167. Geszke, M.; Murias, M.; Balan, L.; Medjahdi, G.; Korczynski, J.; Moritz, M.; Lulek, J.; Schneider, R., Folic acid-conjugated core/shell ZnS: Mn/ZnS quantum dots as targeted probes for two photon fluorescence imaging of cancer cells. *Acta Biomaterialia* **2011**, *7* (3), 1327-1338.
168. Huang, J.-C.; Li, D.-J.; Diao, J.-C.; Hou, J.; Yuan, J.-L.; Zou, G.-L., A novel fluorescent method for determination of peroxyxynitrite using folic acid as a probe. *Talanta* **2007**, *72* (4), 1283-1287.
169. Sauerbrey, G., Verwendung von Schwingquarzen zur Wägung dünner Schichten und zur Mikrowägung. *Zeitschrift für physik* **1959**, *155* (2), 206-222.
170. Li, R.; Li, G.; Hong, W.-C.; Reyes, P. I.; Tang, K.; Yang, K.; Wang, S.-Y.; Ye, H.; Li, Y.; Zhang, L., Tunable surface acoustic wave device using semiconducting MgZnO and piezoelectric NiZnO dual-layer structure on glass. *Smart Materials and Structures* **2018**, *27* (8), 085025.
171. Wang, F.; Xu, L.; Nawaz, M. H.; Liu, F.; Zhang, W., Morphology controlled supramolecular assemblies via complexation between (5, 10, 15, 20-tetrakisphenyl-porphine) zinc and 4, 4'-bipyridine: from nanospheres to microrings. *RSC Advances* **2014**, *4* (106), 61378-61382.
172. Kimura, S., Molecular dipole engineering: new aspects of molecular dipoles in molecular architecture and their functions. *Organic biomolecular chemistry* **2008**, *6* (7), 1143-1148.
173. Gatto, E.; Caruso, M.; Porchetta, A.; Toniolo, C.; Formaggio, F.; Crisma, M.; Venanzi, M., Photocurrent generation through peptide-based self-assembled monolayers on a gold surface: antenna and junction effects. *Journal of peptide science: an official publication of the European Peptide Society* **2011**, *17* (2), 124-131.
174. Grubišić, S.; Chandramouli, B.; Barone, V.; Brancato, G., Chain length, temperature and solvent effects on the structural properties of α -aminoisobutyric acid homooligopeptides. *Physical Chemistry Chemical Physics* **2016**, *18* (30), 20389-20398.

175. Vieira-Pires, R. S.; Morais-Cabral, J. H., 310 helices in channels and other membrane proteins. *The Journal of general physiology* **2010**, *136* (6), 585-592.
176. Toniolo, C.; Crisma, M.; Formaggio, F.; Peggion, C.; Broxterman, Q. B.; Kaptein, B., Molecular spacers for physicochemical investigations based on novel helical and extended peptide structures. *Peptide Science: Original Research on Biomolecules* **2004**, *76* (2), 162-176.
177. Jones, D.; Kenner, G.; Preston, J.; Sheppard, R., 1160. Peptides. Part XVII. Synthesis of peptides and polymers of some sterically hindered amino-acids via oxazolone intermediates. *Journal of the Chemical Society* **1965**, 6227-6239.
178. Zikou, S.; Koukkou, A. I.; Mastora, P.; Sakarellos-Daitsiotis, M.; Sakarellos, C.; Drinas, C.; Panou-Pomonis, E., Design and synthesis of cationic Aib-containing antimicrobial peptides: conformational and biological studies. *Journal of peptide science: an official publication of the European Peptide Society* **2007**, *13* (7), 481-486.
179. Wenschuh, H.; Beyermann, M.; Haber, H.; Seydel, J. K.; Krause, E.; Bienert, M.; Carpino, L. A.; El-Faham, A.; Albericio, F., Stepwise automated solid phase synthesis of naturally occurring peptaibols using Fmoc amino acid fluorides. *The Journal of Organic Chemistry* **1995**, *60* (2), 405-410.
180. Subiros-Funosas, R.; Acosta, G. A.; El-Faham, A.; Albericio, F., Microwave irradiation and COMU: a potent combination for solid-phase peptide synthesis. *Tetrahedron Letters* **2009**, *50* (45), 6200-6202.
181. Palasek, S. A.; Cox, Z. J.; Collins, J. M., Limiting racemization and aspartimide formation in microwave-enhanced Fmoc solid phase peptide synthesis. *Journal of peptide science: an official publication of the European Peptide Society* **2007**, *13* (3), 143-148.
182. Čemažar, M.; Craik, D. J., Microwave-assisted Boc-solid phase peptide synthesis of cyclic cysteine-rich peptides. *Journal of peptide science: an official publication of the European Peptide Society* **2008**, *14* (6), 683-689.
183. De Zotti, M.; Damato, F.; Formaggio, F.; Crisma, M.; Schievano, E.; Mammi, S.; Kaptein, B.; Broxterman, Q. B.; Felock, P. J.; Hazuda, D. J., Total synthesis, characterization, and conformational analysis of the naturally occurring hexadecapeptide integramide A and a diastereomer. *Chemistry—A European Journal* **2010**, *16* (1), 316-327.
184. Formaggio, F.; Crisma, M.; Scipionato, L.; Antonello, S.; Maran, F.; Toniolo, C., Synthesis and Characterization of a Series of Homooligopeptide Peroxyesters. *Organic letters* **2004**, *6* (16), 2753-2756.
185. Altmann, K. H.; Bold, G.; Caravatti, G.; Denni, D.; Flörsheimer, A.; Schmidt, A.; Rihs, G.; Wartmann, M., The Total Synthesis and Biological Assessment of trans-Epothilone A. *Helvetica chimica acta* **2002**, *85* (11), 4086-4110.
186. Carpino, L. A., 1-Hydroxy-7-azabenzotriazole. An efficient peptide coupling additive. *Journal of the American Chemical Society* **1993**, *115* (10), 4397-4398.
187. Barth, A., Infrared spectroscopy of proteins. *Biochimica et Biophysica Acta - Bioenergetics* **2007**, *1767* (9), 1073-1101.
188. Maekawa, H.; De Poli, M.; Toniolo, C.; Ge, N.-H., Couplings between peptide linkages across a 310-helical hydrogen bond revealed by two-dimensional infrared spectroscopy. *Journal of the American Chemical Society* **2009**, *131* (6), 2042-2043.
189. Rao, C. P.; Nagaraj, R.; Rao, C.; Balaram, P., Infrared spectroscopy as a probe for the development of secondary structure in the amino-terminal segment of alamethicin. *FEBS letters* **1979**, *100* (2), 244-248.

190. Zhu, H.; Blom, M.; Compagnon, I.; Rijs, A. M.; Roy, S.; von Helden, G.; Schmidt, B., Conformations and vibrational spectra of a model tripeptide: change of secondary structure upon micro-solvation. *Physical Chemistry Chemical Physics* **2010**, *12* (14), 3415-3425.
191. kumar, E. V.; Balaram, P., Stereochemistry of α -aminoisobutyric acid peptides in solution: Helical conformations of protected decapeptides with repeating Aib-L-Ala and Aib-L-Val sequences. *Biopolymers: Original Research on Biomolecules* **1983**, *22* (9), 2133-2140.
192. Abu Khaled, M.; Renugopalakrishnan, V.; Urry, D. W., Proton magnetic resonance and conformational energy calculations of repeat peptides of tropoelastin: the tetrapeptide. *Journal of the American Chemical Society* **1976**, *98* (24), 7547-7553.
193. Nagaraj, R.; Shamala, N.; Balaram, P., Stereochemically constrained linear peptides. Conformations of peptides containing. α -aminoisobutyric acid. *Journal of the American Chemical Society* **1979**, *101* (1), 16-20.
194. Bai, Y.; Mora-Sero, I.; De Angelis, F.; Bisquert, J.; Wang, P., Titanium dioxide nanomaterials for photovoltaic applications. *Chemical reviews* **2014**, *114* (19), 10095-10130.
195. Gupta, S. M.; Tripathi, M., A review of TiO₂ nanoparticles. *Chinese Science Bulletin* **2011**, *56* (16), 1639.
196. Mor, G. K.; Shankar, K.; Paulose, M.; Varghese, O. K.; Grimes, C. A., Use of highly-ordered TiO₂ nanotube arrays in dye-sensitized solar cells. *Nano letters* **2006**, *6* (2), 215-218.
197. Dastjerdi, R.; Montazer, M., A review on the application of inorganic nano-structured materials in the modification of textiles: focus on anti-microbial properties. *Colloids surfaces B: Biointerfaces* **2010**, *79* (1), 5-18.
198. Kim, H.-S.; Park, N.-G., Parameters affecting I-V hysteresis of CH₃NH₃PbI₃ perovskite solar cells: effects of perovskite crystal size and mesoporous TiO₂ layer. *The journal of physical chemistry letters* **2014**, *5* (17), 2927-2934.
199. Santra, P. K.; Kamat, P. V., Mn-doped quantum dot sensitized solar cells: a strategy to boost efficiency over 5%. *Journal of the American Chemical Society* **2012**, *134* (5), 2508-2511.
200. Diebold, U., The surface science of titanium dioxide. *Surface science reports* **2003**, *48* (5-8), 53-229.
201. Carpino, L. A.; Imazumi, H.; El-Faham, A.; Ferrer, F. J.; Zhang, C.; Lee, Y.; Foxman, B. M.; Henklein, P.; Hanay, C.; Mügge, C., The uronium/guanidinium peptide coupling reagents: finally the true uronium salts. *Angewandte Chemie International Edition* **2002**, *41* (3), 441-445.
202. KVSRG, P.; Bharathi, K.; Haseena Banu, B.; Research, Applications of peptide coupling reagents—An update. *International Journal of Pharmaceutical Sciences Review Research* **2011**, *8*, 108-119.
203. Hung, K.-y.; Harris, P. W.; Brimble, M. A., Synthesis of the peptaibol framework of the anticancer agent culicinin D: Stereochemical assignment of the AHMOD moiety. *Organic letters* **2012**, *14* (22), 5784-5787.
204. Nakade, S.; Matsuda, M.; Kambe, S.; Saito, Y.; Kitamura, T.; Sakata, T.; Wada, Y.; Mori, H.; Yanagida, S., Dependence of TiO₂ nanoparticle preparation methods and annealing temperature on the efficiency of dye-sensitized solar cells. *The Journal of Physical Chemistry B* **2002**, *106* (39), 10004-10010.
205. Guo, Y.-M.; Oike, H.; Aida, T., Chiroptical transcription of helical information through supramolecular harmonization with dynamic helices. *Journal of the American Chemical Society* **2004**, *126* (3), 716-717.

Appendix

List of Abbreviations

FTIR	Fourier transform infrared
ATR	Attenuated total reflection
MCT	Mercury cadmium telluride
FPA	Focal plane array
CuAAC	Cu-catalyzed Azide-Alkyne Click reaction
DSSC	Dye sensitized solar cells
HET	Heterogeneous electron transfer
HOMO	Highest occupied molecular orbital
LUMO	Lowest unoccupied molecular orbital
CB	Conduction band
XRD	X-ray diffraction
MOCVD	Metal-organic chemical-vapor deposition
ZnO _{nano}	ZnO nanorod
MZO _{nano}	Mg _x Zn _{1-x} O nanorod (4% < x < 5%)
FESEM	Field emission scanning electron microscopy
3-MPN	3-methoxypropionitrile
NMR	Nuclear magnetic resonance
ESI	Electrospray ionization
STD	Standard deviation
HAFA	Hexadecyl alkynated folic acid
QCM	Quarz crystal microbalance
TFT	Thin film transistor

Aib	α -aminoisobutyric acid
DTBPe	di- <i>tert</i> -butyl-perylene
ZnTPP	Zinc tetraphenylporphyrin
XPS	X-ray photoemission spectroscopy
UPS	Ultraviolet photoemission spectroscopy
I _{DS}	Current between drain and source
V _{GS}	Potential between gate and source

Table of acronyms, full names, and chemical structures of reagents

<i>Acronyms</i>	<i>Full name</i>	<i>Chemical structure</i>
<i>DCM</i>	Dichloromethane	CH_2Cl_2
<i>EDC·HCl</i>	1-(3-dimethyl-aminopropyl)-3-Ethylcarbodiimide hydrochloride	
<i>TFA</i>	Trifluoroacetic acid	
<i>HOAT</i>	1-Hydroxy-7-azabenzotriazole	
<i>NMM</i>	4-Methylmorpholine	
<i>EtOAc</i>	Ethyl acetate	$\text{CH}_3\text{COOCH}_2\text{CH}_3$
<i>TFFH</i>	Tetramethylfluoroformamidinium hexafluorophosphate	
<i>DMF</i>	N,N-Dimethylformamide	
<i>DIEA</i>	N,N-Diisopropylethylamine	
<i>HATU</i>	1-[Bis(dimethylamino) methylene]-1H-1,2,3-triazolo[4,5-b]pyridinium 3-oxid hexafluorophosphate	
<i>Fmoc</i>	Fluorenylmethyl oxycarbonyl	
<i>Z (Cbz)</i>	Carboxybenzyl	

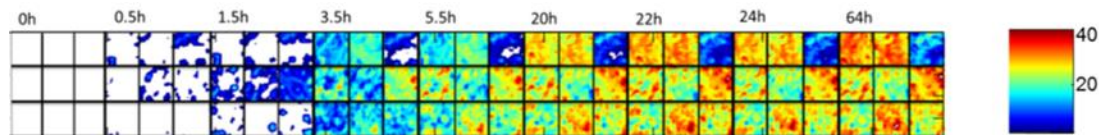


Fig. 0-1 Images of the integrated band area of $1564\text{-}1480\text{ cm}^{-1}$ region (\pm STD) of MZO_{nano} films before and after binding with 10 mM 11-azidoundecanoic acid in 3-MPN solution over time. Adapted with permission from [127]

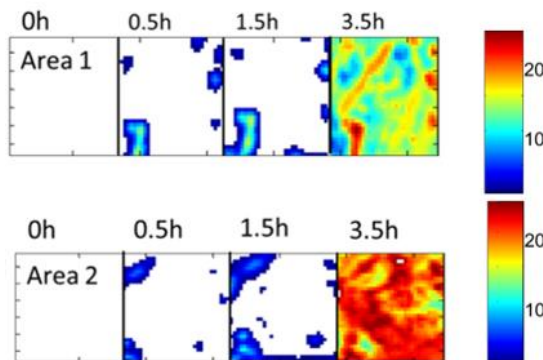


Fig. 0-2 Images of the integrated band area of the azido region $1564\text{-}1480\text{ cm}^{-1}$ (\pm STD) of two areas after binding with 10 mM **1** in 3-MPN as function of time. Adapted with permission from [127]

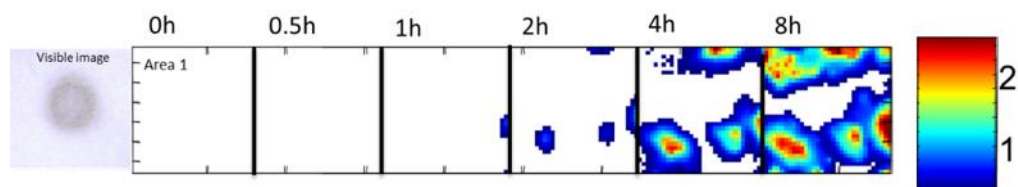


Fig. 0-3 Visible micrograph (before binding, $200 \times 200\text{ }\mu\text{m}^2$) taken of nanorods grown in different orientation type morphology from which FTIR images were acquired as a function of binding time. FTIR images of the integrated band area, $1564\text{-}1480\text{ cm}^{-1}$ (\pm STD) of area 1 after binding with 10 mM **1** in 3-MPN solution as function of time. Adapted with permission from [127]

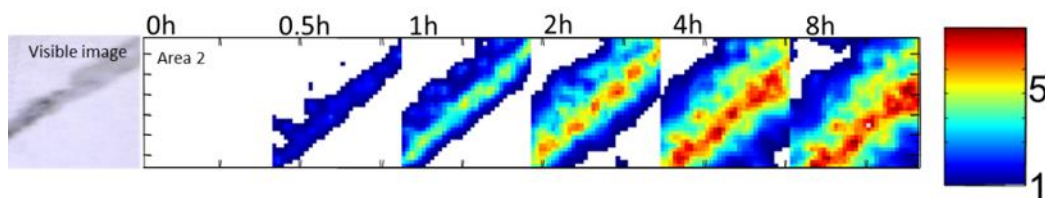


Fig. 0-4 Visible micrograph (before binding, $200 \times 200\text{ }\mu\text{m}^2$) taken of nanorods grown in different orientation type morphology from which FTIR images were acquired as a function of binding time (bottom). FTIR images of the integrated band area, $1564\text{-}1480\text{ cm}^{-1}$ (\pm STD) of area 1 after binding with 10 mM **1** in 3-MPN solution as function of time. Adapted with permission from [127]

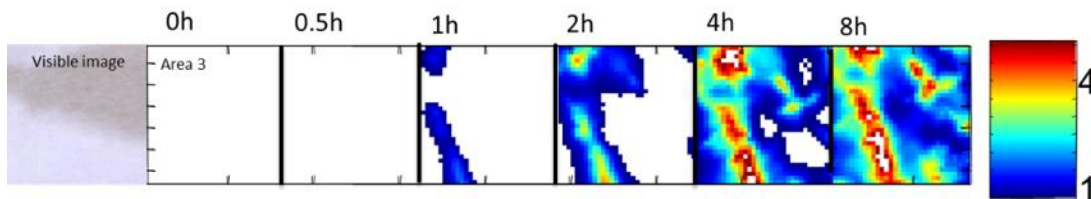


Fig. 0-5 Visible micrograph (before binding, $200 \times 200 \mu\text{m}^2$) taken of nanorods with different growth density type morphology from which FTIR images were acquired as a function of binding time (bottom). FTIR images of the integrated band area, $1564\text{-}1480 \text{ cm}^{-1}$ (\pm STD) of area 1 after binding with 10 mM **1** in 3-MPN solution as function of time. Adapted with permission from [127]

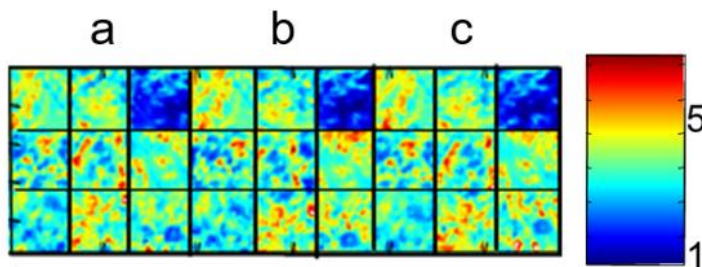


Fig. 0-6 Images of the integrated band area of $1564\text{-}1480 \text{ cm}^{-1}$ (\pm STD) of a MZO_{nano} film (a) after 22h binding with **1**, (b) after immersion of such functionalized film in 3-MPN solution at r.t for 24 h, and (c) after immersion of such functionalized film in 3-MPN solution at 40°C for 24 h

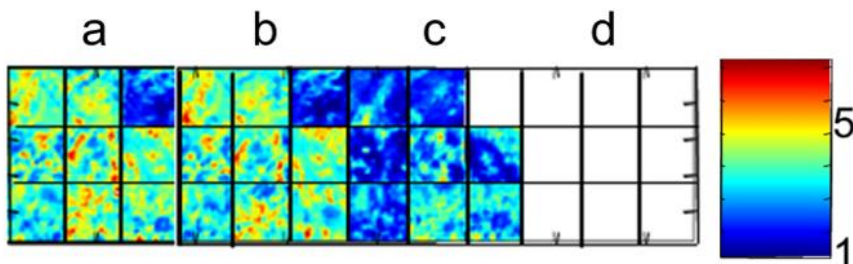


Fig. 0-7 Images of the integrated band area of $1564\text{-}1480 \text{ cm}^{-1}$ (\pm STD) of a MZO_{nano} film (a) after 22h binding with **1** and (b) after immersion of such functionalized film in ethanol solution at r.t for 24 h, (c) after immersion of such functionalized film in ethanol solution at 40°C for 4 h, and (d) after immersion of such functionalized film in ethanol solution at 40°C for 24 h

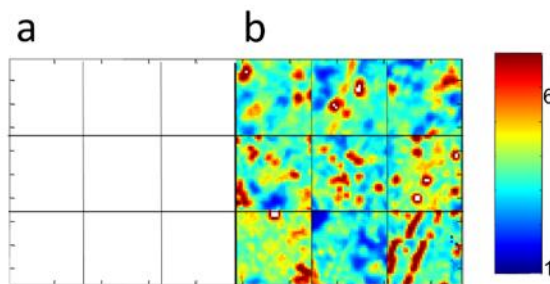


Fig. 0-8 Images of the integrated band area of $1564\text{-}1480 \text{ cm}^{-1}$ (\pm STD) of a functionalized MZO_{nano} film (a) after immersed in ethanol solution at 40°C for 24 h, (b) after 22h binding with 10 mM **1** (solvent: 3-MPN)

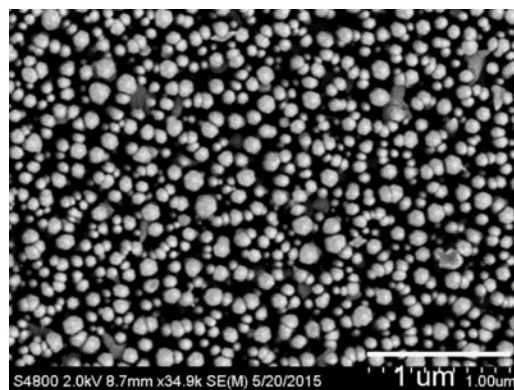


Fig. 0-9 FESEM image of MZO_{nano} film after immersing in EtOH at 40 °C for 24 h

Droplet method



Fig. 0-10 Droplet method

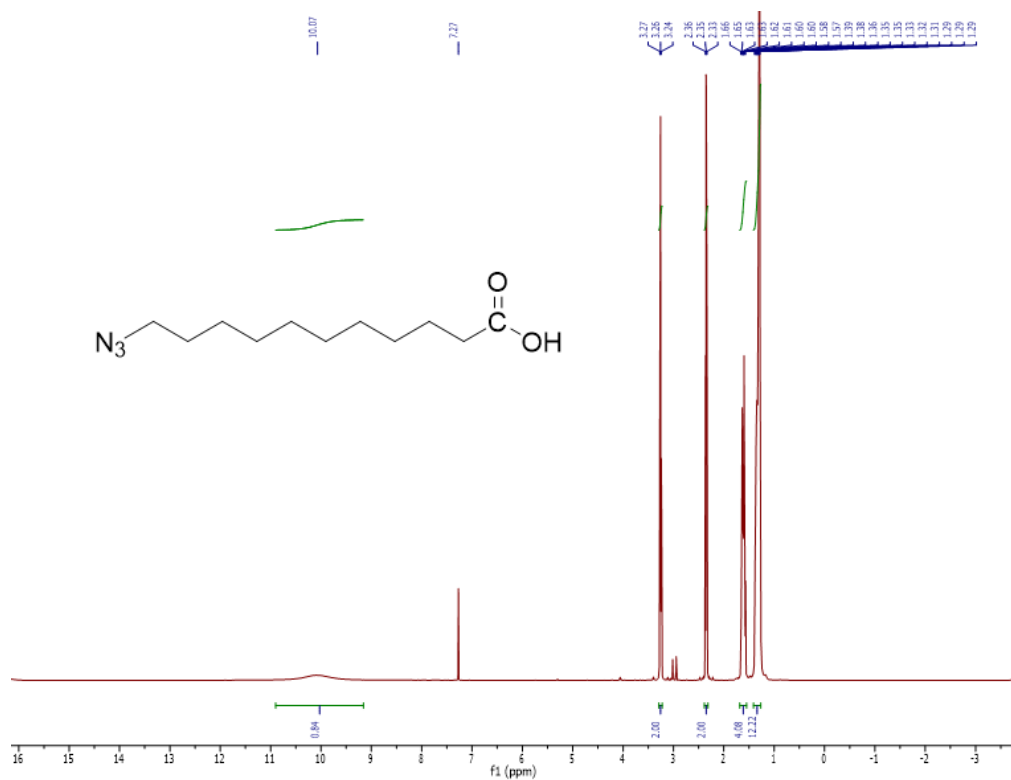


Fig. 0-11 ¹H NMR of **1** in CDCl₃

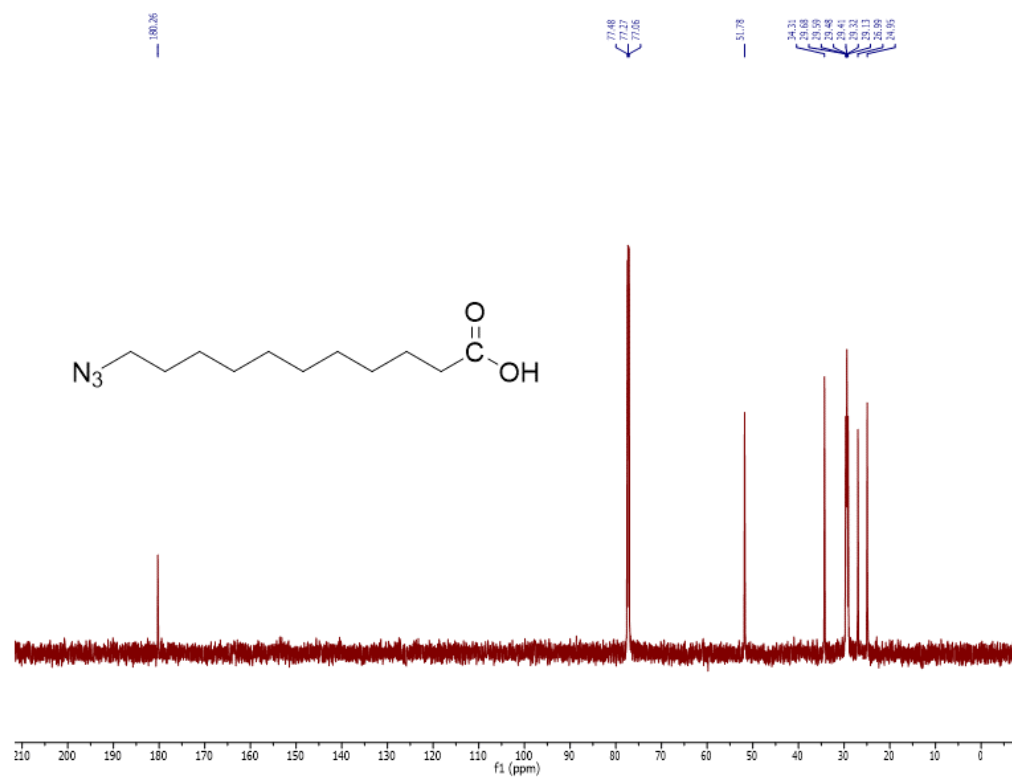


Fig. 0-12 ¹³C NMR of **1** in CDCl₃

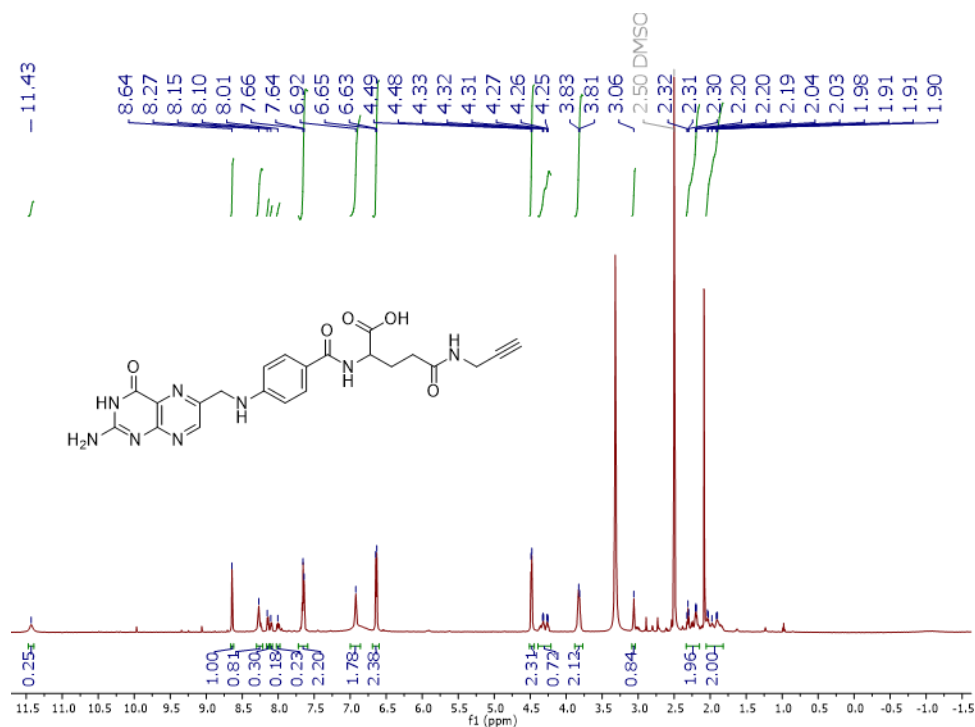


Fig. 0-13 ¹H NMR of II in DMSO-d₆

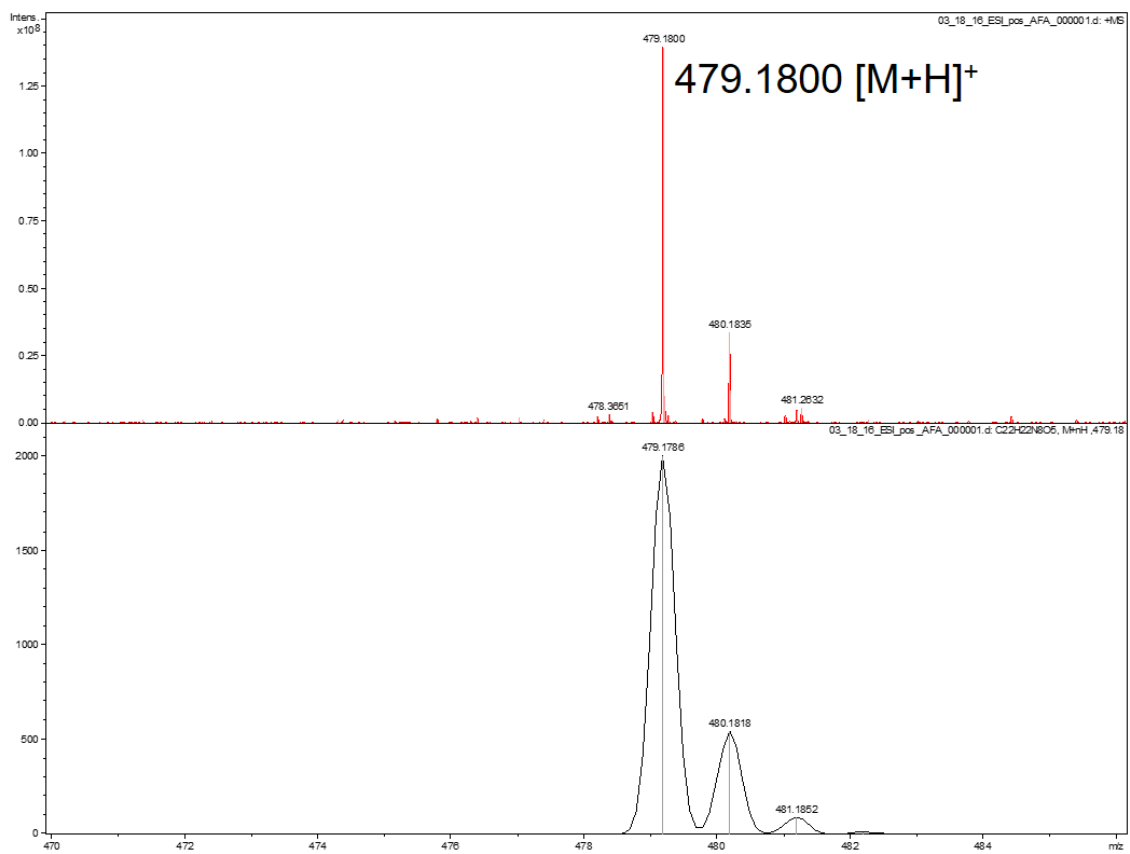


Fig. 0-14 ESI-MS spectra (top) and simulated (bottom) of II

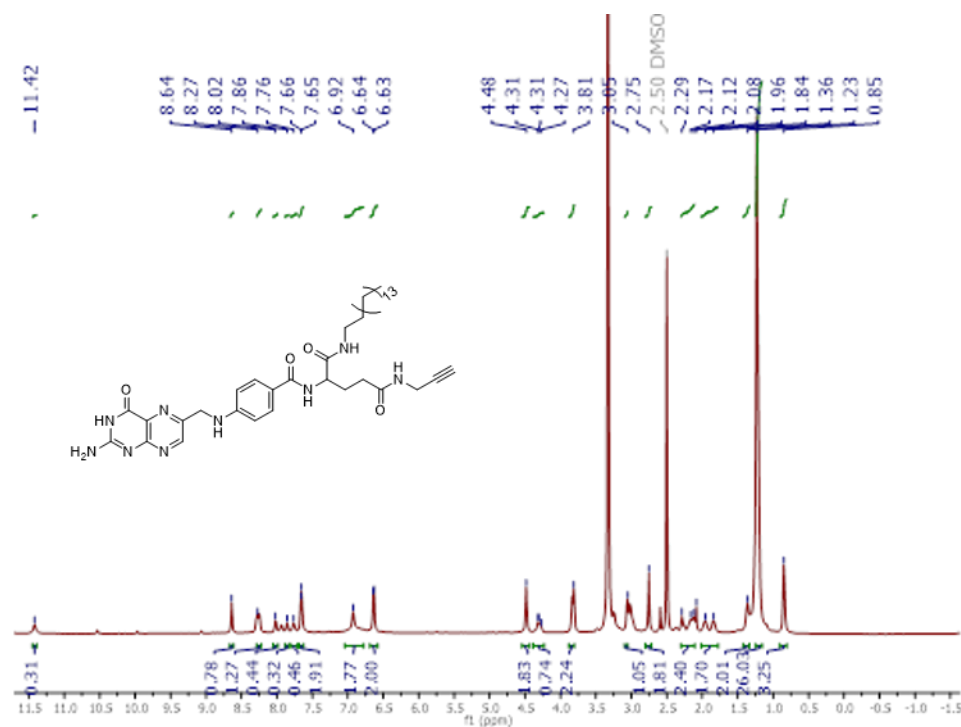


Fig. 0-15 ¹H NMR of **III** in DMSO-d₆

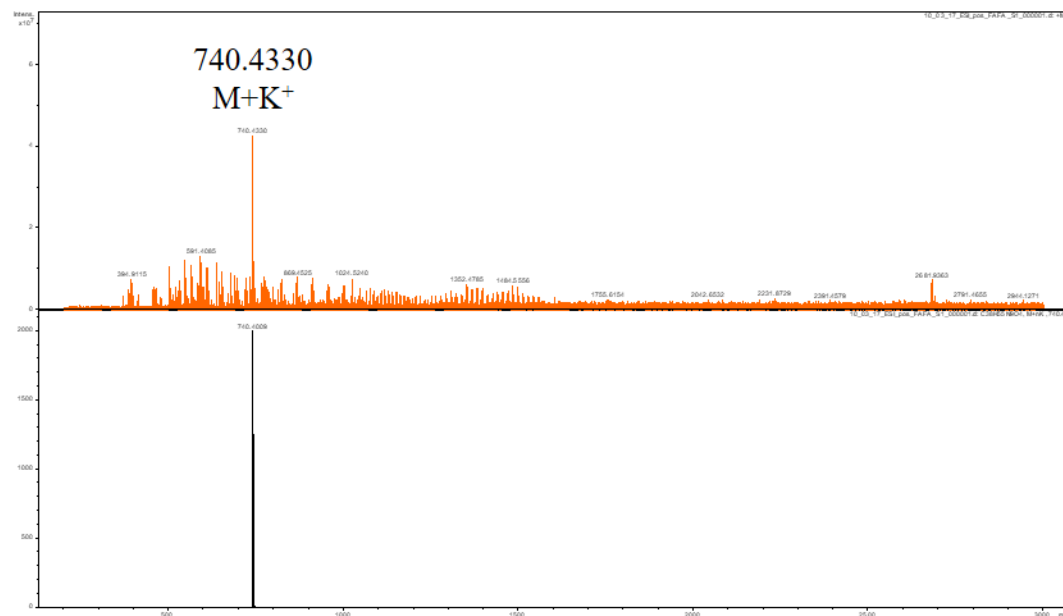


Fig. 0-16 ESI-MS spectra (top) and simulated (bottom) of **III**

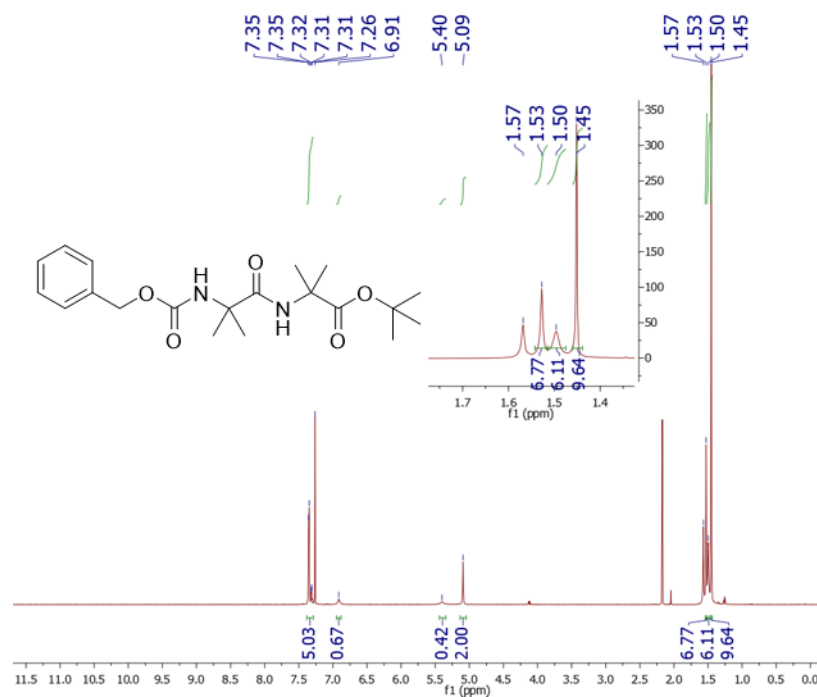


Fig. 0-17 ¹H NMR of **2** in CDCl₃

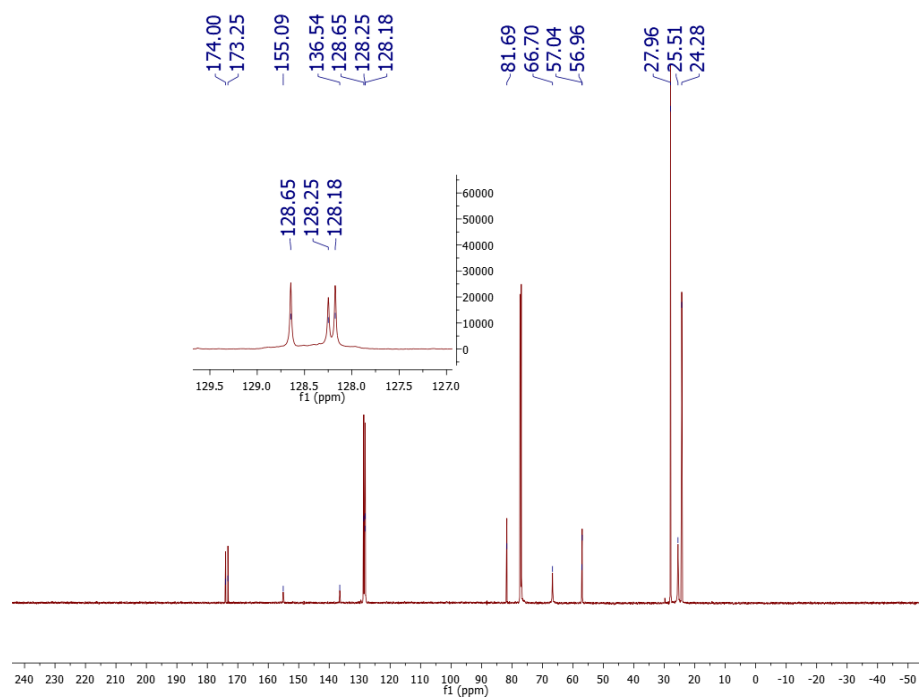


Fig. 0-18 ¹³C NMR of **2** in CDCl₃

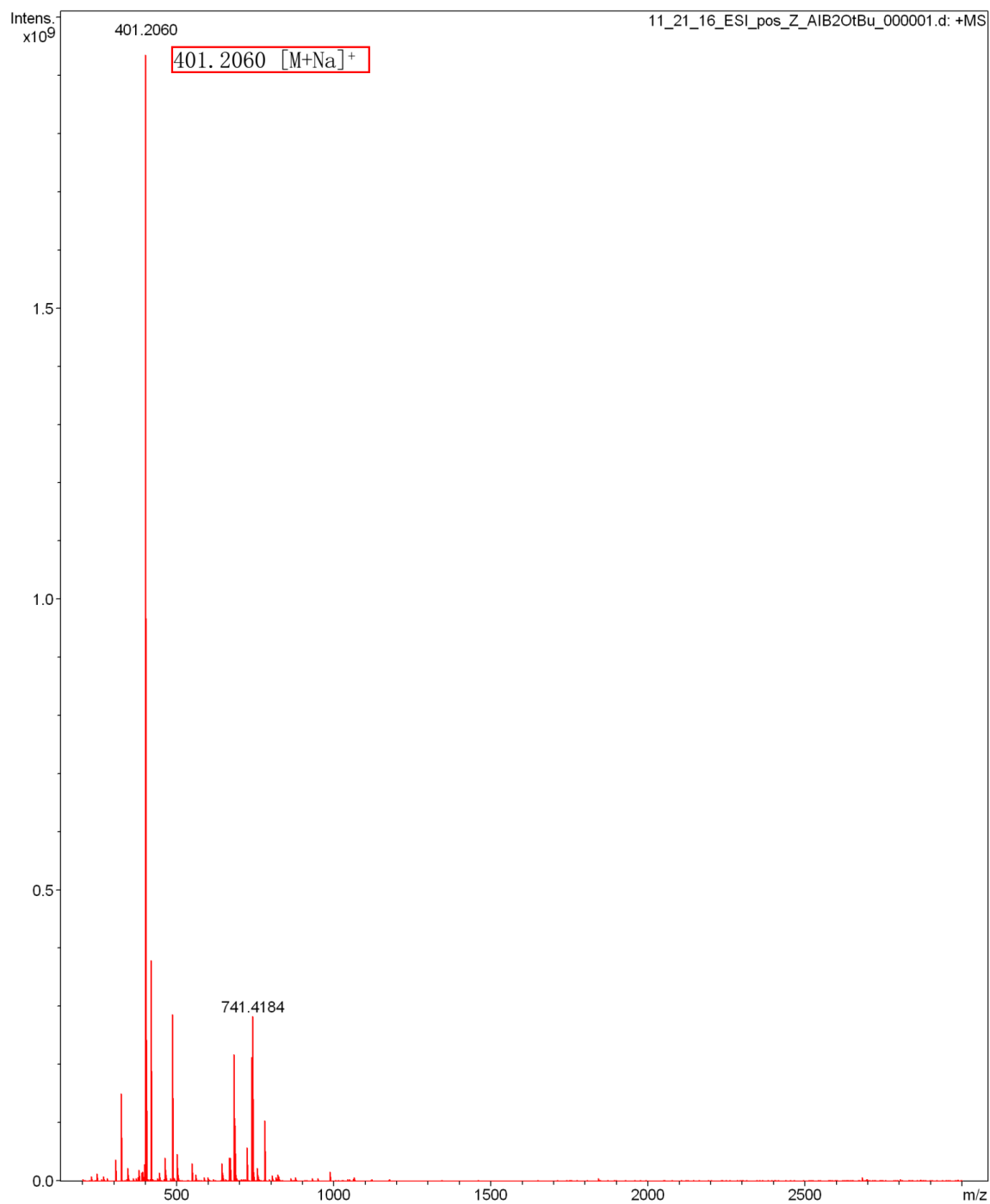


Fig. 0-19 ESI-MS spectra of **2**

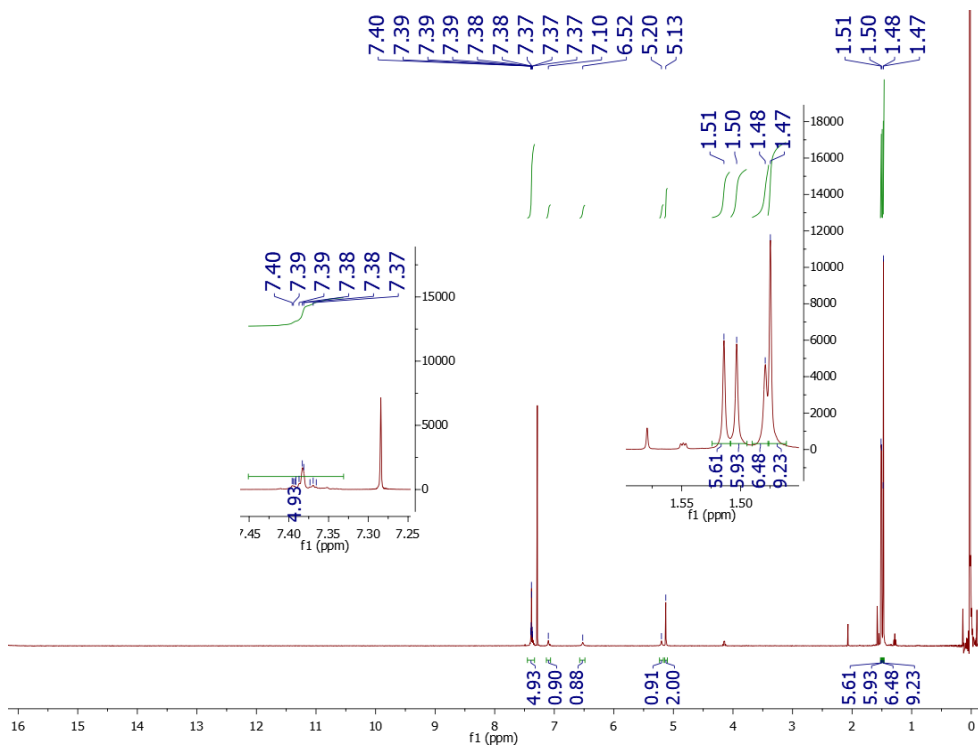


Fig. 0-20 ^1H NMR of **3** in CDCl_3

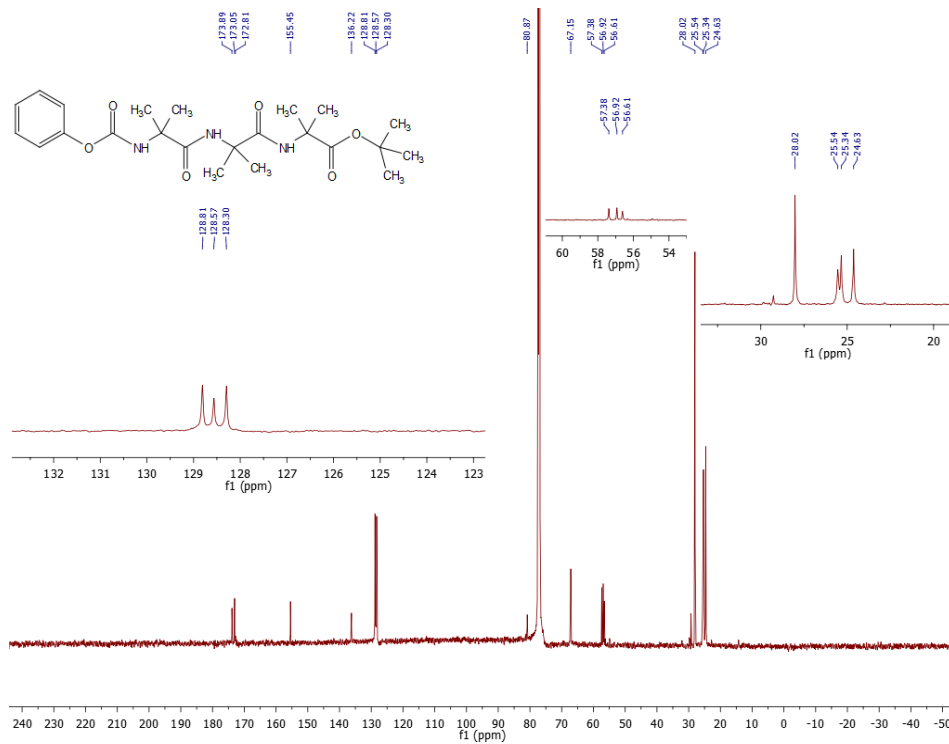


Fig. 0-21 ^{13}C NMR of **3** in CDCl_3

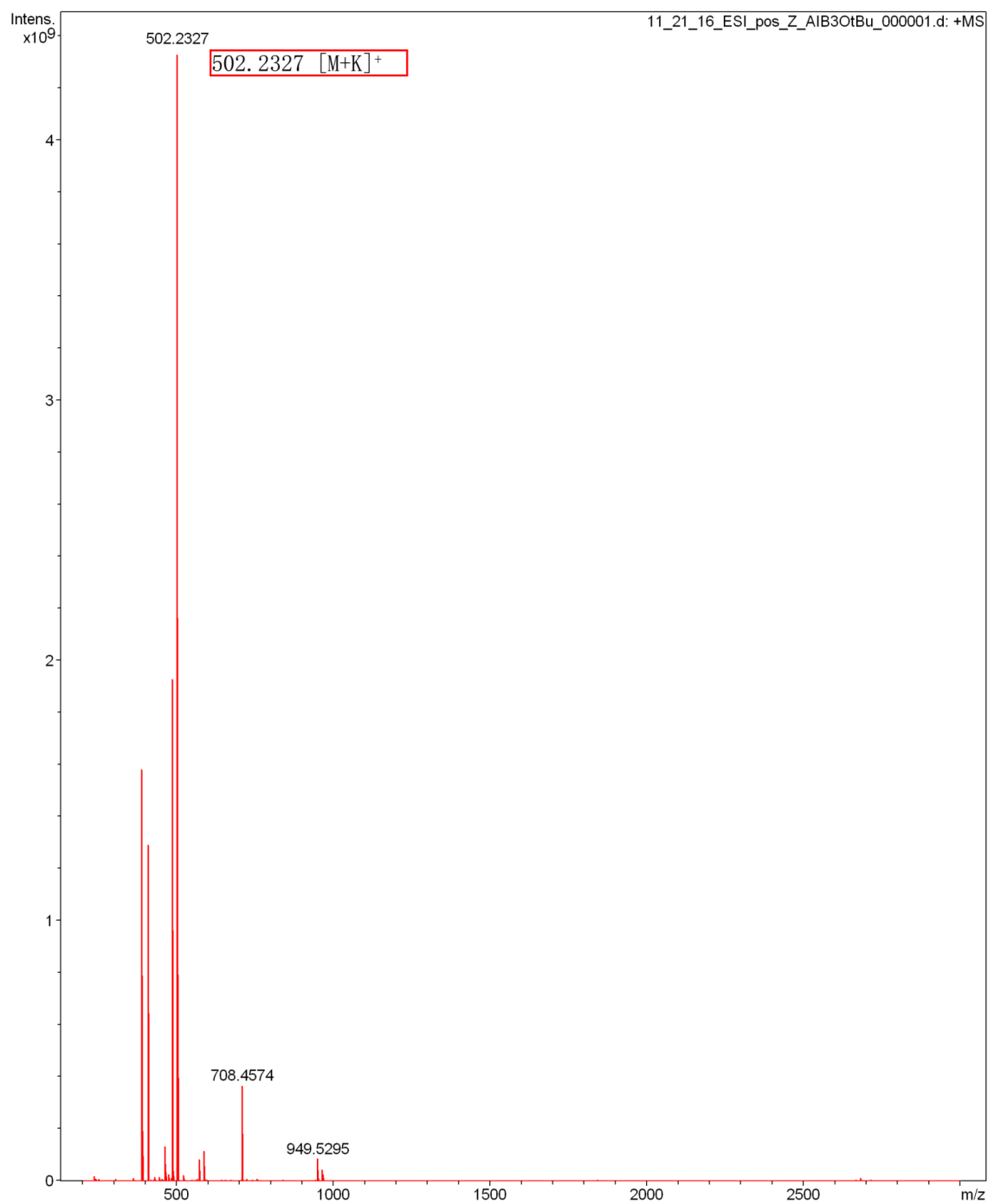
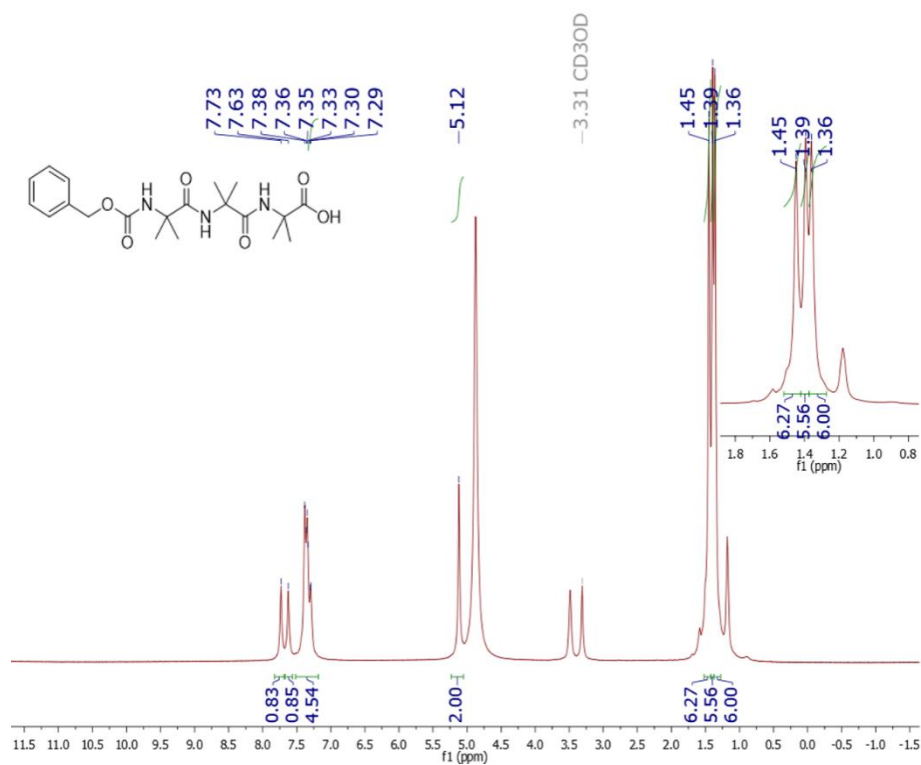
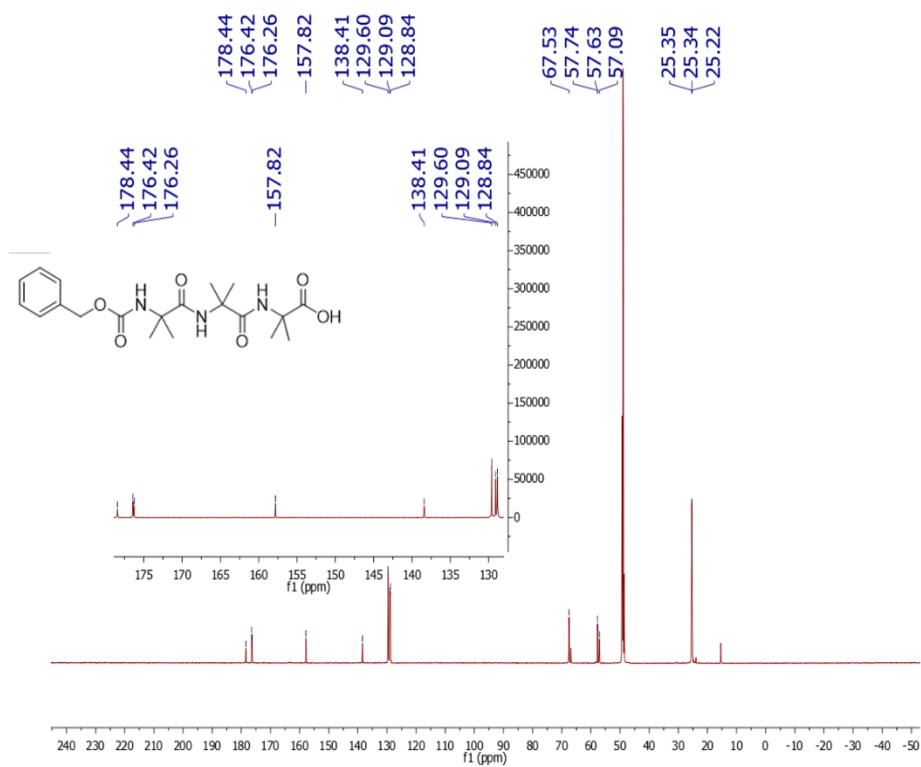


Fig. 0-22 ESI-MS spectra of **3**

Fig. 0-23 ¹H NMR of 4 in CD₃ODFig. 0-24 ¹³C NMR of 4 in CD₃OD

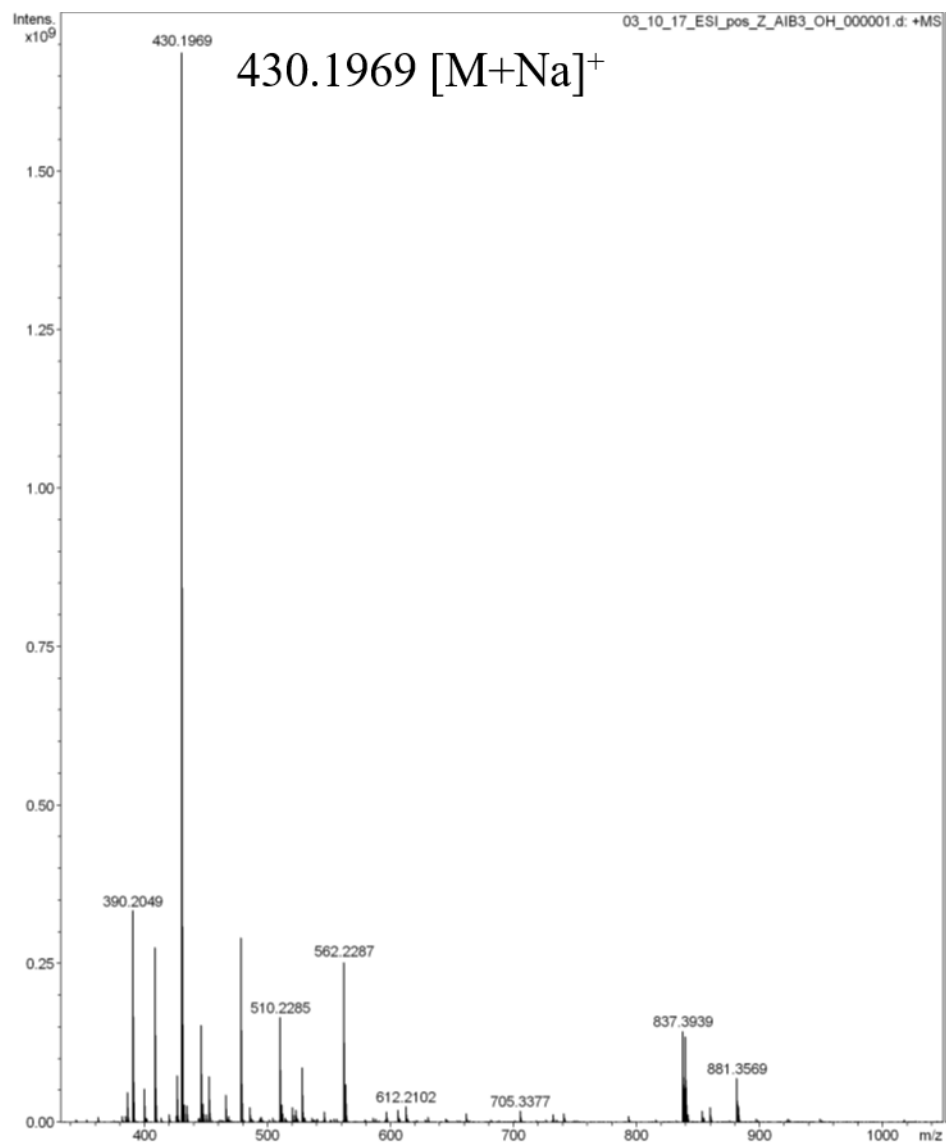


Fig. 0-25 ESI-MS spectra of **4**

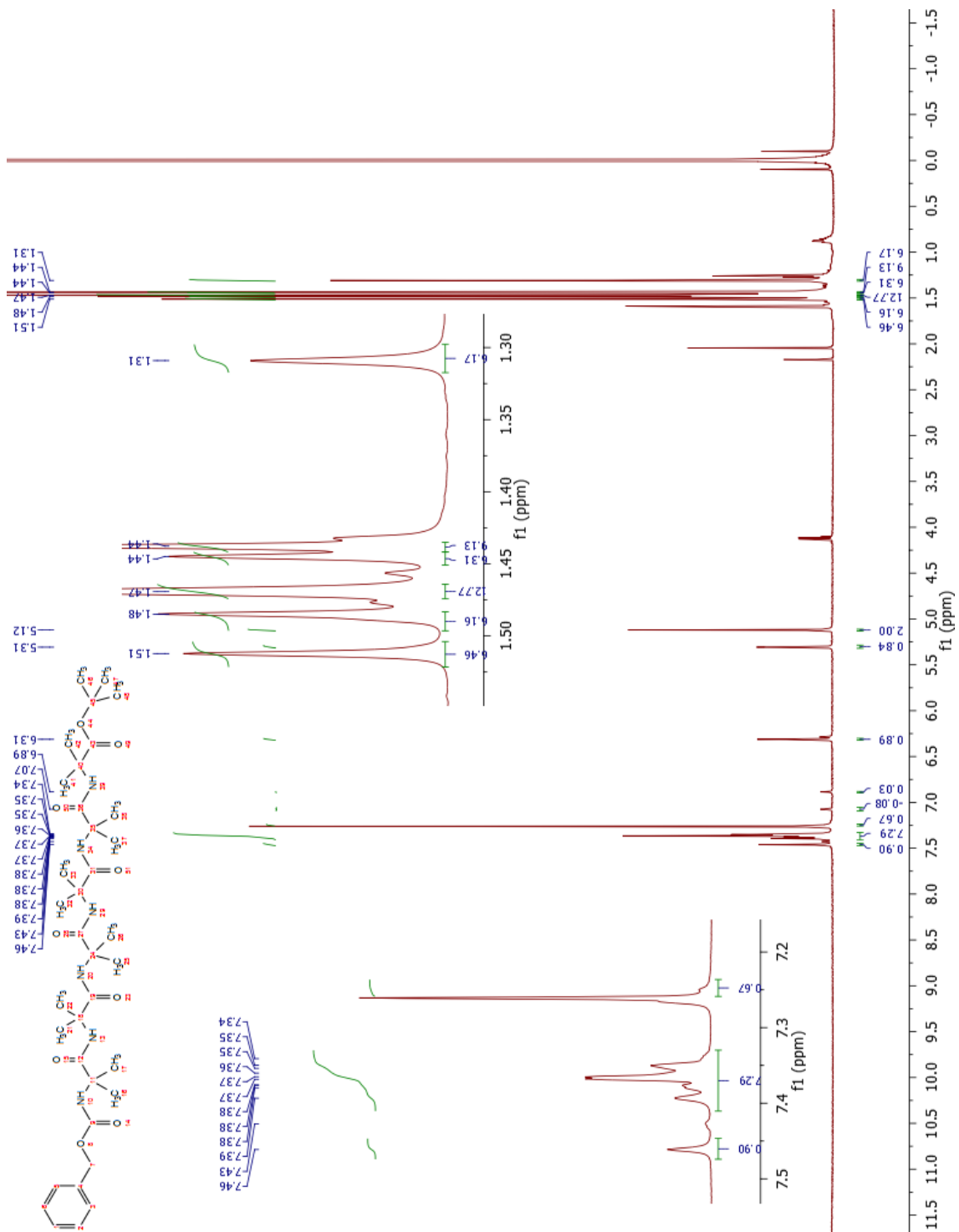


Fig. 0-26 ^1H NMR of **5** in CDCl_3

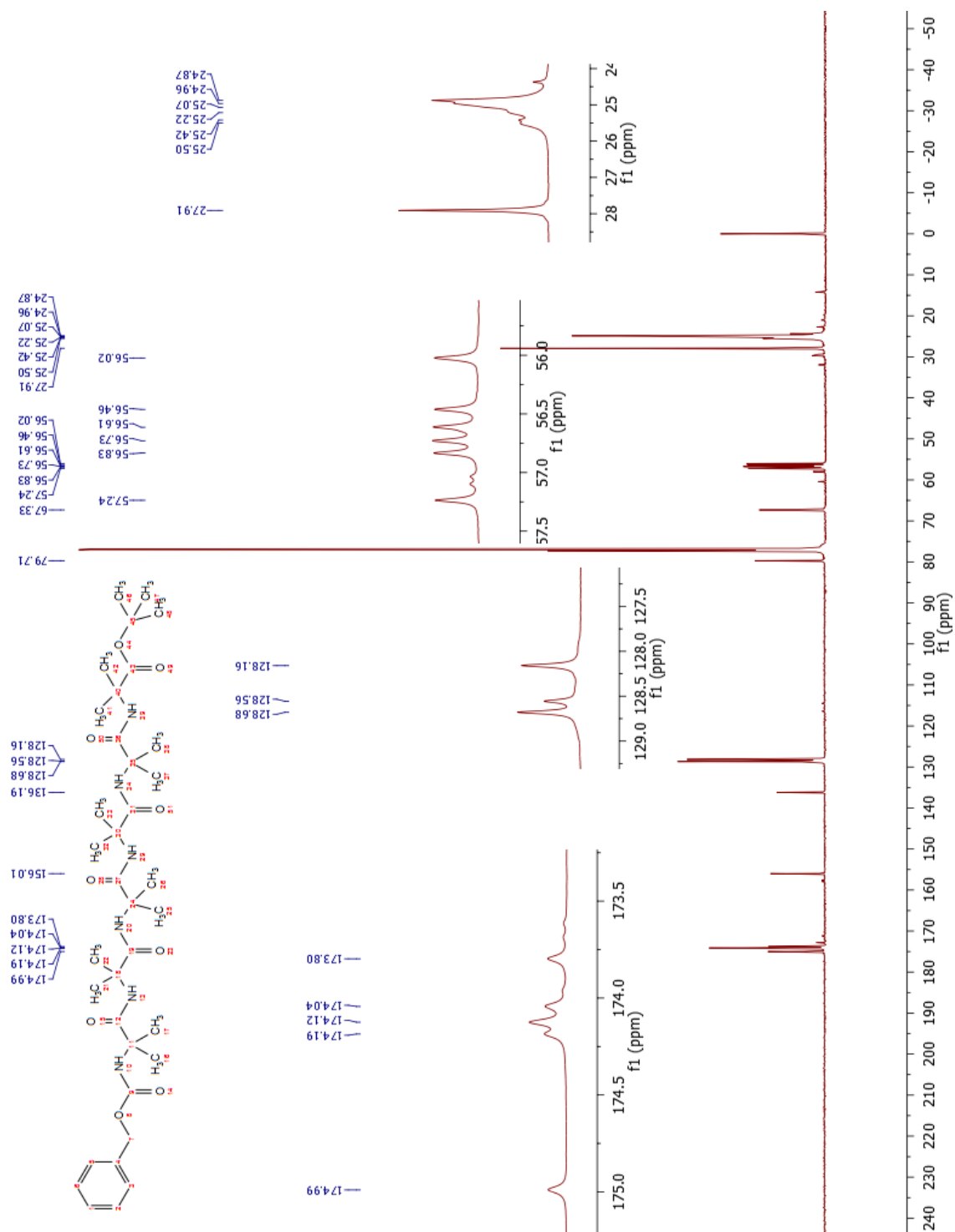


Fig. 0-27 ¹³C NMR of **5** in CDCl₃

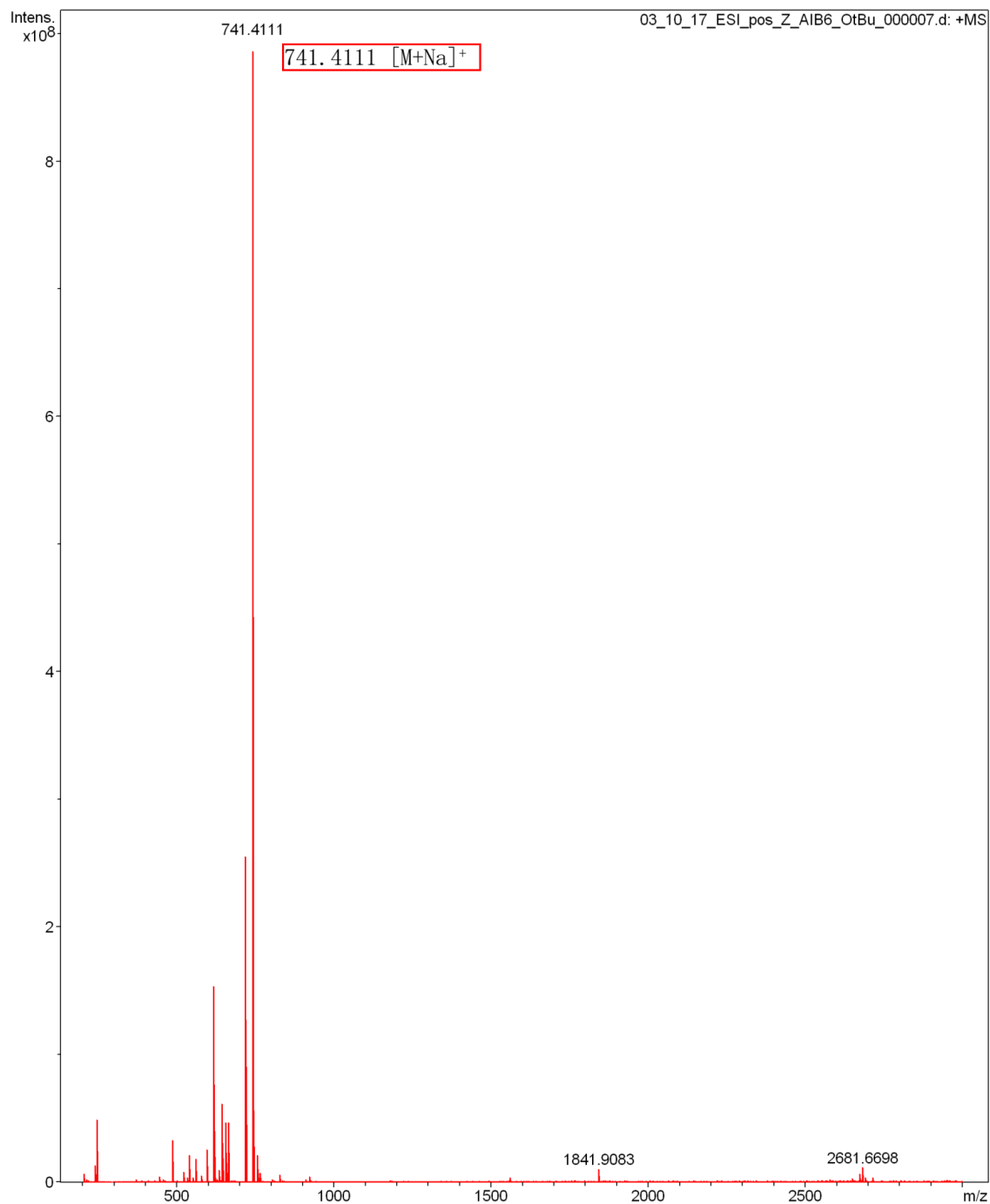
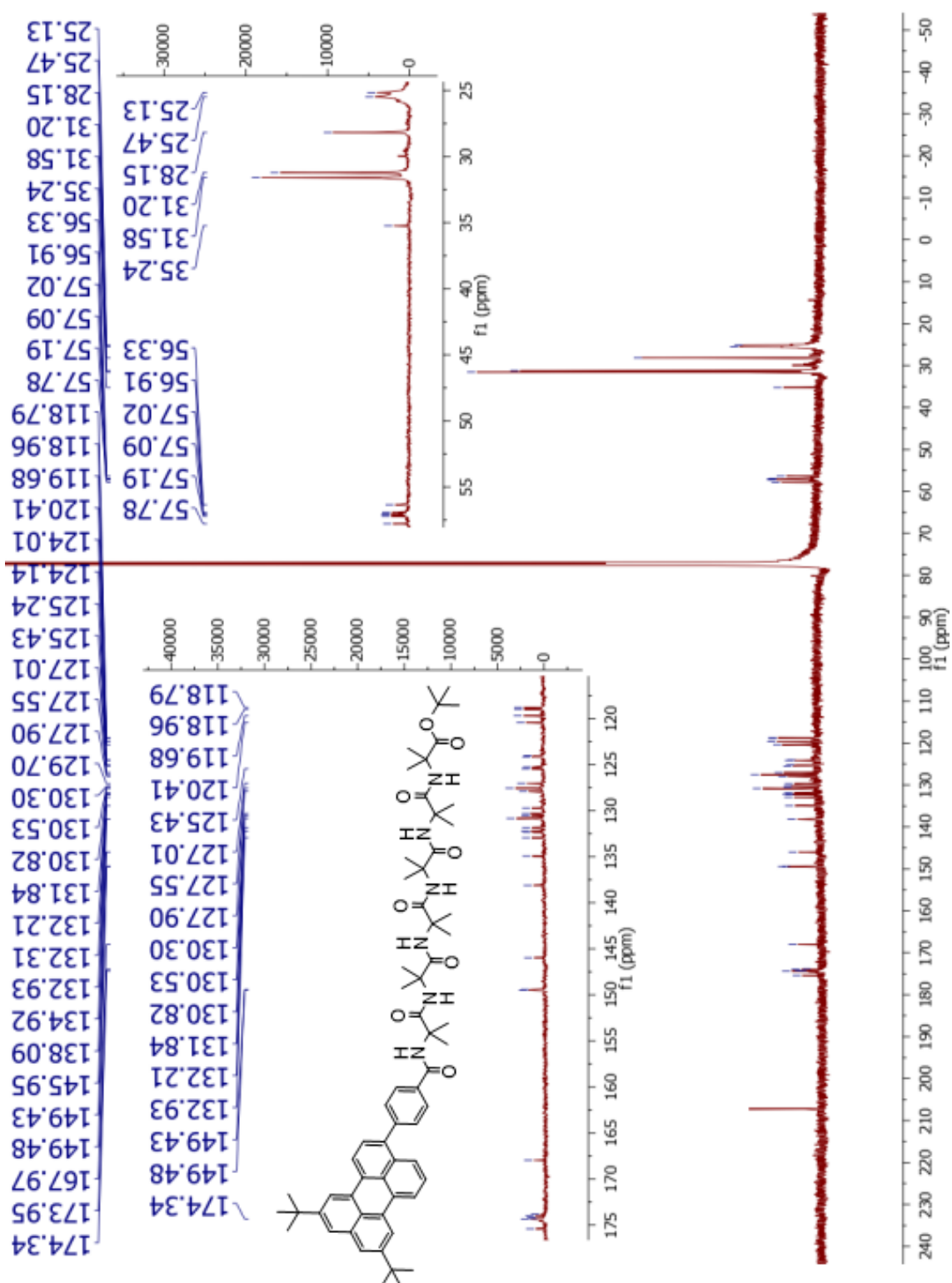


Fig. 0-28 ESI-MS spectra of **5**

Fig. 0-30 ^{13}C NMR of **6** in CDCl_3

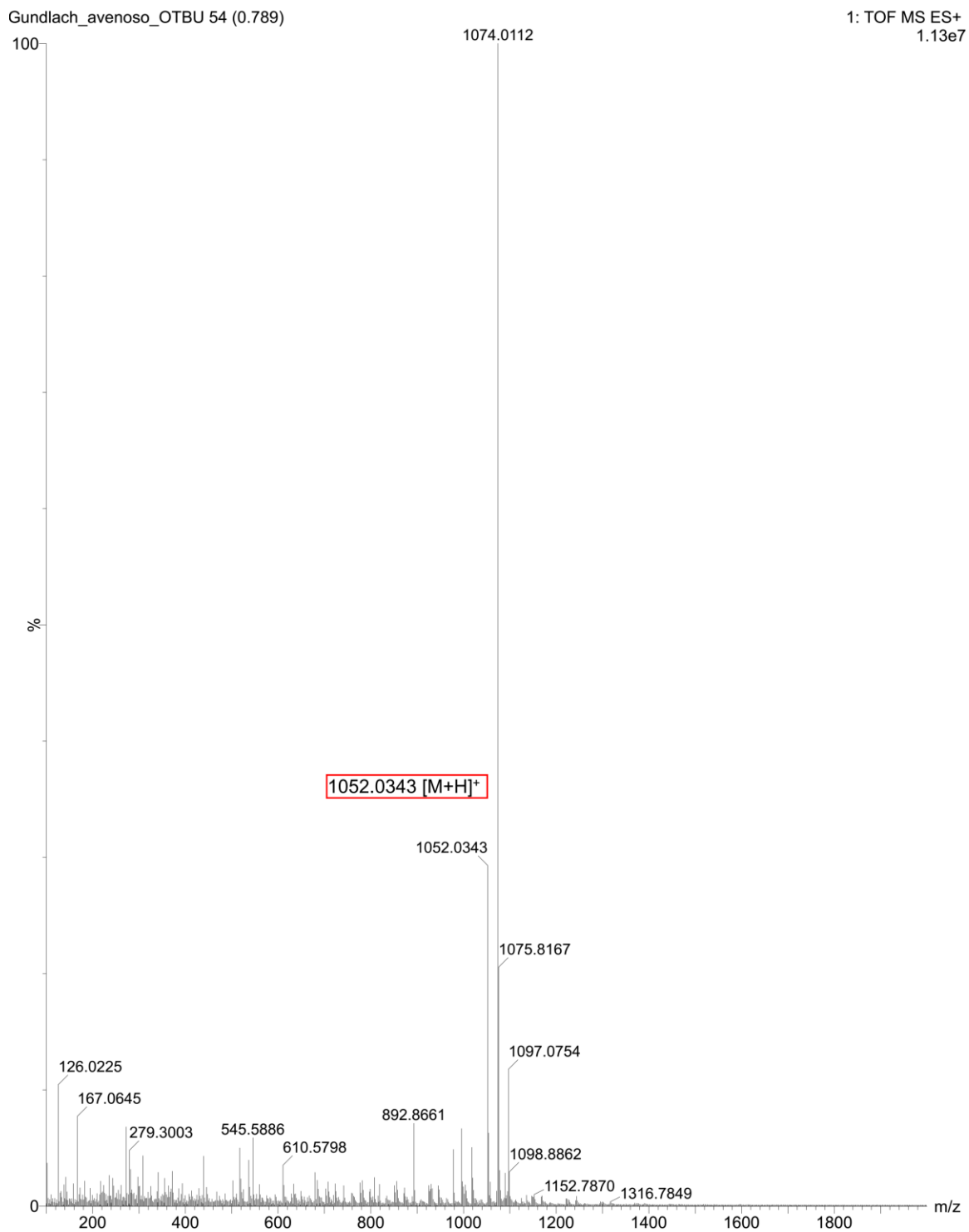


Fig. 0-31 ESI-MS spectra of **6**

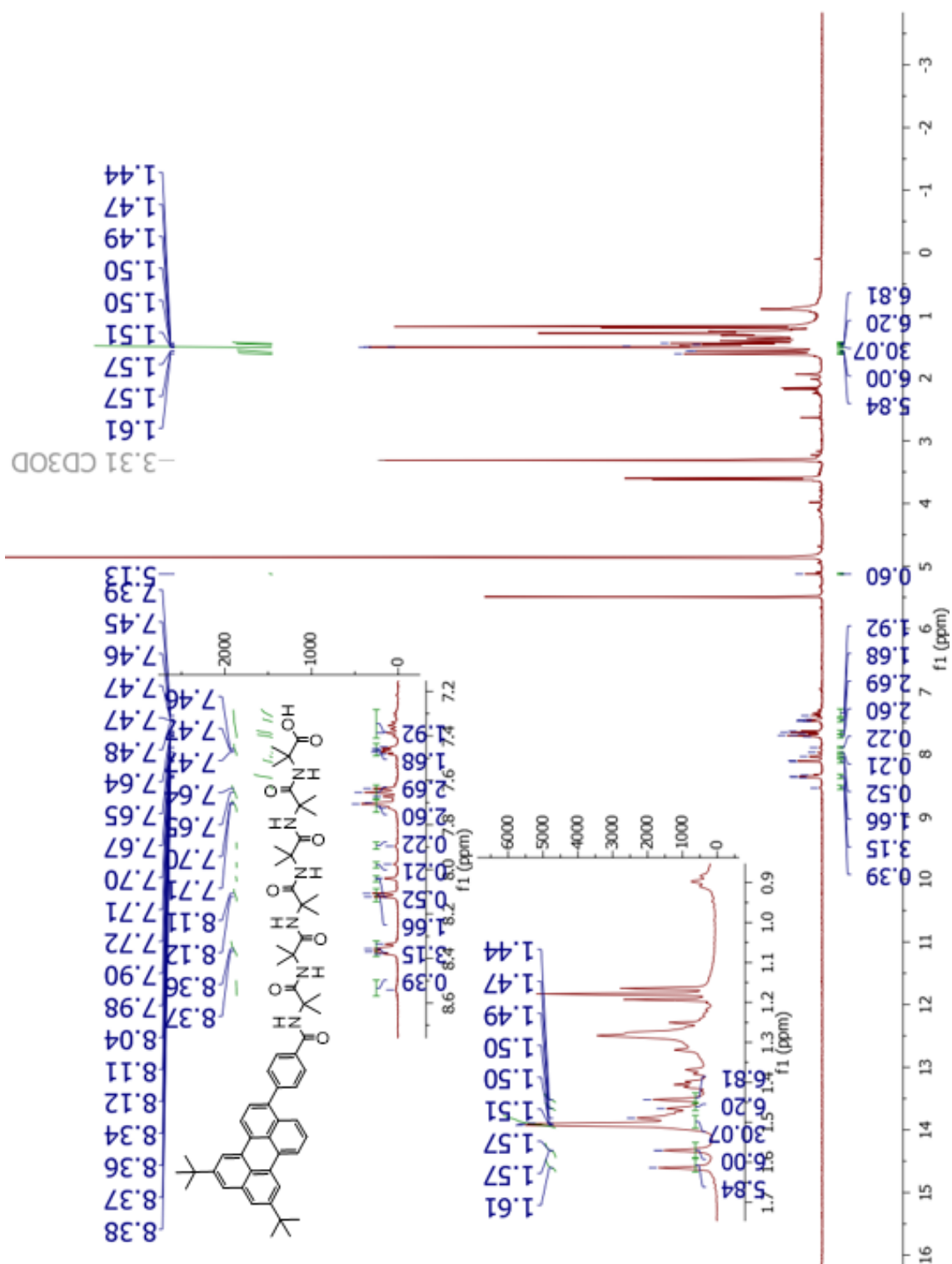


Fig. 0-32 ¹H NMR of 7 in CD₃OD

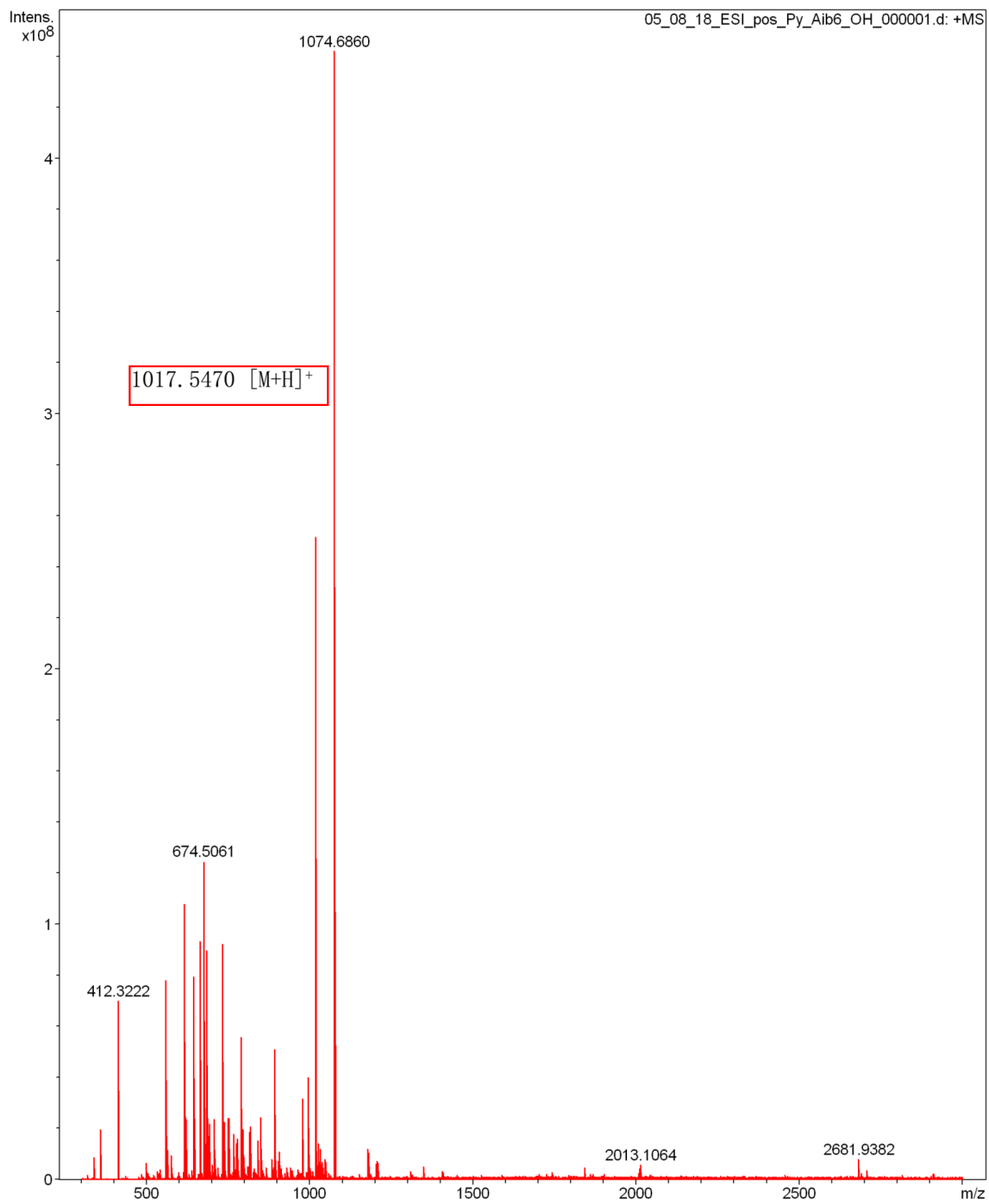


Fig. 0-33 ESI-MS spectra of **7**

Fig. 0-34 ^1H NMR of **8** in DMSO- d_6

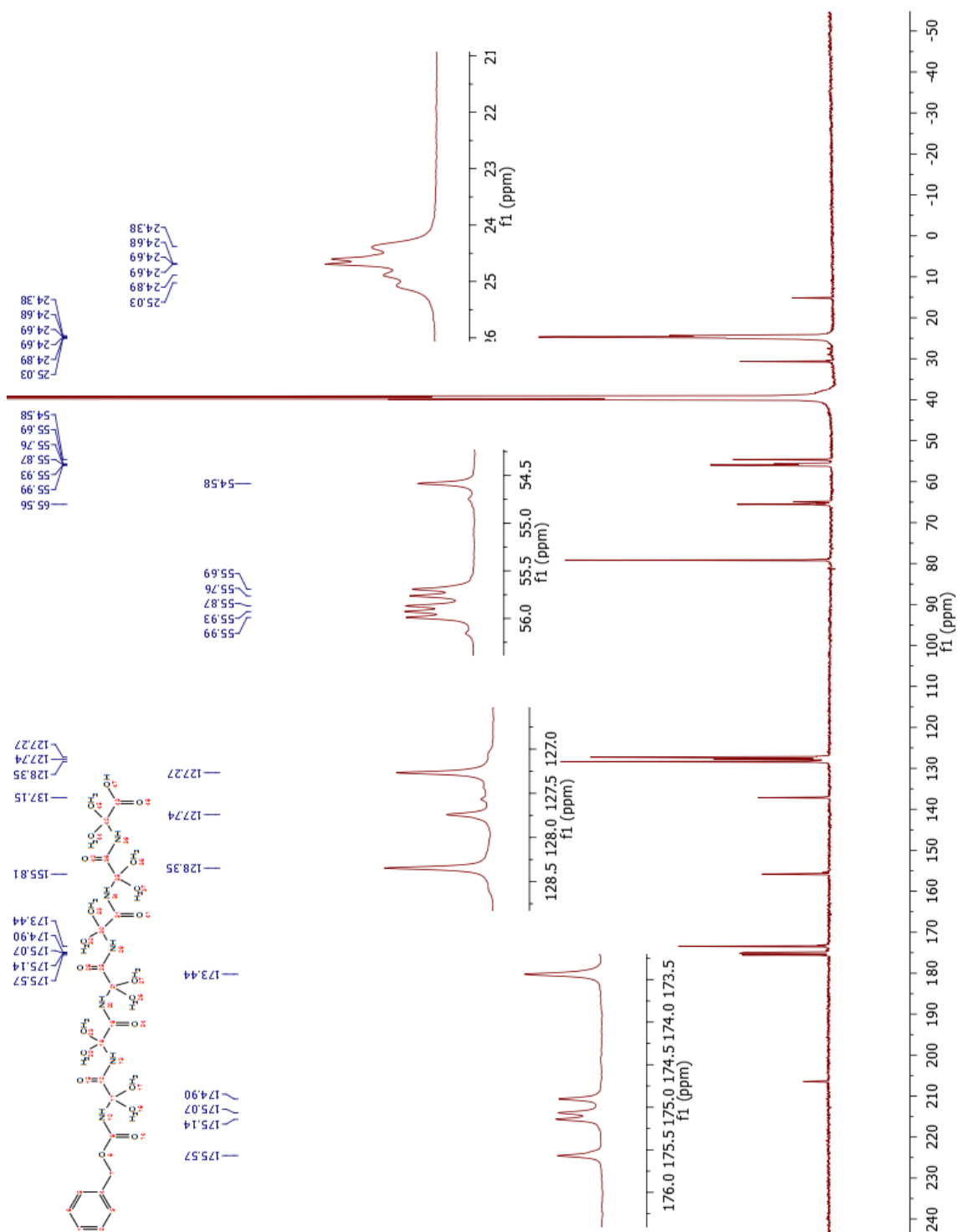


Fig. 0-35 ¹³C NMR of **8** in DMSO-d₆

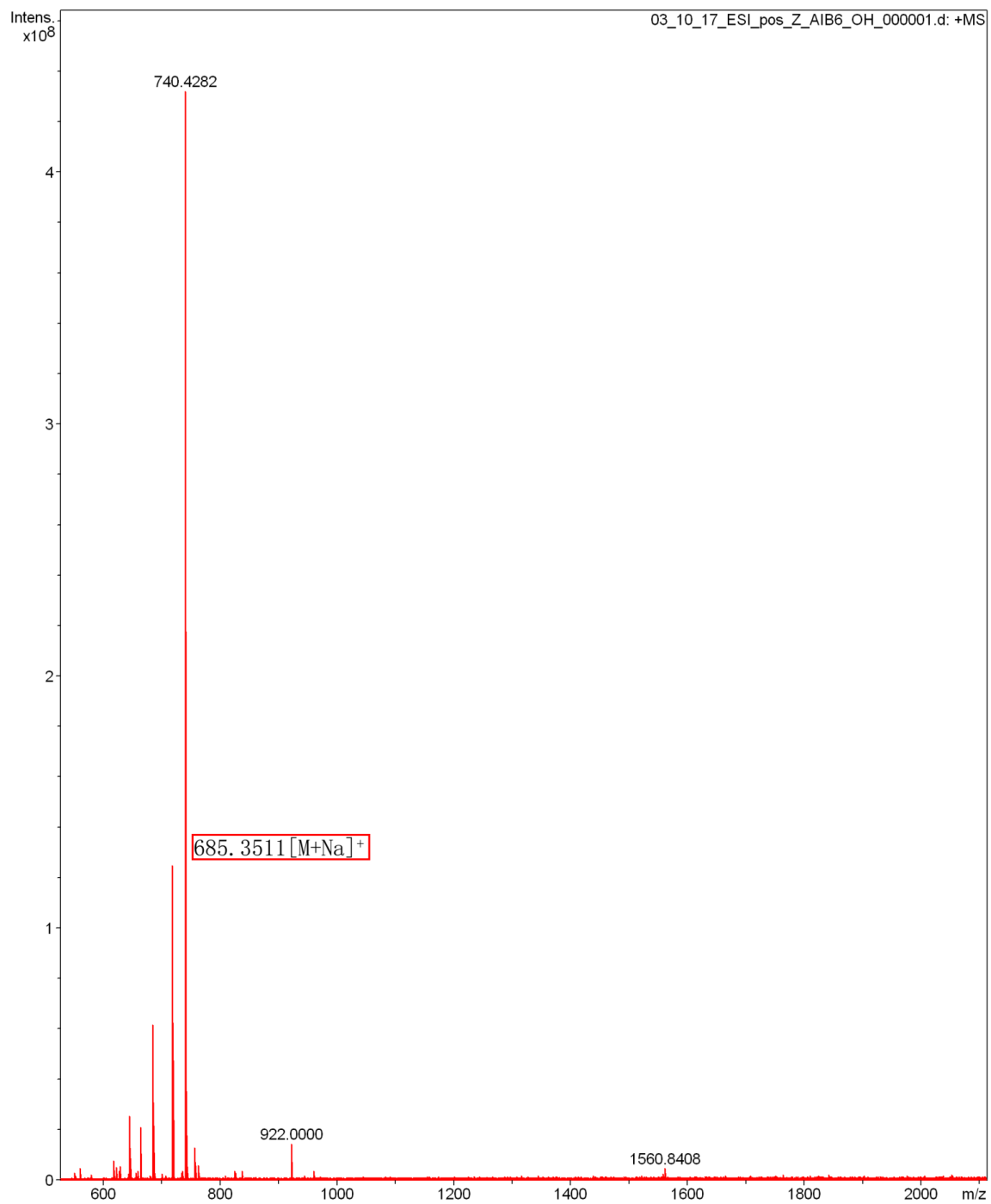


Fig. 0-36 ESI-MS spectra of **8**

Fig. 0-37 ^1H NMR of **9** in CDCl_3

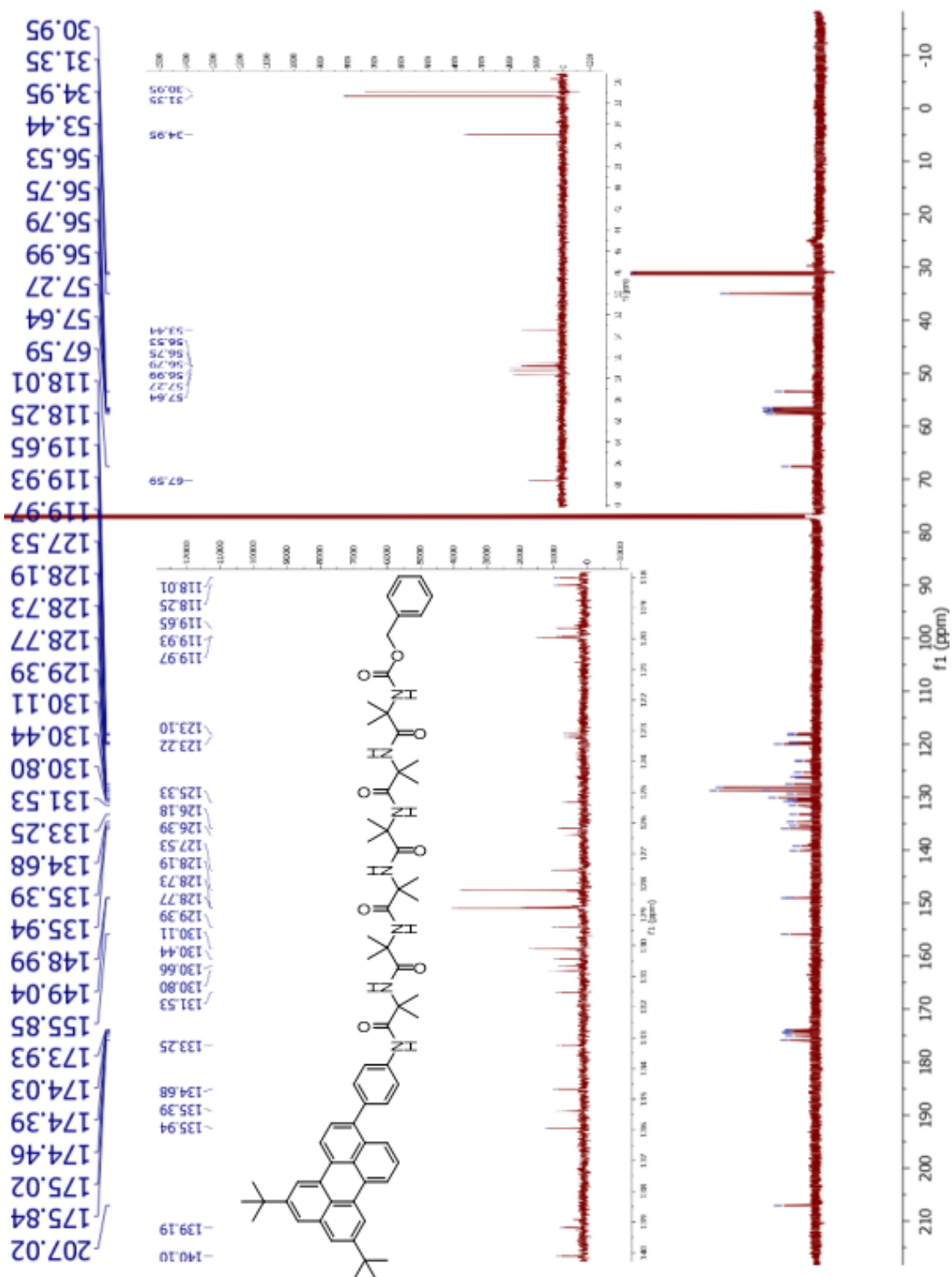


Fig. 0-38 ^{13}C NMR of 9 in CDCl_3

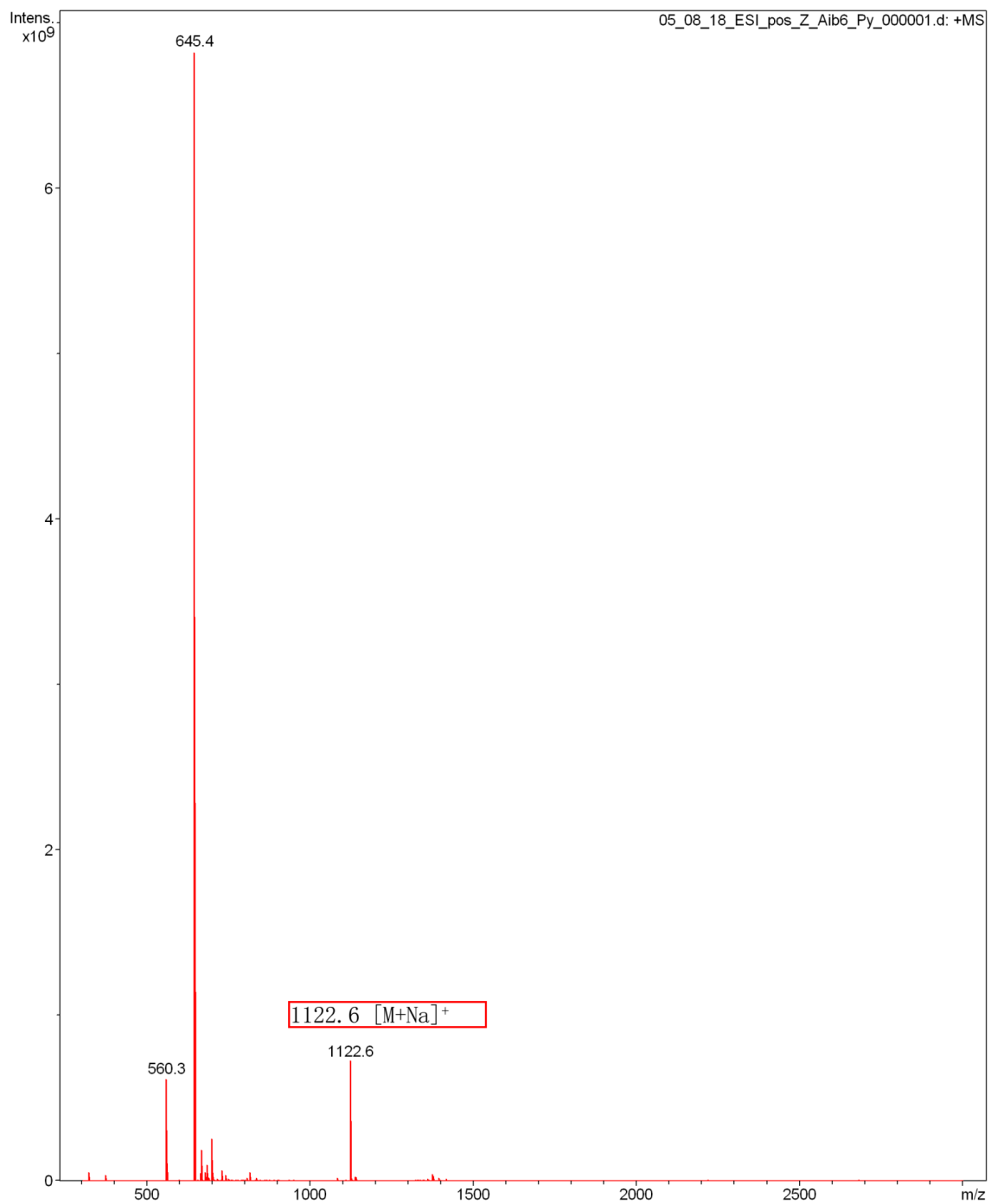


Fig. 0-39 ESI-MS spectra of **9**

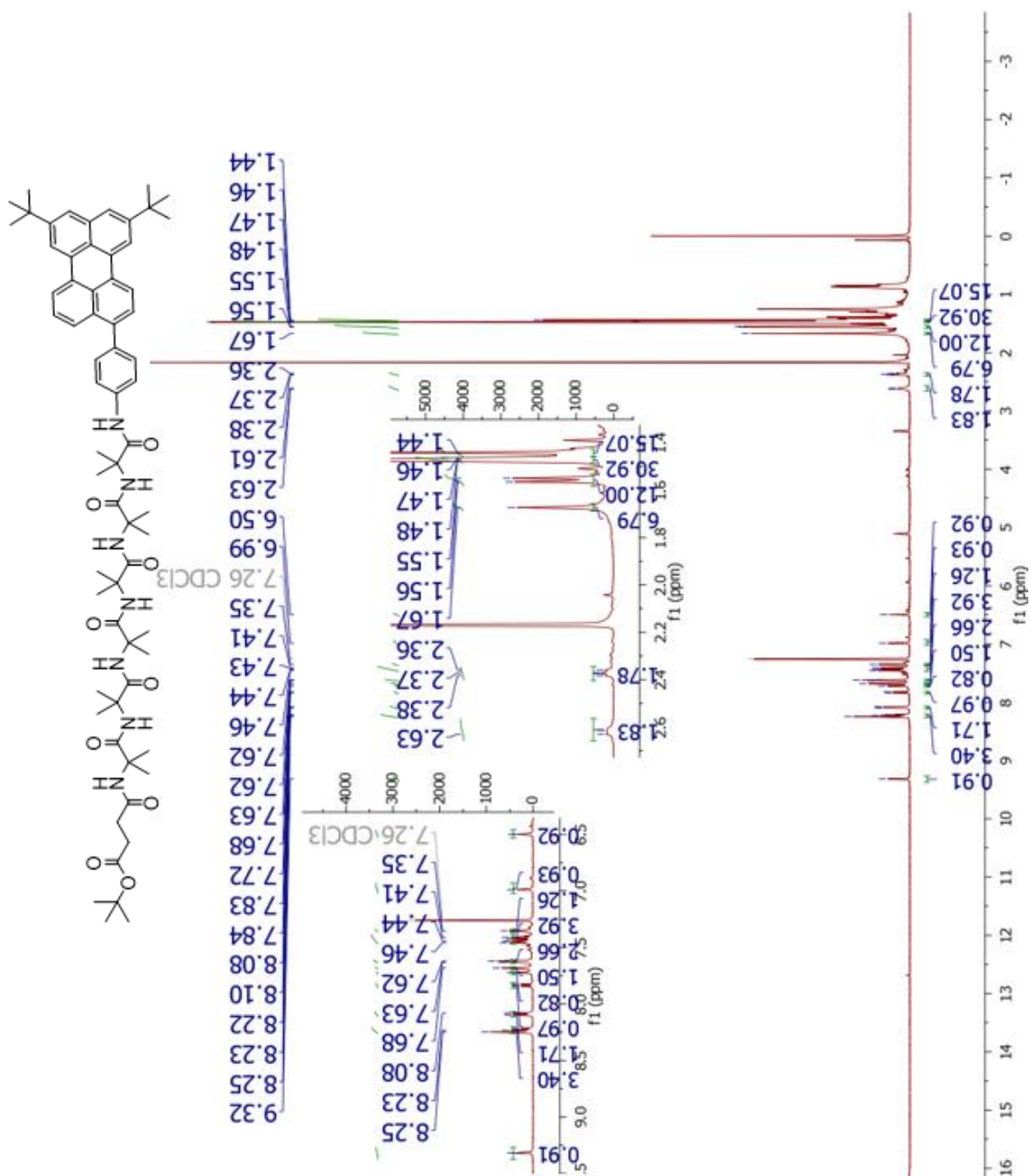


Fig. 0-40 ¹H NMR of **10** in CDCl₃

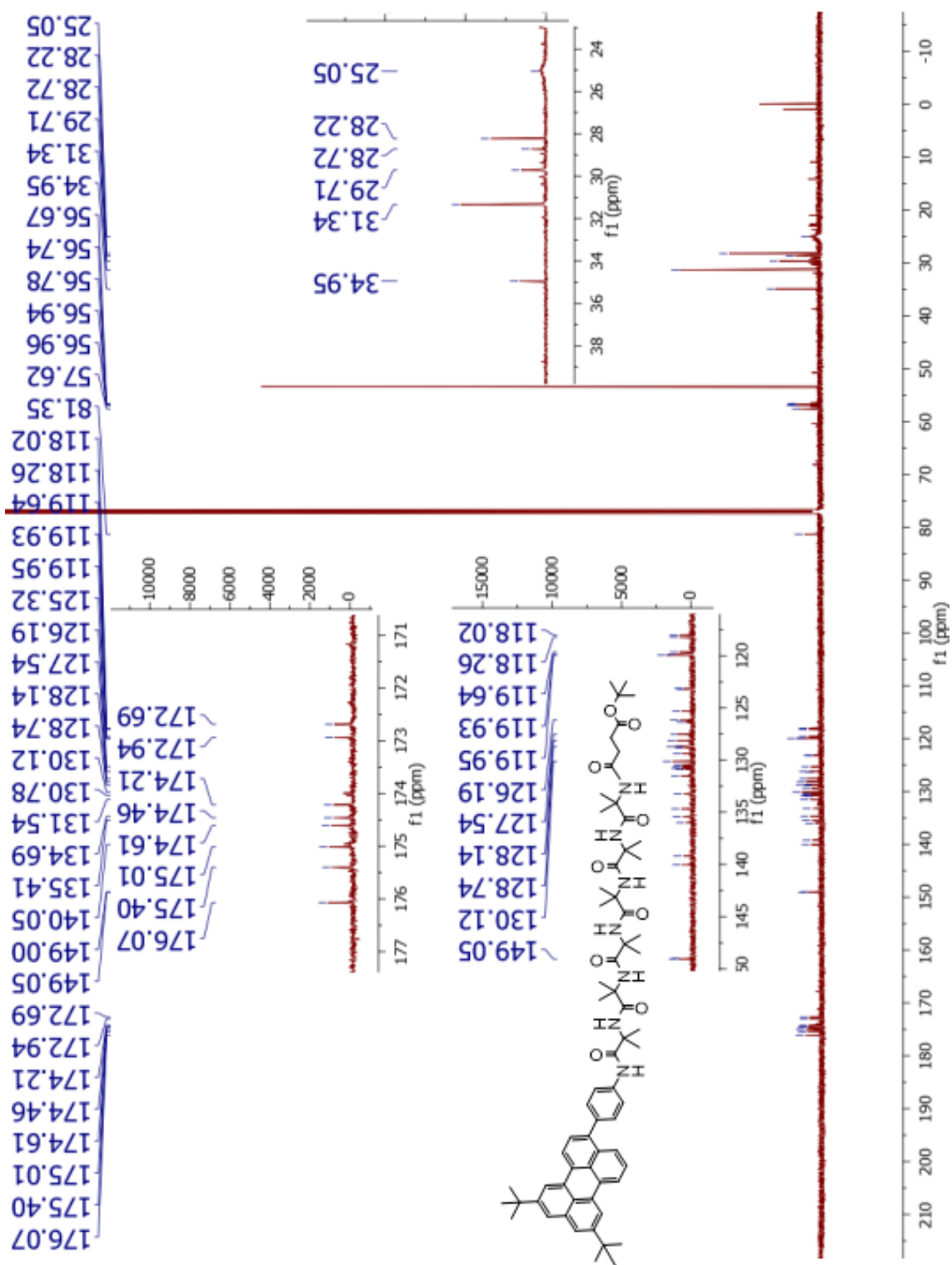


Fig. 0-41 ^{13}C NMR of **10** in CDCl₃

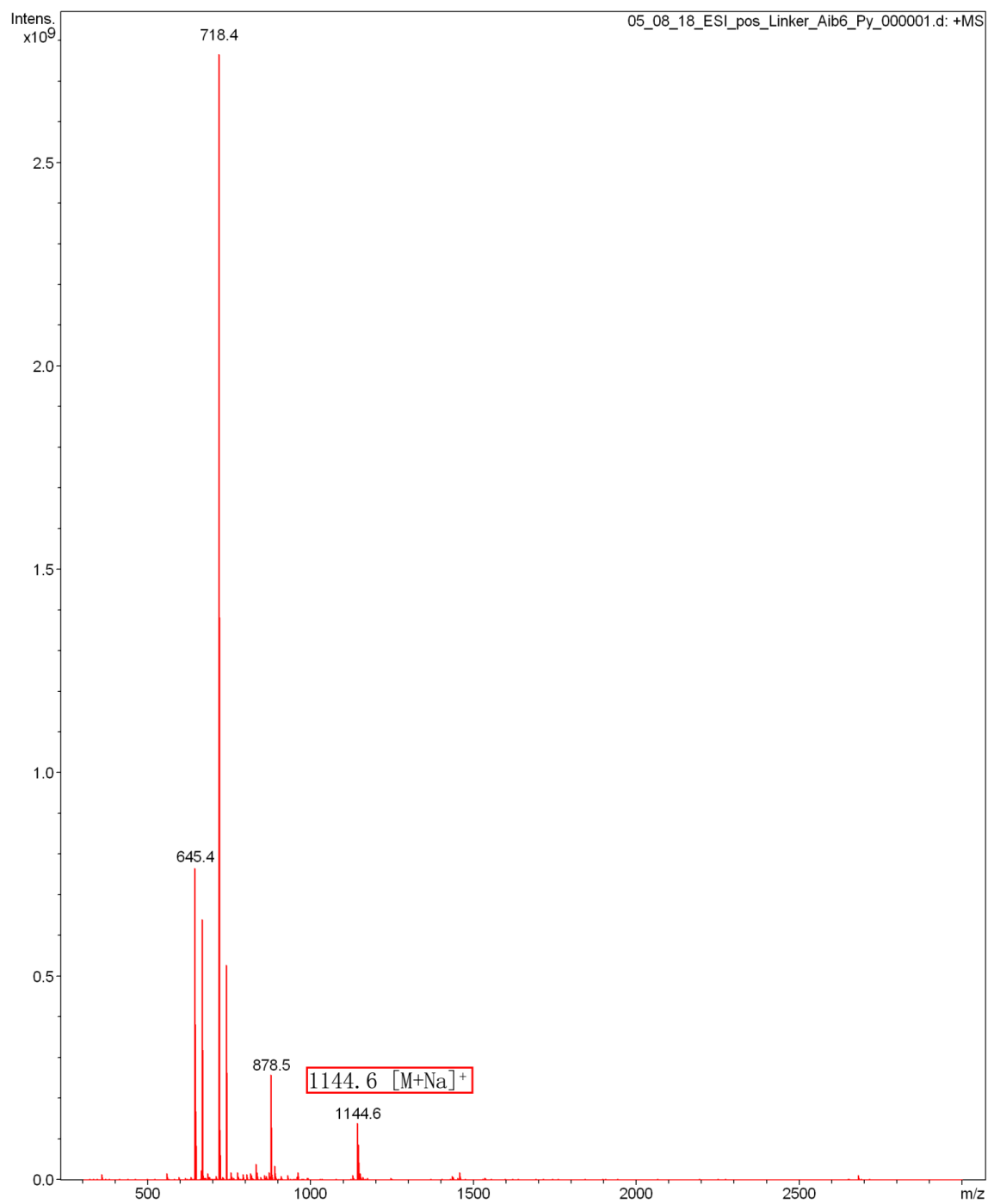


Fig. 0-42 ESI-MS spectra of **10**

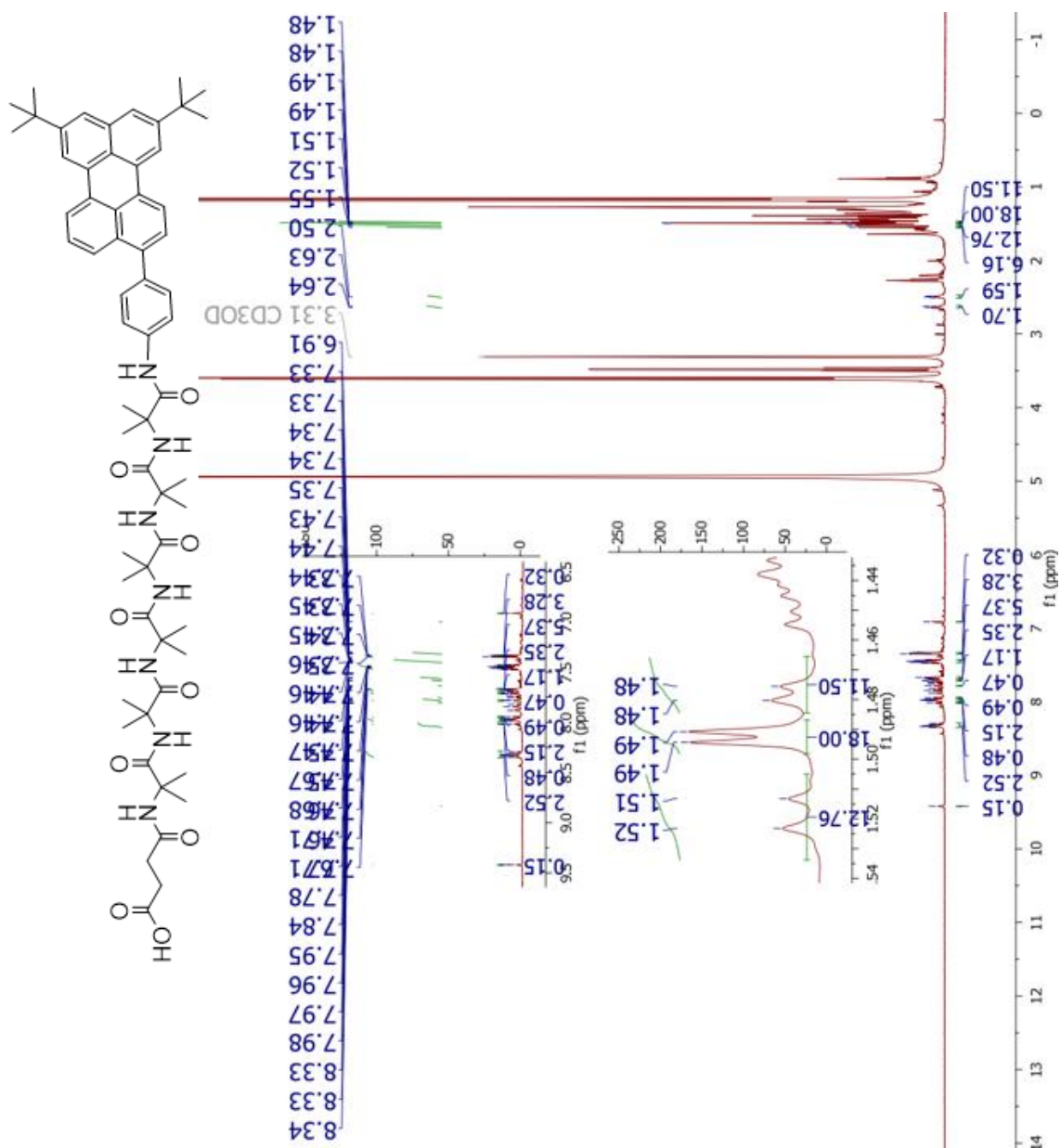


Fig. 0-43 ¹H NMR of 11 in CD₃OD

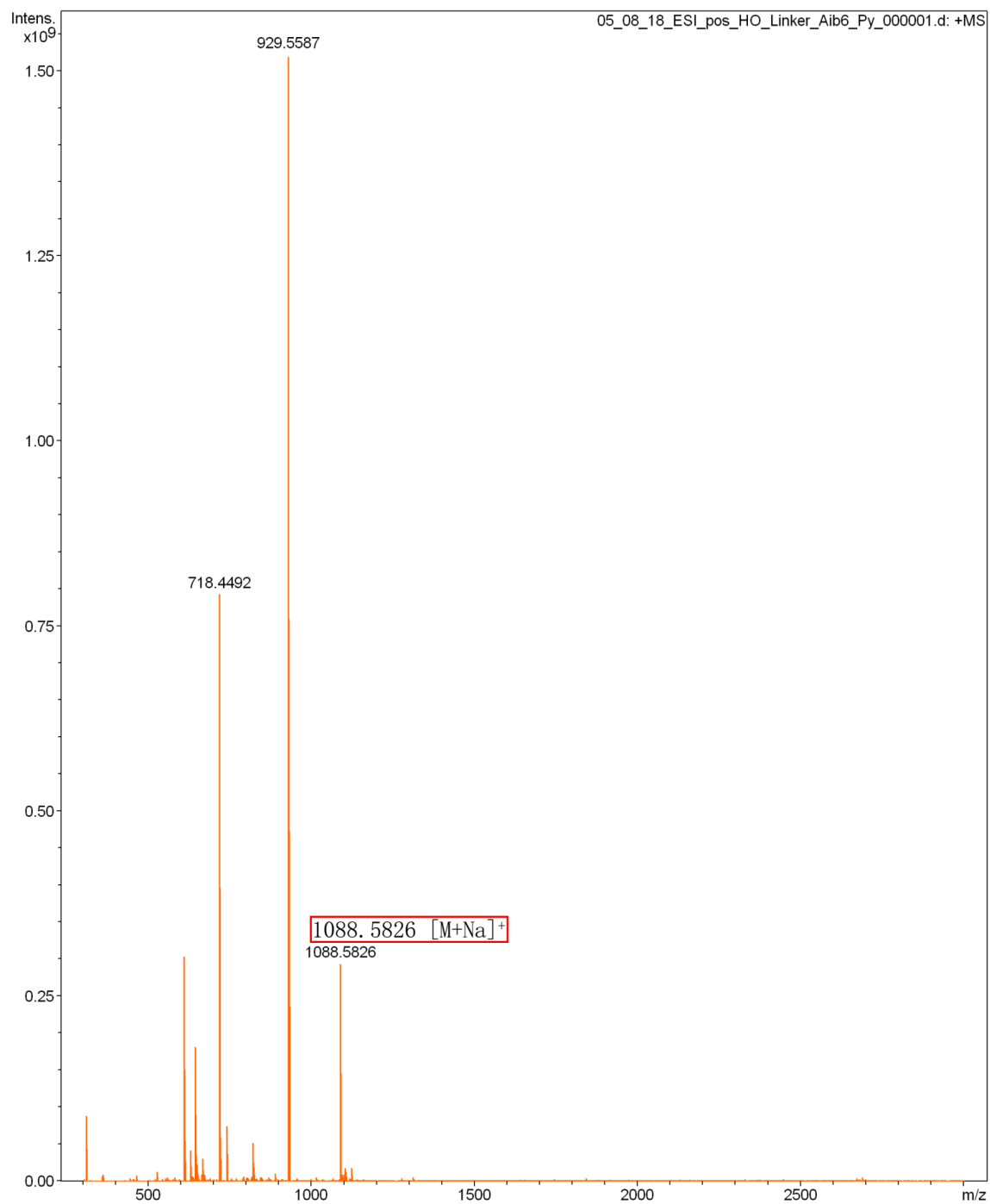
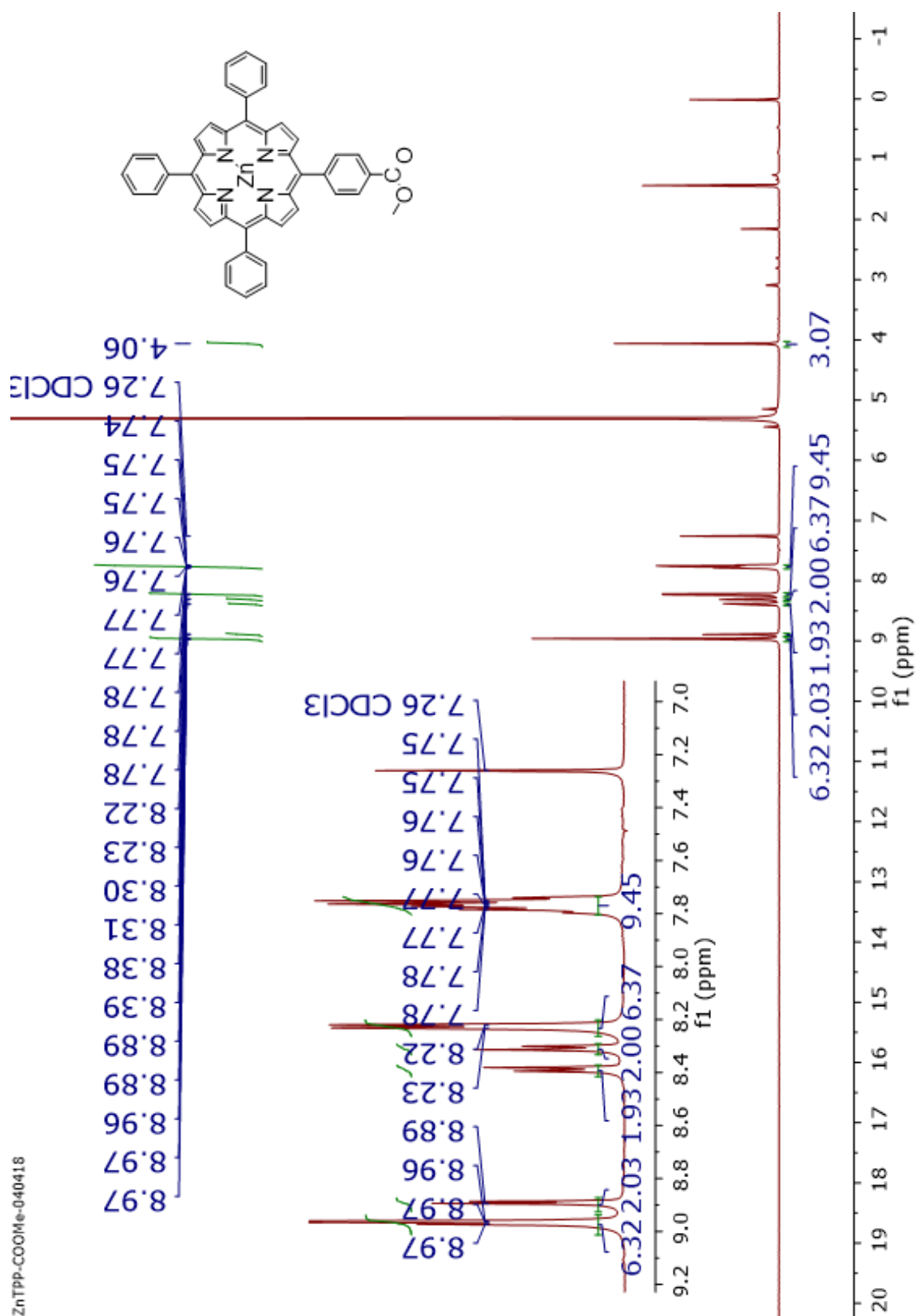


Fig. 0-44 ESI-MS spectra of **11**

Fig. 0-45 ¹H NMR of **12** in CDCl₃

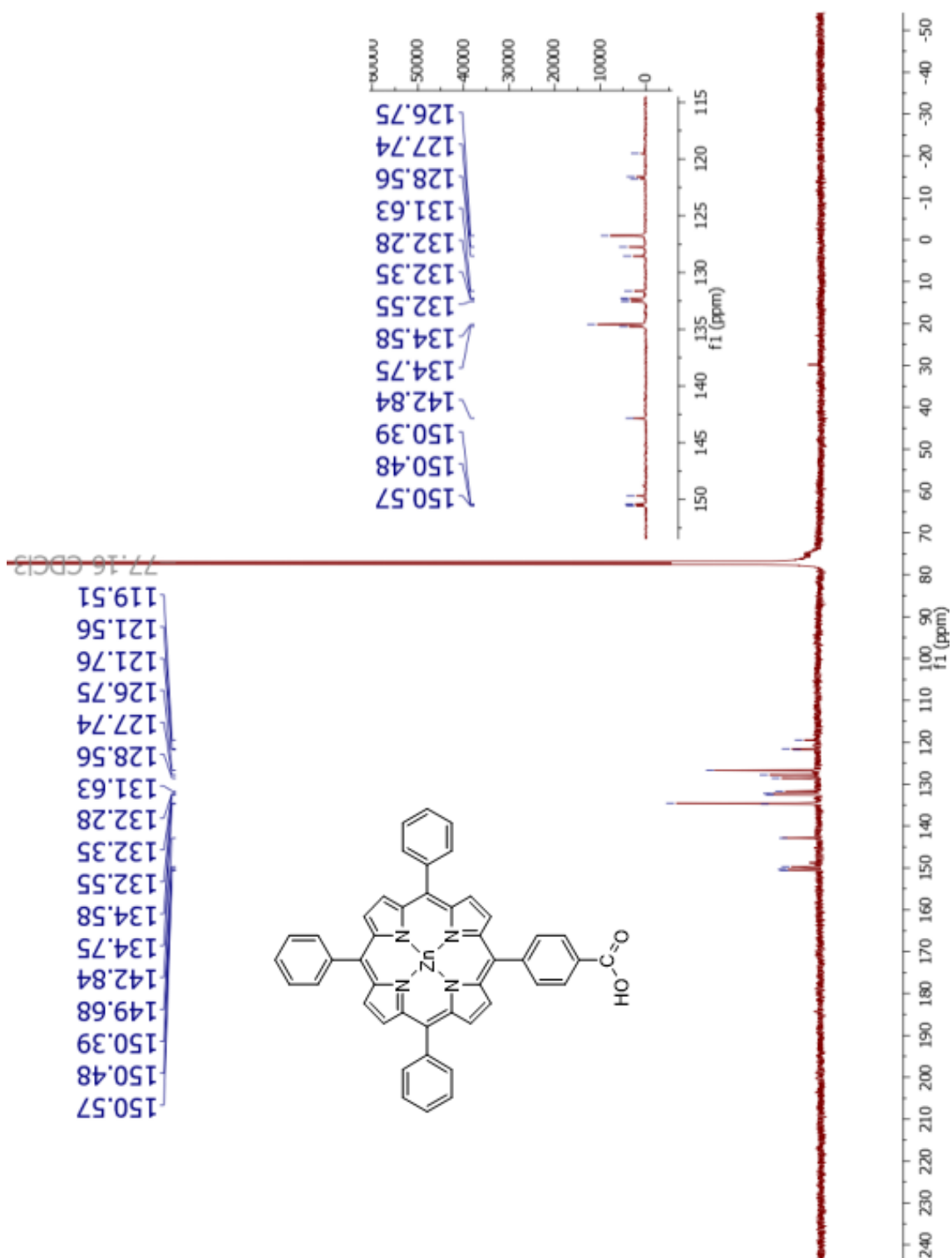


Fig. 0-47 ¹³C NMR of 13 in CDCl₃

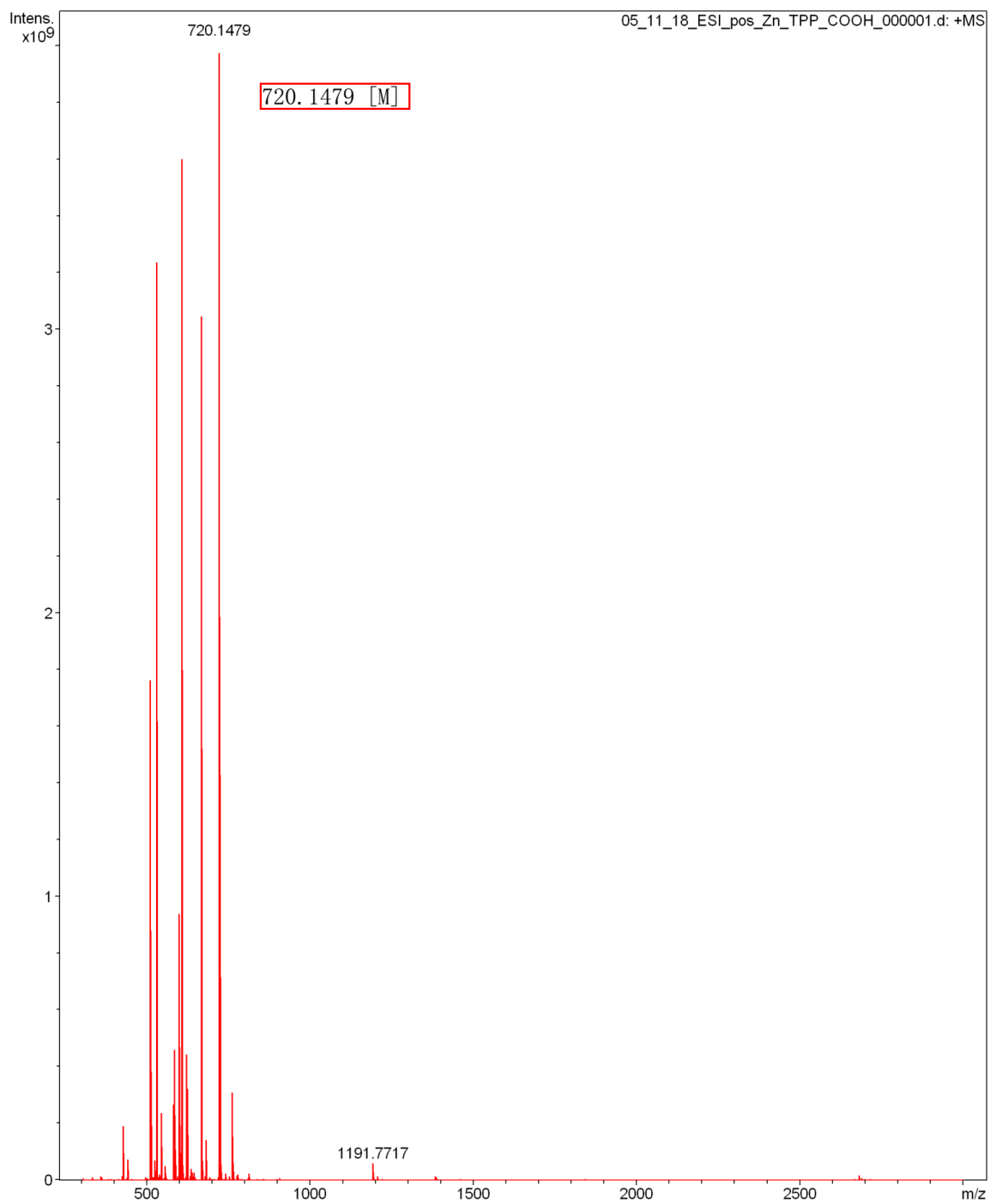


Fig. 0-48 ESI-MS spectra of **13**

Fig. 0-49 ^1H NMR of **14** in CDCl_3

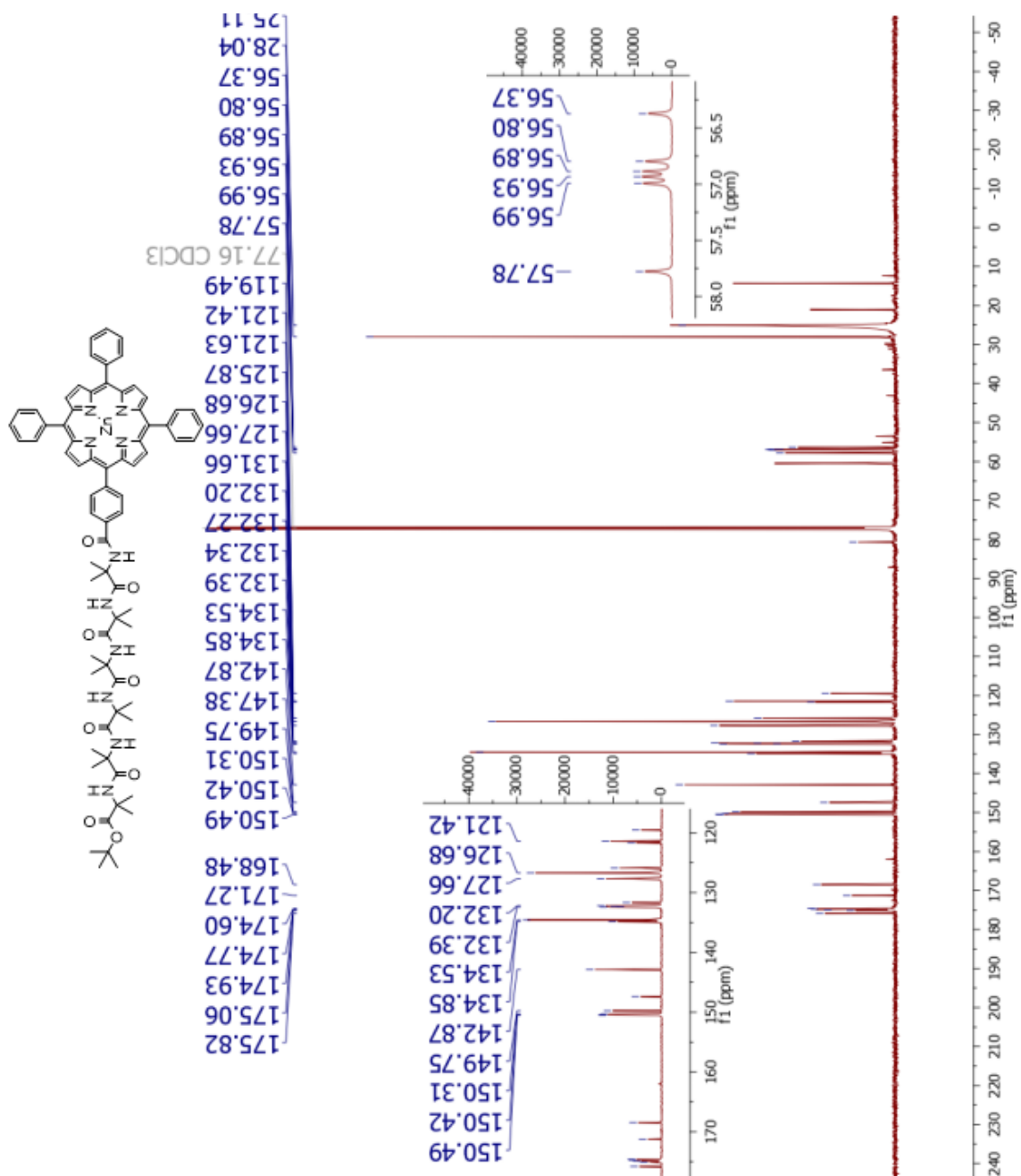


Fig. 0-50 ^{13}C NMR of **14** in CDCl₃

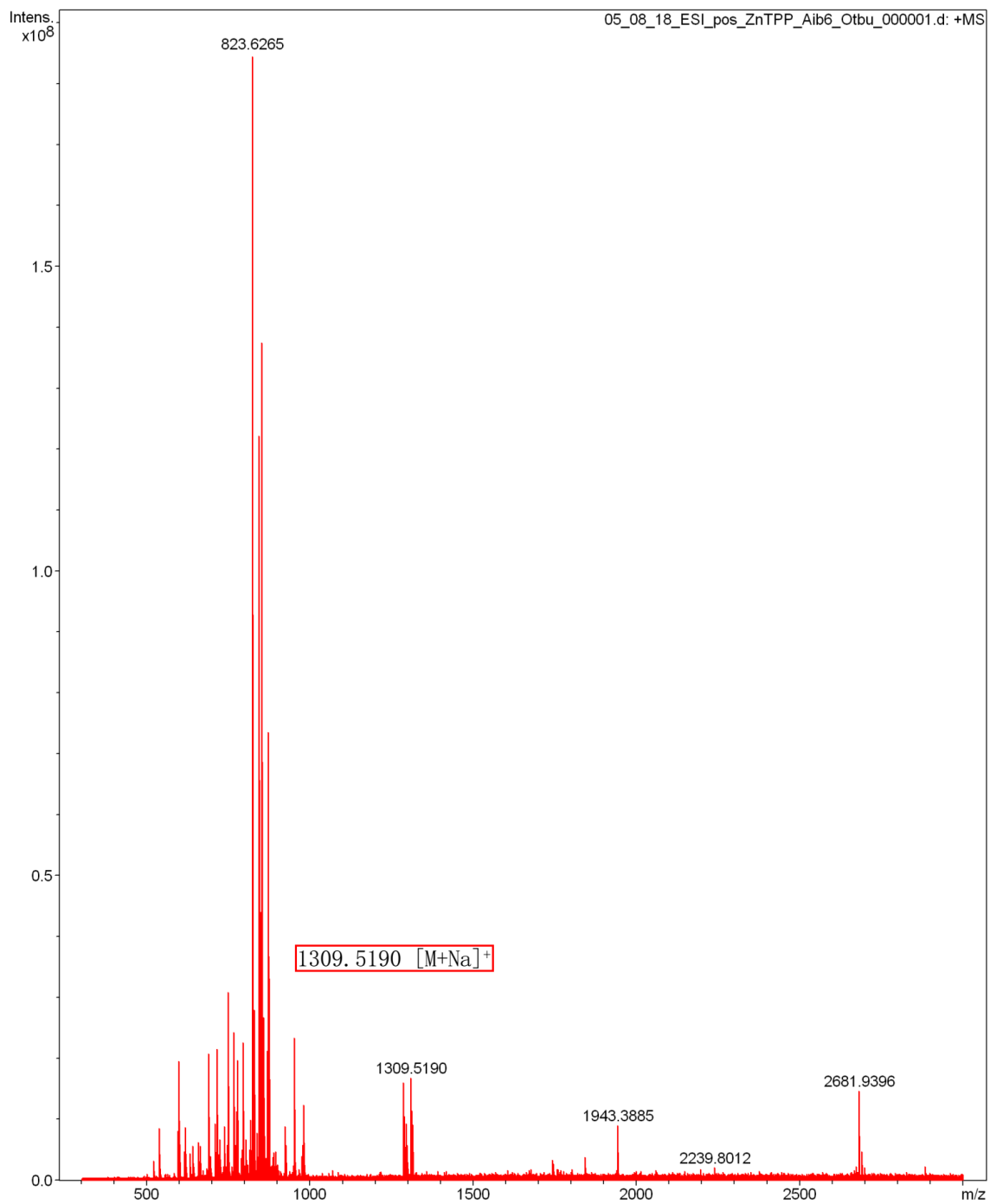


Fig. 0-51 ESI-MS spectra of **14**

Fig. 0-52 ^1H NMR of **15** in CDCl_3

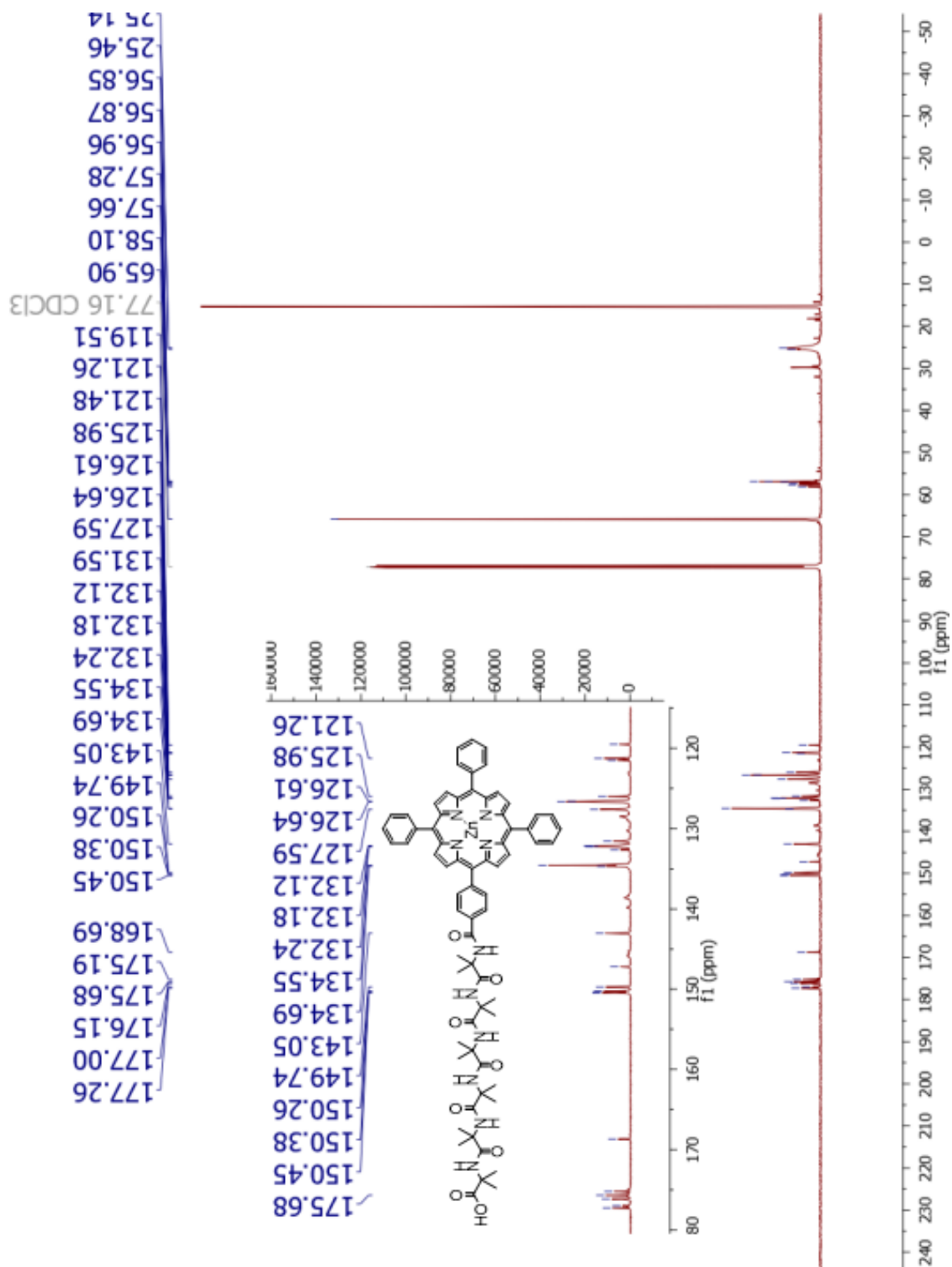


Fig. 0-53 ¹³C NMR of 15 in CDCl₃

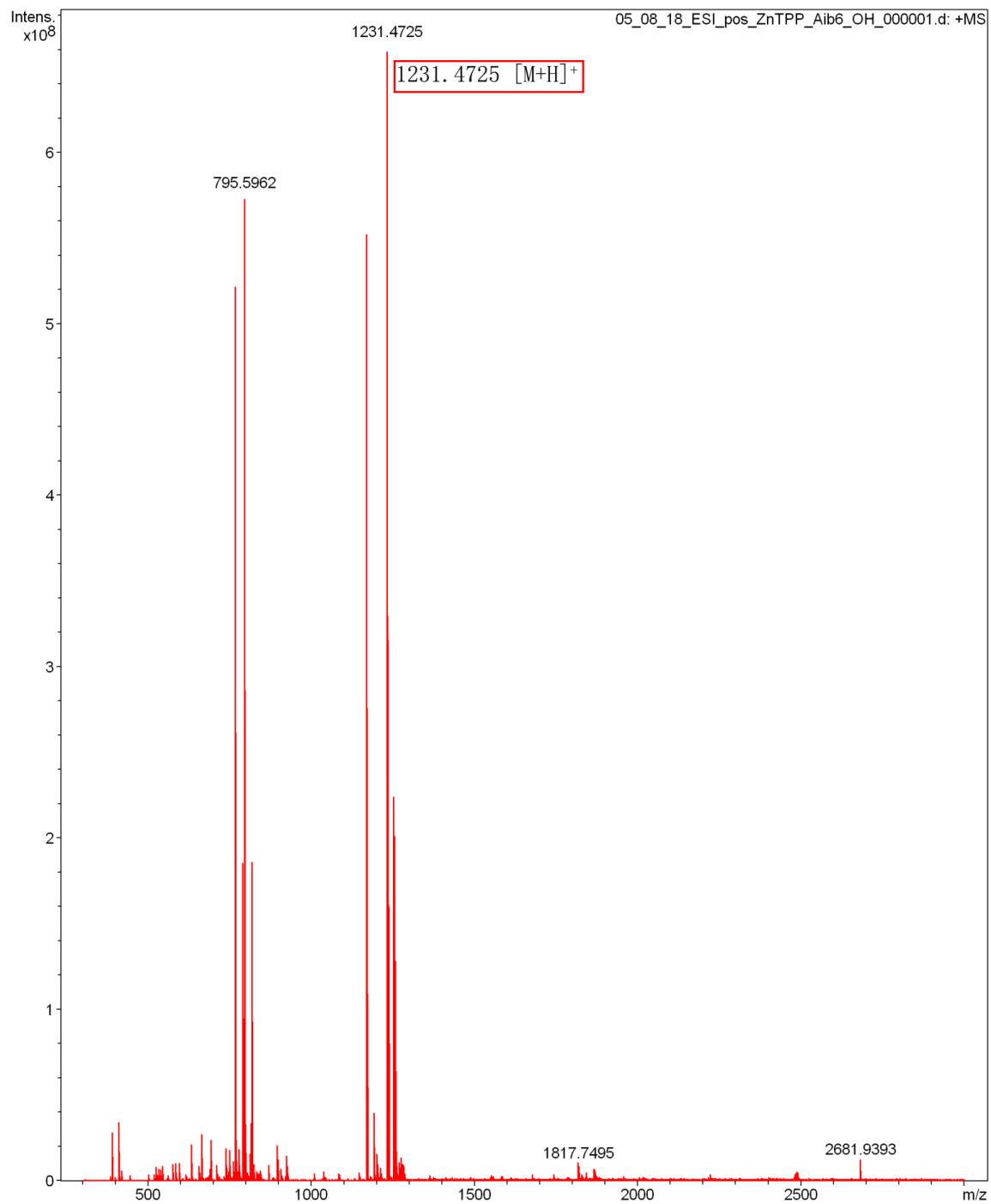


Fig. 0-54 ESI-MS spectra of **15**

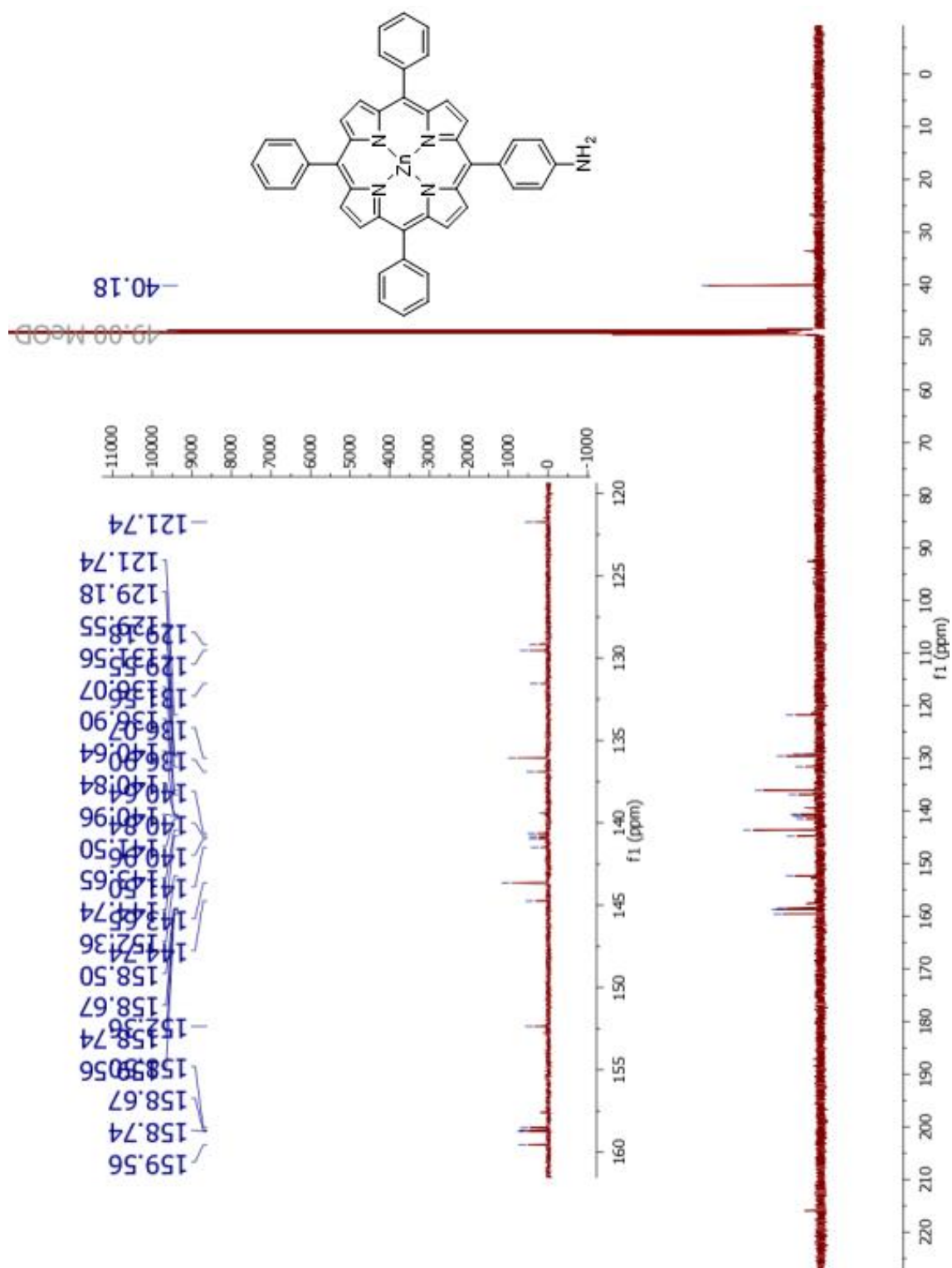


Fig. 0-56 ¹³C NMR of 16 in DMSO-d₆

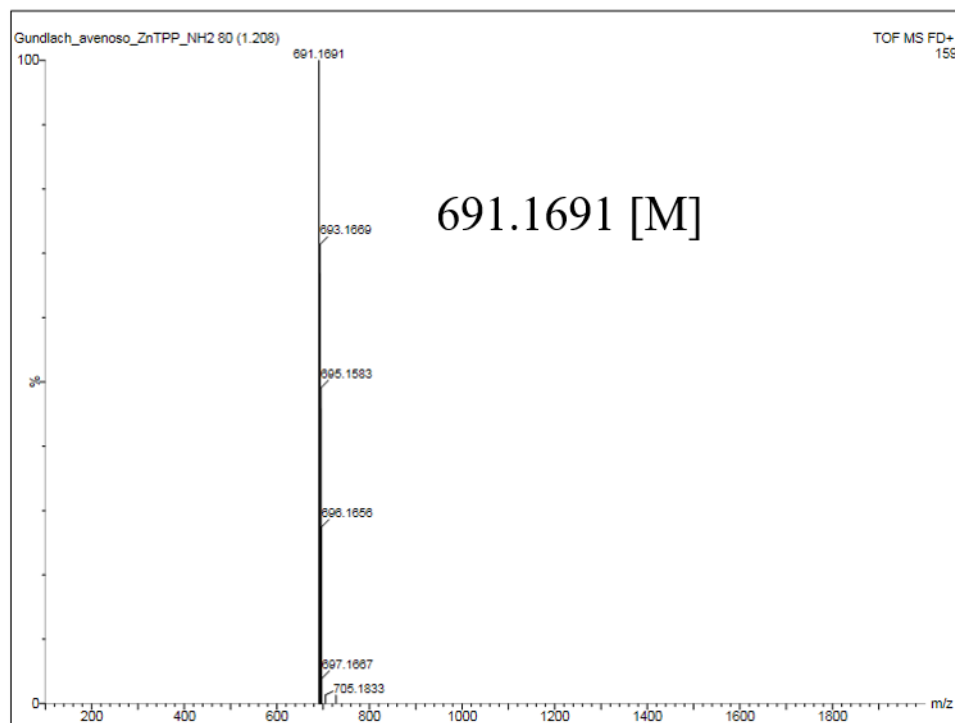


Fig. 0-57 ESI-MS spectra of **16**

Fig. 0-58 ^1H NMR of **17** in CD_3OD

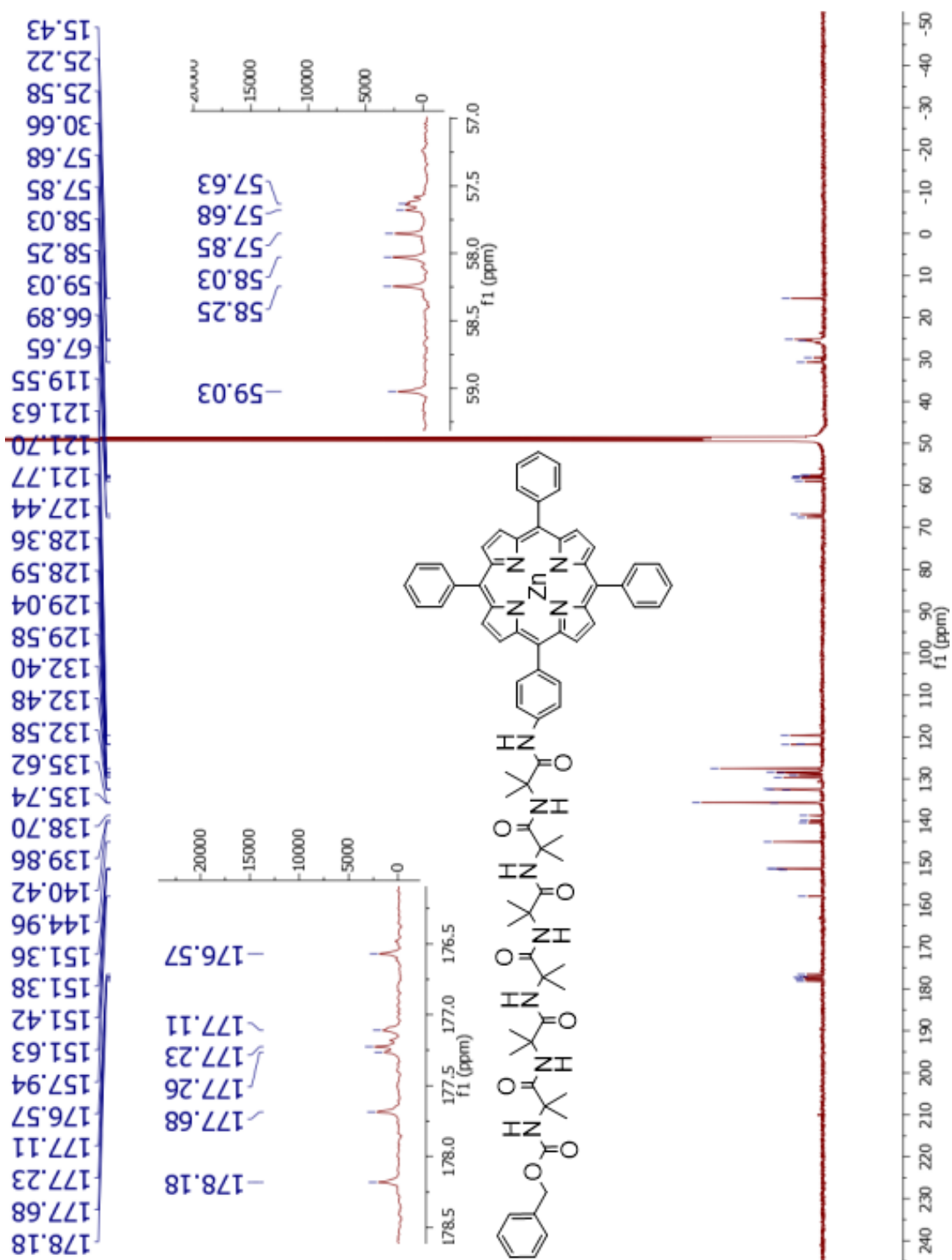


Fig. 0-59 ^{13}C NMR of **17** in CD_3OD

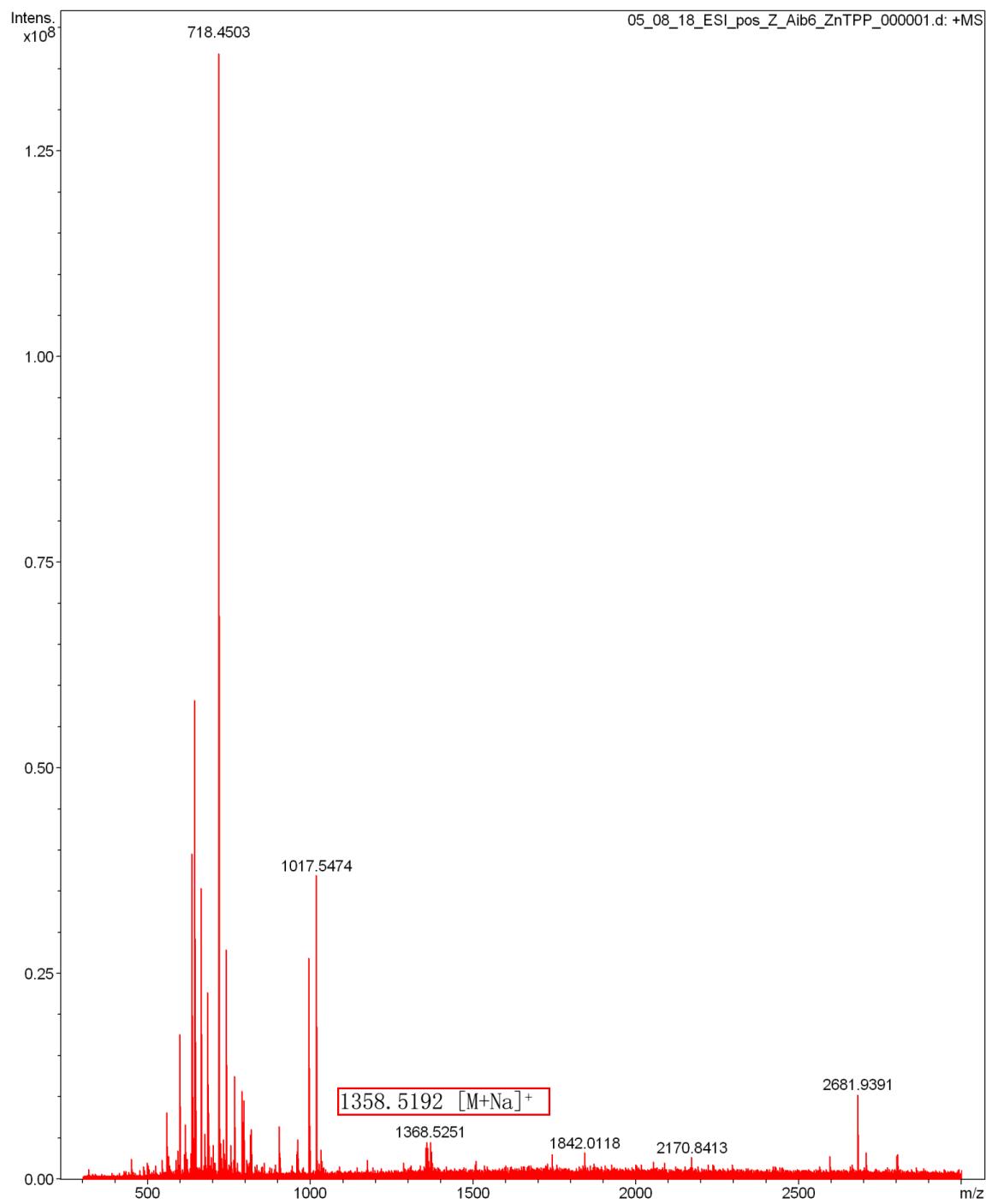


Fig. O-60 ESI-MS spectra of **17**

Fig. 0-61 ^1H NMR of **18** in CDCl_3

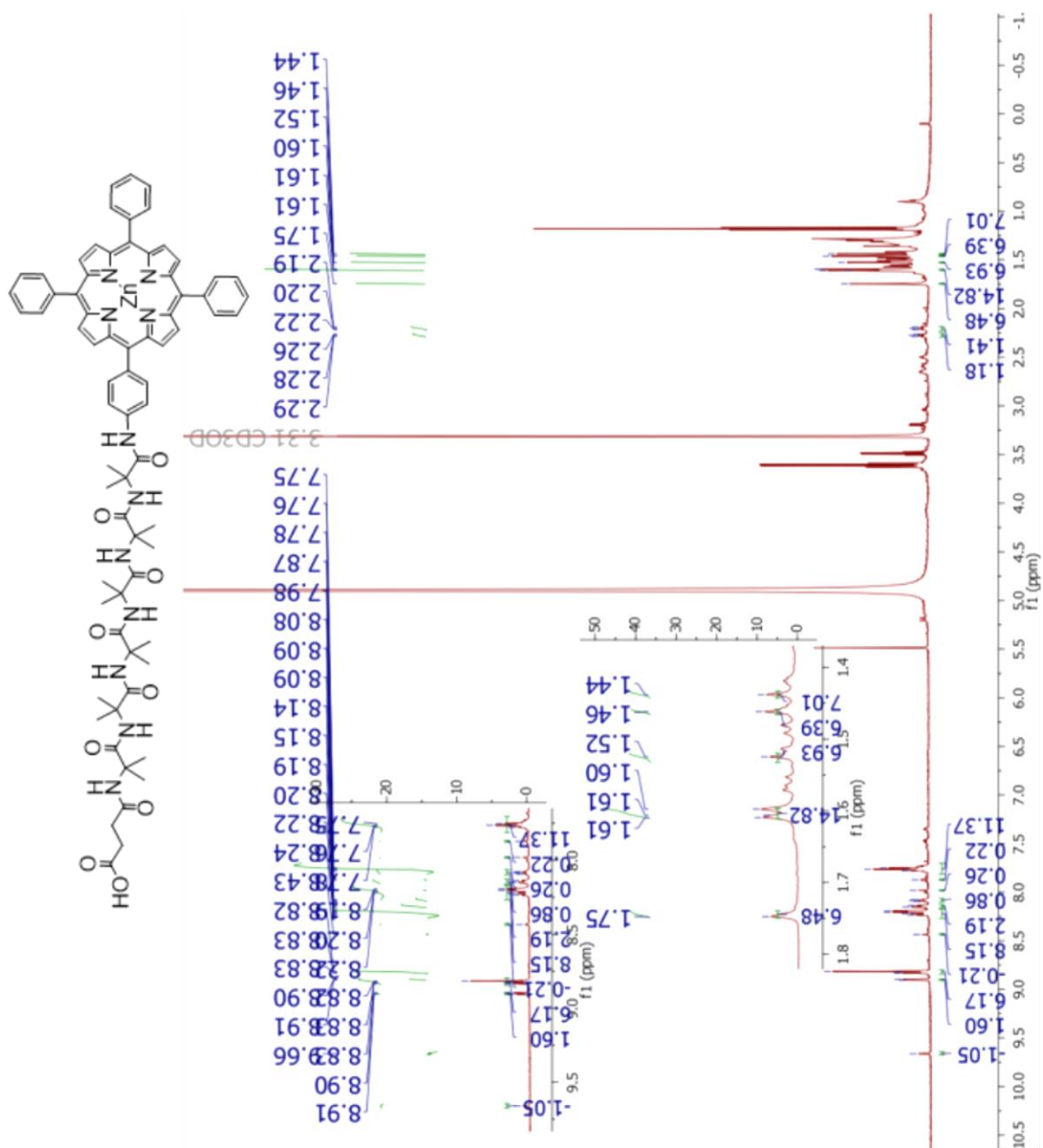


Fig. 0-62 ^1H NMR of **19** in CD_3OD

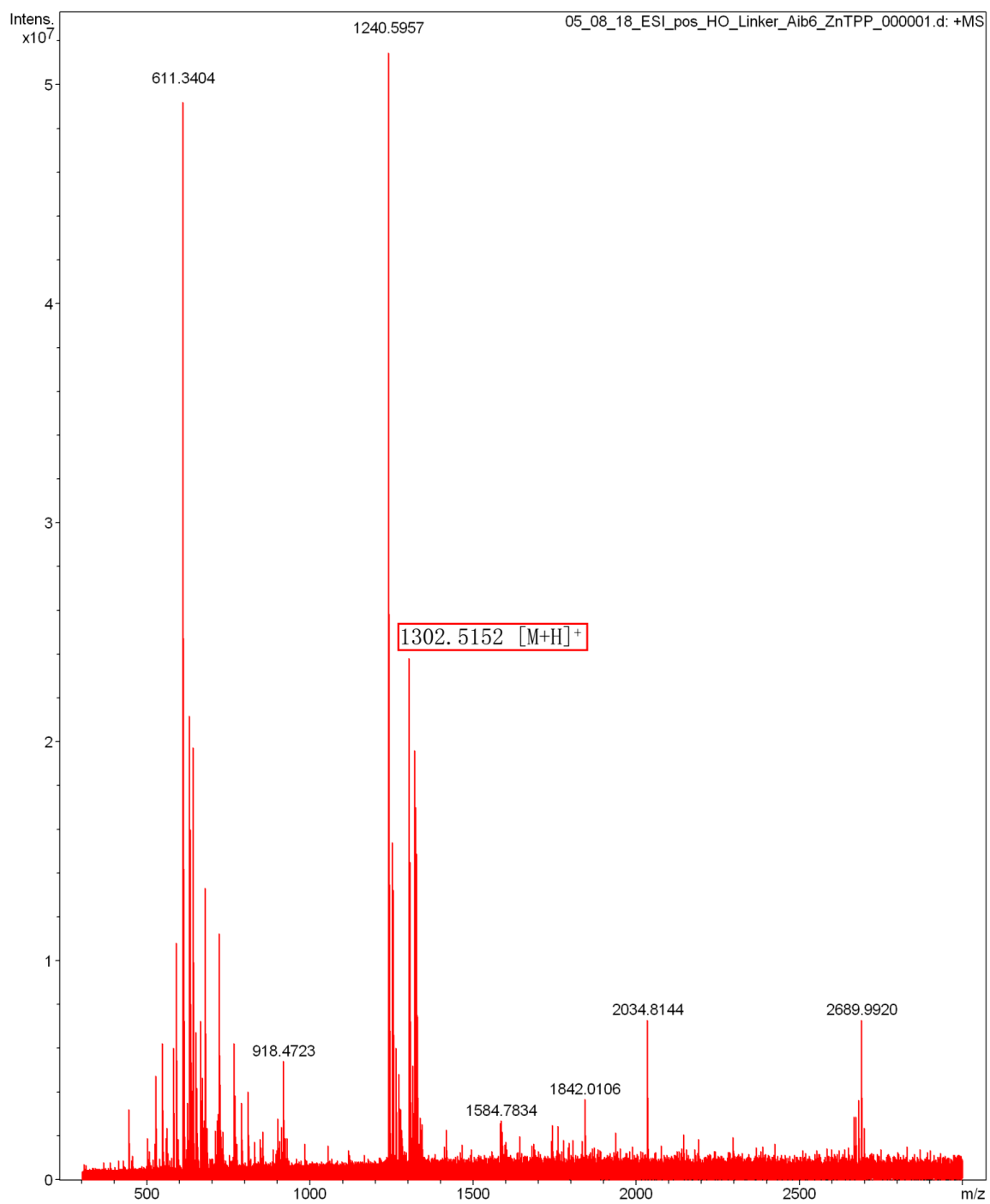


Fig. 0-63 ESI-MS spectra of **19**